Bioinspired Composite Materials

and

Biomimetic Catalysis

Dissertation
zur Erlangung des Grades
“Doktor der Naturwissenschaften”
im Promotionsfach Chemie

am Fachbereich Chemie, Pharmazie und Geowissenschaften
der Johannes-Gutenberg-Universität Mainz

vorgelegt von

M. Sc. –Chem. Rute da Conceição Tavares André

geb. in Barreiro (Portugal)

Mainz, 2012

Dekan:

Erster Berichterstatter:

Zweiter Berichterstatter:

Tag der mündlichen Prüfung: 17.07.2012

Dedication

To my father and my late mother.

ABSTRACT

Man has always taken inspiration in natural systems to develop new design approaches, mostly because Nature already solved many of today´s engineering problems. The field of bioinspired and biomimetic materials chemistry concerns the investigation of nature´s principles to produce complex and functional structures, as well as using its designing principles to develop new devices and materials with technological relevance, a step closer to the so called Green Chemistry. The work presented in this thesis is a compilation of different approaches on bioinspired and biomimetic materials synthesis. On a first approach inspiration is taken on natural biomineralizing systems. Silicatein, the main protein responsible for the synthesis of silica in marine sponge spicules, is used to produce new composite materials. A new soft and direct functionalization method for metal oxides is employed by using a glutamate tagged silicatein-α and core-shell nanostructure assemblies of TiO_2@SiO_2 or TiO_2@ZrO_2 are obtained due to the catalytic activity of the protein. These structures could be successfully characterized using transmission electron microscopy and energy-dispersive X-ray spectroscopy. By using silintaphin-1, a silicatein interactor protein, a fine tuning on the metal oxide shell on TiO_2 nanostructures can be achieved. The protein complex assembly on TiO_2 nanowire surfaces could be detected by confocal laser scanning microscopy. Furthermore silicatein-α is used to synthesized nanostructured cassiterite SnO_2, which could be confirm by transmission electron microscopy and X-ray diffraction. It is demonstrated that the protein has an active role in the catalysis and structuring of the formed material. By immobilizing silicatein-α on glass surfaces it is possible to obtain a SnO_2 coated transparent glass as characterized by scanning electron microscopy. In a step further to simplify the bioinspired deposition of metal oxides, spermine a natural recurring polyamine was used to functionalize glass surfaces and to induce the deposition of a SnO_2 coating which was characterized by atomic force microscopy, scanning electron microscopy and X-ray photoelectron spectroscopy. The SnO_2 coated surface is shown to be reactive when exposed to light by producing superoxide radicals and by changing its hydrophilicity. These surface properties are further applied in the degradation of organic contaminants like rhodamine B

and in antimicrobial activity induced by light exposure (photobiocidal surface). A second approach is shown in this work, by demonstrating that inorganic nanoparticles can mimic enzymes like peroxidases or haloperoxidase. In this case inspiration was taken in the vanadium containing haloperoxidases, to develop V_2O_5 nanostructures that show peroxidase and haloperoxidase (iodination and bromination) activity. V2O5 nanowires were synthesized via a hydrothermal method and characterized by transmission electron microscopy and X-ray diffraction. The material shows a Michaelis-Menten type of kinetics for the oxidation of ABTS in the presence of H_2O_2 (peroxidase activity) and for the bromination of MCD in presence of Br^- and H_2O_2 (haloperoxidase activity). The V2O5 nanowires are shown to be stable in different pH ranges and solvents, making them a versatile catalyst. The material is successfully applied in the synthesis of melanin-like polymers which show semiconductive behavior, as well as in the development of antifouling surfaces, by incorporating the nanoparticles in paint formulations.

ZUSAMMENFASSUNG

Schon immer hat der Mensch Inspiration in der Natur gesucht um neue Techniken und Ideen zu entwickeln. Insbesondere da die heutigen technischen Probleme bereits von der Natur effizient gelöst worden sind. Die interdisziplinäre biologisch inspirierte und biomimetische Materialwissenschaft befasst sich mit der Erforschung von Naturprinzipien. Deren Ergebnisse werden genutzt um komplexe und funktionelle Strukturen zu erzeugen, die wiederum zur Entwicklung neuer Materialien und Geräten mit technologischer Relevanz führen. Insbesondere in der grünen Chemie kommen diese Erkenntnisse zum Einsatz.

In dieser Dissertation werden neue Synthesewege für bioinspirierte und biomimetische Materialien aufgezeigt. Im ersten Teil dieser Arbeit wurde das Enzym Silicatein-α, welches in Schwämmen für die Synthese von Biosilikat verantwortlich ist, eingesetzt, um neue Kompositmaterialien zu entwickeln. Eine N-terminale Modifizierung des Enzyms mit acht Glutamaten ermöglichte die Entwicklung von neuen und schonenden Verfahren zur direkten Immobilisierung des Silicateins an Metalloxide, um deren Oberflächen zu funktionalisieren. Dadurch gelang die Herstellung von TiO_2@SiO_2- oder TiO_2@ZrO_2-Nanostrukturen allein durch die katalytische Aktivität des Proteins. Diese Strukturen konnten erfolgreich mittels Transmissions-elektronenmikroskopie (TEM) und energiedispersiven Röntgen-Spektroskopie (EDX) charakterisiert werden.

Durch die Verwendung von Silintaphin-1, einem Silicatein-α Interaktor, konnten weitere Veränderungen auf der Oberfläche der TiO_2@SiO_2- / ZrO_2-Nanostrukturen erreicht werden. Neben Rasterkraftmikroskopie (AFM) und TEM konnte auch der Protein-Protein-Komplex auf der Oberfläche der TiO_2-Nanodrähte mittels konfokaler Laser-Scanning-Mikroskopie (CLSM) nachgewiesen werden. Des Weiteren wurde Silicatein-α zur Synthese von Zinndioxid-Nanokassiteriten verwendet. Dies konnte mittels TEM und Röntgenbeugung (XRD) bestätigt werden. Es konnte gezeigt werden, dass das Enzym eine aktive Rolle in der Katalyse und Strukturierung des gebildeten Materials einnimmt. Durch die Immobilisierung des Silicatein-α auf Glasoberflächen ist es möglich, eine SnO_2 beschichtetes, transparentes Glas zu erhalten, welches durch Rasterelektronenmikroskopie (SEM) charakterisiert werden

konnte. Um die bioinspirierten Abscheidung von Metalloxiden zu vereinfachen, wurde in einem weiteren Schritt ein natürliches Spermin verwendet, um Glasoberflächen zu funktionalisieren. Die Beschichtung mit SnO_2 wurde durch AFM, SEM und Röntgen-Photoelektronen-Spektroskopie charakterisiert.

Die SnO_2 beschichtete Oberfläche erwies sich als reaktiv, wenn sie durch Licht angeregt wurde, d.h. es wurden Superoxidradikale erzeugt und die hydrophilen Eigenschaften verändert. Diese Oberflächeneigenschaften könnten zum Abbau von organischen Schadstoffen, wie Rhodamin B und zur der Herstellung von antimikrobiellen Oberflächen eingesetzt werden.

Im zweiten Teil dieser Arbeit konnte gezeigt werden, das anorganische Nanopartikel die Eigenschaften von Enzymen wie die der Peroxidase und Haloperoxidase imitieren können. Es wurden, inspiriert durch Vanadium enthaltene Haloperoxidasen, V_2O_5-Nanostrukturen entwickelt, die die Aktivität der Haloperoxidasen (Iodierung und Bromierung) nachahmen können. Die V_2O_5-Nanodrähte wurden mittels eines hydrothermalen Verfahrens synthetisiert und durch TEM und XRD charakterisiert. Das Material zeigte eine Michaelis-Menten Kinetik bei der Oxidation von ABTS [2,2'-Azino-di-(3-ethylbenzthiazolin-6-sulfonsäure)] in Gegenwart von H_2O_2 (Peroxidase-Aktivität) und bei der Bromierung von MCD (Monochlorodimedon) in Gegenwart von Br^--Ionen und H_2O_2 (Haloperoxidase-Aktivität). Die V_2O_5-Nanodrähte waren in verschiedenen pH-Bereichen und Lösungsmittel stabil, was diese zu einem vielseitigen Katalysator macht. Das Material konnte sowohl bei der Synthese von Melanin-ähnlichen Polymeren eingesetzt werden, welche halbleitende Eigenschaften aufzeigen, als auch in der Entwicklung von Antifouling-Oberflächen, indem die Nanopartikel zu Farben beigemischt und im Meer getestet wurden.

CONTENTS

List of Figures VIII
List of Schemes XI

1 Introduction 1
1.1 Bioinspired and Biomimetic approaches in material science 3
1.2 Bioinspired mineralization – the special case of marine sponges 6
1.3 Enzyme mimics – Biomimetic catalysis using nanostructured materials 19
1.4 References

2 Chemical mimicry: hierarchical 1D TiO2@ZrO2/SiO2 core-shell structures reminiscent of sponge spicules by the synergistic effect of silicatein-α and silintaphin 1 41
2.1 Introduction 42
2.2 Results and Discussion 44
2.3 Conclusion 51
2.4 Experimental Section 52
2.5 References 54

3 Enzymatic synthesis and surface deposition of tin dioxide using silicatein-α 58
3.1 Introduction 59
3.2 Results and Discussion 61
3.3 Conclusion 70
3.4 Experimental Section 71
3.5 References 73

4 Self-cleaning antimicrobial surfaces by spermine-catalyzed SnO_2 coatings on glass 77
4.1 Introduction 78
4.2 Results and Discussion 80
4.3 Conclusion 87
4.4 Experimental Section 88
4.5 References 92

5 V_2O_5 nanowires with an intrinsic peroxidase-like activity 96

5.1 Introduction …… 97

5.2 Results and Discussion …… 98

5.3 Conclusion …… 108

5.4 Experimental Section …… 109

5.5 References …… 111

6 Applications of V_2O_5 nanowires as haloperoxidase enzyme mimics 115

6.1 Introduction …… 116

6.2 Results and Discussion …… 118

6.3 Conclusion …… 132

6.4 Experimental Section …… 133

6.5 References …… 137

7 Conclusions and Outlook 141

8 Appendix 145

8.1 Supporting Information …… 146

List of Figures

1.1 Possible nanoparticle modifications and interactions with its environment. ……..… 4

1.2 Several levels of hierarchy in the structure of the skeleton of the glass sponge *Euplectella sp*. ……...… 7

1.3 Some examples of model organism in biosilicification. ……...…. 8

1.4 Silicatein-α catalytic activity. ……..... 9

1.5 Biocatalytic activity of surface-bound silicatein-α immobilized with nitrilotriacetic acid-based ligands. ……..……. 15

1.6 Immobilization of silicatein on different nanostructured surfaces. ……..…. 16

1.7 The horseradish peroxidase (HRP). ……..… 22

1.8 The vanadium dependent haloperoxidase (V-HPO). ……...… 25

1.9 The manganese dependent superoxide dismutase (SOD). ……...… 27

2.1. Modified silicatein-α with an 8x glutamate tag. ……..… 44

2.2. Fluorescence microscopy images of co-localization of silicatein-α and silintaphin-1 on TiO_2 nanowires. …….. 46

2.3. AFM phase contrast images of functionalized TiO_2 nanowires. ……...…. 47

2.4. Formation of silica or zirconia by immobilized glu-tagged silicatein-α on TiO_2 nanowires. ……... 48

2.5. Formation of silica or zirconia by immobilized glu-tagged silicatein-α and silintaphin-1 on TiO_2 nanowires. ……. 49

3.1. Characterization of SnO_2 obtained by silicatein-mediated synthesis. ……. 62

3.2. Characterization of SnO_2 synthesized using silicatein as catalyst, after annealing at 200°C. ……. 63

3.3. UV-Vis spectra of SnO_2 synthesized using silicatein as catalyst. ……..…. 64

3.4. Light and fluorescence optical micrographs of the immunostaining against silicatein for SnO_2 formed in the presence of the protein. ……... 65

3.5. Scheme illustrating the steps for glass slide functionalization with histidine tagged silicatein. …… 66

3.6. Fluorescence microscopy images showing the immunostaing against silicatein-functionalized glass surfaces. ……..…… 67

3.7. SEM images of SnO_2 coated glass slides using silicatein. ……..… 68

3.8. Optical images and UV-vis transmittance spectra of SnO_2 covered glass slides mediated by silicatein. …… 69

3.9. QCM measurement of tin oxide deposition on silicatein functionalized silicon dioxide sensors. …… 70

4.1 Spermine mediated synthesis of SnO_2. …… 80

4.2 Physical characterization of spermine/SnO_2 coated glass slides. …… 83

4.3 Photocatalytic activity of SnO_2 spermine-mediated coated surfaces. ……..…… 85

4.4 Photobiocidal activity of SnO_2 spermine-mediated coated surfaces against *E.coli*. …… 87

5.1. Characterization of V_2O_5 nanowires. ……..… 99

5.2. V_2O_5 nanowires catalytic activity in the oxidation of TMB and ABTS. ……..…… 100

5.3. Dependency of ABTS oxidation activity on the V_2O_5 nanowire concentration. …..… 102

5.4. Steady-state kinetic study of V_2O_5 nanowires. …… 103

5.5. Structure and proposed catalytic mechanism of V_2O_5 nanowires. …… 105

5.6. EPR spectrum of a superoxo-vanadium species formed on the surface of V_2O_5 nanowires in the presence H_2O_2. …… 105

5.7. Re-utilization of V_2O_5 nanowires in the oxidation reaction of ABTS in the presence of hydrogen peroxide. ……...…… 107

5.8. The effect of organic solvents on the ABTS oxidation activity mediated by V_2O_5 nanowires. …… 108

6.1 Iodination of thymol blue by V_2O_5 nanowires. ……...… 118

6.2 Time-course UV-vis analysis of polymerization of dopamine by V_2O_5 nanowires. …. 120

6.3 Physical characterization of the synthetic melanin obtained by polymerization of dopamine with V_2O_5 nanowires. ……... 121

6.4 UV-Vis and FTIR characterization of the synthetic melanin product. ……..…… 122

6.5 Concentration dependence of bromination activityof MCD by V_2O_5 nanowires and bulk V_2O_5. …… 125

6.6 Steady-state kinetics of the V_2O_5 nanowires and proposed reaction mechanism. ……. 127

6.7 Influence of the catalytic activity of V_2O_5 nanowires on the growth of Gram positive (*S. aureus*) and Gram negative (*E. coli*) bacteria. ……..…… 130

6.8 Application of V_2O_5 nanowires in marine paint with antibacterial/antifouling properties. ……. 130

6.9 Summary of in situ experiments with V_2O_5 nanowires as additive in paint formulations. 132

List of Tables and Schemes

Table 2.1 Ratios of Si/Ti and Zr/Ti for the samples using only silicatein or silicatein and silintaphin. ……..…… 50

Scheme 6.1 Proposed mechanism for the formation of the melanin-like polymer by the catalytic action of V_2O_5 nanowires. ……..… 124

CHAPTER 1

INTRODUCTION

Biomimetics or bio-inspired approaches rely on the observation of Nature´s systems, processes and elements in order to retrieve inspiration for the design of new solutions to several mechanical or functional problems. Even though this is a emerging field in materials science, Humans have always taken inspiration in natural systems to develop new design approaches, mostly because Nature already solved many of today´s engineering problems (self-cleaning surfaces, mechanical resistance, etc.) through a trial and error process that has been lasting for billions of years, in constant evolution. Leonardo da Vinci was probably one of the first to take a biomimetic approach to many of his inventions. He studied the mechanical functions of the skeleton and the muscular forces that are applied to it which prefigured the modern science of biomechanics. He also invented several flying apparatus in the process, based on his studies of the mechanics of flight in birds. [1,2] Nevertheless the term biomimicry was mostly made popular by the author Janine Benyus with her book "Biomimicry: Innovation Inspired by Nature" from 1997 where she defines it as "a new science that studies nature´s models and then imitates or takes inspiration from these designs and processes to solve human problems."[3] In the last years an increasing amount of publications has been released with research based or dedicated to biomimetic processes or bio-inspired materials. The work here presented contributes with new insights in these two

approaches by bringing naturally available biomolecules and synthetic produced materials in a common platform to produce hybrid products that can have economically interesting intrinsic properties.

This dissertation is divided in basically three parts, which complement each other by showing different approaches in functional material synthesis. The first part gives a state of the art and background information on the design of bioinspired materials. The second part deals with bio-inspired mineralization using available biomolecules while the third part describes the synthesis of inorganic nanoparticles with a mimetic enzymatic activity. In brief, **Chapter 1** gives an overview about bio-inspired materials synthesis with special emphasis on the use of silicatein for metal oxide synthesis, as well as an overview on the use of nanoparticles as enzyme mimics. **Chapter 2** describes the use of Glu-tagged silicatein-α for specific functionalization of metal oxides (i.e. TiO_2) and how its catalytic activity for the formation of SiO_2 and ZrO_2 is affected by the present of another interactor protein, silintaphin-1. The synthesis of core-shell nanowires of TiO_2@ZrO_2 and TiO_2@SiO_2 is demonstrated.

In **Chapter 3** silicatein-α is used for the synthesis of SnO_2 and a simple route for its functionalization on glass surfaces is demonstrated. Furthermore it is shown that the protein retains activity when bound to the glass surfaces producing a transparent coating of SnO_2.

In **Chapter 4** a polyamine, spermine is used for the synthesis of SnO_2 and could be functionalized on glass surfaces to produce SnO_2 coatings. This surfaces show to be photocatalytically active, producing radicals when exposed to light which could be demonstrated for the use in organic dyes degradation and as a photobiocidal surface.

Chapter 5 reports the synthesis of V_2O_5 nanowires which have a catalytic activity similar to peroxidase enzymes. The nanostructures show a Michelis-Menten type of kinetics and its mechanism of catalysis is address. **Chapter 6** is an extension of the previous chapter where the same V_2O_5 nanostructures are show to be a mimic of haloperoxidase enzymes which could be further applied to the synthesis of synthetic melanin and to the development of antifouling surfaces to apply on boat hulls. **Chapter 7** includes brief conclusions and outlook over the work demonstrated. An appendix with supporting information is given in **Chapter 8**.

1.1 Bioinspired and Biomimetic approaches in material science

Recent scientific developments have allowed us to have a greater insight in the complexity of biological systems and its structural and functional relationships. This combined with recent advances in nanotechnology, has allowed the creation of new nanomaterials which can have the best of both worlds – the highly specificity, molecular recognition and self-assembly properties of natural biomolecules like enzymes or DNA with the unique physical properties of nanomaterials (catalytic, electronic, photonic). Several different approaches have been taken to the development of bioinspired materials in chemistry. Special focus has been put on nanostructure control or precise binding of biological molecules to technological relevant solid interfaces. Structures with potential applications in nano-devices have been developed by incorporating techniques such as lithography, atomic force microscopy (AFM) or self-assembled monolayers (SAMs) and the complex functions and recognition abilities of different biological systems.[4-6] Diverse surfaces like silica, gold, iron oxide or graphite have been functionalized with biomolecules (proteins, peptides, small biomolecules) either by non-specific binding, specific surface interactions of using bridging ligands, to produce materials that are able to recognize natural substrates. A great amount of work has been done on nanoparticle functionalization with specific targeting molecules that possess high affinity to certain cell types which is particularly useful in therapies against cancer or in drug delivery.[7] Other types of functionalization have been achieved with monoclonal antibodies or other molecules like folic acid for example, for specific targeting of tumor cells.[8,9] (Figure 1.1)

Man has developed several different materials with special properties mostly recurring to a wide variety of elements and alloys and complicated fabrication methods. On the other side natural materials are based on a relative small group of constituent elements that are used to synthesize a variety of functional (or multifunctional) materials, be it polymers or minerals, or mixtures of both. While in industrial fabrication of man-made materials, reaction conditions often require the use of high temperatures, aggressive reaction media or demanding techniques, in nature everything is synthesized in mild, physiological conditions, meaning mostly neutral or slightly acidic/basic pH, ambient temperature (or even extreme low temperatures) and aqueous media. Nature as perfected the concept of *green chemistry* to synthesize either inorganic materials with intricate structures or even for extremely efficient

and selective catalysis of organic molecules or energy conversion like in photosynthesis, to a level still not achieved in a bench.

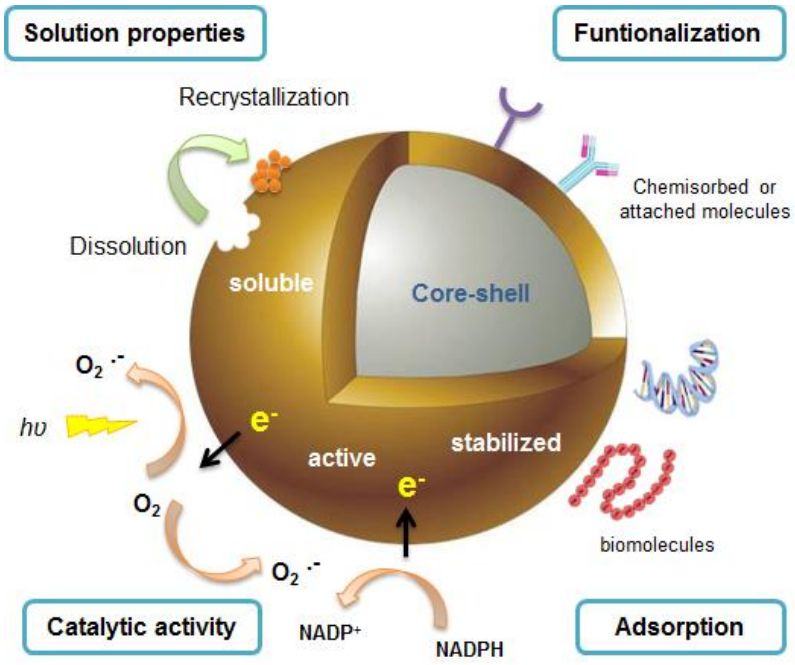

Figure 1.1 Possible nanoparticle modifications and interactions with its environment. The interface properties can be controlled by surface functionalization and lead to changes in the dissolution and degradation. Chemical stabilization can be achieved by core-shell functionalization, by protective surface ligands or macromolecules. Particle uptake behavior may be changed via attached molecules, either for receptor binding, by corona formation or particle aggregation and subsequent precipitation. Finally, any catalytic (i.e. redox, acid-base, atom transfer) activity changes the interaction with the particle environment by being involved in redox cycles, by oxidation, photochemical reactions, or leaching of metal atoms via complexation by proteins or pH changes.

The hierarchical composition of biomaterials brings also special properties, like is the case of bone with its great mechanical properties[10], or glass spicules of sea sponges which can guide light like an optical fiber.[11] Since these biomaterials are included in living, ever changing organisms, they can be constantly repaired, providing an important aspect of self-healing or self-maintenance which of course is of great interest in developing new materials decreasing the maintenance and renewal costs, for example.[12] Most biomaterials or other biological structures are also multifunctional. For example chitin and chitosan which are present in the cuticles of insects, shells of crustaceans or even in the cell wall of fungi, besides providing an important structural protection due to its resistance to environmental conditions, it has also an

important antimicrobial activity.[13] This is also the ultimate goal in many engineering challenges or specialized materials, to achieve several functionalities in one single material.

Biosynthesis of inorganic materials has received particular attention in the last years. Many groups have studied the use of natural recurring proteins, their domains or other smaller molecules and peptides for the precipitation of inorganic materials.[14,15] (*see section 1.2*) Alternatively whole cells or cell extracts have been used has substrates for biosynthesis of nanoparticles. Researchers have identified many strains of bacteria, fungi and algae for this purpose, mostly by adding gold, silver or platinum salts in the growing media or cell extracts. Bigall et al. showed, the synthesis of noble metal materials can be achieved by growing several fungal species directly in a colloid (Ag, Au, Pd, Pt) solution.[16] Focus has also been given in the in the special physical/chemical properties of these nanomaterials, in particular their enhanced catalytic activity (*see section 1.3*) mostly due to their increased surface area and reactive surface atoms. Noble metal nanoparticles for example, (Pd,Pt, Au, Ag) have been for long used as catalysts in organic chemistry.[17,18]

1.2 Bioinspired mineralization – the special case of marine sponges

In biological mineralizing systems, the formation of inorganic structures occurs in aqueous media at neutral pH by a set of biomolecules, such as proteins and polysaccharides. A prototypical case is provided by marine sponges and diatoms.[19,20] Organisms are able to synthesize a variety of inorganic materials (calcium carbonate, calcium phosphate, silica, iron oxide, etc.) from simple precursors under mild reaction conditions, resulting in highly complex structures with several levels of hierarchy, ranging from the nano-level to the macro-level.[21,22] (Figure 1.2) These mineralized inorganic–bioorganic composite materials are formed either by controlled condensation in specific compartments or by regulation of the concentration of the inorganic precursors with the help of enzymes. Diatoms[23] sponges[24] and grasses[25] provide classical examples of biosilicification processes whereby complex and unique 3D structures are synthesized even with very low concentrations of silicon present in the surrounding environment. Great efforts have been made to isolate, purify and characterize proteins and other biomolecules driving the mild synthetic route of silica polymerization in vivo. Prominent examples include long-chain polyamines and sillafins from diatom shells,[26-29] and silicateins from marine sponges.[21,30-32] (Figure 1.3) The formation of silica spicules in marine sponges is of particular interest, because of their hierarchical structures and the resulting properties; that is, the spicules have high mechanical strength and are excellent optical waveguides. Other examples are the hexactinellid sponge *Euplectella marshalli*, whose skeletal structure is composed of elaborate cylindrical structures with six hierarchical levels,[14] (Figure 1.2)and the giant basal spicules of *Monoraphis chunii* (also a hexactinellid), which can reach a length of up to 3 m and a thickness of up to 8.5 mm.[33] By emulation of the chemistry behind natural mineralization pathways, the known biomineralization agents might be employed to fabricate materials with non-natural compositions and a wide spectrum of properties.[14]

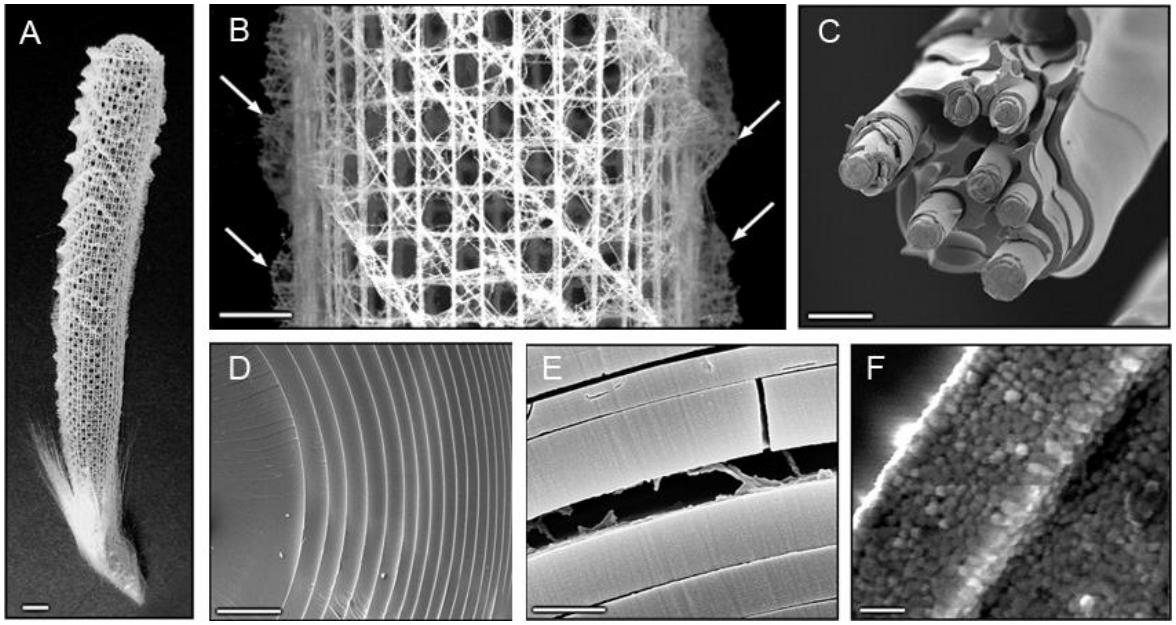

Figure 1.2 Several levels of hierarchy in the structure of the skeleton of the glass sponge *Euplectella sp*. (A) photograph of entire skeleton, scale bar: 1 cm; (B) Fragment of the cage structure showing the square-grid lattice, scale bar: 5 mm; (C) fractured and partially HF-etched single beam revealing its ceramic fiber-composite structure, scale bar: 20 μm; (D) cross section through a typical spicule in a strut, showing its characteristic laminated architecture, scale bar: 5 μm; (E) fractured spicule, revealing an organic interlayer, scale bar: 1 μm; (F) bleaching of biosilica surface revealing its consolidated nanoparticulate nature, Scale bar: 500 nm. (*Science* **2005**, *8*, 5732.)

Reaction mechanism of silicatein and versatility of the precursors

The isolated biomolecules involved in silica formation, e.g. silaffins, siladicins, and silicateins are also a source of inspiration for the use of other biomolecules, such as synthetic polyamines, polypeptides, and a variety of polymers that mimic the active site of either silaffins or silicatein (e.g diblock copolymers) to perform similar tasks.[21,27,34-38] The structures, compositions and molecular masses of the bioinspired polymers, as well as the experimental conditions used in the laboratory (e.g. buffer composition and pH), have been shown to significantly affect the kinetics of the condensation and precipitation processes, and also the shape of the formed silica colloids, which can range from typical spherical shapes to hexagons or other more complex forms.[34-38] For bioinspired silaffin-related silicification, the mechanism of silica formation from solutions containing such additives involves an electrostatic interaction between positively charged amines and negatively charged silica precursors, facilitating the passive condensation of silica around the amine group.

Additionally, the molecular backbone acts as a template for the structure of the deposited material.[28,39-42] In contrast to other organisms that deposit silica in a passive, template-controlled manner,[26-29,34-38,41-43] marine sponges (phylum Porifera) show the singular ability to actively synthesize their siliceous skeleton enzymatically;[21,30-32,39,40,44-48] silicatein-α, silicatein-β, silicatein-γ (subunits), silicase and silintaphin-1 and 2 are known representatives of the proteins involve in biosilification in sponges. (Figure 1.3) These proteins have been isolated and cloned from different siliceous sponges (e.g. *Tethya aurantium* and *Suberites domuncula*).[23,31-32,40,44-47]

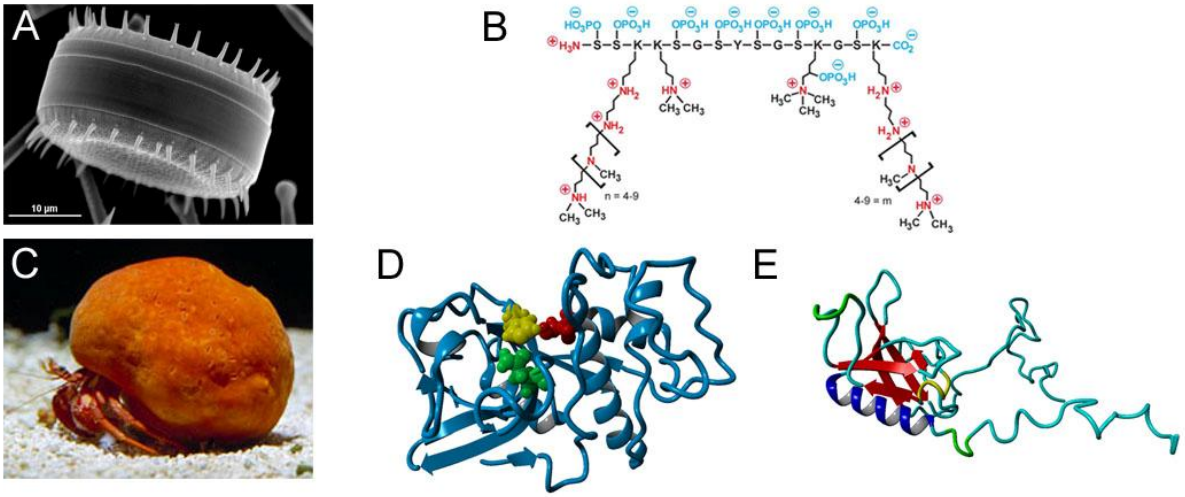

Figure 1.3 Some examples of model organism in biosilicification. (A) Diatom (*Stephanodiscus neoastraea*) and (B) the protein silaffin responsible for silica precipitation in diatoms. (C) An example of a marine sponge (Demospongeae, *Suberites domuncula*) and some of the proteins found to be involved in spicule formation: (D) silicatein-α and (E) silintaphin-1.

Silicatein-α possesses a high homology with cathepsin L, and the cystein residues present in the later are fully conserved in silicatein indicating that both proteins have a similar 3-D structure. Two of the three residues (His and Asn) of the "catalytic" triad of the cathepsin L active site are also conserved in silicatein, but the third active site Cys in the cathepsin is replace by a Ser residue in silicatein. The interaction between the Ser and His residues in the active center is essential for the catalytic activity.[39] (Figure 1.4 A) The reaction mechanism for polycondensation of orthosilicate can be described in 3 steps: Step 1 starts with

nucleophilic attack of the (negatively charged) Ser oxygen atom at the (positively charged) silicon atom of the orthosilicic acid, with transfer of one proton from the imidazole nitrogen of the His to an OH ligand of the substrate molecule. One water molecule is released, followed by a nucleophilic attack of the oxygen atom of one of the OH ligands of the covalently bound silicic acid molecule at the silicon atom of a second substrate molecule. In Step 2 loss of a second molecule of water occurs after proton transfer from the imidazole group. Then rotation of the Si-O-C bond occurs between the resulting disilicic acid and the Ser residue. Nucleophilic attack of an oxygen atom of a second OH ligand of the first silicic acid molecule to a third substrate moiety occurs. In Step 3 occurs the cyclization of the resulting trisilic acid initiated by nucleophilic attack of the (negatively charged) oxygen of an OH ligand of the third condensated orthosilic acid. Finally a reactive trisiloxane ring is released after hydrolysis of the Si-O-C bond.[30] (Figure 1.4 B)

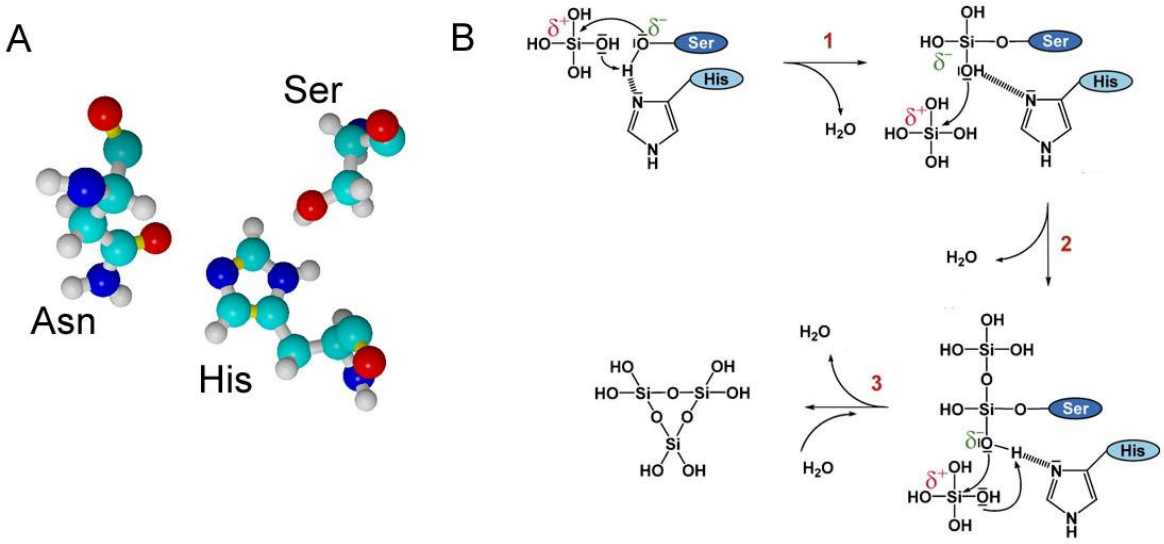

Figure 1.4 Silicatein-α catalytic activity. (A) the catalytic center with the 3 main aminoacids (Asn: asparagine; His: histidine; Ser: serine); (B) proposed mechanism for the polycondensation of orthosilicate by silicatein-α (see text above).

Besides the formation of silica and polysilsesquioxanes,[39,49-50] these proteins can also catalyze the formation of different metal oxides such as TiO_2,[51] ZrO_2,[52] $CaTiO_3$,[53] and GaOH/Ga_2O_3.[54] Furthermore, the materials formed often exhibit crystalline polymorphs that normally require high temperatures[51,54,55] or extreme pH conditions for preparation by classical synthetic

methods.[56-58] This indicates that silicateins have a relatively flexible active center, and a very general mechanism can therefore be assumed to underlie their catalytic activity. The charge density associated with the polarity of the Si–O–C bonds makes metal alkoxide precursors (e.g. Si, Ge, Sn, Ti, Zr, and Hf) susceptible to hydrolysis. However, simple alkoxides such as tetraethoxysilane (TEOS) do not occur in nature; therefore, other molecules, such as esters, alcohols, sugars, and catechols, may play an active role in the transport, storage and sequestration of silicic acid. It is known that, in both diatoms (silica deposition vesicles) and marine sponges (silicassomes), silica is accumulated in intracellular vesicles in higher concentrations than in those where spontaneous polymerization occurs (> 100 p.p.m.).[59] This suggests that, parallel with the sequestration ⁄ storage mechanism, a stabilization process preventing the spontaneous polymerization of silica must be active.[34,60-62] The natural substrate for silicatein has not been identified unambiguously, although the most likely candidate seems to be orthosilicic acid, because of its natural abundance in seawater. Several other silicon alkoxides or other metal alkoxides have been used in vitro (as synthetic substrates) to assess the intrinsic catalytic activity of silicatein.[63,64] Typically, the sol–gel synthesis of metal oxides from the corresponding alkoxides proceeds in two steps: (a) hydrolysis of a metal alkoxide to yield a metal hydroxide (olation); and (b) polycondensation (oxolation) through the condensation of two metal hydroxide species, with concomitant release of water (oxolation), or of a metal hydroxide with a metal alkoxide, with release of alcohol (alkoxolation),[65] leading, ultimately, to an oxide network.[66,67] Depending on the charge density of the metal and the coordinating strength of the ligand, the hydrolysis and the polycondensation reactions rates vary to a considerable extent; they can be very fast for sterically less hindered metal alkoxides. As a result, early transition metals of groups 4 and 5, such as titanium, zirconium, hafnium, and niobium, are more prone to nucleophilic attack by water molecules, whereas silicon alkoxides are more resistant to nucleophilic substitution by water molecules. Therefore, synthetic hydrolysis and polycondensation of silicon alkoxides must be initiated either by a catalyst (acid, base, fluoride, or biomolecule) or elevated temperatures,[66] as opposite when using silicatein-α (neutral pH and ambient temperature).[21,39,48]

Synthesis of nonbiological metal oxides with silicatein

As described above, silicatein-α possesses the ability to catalyze the hydrolysis and condensation of various metal oxides that do not occur in nature. This nonbiological activity

of silicatein can be attributed to the similarity in size and charge of the electrophilic centers of the substrate molecules and the steric tolerance of the silicatein-α active center. One of the most difficult tasks in demonstrating the catalytic activity of silicatein-α towards nonbiological metal oxides is the choice of suitable precursor compounds, because most metal alkoxides are very unstable and will spontaneously react with water at room temperature to form an amorphous metal oxide precipitate,[65,67] precluding their use as silicatein-α precursors. For titania, this problem could be circumvented by using titanium bis(ammonium lactato) dihydroxide as a water-stable, alkoxide-like precursor,[50] whereas for zirconia, the hexafluoro complex (ZrF_6^{2-}) proved to be a suitable choice.[68] The energetics imposed by the surface and bulk lattice energies lead to the formation of otherwise metastable polymorphs. The mobility of the reactant atoms at ambient temperatures prevents the formation of well-crystallized products, yielding nanocrystalline or partially amorphous compounds (e.g. rutile-TiO2 and γ-Ga_2O_3)[53,69] with reduced free surface area, owing to particle aggregation. The formation of stabilized amorphous or a nanocrystalline phase for structural purposes is favored from a biological perspective.[26,69] Native silicatein filaments can catalyze and template the in vitro formation of nanocrystalline gallium oxohydroxide (GaOOH) and the spinel polymorph of gallium oxide (γ-Ga_2O_3), using stable gallium nitrate as precursor.[53] Gallium (Ga^{3+}), like its Al^{3+} congener, is an example of aquo acid formation; that is, at neutral pH, the $[Ga(H_2O)_6]^{3+}$ hexaaquo complex predominates, whereas in acidic or basic solution, protonation / deprotonation reactions lead to the formation of unstable aquo / hydroxo complexes such as $[Ga(H_2O)_{6-n}(OH)_n]^{(3-n)+}$.[60-62,70,71] Consequently, in acidic media, the condensation of hydrolyzed Ga^{3+} will proceed via either olation or oxolation.[65] In contrast, under neutral pH conditions or in the presence of thermally denatured protein filaments, no hydrolysis of $[Ga(H_2O)_6]^{3+}$ occurred. However, upon incubation of gallium nitrate with protein filaments, nanocrystalline GaOOH was formed.[71] Moreover, when lower Ga^{3+} concentrations were present, silicatein-mediated hydrolysis of gallium nitrate yielded nanocrystalline spinel-type gallium oxide (γ-Ga_2O_3) as the kinetically preferred product. Electron diffraction analysis showed that, in both cases, the nanocrystals formed via the silicatein-mediated route exhibit a preferred orientation relative to the axis of the main protein filament. This suggests that, in the case of γ-Ga_2O_3, the protein filaments are responsible not only for catalyzing the hydrolysis of the water-stable gallium nitrate precursor, but also for influencing the preferred pseudo-oriented crystal growth relative to the protein. From a materials science perspective, perovskites with a generic structure ABO_3 drawn from a range of metals, subject to certain

size constraints, represent a very flexible system. The different physical properties (ferroelectric, dielectric, pyroelectric, piezoelectric, ferromagnetic / ferrimagnetic, electrically (super)conducting or catalytic behavior) of perovskite-phase materials are related to their phase transitions, which in turn are sensitive to variables such as chemical composition, purity, numbers of surface and bulk defects, grain size, and sintering conditions.[60,72] Hence, the control of these parameters is critical for effective property control. The methods for synthesizing perovskites with an ABO_3 generic structure are far from the physiological conditions. However, sponge filaments isolated from *T. aurantium* are able to template barium titanium oxyfluoride ($BaTiOF_4$) as dispersed florets of nanocrystals.[73] Unlike previous silicatein-catalyzed reactions involving the formation of silica, titania, or gallium oxide, the synthesis of $BaTiOF_4$ required a cofactor, H_3BO_3, which was proposed to scavenge excess fluoride ions generated by the hydrolysis of the $BaTiF_6$ precursor.[69]

Deposition of thin films with surface-bound recombinant silicatein-α

For many applications, it is necessary to synthesize thin films of metal oxides on solid surfaces rather than in solution, with simultaneous control of the pattern and shape of the deposited inorganic materials over more than the micrometer scale. However, the chemically driven deposition of uniform silica coatings on solid surfaces has not been achieved under ambient conditions, despite many potential applications for such materials in sensors,[74] membranes, and structural materials.[75] Metal oxide thin films on solid supports could be prepared by immobilizing silicatein-α and making use of its catalytic properties. Moreover, the creation of silica patterned thin films by the use of immobilized polypeptides and polyamines that act as templates has been reported with several methods, such as electrostatic deposition,[76,77] direct write assembly,[78] holographic patterning,[79] photolithography,[78] and surface-initiated polymerization.[80] Silicatein-α was immobilized on various inorganic substrates with His-tags, Glu-tags, and Cys-tags. Initially, the immobilization and activity of surface-bound recombinant silicatein-α containing a His-tag (His_6 additional sequence) was demonstrated on solid supports by the formation of heterogeneous silica, titania and zirconia films.[71,81,82] In the initial experiments, silicatein-α was immobilized on self-assembled monolayers (SAMs) on Au(111) surfaces by use of a nitrilotriacetic acid-terminated organic thiol (Figure 1.5A). The thiol binds to the gold surface, and the nitrilotriacetic acid terminus remains free for Ni^{2+} and His-tag protein complexation.[83] The hydrolytic activity of surface-bound silicatein-α was confirmed by the formation of a thin layer of silica (SiO_2, surface

coverage ≈ 70% with TEOS as a metal alkoxide precursor; Figure 1.5B–D). The nitrilotriacetic acid–Ni^{2+} linker group selectively binds to the His-tag of the recombinant protein, thereby providing a controlled spatial orientation. These factors (linker and well-defined spatial orientation) are of major importance for the catalytic activity of surface-bound enzymes, which is constrained by: (a) the accessibility of the active site of the enzyme to the substrate; and (b) protein folding (e.g. denaturation). In an alternative biomimetic silicification approach – based on kinetically controlled catalytic hydrolysis and polycondensation – synthetic analogs of the active site of the enzyme were immobilized on surfaces. Therefore, attempts were made to anchor recombinant silicatein-α (His-tagged) on gold surfaces with a reactive ester polymer (Figure 1.5E).[70] After protein complexation, the film thickness increased by 3.4 nm, which is close to the theoretical diameter of the 24-kDa silicatein-α. This was confirmed by a positive cross-reaction between polyclonal antibodies raised against silicatein-α and the surface, which was observed by confocal laser microscopy (Figure 1.5F). The catalytic activity was verified by the formation of 50–60-nm layered particles of TiO_2 and a thin film of cubic ZrO_2 (an unusual ZrO_2 polymorph, in particular at ambient reaction conditions) on surface-bound silicatein-α, with titanium bis(ammonium lactato) dihydroxide and hexafluoro-zirconate (ZrF_6^{2-}) as stable nonbiological precursors (Figure 1.5G,H). In a similar manner, silica-coated magnetic nanoparticles γ-Fe_2O_3@SiO_2 could be fabricated.[84] For this purpose, His-tagged silicatein-α was immobilized on γ-Fe_2O_3 nanoparticles functionalized with a nitrilotriacetic acid-containing polymeric ligand and by making use of the efficient chelating properties of Ni^{2+}. The particle-bound silicatein-α was shown to be active for catalyzing and structurally directing the deposition of a protective biosilica shell around the magnetic oxide nanoparticles. This convenient surface modification strategy based on a multifunctional nitrilotriacetic acid-containing polymeric ligand could be generalized for other surfaces. His-tagged silicatein-α was immobilized on the highly hydrophobic surface of WS_2 nanotubes, which – in turn – made WS_2 highly water-soluble (Figure 1.6A).[85] The activity of WS_2 surface-bound silicatein-α was demonstrated by the formation of a dense and hydrophilic TiO_2 coating on hydrophobic WS_2 surfaces (Figure 1.6B). High-resolution transmission electron microscopy (TEM) images showed nanocrystalline domains with a fringe spacing of 0.32 nm, which is close to the (110) lattice spacing of rutile-type TiO_2 (Figure 1.6C). Whereas most of the above examples rely on the hydrolytic abilities of silicatein-α, its (nonphysiological) reductive properties can be utilized for the fabrication of unusual structured composites. This was demonstrated by

functionalizing TiO_2 nanowires,[86] first with a bifunctional polymeric ligand containing pendant catechol moieties (specific anchor groups for metal oxides) and nitrilotriacetic acid functionalities (complexation with Ni^{2+}), and then with recombinant His-tagged silicatein-α, which allowed the subsequent silicatein-mediated growth of gold nanocrystallites on the TiO_2 surface with $AuCl_4^-$ as precursor (Figure 1.6D).[82,87] The reductive properties of recombinant silicatein-α were attributed to free thiols present in the protein.[33] Moreover, the nanocrystals possess an unusual S3 symmetry axis, which suggests chiral induction from the protein to the triangular shaped nanocrystals (Figure 1.6E,F). In order to expand the affinity of silicatein-α to other solid supports and to simultaneously reduce the number of reaction steps, new tags were introduced during protein expression. For example, silicatein-α containing a Glu-tag (Glu_8) in its C-terminus was developed, allowing specific immobilization on hydroxyapatite.[88] Comparative studies of the strengths of adhesion of silicatein-α and Glu-tagged silicatein-α to hydroxyapatite showed that the additional Glu-rich sequence is, indeed, required for a strong binding affinity / interaction. Its potential application in dentistry was explored; that is, the treatment of dentin tubules with Glu-tagged silicatein-α and exposure to a silica source (sodium metasilicate was used, owing to its negligible toxicity) led to tubule occlusion, suggesting that this integration of protein into toothpastes can reduce significantly hypersensitivity. It may be expected that this method can be generalized for other surfaces, with the development of other material-specific tags that would allow the synthesis of a wide range of nanocomposite materials under physiological conditions.

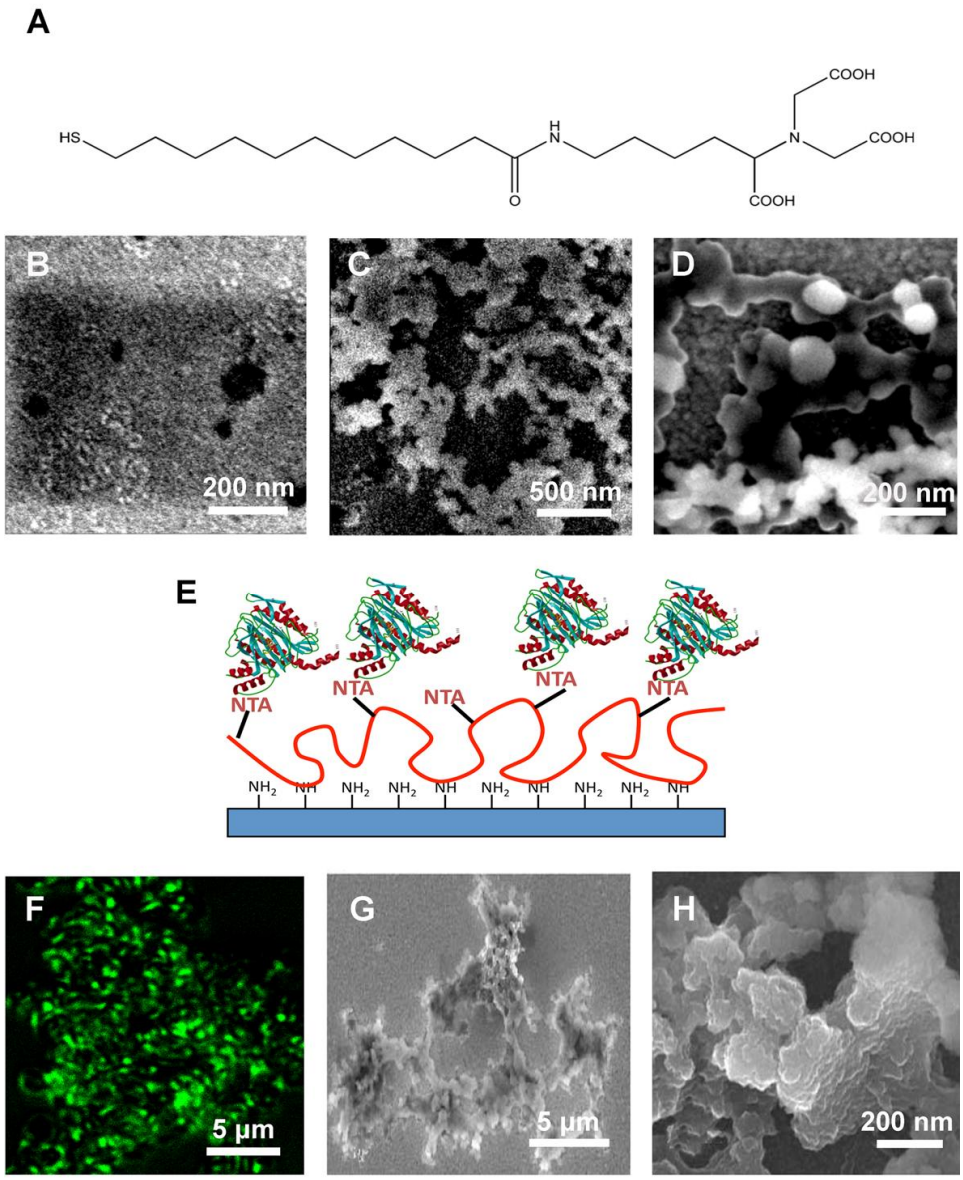

Figure 1.5 Biocatalytic activity of surface-bound silicatein-a immobilized with nitrilotriacetic acid-based ligands. (A) Chemical structure of nitrilotriacetic acid-terminated alkanethiol used as a SAM to immobilize His-tagged silicatein-α to gold (111) surfaces. (B–D) SEM images of silicatization onto surfaces functionalized with nitrilotriacetic acid alkanethiol without Ni^{2+} (A) and nitrilotriacetic acid alkanethiol with Ni^{2+} chelating silicatein (B, C). No observable formation of SiO_2 occurred on nitrilotriacetic acid alkanethiol-modified surfaces (A). In contast, Ni^{2+}-chelated silicatein immobilization onto nitrilotriacetic acid alkanethiol surfaces induced the formation of SiO_2. (E) Schematic representation of the immobilization of His-tagged silicatein-α via a SAM. Silicatein-α was immobilized by tailoring the Au(111) surface by using: (a) cysteamine SAMs; (b) reactive ester polymer that was covalently bound to the amine head group of cysteamine; (c) and nitrilotriacetic acid molecules that were further immobilized by using the remaining reactive ester group present in the backbone of the polymer. (F) Confocal laser scanning microscopy images of immunodetection of immobilized silicatein-α with

polyclonal antibodies raised against silicatein-α (PoAb-SILA). (G, H) High-resolution SEM images of TiO_2 and ZrO_2 formed by catalysis with surface-bound silicatein.

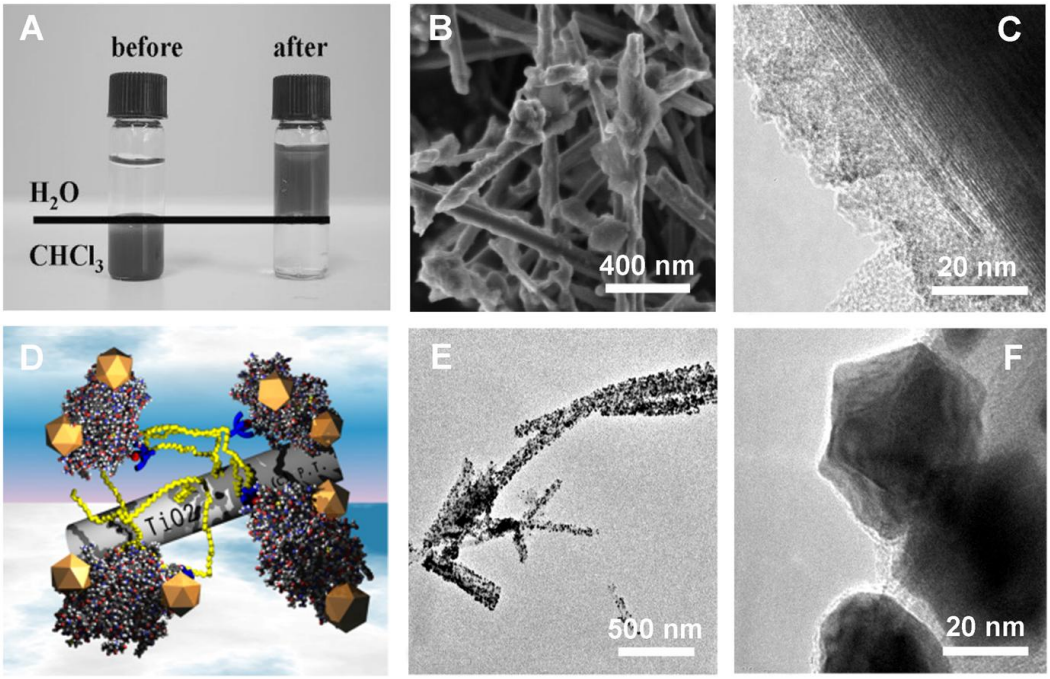

Figure 1.6 Immobilization of silicatein on different nanostructured surfaces. (A) Digital photographs of WS_2 nanotube dispersions before (left) and after (right) functionalization with silicatein-α, showing the change in hydrophilicity of the functionalized material. (B) SEM image showing the deposition of TiO_2 in the WS_2 nanotubes, catalyzed by silicatein-α. (C) High-resolution TEM image showing the interface between the WS_2 nanotube surface and the newly formed TiO_2 layer, where crystalline domains are visible, corresponding to the rutile phase of titania. (D) Schematic representation of polymer/silicatein-a-functionalized TiO2 nanowires with deposited gold nanoparticles. (E) TEM overview of TiO_2 nanowires covered with gold nanocrystallites, catalyzed by silicatein-α. (F) High-resolution TEM image of the gold nanocrystals.

Complex mineralization matrixes – silicatein interactors

Silicateins are the main proteins responsible for silica polymerization, but, recently, another group of proteins – silintaphins – were discovered that interact strongly with silicatein. (Figure 1.3) It was shown that both proteins could be colocalized in the spicule filaments and – when incubated together – they tended to assemble in a stoichiometric manner to form filamentous aggregates.[88,89] The role of silintaphin-1 in the activity of silicatein was also explored. For proteins present in a 4 : 1 ratio (silicatein / silintaphin), maximum polymerization of SiO_2 from TEOS was observed. The use of silintaphin-1 was shown to affect assembly of the synthetic materials. For example, when γ-Fe2O3 nanoparticles

functionalized with polymeric ligand carrying silicatein-α on its surface were coincubated with silintaphin-1, needle-like spicules with lengths of up to hundreds of nanometers, with clearcut edges, were formed by the assembly of the nanoparticles.[88] This phenomenon points to the importance of complex matrices in biomineralization mimetics, where increasing the complexity of the organic matrix can lead to fine-tuning of the produced materials.

Synthetic analogs of silicatein-α

One of the limitations of the protein-catalyzed synthetic systems is that – in general – only low concentrations of the proteins are available from natural sources (e.g. spicules) or as products of laboratory genetic manipulation.[39,48] However, in recent years, numerous strategies have been introduced to mimic bioinspired catalysts, such as silicatein from sponges and silaffins from diatoms. Organic templates such as polymers,[90,91] polymer–peptide hybrids,[92,93] diblock copolypeptides,[54] self-assembling peptides[94-98] and cationic peptide amphiphiles[99] were used to promote sol–gel condensation of silica and other inorganic materials. Template sol–gel processes yield hybrid materials with a wide range of different morphologies that are strongly influenced by factors such as temperature, concentration, and the pH of the reaction medium.[100] Even simple bifunctional compounds might act as functional analogs of the silicatein-α active site for hydrolytic catalysis, as confirmed by use of a series of small molecules with a nucleophilic terminus (e.g. –OH, –SH, and $–SC_2H_5$) and a hydrogen bond acceptor (e.g. a primary or tertiary amine) at the other end.[101] In the absence of catalyst, TEOS mixed with the buffered aqueous solution remained stable for several days. Cysteamine (followed by ethanolamine) promoted the highest yield of silica condensation. This result is consistent with previous results obtained with synthetic block copolypeptides and with the observation that proteases possessing Cys residues in the catalytic triad are enzymatically more active than proteases that contain Ser residues instead.[30,95] These nucleophilic and basic functionalities (which influence the catalytic formation of silica) are not required to be part of a single molecule or a polymer; they may be different molecules functionalized/chemisorbed separately onto different active surfaces. This was demonstrated for a synthetic system where an appropriate nucleophilic function (e.g. hydroxyl) and nitrogen bases (e.g. imidazole) were immobilized onto two populations of gold nanoparticles (as carriers) via self-assembled monolayers of ω-functionalized organic thiols.[102] The mechanistic assumption of the nanoparticle- bound system is that, when two nanoparticles with different functionalities come close enough to allow hydrogen bonding (e.g. 2–3 Å), an

active catalyst is formed. This would correspond to the interaction of a hydroxyl group from Ser and the imidazole group from His (separation ≈ 2 Å), which is essential for promoting silica alkoxide hydrolysis, i.e. for cleaving the silicic ester bonds. Little or no hydrolysis occurred when: (a) only one type of functional nanoparticle was present; (b) either class of functional nanoparticle was replaced with a noninteracting molecule; or (c) unfunctionalized gold nanoparticles were used. The awareness that silica can be catalyzed efficiently by cysteamine led to useful, convenient and low-cost encapsulation of biological materials, such as enzymes, antibodies, and cells, that otherwise might be damaged by exposure to the acid, base, or heat.[103] This was shown elegantly by encapsulating blue fluorescent protein and live Escherichia coli cells expressing green fluorescent protein with cysteamine in 2D micropatterned matrices. The 2D micropatterned matrices (obtained by microcontact printing of live cells expressing green fluorescent protein or a solution of blue fluorescent protein mixed with the silica precursor and cysteamine) displayed stable and active fluorescence, confirming that the encapsulation with cysteamine was successful in maintaining the activity of the biological materials, and that this method could therefore potentially be extended to the encapsulation and micropatterning of a whole host of live cells, enzymes, antibodies, receptors, and fluorescent and other functional proteins.[104]

1.3 Enzyme mimics - Biomimetic catalysis using nanostructured materials

In the previous section it was shown that using enzymes can sometimes be a limiting process in terms of application, due to their relative instability. Hence, a lot of effort has been put in developing enzyme mimics either from a structural or reactive point of view. Several important enzymes have metal atoms or clusters as co-factors. Nanoparticles on one side, are highly reactive species. This is demonstrated convincingly by the use of transition metal nanoparticles in catalysis,[105] that mimic metal surface activation and catalysis at the nanoscale thereby bringing selectivity and efficiency to heterogeneous catalysis. Transition metal nanoparticles are clusters containing from a few tens to several thousand metal atoms, stabilized by ligands, surfactants, polymers or dendrimers protecting their surfaces. Their activity and selectivity are determined by characteristics such as size and the atomic-level structure of the planes that they expose.[106-108] One possible flipside to the reactivity of nanoparticles is nanotoxicity, their unintended and harmful reactivity in vivo. Therefore, the need to evaluate the possible risk of human exposure to different kinds of nanomaterials has become a central issue in modern materials and biomedical science.[109] Although inorganic nanoparticles and enzymes might seem very different, their chemical behavior turns out to be quite similar in an increasing number of examples. Proteins may be chemically much better defined, i.e. with size and shape determined by their molecular weight, a multitude of covalent and non-covalent interactions that lead to a (dynamic) three-dimensional structural organization inside the protein, a charge determined by the amino acid sequence and the given pH value, and functional groups and active sites operating according to the lock-and-key-principle, whereas related functionalities are not present on the hard crystalline surfaces of nanoparticles. However, nanoparticles and enzymes have some similarities in their sizes, charges, and shapes and exterior surfaces of nanoparticles may be coated with organic functional groups similar to those exposed by enzymes, which suggest that nanoparticles might indeed act as enzyme mimics. This option is very attractive because nanoparticles are much cheaper and more stable than proteins. Enzymes not only speed up reactions, they have an exceptional substrate specificity and activity, but they suffer from a short shelf live and thermal instability. Furthermore, they are difficult to separate from the products, which is important for most practical applications. Nanoparticles as artificial enzymes, on the other hand, would offer the advantage that the products are readily separated and the particles are

more stable and degrade much slower than molecular catalysts. However, heterogeneous catalysts are difficult to study, and their reaction mechanisms are therefore often unknown.

The term "artificial enzyme" was coined originally by Breslow.[110] Enzymes generally bind their substrates and then use the action of two or more well-placed functional groups to achieve catalysis. This chemical picture leads to substrate selectivity, reaction selectivity, and stereo-selectivity. Substrate binding can be achieved by metal coordination, ion pairing, Lewis acid-base coordination, hydrogen-bonding in non-aqueous solvents, by metal or Lewis acid-base coordination or hydrophobic interaction in aqueous solution. This binding of a substrate close to functional groups in the enzyme causes catalysis by so-called proximity effects. It is therefore possible to create similar catalysts from small molecule mimics of enzyme active sites by combining, in a molecule or polymer, the ability to bind a substrate with catalytic functional groups. As the artificial enzymes need to bind molecules, they must contain a host-molecule (e.g. a cyclodextrin or calixarenes). A number of artificial enzymes have been reported catalyzing various reactions with rate increases up to 10^3. [111,112]

Nanoparticles properties and chemical activity

Nanoparticles perfectly bridge the microscopic world of molecular chemistry and the macroscopic world of extended solids. They behave like molecules in that they can be dissolved, precipitated, re-dissolved, sublimed, crystallized, etc. This permits the use of characterization techniques such as solution NMR and time-of-flight MS that are not normally suitable for the study of solids. On the other hand, nanoparticles exhibit many properties of solids like collective magnetism, and they possess a distinct solid surface.

Independent of their small size, elemental composition, charge, morphology, order/crystallinity, surface area, solubility, surface chemistry and derivatization play an important role for their magnetic, electrical, optical, mechanical and structural properties.[113] Many of these characteristics have potential implications for nanoparticle reactivity as well. The large surface area of nanoparticles induces an enhanced reactivity with any type of surface ligand. Surfaces, in particular surface defects, steps and edges are under-coordinated and therefore highly reactive sites that can routinely be stabilized by special surface ligands, chemisorbed molecules, tensides, macro- or biomolecules. (Figure 1)

The reactivity of the nanoparticles is intimately associated with unwanted (nanotoxicity) and desired (enzymatic) effects. Besides mobility and agglomeration the solubility or degradation behavior of nanoparticles are important contributors to their reactivity in a biological

environment.[114] Typically, the pH inside cells is neutral (pH 7) and not surprisingly, most enzymes have evolved to optimum function at this pH. However, intracellular compartments (lysosomes and autophagosomes) and specialized organs (stomach) significantly extend the possibility for degradation or chemical modification of a material. As a rule of thumb, the highly polymeric basic oxides of the early transition metals (e.g. Ti or V) and silica are inert, whereas the more salt-like amphoteric and acidic compounds of the late transition metals (e.g. in particular Zn, Cd) metals are easily dissolved under acidic conditions. Most compounds of the 3d metals such as Mn, Fe or Co will be processed under acidic conditions in the presence of coordinating ligands. It is obvious that degrading nanoparticles will show a very different chemical behavior than the inert ones. As a consequence, dissolving nanoparticles release a considerable local concentration of ions. Many metal ions cause considerable stress and often affect the production/degradation/activation of reactive oxygen species (ROS) inside the cell. This uptake mechanism is particularly apparent for oxides of the late 3d metals manganese, iron, cobalt and zinc.[115] In the ROS formation reaction the particles assist in reducing an oxygen molecule (thus, activating it $O_2 + e^- \rightarrow O_2^-$) which reacts subsequently with the internal/external structure of the cell. This mechanism is even active stoichiometrically if reduced iron oxide or even iron particles get inside a cell or close to a (micro-)organism.[116] For catalytic nanoparticles, the oxidized site (for example, Fe^{3+} or redox-active rare-earth oxides)[117] is embedded in the cytosol, where reducing agents (for example, NADH) are abundant and can re-establish the active form of the heavy-metal center through reduction ($Fe^{3+} + e^- \rightarrow Fe^{2+}$).[118] Jia et al. most recently reported on the gold-catalyzed formation of NO in blood plasma.[119] Since the particles are not degraded during this process even small amounts of catalytically active, yet persistent (non-biodegrading), particles may result in chronic effects, or it may assist a therapy. It is known that algae, daphnids, and trout are affected by (photoactive) titania.[120,121] Here, the toxicity is again linked to a non-classical activity of the material. In contrast to this negative impact, Chen et al.[122] and Karakoti et al.[123] described some beneficial effects of ceria nanoparticles, based on catalytically reduced oxidative stress level in retinal tissue.

Peroxidase mimics

Peroxidases are widely distributed and structurally diverse enzymes. They catalyze the two-electron oxidation of several types of substrates using hydrogen peroxide, although other reactive peroxides can also be used as well.

$H_2O_2 + AH_2 \rightarrow 2\ H_2O + A$ (*equation 1*)

$H_2O_2 + 2\ AH_2 \rightarrow 2\ H_2O + 2\ AH^*$ (*equation 2*)

A heme prosthetic group is most common in peroxidases, usually with iron (III), although manganese or vanadium containing peroxidases have been described. One of the best-studied peroxidases is horseradish peroxidase (HRP), which has a heme-iron co-factor.[124] (Figure 1.7A) In most heme-peroxidases the iron atom in the active center undergoes a reversible change of its oxidation state. In the resting state high-spin Fe(III) is present, which is oxidized by hydrogen peroxide to form an unstable intermediate called compound I (Co-I) with Fe(IV), releasing water in the process. This reactive intermediate oxidizes one substrate molecule forming the so-called compound II (Co-II), releasing a free radical substrate molecule. This intermediate is further reduced by a second substrate molecule, thereby regenerating iron to its original oxidation state (III) and releasing another radical substrate molecule.[125] (Figure 1.7B) Due to its ability to oxidize a wide range of organic substrates by reducing peroxides, peroxidases find also applications in several areas of industry as well as for analytical methods. Therefore, attempts have been made to improve their stability and to up-scale the production of these enzymes either via recombinant production or by engineering the global protein structures or the active centers, as well as by stabilizing of the enzymes in micelles, polymers, or immobilize them on nanoparticles and other materials.[126-128] Also several organometallic complexes have been synthesized containing iron (either in III or V oxidation states) and different ligands like TAML or porphyrin rings.[129,130]

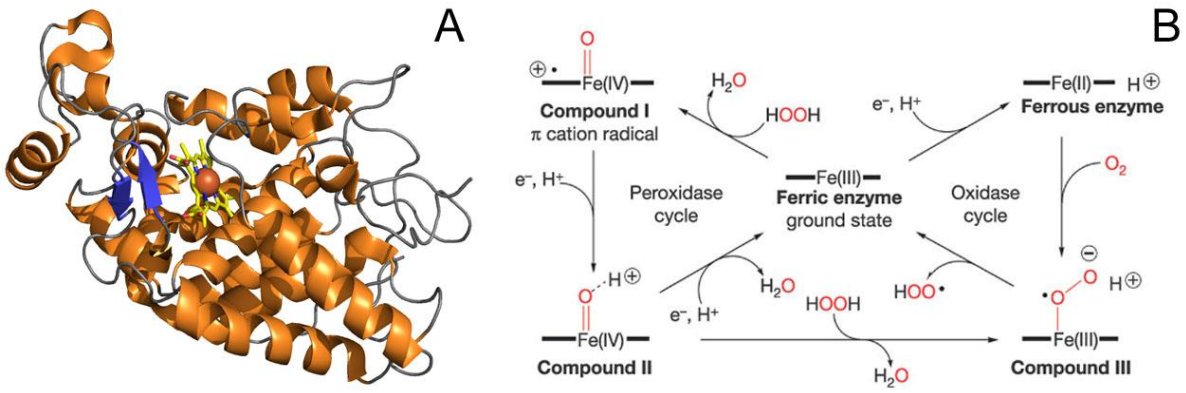

Figure 1.7 The horseradish peroxidase (HRP). (A) tridimensional structure of HRP with the iron center (orange sphere) and (B) the mechanism of the iron center of HRP with changes in oxidation state of the iron atom.

The oldest peroxidase mimic would definitely be the Fenton reagent created by Fenton in the 1890´s, which is no more than a solution Fe^{2+}/Fe^{3+} ions, which catalyze the breakdown of peroxide.[126] This catalyst is still widely used in particular in organic synthesis for radical substitution or for waste water treatment, by oxidizing organic contaminants. Actually it was observed that solutions of several different transition metal ions showed a peroxidase like activity, like Cu^{2+}, Co^{2+} or Mn^{2+} besides iron.[127]

Gao et al.[128] demonstrated that Fe_3O_4 nanoparticles with different sizes (30, 150, 300 nm) can oxidize peroxidase substrates such as 3,3,5,5-tetramethylbenzidine (TMB), di-azo-aminobenzene (DAB) and o-phenylenediamine (OPD) all of which form colored oxidation products. The particles were compared directly with HRP, and studies of their stability for different H_2O_2 concentrations, pH values, temperatures and sizes were carried out. The optimum pH and temperature (pH 3.5, 40°C) were in fact very similar to the values reported for HRP. The reaction of the particles was dependent on the H_2O_2 concentration (similar as for HRP), but their activity decreased at high peroxide concentrations. The reactivity of the particles increased with decreasing size due to the increased surface/volume ratio. Fe_3O_4 nanoparticles show a typical Michaelis-Menten-type behavior, and a determination of the catalytic constants revealed that they have a higher affinity for TMB than for H_2O_2 (compared to HRP), although − for TMB as a substrate and the same molar concentrations − the Fe_3O_4 nanoparticles had a higher catalytic activity than HRP (k_{cat} of 3.02 $x10^4$ (Fe_3O_4) and 4.00 $x10^3$ (HRP) respectively). Nanoparticles are more robust than HRP, maintaining most of their activity even at high temperatures or extreme pH values prior to reaction. The magnetic properties make Fe_3O_4 particles attractive for biomedical applications and were used for developing an immunoassay in which the nanoparticles allow to capture, separate and detect biomolecules.[128]

Later on Wei et al.[129] used Fe_3O_4 nanoparticles for H_2O_2 detection. Using 2,2´-azino-bis(3-ethylbenzo-thiazoline-6-sulfonic acid (ABTS) they were able to quantify the amount of H_2O_2. By addition of glucose oxidase to the system, a glucose detection system could be devised. A similar approach was used by Ding et al.[130] for the determination of melamine in milk products, and Chang and Zhu used both Fe_3O_4 and $BiFeO_3$ nanoparticles for the determination of hydrogen peroxide.[131,132] With $BiFeO_3$ nanoparticles it was possible to detect H_2O_2 concentrations as low as 4.5 x 10^9 mol L^{-1} using fluorometric detection, with benzoic acid as substrate. Shi et al.[133] used $CoFe_2O_4$ nanoparticles for the detection of peroxide with the aid of chemiluminescence and glucose. Again, the enzyme-mimetic behavior was demonstrated

through the pronounced Michaelis-Menten behavior as well as the pH and temperature dependent activity. Considering all reports on different types of iron oxides exhibiting an apparent peroxidase activity, we might assume that the reaction mechanism is related to that of iron containing peroxidases. The catalytic activity seems to be related to the presence of both, Fe^{2+} and Fe^{3+} sites on the surface of the nanoparticles, and it appears to be relatively independent of the particle composition. Nevertheless, a variety of metal, metal oxide, and metal sulfide particles have been reported to mimic peroxidases, which do not have a composition directly related to the prosthetic groups of peroxidases. Examples include CuO and Au nanoparticles, FeS "nanosheets" as well as single-walled carbon nanotubes (SWNTs).[134-137]

Haloperoxidase mimics

Other types of peroxidases have the capability of catalyzing the two-electron oxidation of halides (Cl^-, Br^-, I^-) by H_2O_2 to hypohalous acids, and when suitable nucleophilic acceptors are present, halogenated compounds can be formed. (equation 3) These peroxidases are generally named haloperoxidases.[138,139]

$$R - H + H_2O_2 + X^- + H^+ \rightarrow X - R + 2\,H_2O \qquad (\textit{equation 3})$$

Different classes of haloperoxidases have been identified, some of them carrying a prosthetic group which can be either a heme-group or a vanadate ion (VO_4^{3-}). The latter (vanadium-dependent haloperoxidases) are the best-studied class of haloperoxidases (V-HPO).[140] (Figure 1.8 A) V-HPOs have been used in a variety of biotransformations, not only in halogenations[141,142] but also in sulfoxidation,[143] showing a remarkable stereoselectivity and regiospecificity.[144] Haloperoxidases also show activity towards classical peroxidase substrates,[145] in the same fashion as HRP, and and are extensively used in biochemistry, biological assays,[146] as well as in wastewater treatment (i.e., to remove aromatic compounds).[147] Studies on the active center showed that the proteins were inactivated upon removal or reduction of the prosthetic group (VO_4^{3-}). (Figure 1.8B) The mechanism of the catalytic cycle is assumed to involve a peroxide species that eliminates a water molecule to form a reactive peroxo species.[148-149] Several studies indicated that the peroxo group is activated by protonation before oxidizing the halide ion in a second step.[150] Then, the halide ion attacks the reactive oxygen atom in a nucleophilic manner and a hypohalous acid or

similar "X^+ " species is formed. (Figure 1.8C) Furthermore, it was possible to incorporate ions of similar size as vanadate (e.g. molybdate, MoO_4^{2-}) into the active center, resulting in a total loss of catalytic activity.[151,152] These findings prompted research on inorganic and organometallic haloperoxidase mimics with vanadium and other elements and dioxovanadium (V) (VO_2^+) as one of the first active protein mimics in acidic solution.[153] Other vanadium organometallic complexes or peroxocomplexes were studied,[154] which exhibited good efficiency and selectivity in several oxidation reactions such as halogenation,[155] sulfoxidation,[156] epoxidation, hydroxylation of alkenes,[157] and oxidation of primary and secondary alcohols.[158] The active species in most of these complexes has been identified as oxoperoxovanadium (V) species, and some structural characterization has been carried out.[159] Mimics with molybdenum (VI), tungsten (VI) and rhenium (VII) have been reported where similar peroxo-metal complexes were identified as reactive intermediates.[160-162]

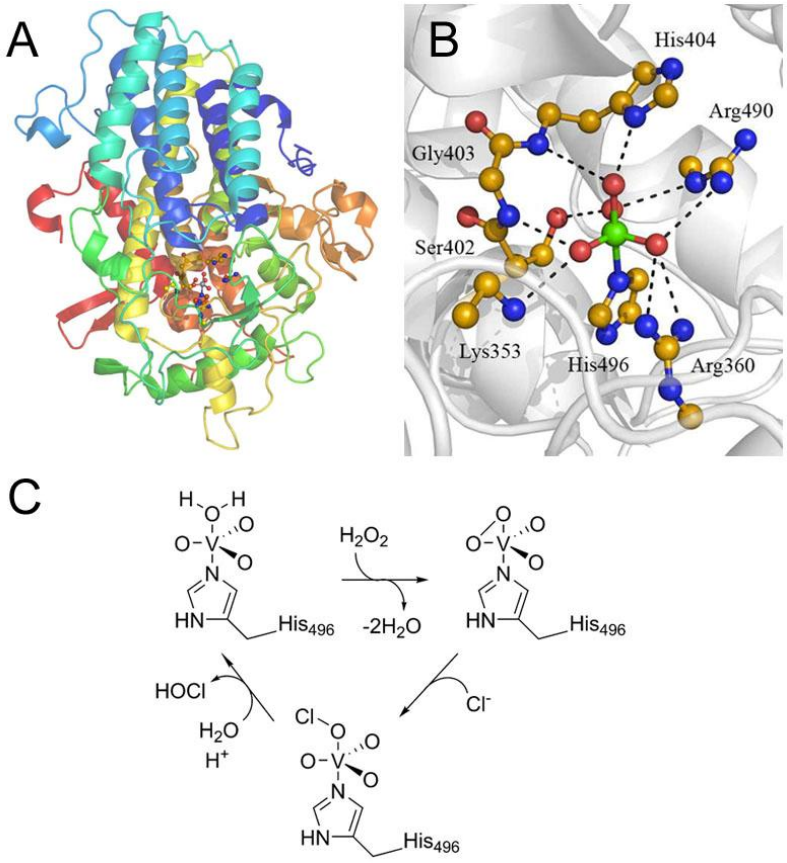

Figure 1.8 The vanadium dependent haloperoxidase (V-HPO). (A) tridimensional structure of the chloroperoxidase (V-CPO) from Curvularia ineaqualis and (B) its active center with the vanadium atom in bright green. (C) The chlorination mechanism of V-CPO.

Other oxidoreductase mimics – superoxide dismutases and oxidases

Besides several reports on peroxidase mimics, also other related enzyme mimics have been studied recently, in particular oxidase and superoxide dismutase (SOD) mimics. All these enzymes are somehow related as they are involved in the formation or consumption and scavenging of peroxides and other reactive oxygen species (ROS). There is some evidence indicating that high intracellular concentrations of inorganic manganous ions render some cells resistant to ionizing radiation and provide substantial antioxidant protection to aerobic cells lacking superoxide dismutase (SOD) enzymes.[163-166] These reactions are biologically important in the neutralization of harmful organic compounds, by oxidation, as well as in the production of ROS which can have, to a certain degree a defensive role in the cells. Nevertheless ROS have also damaging effects in the cells and imbalance in these chemical species *in vivo* can lead to oxidative stress which has been implicated in the development of several diseases like Alzheimer or different types of cancer.[167,168] (Figure 1.9C) SODs are metalloenzymes which catalyze the dismutation of the superoxide (O2•−) to oxygen (O2) and hydrogen peroxide (H2O2),[169] (equation 4-5) SOD enzymes are encountered in different structural families; copper-zinc, manganese, iron or nickel SOD.[170-172] In the case of the manganese (Figure 1.9 A and B) and iron SODs the mechanism of the catalytic conversion of superoxide to oxygen is assumed to start by binding the superoxide radical anion to the Mn^{III} monomer leading to its reduction to Mn^{II} and concomitant oxidation of superoxide into oxygen.[173] The catalytic cycle is closed by binding a second superoxide to the Mn^{II} ion which leads to the oxidation of Mn^{II} and reduction of the superoxide anion to H_2O_2.

$$O_2^{\bullet-} + Mn(III) \rightarrow Mn(II) + O_2 \qquad (\textit{equation 4})$$

$$O_2^{\bullet-} + Mn(II) + 2\,H^+ \rightarrow H_2O_2 + Mn(III) \qquad (\textit{equation 5})$$

Non-enzymatic manganese was shown to provide protection against superoxide toxicity in vivo more than 30 years ago,[174] but the chemical mechanism responsible for this protection subsequently became controversial due to conflicting reports concerning reproducibility of the activity in vitro. In essence the requirement of the active center of most SODs can even be resumed to the presence of oxygen-affine metal cations in solids, which can easily change their oxidation state by one unit. Cerium oxide also fits well with these criteria since it can occur in the trivalent and tetravalent states simultaneously in the same particle, and it is common to bounce between this two oxidation states in redox reactions.[175,176] As some SOD-

like catalysts, in particular manganese porphyrins showed catalase activity as well,[177] ceria nanoparticles where tested for the disproportionation of hydrogen peroxide into molecular oxygen and water. By tuning the oxidation state of Ce to (+4) in ceria nanoparticles a high catalase activity could be achieved.[178] This allows to oscillate between complementary reactions, in this case the production (SOD activity) or the consumption (catalase activity) of hydrogen peroxide by adjust the oxidation state of the particles. Oxidase activity was also observed for ceria nanoparticles by Perez et al.[179] who demonstrated that dextran coated CeO_2 could oxidize organic substrates like TMB, ABTS or dopamine without aid of any external oxidizing agent. These particles showed to have a pH-dependent activity, and could replace HRP in ELISA-type assays.

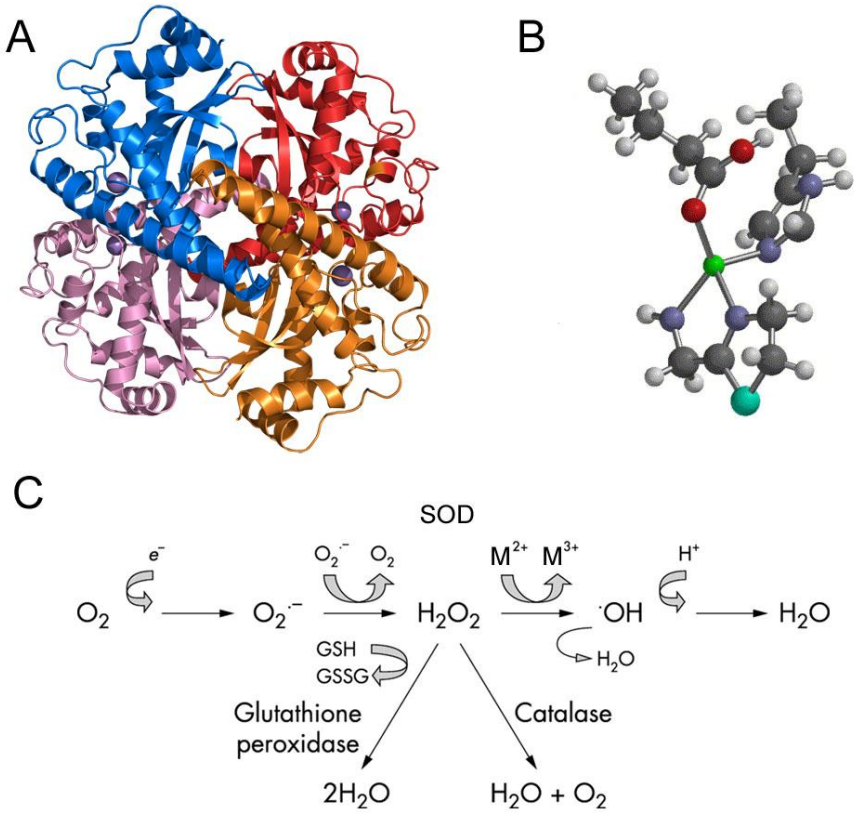

Figure 1.9 The manganese dependent superoxide dismutase (SOD). (A) Tridimensional structure of a human superoxide dismutase 2 (SOD2) tetramer and (B) the coordination of the manganese atom (bright green) in the active center. (C) Generation of reactive oxygen species. Molecular oxygen (O_2) reacts with an impaired electron (e^-) to form the superoxide anion ($O_2^{\cdot-}$). Superoxide is converted to hydrogen peroxide (H_2O_2) by the enzyme superoxide dismutase. Hydrogen peroxide undergoes spontaneous conversion to the highly reactive hydroxyl radical ($^{\cdot}OH$). Alternatively, it can be detoxified via either glutathione peroxidase or catalase to water (H_2O) and oxygen (GSH, reduced glutathione; GSSG, oxidised glutathione).

In earlier reports of the effects of ceria nanoparticles in cell cultures, it was observed that these particles can act as radical scavengers and antioxidants.[180,181] Korsvik et al.[182] proposed that ceria nanoparticles with mixed valence state (Ce^{3+}/Ce^{4+}) have a SOD-like activity. Particles with different compositions and sizes where studied, whereas smaller particles had a higher Ce3+ concentration (40%) than the bigger ones (22%). The activity was tested by detection of the level of H_2O_2 produced when the particles are in the presence of superoxide radicals. The in-situ production of $O_2^{\bullet-}$ is achieved by the hypoxanthine/xanthine oxidase system.[183] Some kinetic studies were done regarding the competition assays with ferricytochrome C where the catalytic rate constant of the ceria nanoparticles was found to be 3.6×10^9 M^{-1} s^{-1}, while the CuZn SOD rate constant was determined to be between 1.3 and 2.8×10^9 M^{-1} s^{-1}. The proposed catalytic mechanism was based on the same redox reaction occurring in the metal center of many SODs as exemplified by the equation above (equations 4-5). McGinnis and coworkers[184] showed that nanoceria particles prevent the increase in the intracellular concentrations of ROS in primary cell cultures of rat retina and, in vivo, prevented loss of vision due to light-induced degeneration of photoreceptor cells. These data indicate that the nanoceria particles may be effective in inhibiting the progression of ROS-induced cell death, which is believed to be involved in macular degeneration, retinitis pigmentosa and other blinding diseases, as well as the ROS-induced death of other cell types in diabetes, Alzheimer's disease, atherosclerosis, stroke and so on.

Other enzyme mimics

Molybdenum oxides are well-known heterogeneous catalysts for selective oxidation of light alkanes and alkenes,[185,186] but the trace elements molybdenum and tungsten are also essential for nearly all organisms and form the catalytic centers of a large variety of enzymes such as nitrogenase, nitrate reductases, sulphite oxidase and xanthine oxidoreductases. Nature has developed two scaffolds holding molybdenum in place, the pterin-based molybdenum and the iron–molybdenum cofactors. Molybdenum is bioavailable as molybdate (MoO_4^{2-}). Once the molybdate enters the cell, it is incorporated by complex biosynthetic machineries into metal cofactors.[187] Within the enzymes, molybdenum shuttles between the oxidation states +4, +5 and +6, thereby catalyzing two-electron reduction–oxidation (redox) reactions.[188] In most cases, regeneration of the active site involves single-electron steps, resulting in a paramagnetic molybdenum intermediate. Many anaerobic archaea and some bacteria are not molybdenum dependent but rather require tungsten for their growth. Tungstate, which is 100-

fold less abundant than molybdate, is enriched in deep-sea hydrothermal vents, reflecting conditions on the primitive Earth. Many of the known tungsten-dependent hyperthermophilic bacteria and archaea are found in such vents.[189]

Molybdenum and tungsten oxide were reported to exhibit both an increased photocatalytic activity and an increased antimicrobial activity at the same time.[190,191] Thin film coating containing these group 6 oxides either in pure or as additives impart an antimicrobial activity to surfaces. These coatings can be obtained by sol-gel techniques[192] or by anodization.[193] Although the reasons for the antimicrobial activity is not clear, it seems reasonable to attribute the effect to the enzyme-like activity of molybdenum and tungsten oxide. The peroxidase-like activity of molybdenum and tungsten has been known for a long time, although no functional molecular enzyme mimic based on these metals have been reported so far. Meister et al. reported the bromination of TMB with H_2O_2 in the presence of $MoO(O_2)_2(H_2O)_2$ and $WO(O_2)_2(H_2O)_2$.[194] The catalysis of the reaction in solution proceeded faster than the reaction catalyzed with V(V), i.e. the group 6 oxides appear to be more reactive than the corresponding vanadium compounds. This may be attributed to the higher oxidation state of Mo(VI) and W(VI) and a more reactively bound peroxide.

Noble metal particles are typical catalysts for hydrogenation reactions for example, but they have also received great attention due to their optical and electronic properties. Also the activity as SOD/catalase of Pt nanoparticles, Au nanoparticles and their alloys was demonstrated, and they could be used in reducing oxidative stress in the model organism *C. elegans*. The Pt/Au alloy nanoparticles are found to be particularly interesting due to their enhanced response in surface plasmon resonance (SPR) and surface-enhanced Raman scattering (SERS).[195,196] These particles find a promising application in protection against oxidative stress, and consequently deceleration of the evolution of certain diseases in which formation of ROS might be involved. Furthermore more insight in this type of redox catalysis can bring exciting developments in conservation, transduction and utilization of energy.

1.4 References

1. da Vinci, L. (translation by Jean Paul Richter) *The notebooks of Leonardo da Vinci*. Createspace, 2010.

2. Clayton, M.; Philo, R. *Leonardo da Vinci: The mechanics of Man.* J.P. Getty Trust Publications, 2010.

3. Benyus, J. *Biomimicry: Innovation Inspired by Nature*. New York: William Morrow & Company, Inc., 1997.

4. Xia, Y. and Whitesides, G. M. *Angew. Chem. Int. Ed*. **1998**, *37*, 550.

5. Decossas, S.; Mazen, F.; Baron, T.; Brémond, G.; Souifi, A. *Nanotechnology* **2003**, 14, 1272.

6. Schreiber, F. *J. Phys.: Condens. Matter* **2004**, *16*, R881.

7. Corot, C.; Robert, P.; Idee, J.-M.; Port, M. *Adv. Drug Delivery Rev.* **2006**, *58*, 1471.

8. Tiefenauer, L. X.; Kuehne, G.; Andres, R. Y. *Bioconjugate Chem.* **1993**, *4*, 347.

9. Zhang, Y.; Kohler, N.; Zhang, M. *Biomaterials* **2002**, *23*, 1553.

10. Weinera, S.; Trauba, W.; Wagnerb, H.D. *J. Struct. Biol*. **1999**, *126*, 241.

11. Aizenberg, J.; Sundar, V.C.; Yablon, A.D.; Weaver, J.C.; Chen, G. *Proc Natl Acad Sci USA* **2004**, *101*, 3358.

12. van der Zwaag, S.; van Dijk, N.H.; Jonkers, H.M.; Mookhoek, S.D.; Sloof , W.G. *Phil. Trans. R. Soc. A* **2009**, *367*, 1689.

13. Dutta, J.; Tripathi, S.; Dutta, P.K. *Food Sci. Technol. Int.* **2012**, *18*, 3.

14. Dickerson, M.B.; Sandhage, K.H.; Naik, R.R. *Chem. Rev.* **2008**, *108*, 4935.

15. Xu, A.W.; Ma, Y.; Cölfen, H. *J. Mater. Chem.* **2007**, *17*, 415.

16. Bigall, N.C., Reitzig, M., Naumann, W., Simon, P., van Pée, K.-H.; Eychmüller, A. *Angew. Chem. Int. Ed.* **2008**, *47*, 7876.

17. Narayanan, R. *Molecules* **2010**, *15*, 2124.

18. Astruc, D. *Nanoparticles and Catalysis*; Wiley-VCH: Weinheim, 2008.

19. Bäuerlein, E.; Behrens, P.; Epple, M. *Handbook of Biomineralization*, 1st edn. Wiley-VCH: Weinheim, 2007.

20. Mann, S.; Archibald, D.D.; Didymus, J.M.; Douglas, T.; Heywood, B.R.; Meldrum, F.C.; Reeves, N.J. *Science* **1993**, *261*, 1286.

21. Shimizu, K.; Cha, J.; Stucky, G.D.; Morse, D.E. *Proc Natl Acad Sci USA* **1998**, *95*, 6234.

22. Brutchey, R.L.; Morse, D.E. *Chem Rev.* **2008**, *108*, 4915.

23. Wetherbee, R. *Science* **2002**, *298*, 547.

24. Schröder, H.C.; Wang, X.; Tremel, W.; Ushijima, H.; Müller, W.E.G. *Nat Prod Rep* **2008**, *25*, 455.

25. Lux, A.; Luxova, M.; Morita, S.; Abe, J.; Inanaga, S. *Can J Bot* **1999,** *77*, 955.

26. Kröger N & Poulsen N (2008) Diatoms – from cell wall biogenesis to nanotechnology. Annu Rev Genet 42, 83–107.

27. Kröger, N.; Deutzmann, R.; Sumper, M. *Science* **1999**, **286**, 1129.

28. Kröger, N.; Deutzmann, R.; Bergsdorf, C.; Sumper, M. *Proc Natl Acad Sci USA* **2000**, *97*, 14133.

29. Kröger, N.; Lorenz, S.; Brunner, E.; Sumper, M. *Science* **2000**, *298*, 584.

30. Aizenberg, J.; Weaver, J.C.; Thanawala, M.S.; Sundar, V.C.; Morse, D.E.; Fratzl, P. *Science* **2005**, *309*, 275.

31. Foo, C.W.P.; Huang, J.; Kaplan, D.L. *Trends Biotechnol* **2004**, *22*, 577.

32. Cha, J.N.; Shimizu, K.; Zhou, Y.; Christiansen, S.C.; Chmelka, B.F.; Stucky, G.D.; Morse, D.E. *Proc Natl Acad Sci USA* **1999**, *96*, 361.

33. Wang, X.; Schloßmacher, U.; Wiens, M.; Batel, R.; Schröder, H.C.; Müller, W.E.G. *FEBS J* **2012**, *279*, 1721.

34. Menzel, H.; Horstmann, S.; Behrens, P.; Bärnreuther, P.; Krueger; I.; Jahns, M. *Chem. Commun.* **2003**, *24*, 2994.

35. Annenkov, V.V.; Patwardhan, S.V.; Belton, D.; Danilovtseva, E.N.; Perry, C.C. *Chem. Commun.* **2006**, *14*, 1521.

36. Bellomo, E.G.; Deming, T.J. *J Am Chem Soc* **2006**, *128*, 2276.

37. Belton, D.J.; Patwardhan, S.V.; Annenkov, V.V.; Danilovtseva, E.N.; Perry, C.C. *Proc Natl Acad Sci USA* **2008**, *105*, 5963.

38. Spinde, K.; Kammer, M.; Freyer, K.; Ehrlich, H.; Vournakis, J.N.; Brunner, E. *Chem Mater* **2011**, *23*, 2973.

39. Zhou, Y.; Shimizu, K.; Cha, J.N.; Stucky, G.D.; Morse, D.E. *Angew Chem Int Ed* **1999**, *38*, 779.

40. Müller, W.E.G.; Schröder, H.C.; Lorenz, B.; Krasko, A. *Silicatein-mediated synthesis of amorphous silicates and siloxanes and use thereof.* US Patent 7169589, 2001.

41. Sumper, M.; Kröger, N.J. *J Mater Chem* **2004**, *14*, 2059.

42. Kent, M.S.; Murton, J.K.; Zendejas, F.J.; Tran, H.; Simmons, B.A.; Sajita. S.; Kuzmenko, I. *Langmuir* **2009**, *25*, 305.

43. Müller, W.E.G.; Belikov, S.I.; Tremel, W.; Schloßmacher, U.; Natoli, A.; Brandt, D.; Boreiko, A.; Tahir, M.N.; Müller, I.M.; Schröder, H.C. *Formation of siliceous spicules in demosponges: example Suberites domuncula. In Handbook of Biomineralization, Vol. 1* (Bäuerlein, E. ed.), Wiley-VCH: Weinheim, 2007.

44. Martin-Jezequel, V.; Hildebrand, M.; Brzezinski, M.A. *J Phycol* **2000**, *36*, 821.

45. Müller, W.E.G.; Belikov, S.I.; Tremel, W.; Gamulin, V.; Perry, C.C.; Boreiko, A.; Schröder, H.C. *Micron* **2006**, *37*, 107.

46. Krasko, A.; Lorenz, B.; Batel, R.; Schröder, H.C.; Müller, I.M.; Müller, W.E.G. *Eur J Biochem* **2000**, *267*, 4878.

47. Schröder, H.C.; Boreiko, A.; Korzhev, M.; Krasko, A.; Tahir, M.N.; Tremel, W.; Eckert, C.; Müller, I.M.; Müller, W.E.G. *J Biol Chem* **2006**, *281*, 12001.

48. Müller, W.E.G.; Eckert, C.; Kropf, K.; Wang, X.; Schloßmacher, U.; Seckert, C.; Wolf, S.E.; Tremel, W., Schröder, H.C. *Cell Tissue Res* **2007**, *329*, 363.

49. Wolf, S.E.; Schloßmacher, U.; Pietuch, A.; Mathiasch, B.; Schröder, H.C.; Müller, W.E.G.; Tremel, W. *Dalton Trans* **2010**, *39*, 9245.

50. Sumerel, J.L.; Yang, W.; Kisailus, D.; Weaver, J.; Choi, J.H.; Morse, D.E. *Chem Mater* **2003**, *15*, 4804.

51. Tahir, M.N.; Theato, P.; Müller, W.E.G.; Schröder, H.C.; Boreijko, A.; Faiß, S.; Janshoff, A.; Huth, J.; Tremel, W. *Chem Commun* **2005**, *28*, 5533.

52. Ould-Ely, T.; Luger, M.; Kaplan-Reinig, L.; Niesz, K.; Doherty, M.; Morse, D.E. *Nat Protoc* **2011**, *6*, 97.

53. Kisailus, D.; Choi, J.H.; Weaver, J.C.; Yang, W.; Morse, D.E. *Adv Mater* **2005**, *17*, 314.

54. Cha, J.N.; Stucky, G.A.; Morse, D.E.; Deming, T.E. *Nature* **2000**, *403*, 289.

55. Mueller, W.E.G.; Wang, X.H.; Kropf, K.; Ushijima, H.; Geurtsen, W.; Eckert, C.; Tahir, M.N.; Tremel, W.; Boreiko, A.; Schlossmacher, U.; Shröder, H.C. *J Struct Biol* **2008**, **161**, 188.

56. Jovilet, J.P. *Metal Oxide Chemistry and Synthesis: From Solution to Solid State*. Wiley: New York, 2000.

57. Ovenstone, J.; Yanagisawa, K. *Chem Mater* **1999**, *11*, 2770.

58. Roy, R.; Hill, V.G.; Osborn, E.F. *J Am Chem Soc* **1952**, *74*, 719.

59. Iler, R.K. *The Chemistry of Silica*. Wiley: New York, 1979.

60. Son, J.H.; Kwon, Y.U. *Inorg Chem* **2003**, *42*, 4153.

61. Swaddle, T.W.; Rosenqvist, J.; Yu, P.; Bylaska, E.; Phillips, B.L.; Casey, W.H. *Science* **2005**, *308*, 1450.

62. Rao, C.N.R.; Raveau, B. *Transition Metal Oxides,2nd edn.* Wiley-VCH: Weinheim, 1998.

63. Shimizu, K.; Morse, D.E. *The biological and biomimetic synthesis of silica and other polysiloxanes. In Biomineralization* (Bäuerlein, E. ed.). Wiley-VCH: Weinheim, 2000.

64. Weaver, J.C.; Morse, D.E. *Microsc Res Tech* **2003**, *62*, 356.

65. Bradley, D.C.; Mehrotra, R.C.; Gaur, D.P. *Metal Alkoxides*. Academic Press: London, 1978.

66. Henry, M.; Jolivet, J.P.; Livage, J. *Aqueous chemistry of metal cations: hydrolysis, condensation and complexation. In: Chemistry, Spectroscopy and Applications of Sol-Gel Glasses* (Reisfeld, R. ed.). Springer Verlag: Heidelberg, Berlin, 1992.

67. Brinker, C.J.; Scherer, G.W. *Sol-gel Science: The Physics and Chemistry of Sol-gel Processing*. Academic Press: New York, 1990.

68. Tahir, M.N.; Theato, P. Müller, W.E.G.; Schröder, H.C.; Boreiko, A.; Faiß, S.; Janshoff, A.; Huth, J.; Tremel, W. *Chem Commun* **2005**, *44*, 5533.

69. Mann, S. *Biomineralization Principles and Concepts in Bioinorganic Materials Chemistry*. Oxford University Press: Oxford, 2001.

70. Wiberg, N.; Wiberg, E.; Holleman, A.F. *Lehrbuch der Anorganischen Chemie, 102nd edn*. de Gruyter: Berlin, 2007.

71. Bradley, S.M.; Kydd, R.A.; Yamdagni, R. *J Chem Soc* **1990**, *41*, 3.

72. West, A.R. *Solid State Chemistry, 2nd edn*. Wiley: New York, 1992.

73. Brutchey, R.L.; Morse, D.E. *Angew Chem Int Ed* **2006**, *45*, 6564.

74. Schmidt, H. *J Sol-Gel Sci Technol* **2006**, *40*, 115.

75. Caruso, R.A.; Antonietti, M. *Chem Mater* **2001**, *13*, 3272.

76. Glawe, D.D.; Rodriguez, F.; Stone, M.O.; Naik, R.R. *Langmuir* **2005**, *21*, 717.

77. Pogula, S.D.; Patwardhan, S.V.; Perry, C.C.; Gillespie, J.W.; Yarlagadda, S.; Kick, K.L. *Langmuir* **2007**, *23*, 6677.

78. Xu, M.; Gratson, G.M.; Duoss, E.B.; Shepherd, R.F.; Lewis, J.A. *Soft Matter* **2006**, *2*, 205.

79. Brott, L.L.; Naik, R.R.; Pikas, D.J.; Kirkpatrick, S.M.; Tomlin, D.W.; Whitlock, P.W.; Clarson, S.J.; Stone, M.O. *Nature* **2001**, *413*, 291.

80. Kim, D.J.; Lee, K.B.; Lee, T.G.; Shon, H.K.; Kim, W.J.; Paik, H.J., Choi, I.S. *Small* **2005**, *1*, 992.

81. Tahir, M.N.; Theato, P.; Müller, W.E.G.; Schröder, H.C.; Janshoff, A.; Jiang, J.; Huth, J. ; Tremel, W. *Chem Commun* **2004**, *24*, 2848.

82. Müller, W.E.G.; Schlossmacher, U.; Wang, X.; Boreiko, A., Brandt, D.; Wolf, S.E.; Tremel, W.; Schröder, H.C. *FEBS J* **2008**, *275*, 362.

83. Sigal, G.B.; Bamdad, C.; Barberis, A.; Strominger, J.; Whitesides, G.M. *Anal Chem* **1996**, *68*, 490.

84. Shukoor, M.I.; Natalio, F.; Tahir, M.N.; Metz, N.; Ksenofontov, V.; Theato, P.; Schröder, H.C.; Müller, W.E.G.; Tremel, W. *Chem Mater* **2008**, *20*, 3567.

85. Tahir ,M.N.; Natalio, F.; Therese, H.A.; Yella, A.; Shah, M.R.; Berger, R.; Butt, H.J.; Metz, N.; Theato, P.; Schröder, H.C., Müller, W.E.G.; Tremel, W. *Adv Funct Mater* **2009**, *19*, 285.

86. Tahir, M.N.; Eberhardt, M.; Theato, P.; Faiß, S.; Janshoff, A.; Gorelik, T.; Kolb, U.; Tremel, W. *Angew Chem Int Ed* **2006**, *45*, 908.

87. Müller, W.E.G.; Rothenberger, M.; Boreiko, A.; Tremel, W.; Reiber, A.; Schröder, H.C. *Cell Tissue Res* **2005**, *321*, 285.

88. Wiens, M.; Bausen, M.; Natalio, F.; Link, T.; Schlossmacher, U.; Müller, W.E.G. *Biomaterials* **2009**, *30*, 1648.

89. Schlossmacher, U.; Wiens, M.; Schröder, H.C.; Wang, X.; Jochum, K.P.; Müller, W.E.G. *FEBS J* **2011**, *278*, 1145.

90. Patwardhan, S.V.; Mukherjee, N.; Clarson, S.J. *J Inorg Organomet Polym* **2011**, *11*, 193.

91. Patwardhan, S.V. *Chem Commun* **2011**, *47*, 7567.

92. Kessel, S.; Thomas, A.; Börner, H.G. *Angew Chem. Int. Ed.* **2007**, *46*, 9023.

93. Kessel, S.; Börner, H.G. *Macromol Rapid Commun* **2008**, *29*, 419.

94. Meegan, J.E.; Aggeli, A.; Boden, N.; Brydson, R.; Brown, A.P.; Carrick, L.; Brough, A.R.; Hussain, A.; Ansell, R.J. *Adv Funct Mater* **2004**, *14*, 31.

95. Tomczak, M.M.; Glawe, D.D.; Drummy, L.F.; Lawrence, G.G.; Stone, M.O.; Perry, C.C.; Pochan, D.J.; Deming, T.J.; Naik, J.J. *J Am Chem Soc* **2005**, *127*, 12577.

96. Holmström, S.C.; King, P.J.S.; Ryadnov, M.G.; Butler, M.F.; Mann, S.; Woolfson, N. *Langmuir* **2008**, *24*, 11778.

97. Liang, Q.; Guan, B.; Jiang, M. *J Mater Chem* **2010**, *20*, 8236–8239.

98. Wang, S.; Ge, X.; Xue, J.; Fan, H.; Mu, L.; Li, Y.; Xu, J.; Lu, J.R. *Chem Mater* **2011**, *23*, 2466.

99. Yuwono, V.M.; Hartgerink, J.D. *Langmuir* **2007**, *23*, 5033.

100. Yang, H., Ozin, G.A.; Kresge, C.T. *Adv Mater* **1998**, *10*, 883.

101. Roth, K.M.; Zhou, Y.; Yang, W.; Morse, D.E. *J Am Chem Soc* **2005**, *127*, 325.

102. Kisailus, D.; Najarian, M.; Weaver, J.C.; Morse, D.E. *Adv Mater* **2005**, *17*, 1234.

103. Beck, J.S.; Vartuli, J.C.; Roth, W.J.; Leonowicz, M.E.; Kresge, C.T.; Schmitt, K.D.; Chu, C.T.W.; Olson, D.H.; Sheppard, E.W.; McCullen, S.B. et al. *J Am Chem Soc* **1992**, *114*, 10834.

104. Luckarift, H.R.; Spain, J.C.; Naik, R.R.; Stone, M.O. *Nat Biotechnol* **2004**, *22*, 211.

105. Klabunde, K. J.; Mulukutla, R.S. *Nanoscale Materials in Chemistry* (Klabunde, K.J. ed.), Wiley Interscience: New York, NY, 2001.

106. Ertl, G. *Catal. Rev. Sci. Eng.* **1980**, *21*, 201.

107. Somorjai, G. A.; Materer, N. *Top. Catal.* **1994**, *1*, 215.

108. Falicov, L. M.; Somorjai, G. A. *Proc. Natl. Acad. Sci.* **1985**, *82*, 2207.

109. Nel, A.; Xia, T.; Mädler, L.; Li, N. *Science* **2006**, *311*, 622.

110. Breslow, R. *Science* **1982**, *218*, 532.

111. Breslow, R. *Artificial Enzymes.* Wiley-VCH: Weinheim, 2005.

112. Wiester, M.J.; Ulmann, P. A.; Mirkin, C.A. *Angew. Chem. Int. Ed.* **2011**, *50*, 114.

113. Schmid, G. *Nanoparticles: From Theory to Application*, Wiley VCH: Weinheim, 2nd Edition, 2010.

114. Buzea, C.; Pacheco, I. I.; Robbie, K. *Biointerphases* **2007**, *2*, 17.

115. Brunner, T. J.; Wick, P.; Manser, P.; Spohn, P.; Grass, R. N.; Limbach, L. K.; Bruinink, A.; Stark, W. J. *Environ. Sci. Technol.* **2006**, *40*, 4374.

116. Lubick, N. *Environ. Sci. Technol.* **2007**, *41*, 7958.

117. Heckert, E. G.; Seal, S.; Self, W. T. *Environ. Sci. Technol.* **2008**, *42*, 5014.

118. Limbach, L. K.; Wick, P.; Manser, P.; Grass, R. N.; Bruinink, A.; Stark, W. J. *Environ. Sci. Technol.* **2007**, *41*, 4158.

119. Jia, H.Y.; Liu, Y.; Zhang, X.J.; Han, L.; Du, L.B.; Tian, Q.; Y.C. Xut, Y.C. *J. Am. Chem. Soc.* **2009**, *131*, 40.

120. Hund-Rinke, K.; Simon, M. *Environ. Sci. Pollut. Res*. **2006**, *13*, 225.

121. Federici, G.; Shaw, B. J.; Handy, R. D. *Aquat. Toxicol.* **2007**, *84*, 415.

122. Chen, J. P.; Patil, S.; Seal, S.; McGinnis, J. F. *Nat. Nanotechnol*. **2006**, *1*, 142.

123. Karakoti, A. S.; Monteiro-Riviere, N. A.; Aggarwal, R.; Davis, J. P.; Narayan, R. J.; Self, W. T.; McGinnis, J.; Seal, S. *JOM* **2008**, *60*, 33.

124. W.C. Ellis, W.C.; Tran, C. T.; Denardo, M. A.; Fischer, A.; Ryabov, A.D.; Collins, T.J. *J. Am. Chem. Soc*., **2009**, *131*, 18052.

125. Daeid, N. N.; Atkinson, S. T.; Nolan, K.B. *Pure & Appl. Chem*. **1993**, 65, 1541.

126. Fenton, H. J. H. *J. Chem. Soc., Trans.* **1894**, *65*, 899.

127. Sawyer, D. T. *Coordination Chemistry Reviews* **1997**, *165*, 297.

128. Gao, L. Z.; Zhuang, J.; Nie, L.; Zhang, J. B.; Zhang, Y.; Gu, N.; Wang, T. H.; Feng, J.; Yang, D. L.; Perrett, S.; Yan, X. *Nat. Nanotechnol.* **2007**, *2*, 577.

129. Wei, X.; Liu, T.; Li, J.; Chen, X. *Int. J. Electrochem. Sci*. **2011**, *6*, 4953.

130. Ding, N.; Yan, N.; Ren, C.; Chen, X. *Anal. Chem*. **2010**, *82*, 5897.

131. Chang, Q.; Deng, K.; Zhu, L.; Jiang, G.; Yu, C.; Tang, H. *Microchim. Acta* **2009**, *165*, 299.

132. Luo, W.; Li, Y. S.; Yuan, L.; Liu, Z.; Tang, H.; Liu, S. *Talanta* **2010**, *81*, 901.

133. Shi, W.; Zhang, X.; Hea, S.; Huang, Y. *Chem. Commun*. **2011**, *47*, 10785.

134. Chen, W.; Chen, J.; Liu, A. L.; Wang, L. M.; Li, G. W.; Lin, X. H. *Chem. Cat. Chem*. **2011**, *13*, 1151.

135. Jv, Y.; Li, B.; Cao, R. *Chem. Comm* **2010**, *46*, 8017.

136. Dai, Z.; Liu, S.; Bao, J.; Ju, H. *Chem. Eur. J.* **2009**, *15*, 4321.

137. Song, Y.; Qu, K.; Zhao, C.; Ren, J.; Qu, X. *Adv. Mater*. **2010**, *22*, 2206.

138. Franssen, M.C.R.; van der Plas, H. C. *Adv. Appl. Microbiol*. **1992**, *37*, 41.

139. Wever, R.; Hemrika, W. *Handbook of Metalloproteins* (Messerschmidt, A.; Huber, R.; Wieghardt, K.; Poulos T. ed.) Wiley & Sons (England) Ltd.,: Chichester, 2001.

140. Messerschmidt, A.; Prade, L.; Wever, R. *Biol. Chem.* **1997**, *378*, 309.

141. Martinez, J. S.; Carroll, G. L.; Tschirret-Guth, R. A.; Altenhoff, G.; Little, D. R.; Butler, A. *J. Am. Chem. Soc.* **2001**, *123*, 3289.

142. P. Coughlin, S. Roberts, C. Rush, A. Willetts, *Biotechnol. Lett.* **1993**, *15*, 907

143. H. B. Ten Brink, A. Tuyman, H. L. Dekker, W. Hemrika, Y. Izumi, T. Oshiro, H. E. Schoemaker, R. Wever , *Inorg. Chem.* **1998**, *37*, 6780

144. A. Butler, M. Sandy, *Nature* **2009** , *460* , 848

145. Ten Brink, H. B.; Dekker, H. L.; Schoemaker, H. E.; Wever, R. *J. Inorg.Biochem.* **2000**, *80*, 91.

146. Rubtsova, M. Y.; Kovba, G. V.; Egorov, A. M. *Biosens. Biolectron.* **1998**, *13*, 75

147. Karam, J.; Nicell, J. A.; *J. Chem. Tech. Biotechnol.* **1997**, *69*, 141.

148. Messerschmidt, A.; Wever, R. *Proc. Natl. Acad. Sci*. USA **1996** , *93* , 392–396.

149. Zampella, G.; Fantucci, P.; Pecoraro, V. L.; De Gioia, L. *J. Am. Chem. Soc.* **2005** , *127* , 953.

150. Colpas, G. J.; Hamstra, B. J.; Kampf, J. W.; Pecoraro, V. L. *J. Am. Chem. Soc.* **1996** , *118* , 3469.

151. De Boer, E.; Boon, K.; Wever, R. *Biochemistry* **1988**, *27*, 1629.

152. De Boer, E.; Keijzers, C. ; Laasen, A. A. K.; Reijerse, E. J.; Collision, D.; Garner, C. D.; Wever, R. *FEBS Lett*. **1988**, *235*, 93.

153. De la Rossa, R. I.; Clague, M. J.; Butler, A. *J. Am. Chem. Soc.* **1992**, *114*, 760.

154. Ligtenbarg, A. G. J.; Hage, R.; Feringa, B. L. *Coord. Chem. Rev*. **2003**, *237*, 89.

155. Clague, M. J.; Keder, N. L.; Butler, A. *Inorg. Chem.* **1993**, *32* , 4754.

156. Smith, T. S.; Pecoraro, V. L. *Inorg. Chem.* **2002**, *41*, 6754.

157. Mimoun, H.; Saussine, L.; Daire, E.; Postel, M.; Fischer, J.; Weiss, R. *J. Am. Chem. Soc.* **1983**, *105*, 3101.

158. Velusamy, S.; Punniyamurthy, T. *Org. Lett.* **2004**, *6*, 217.

159. Butler, A.; Clague, M. J.; Meister, G. E. *Chem. Rev*. **1994**, *94*, 625.

160. Meister, G. E.; Butler, A. *Inorg. Chem*. **1994**, *33*, 3269.

161. Espenson, J. H.; Pestovsky, O.; Hansen, P.; Staudt, S. *J. Am. Chem. Soc*. **1994**, *116*, 2869.

162. Hansen, P.; Espenson, J. H. *Inorg. Chem*. **1995**, *34*, 5839.

163. Daly, M. J.; Gaidamakova, E. K.; Matrosova, V. Y.; Vasilenko, A.; Zhai, M.; Leapman, R. D.; Lai, B.; Ravel, B.; Li, S. M.; Kemner, K. M.; Fredrickson, J. K. *PLoS Biol.* **2007**, *5*, e92

164. Daly, M. J.; Gaidamakova, E. K.; Matrosova, V. Y.; Vasilenko, A.; Zhai, M.; Venkateswaran, A.; Hess, M.; Omelchenko, M. V.; Kostandarithes, H. M.; Makarova, K. S.; Wackett, L. P.; Fredrickson, J. K.; Ghosal, D. *Science* **2004**, *306*, 1025.

165. Al-Maghrebi, M.**;** Fridovich, I.; Benov, L. *Arch. Biochem. Biophys.* **2002**, *402*, 104.

166. Chang, E. C.; Kosman, D. J. *J. Biol. Chem.* **1989**, *264*, 12172.

167. Emerit, J.; Edeas, M.; Bricaire, F. *Biomed. Pharm.* **2004**, *58*, 39.

168. van Remmen, H.; Ikeno, Y.; Hamilton, M.; Pahlavani, M.; Wolf, N.; Thorpe, S. R.; Alderson, N. L.; Baynes, J. W.; Epstein, C. J.; Huang, T. T.; Nelson, J.; Strong, R.; Richardson, A. *Physiol. Genomics* **2003**, *342*, 86.

169. Fridovich, I. *J. Biol. Chem.* **1989**, *264*, 7761.

170. Riley, D. P. *Chem. Rev.* **1999**, *99*, 2573.

171. Jakoby, W. R. ; Ziegler, D. M. *J. Biol. Chem.* **1990**, *265*, 20715.

172. Barondeau, D. P.; Kassmann, C. J.; Bruns, C. K.; Tainer, J. A.; Getzoff, E. D. *Biochemistry* **2004**, *43*, 8038.

173. Browne, W.R; de Boer, J.W.; Pjiper, D.; Brinksma, J.; Hage, R.; Feringa, B.L. *Modern Oxidation Methods* (Bäckvall, J.E. ed.), 2nd Ed. Wiley-VCH: Winheim, 2010.

174. Archibald, S.; Fridovich, I. *J. Bacteriol.* **1981**, *145*, 442.

175. Conesa, J. C. *Surf. Sci*. **1995**, *339*, 337.

176. Esch, F.; Fabris, S.; Zhou, L.; Montini, T.; Africh, C.; Fornasiero, P.; Comeli, G.; Rosei, R. *Science* **2005**, *309*, 752.

177. Gonzalez, P. K.; Zhuang, J.; Doctrow, S. R.; Malfoy, B.; Benson, P. F.; Menconi, M. J.; Fink, M. P. J. *Pharmacol. Exp. Ther*. **1995**, *275*, 798.

178. Pirmohamed, T.; Dowding, J. M.; Singh, S.; Wasserman, B.; Heckert, E.; Karakoti, A. S.; King, J. E.S.; Self, W. T.S. *Chem. Comm.* **2010**, *46*, 2736.

179. Perez, J. M.; Asati, A.; Nath, S.; Kaitlanis, C. *Small* **2008**, *4*, 552.

180. Tamuzzer, R. W.; Colon, J.; Patil, S.; Seal, S. *Nano Lett.* **2005**, *5*, 2573.

181. Silva, G. A. *Nat. Nanotechnol*. **2006**, *1*, 92.
182. Korsvik, C.; Patil, S.; Seal, S.; Self, W. T. *Chem. Comm*. **2007**, 1056.

183. Britigan, B. E.; Pou, S.; Rosen, G. M.; Lilleg, D. M.; Buettner, G. R. *J. Biol. Chem.* **1990**, *265*, 17533.

184. Chen. J.; Patil, S.; Seal, S.; McGinnis, J. F. *Nat. Nanotechnol*. **2006**, *1*, 142.

185. Haber, G. M J.; Lalik, E. *Catal. Today* **1997**, *33*, 119.

186. Grzybowska-Swierkosz, B. *Top. Catal*. **2000**, *11-12*, 23.

187. Dos Santos, P. C.; Dean, D. R.; Hu, Y.; Ribbe, M. W. *Chem. Rev*. **2004**, *104*, 1159.

188. Hille, R. *Trends Biochem. Science* **2002**, *27*, 360.

189. Bevers, L. E.; Hagedoorn, P.-L.; Hagen, W. R. *Coord. Chem. Rev*. **2009**, *253*, 269.

190. Guggenbichler, J. P.; Eberhardt, N.; Martinz, H.-P.; Wildner, H. *Substance with an antimicrobial effect.* PCT/EP2007/009814

191. Sayama, K.; Konishi, Y. *Tungsten oxide secondary structure having antimicrobial activity*. PCT/JP2011/057146

192. Zollfrank, C.; Gutbrod, K.; Wechsler, P.; Gugenbichler, J.P. *Mater. Sci. Eng*. **2012**, *32*, 47.
193. Lorenz, K.; Bauer, S.; Gutbrod, K.; Guggenbichler, J. P.; Schmuki, P.; Zollfrank, C. *Biointerphases* **2011**, *6*, 16.

194. Meister, G.; Butler, A. *Inorg. Chem*. **1994**, *33*, 3269.

195. Kajita, M.; Hikosaka, K.; Iitsuka, M.; Kanayama, A.; Toshima, N.; Miyamoto, Y. *Free Radical Res*. **2007**, *41*, 615.

196. Kim, J.; Takahashi, M.; Shimizu, T.; Shirasawa, T.; Kajita, M.; Kanayama, A.; Miyamoto, Y. *Mech. Ageing Dev*. **2008**, *129*, 322.

Part II

Enzymatic and templated production of inorganic materials: Taking inspiration in biomineralization

CHAPTER 2

Chemical mimicry: hierarchical 1D TiO_2@ZrO_2/SiO_2 core-shell structures reminiscent of sponge spicules by the synergistic effect of silicatein-α and silintaphin–1

Associated publication: *Langmuir, 2011, 27 (9), 5464-5471*

2.1 Introduction

Controlling the surface binding, distribution, and targeting of nanoparticles is a key requirement for the technology to use them in applications.[1,2] Utilizing the special properties of nanoparticles such as mechanical, optical, or magnetic depends on our means of positioning and organizing them in a functional context. For this, self-assembly is a very attractive strategy. Ideally, the components contain in their structures the information needed for finding their correct place and position to build functional assemblies.[3-6] Self-assembly is ubiquitous in biology, where numerous examples have been studied in much detail, and it is a challenge for current technology to make use of self-assembly in manufacturing materials, electronics, devices, etc.[7,8]

As self-assembly is essential to biology at the molecular scale, it is interesting to turn to biology for understanding and inspiration.[9] In nature, hard tissues are formed typically by composite materials which exhibit multiple levels of hierarchical organization and complex architectures.[10,11] This structural hierarchy can play a major role in determining the bulk material properties.[12] Understanding the growth of these hierarchical structures *in vivo*, can guide the synthesis of new materials *in vitro* with improved physical properties and tailored for specific applications.[12-14] One example is the hierarchically ordered mineral skeleton of some marine sponges, like *Euplectella sp.* [15]. In some siliceous sponges (demosponges and hexactinellids), silica is deposited around an organic, axial filament formed by several different proteins, like galactins, lectins, colagen, different isoforms of silicatein (α, β and γ), silintaphin, among other components still under study. All these components have different functions, from the catalytic formation of silica (like silicatein) to templating (collagen) and structure guiding (silintaphin) of the final spicule structure. [16-18] The needle-like spicules formed in this way have a lamellar structure resulting in an organic-inorganic composite.[19] Spicule formation in some of the demosponges starts within the cell and then proceeds outside the cell.[20,21] The spicule growth proceeds in a radial fashion. We could demonstrate that the appositional formation of silica lamellae around the spicules is preceded by the formation of hollow cylinders, formed by matrix-guided silicatein which mediate biocatalytic synthesis and deposition of nanostructured silica.[16] It has been demonstrated that silicatein-α does not only mediate the synthesis of biosilica but also the formation of other metal oxides such as titania (TiO_2)[22-24] zirconia (ZrO_2)[24] and GaOOH/spinel gallium oxide,[25] among others, from water stable precursors at room temperature and neutral pH, whereas the chemical synthesis of these

materials requires acidic pH and elevated temperatures. Such flexibility in uptaking different substrates makes silicatein a very atractive tool for new material synthesis in mild conditions and as an inspirational tool for development of other biomimetic small molecules. [26]

The organic-inorganic assembly in biocomposite materials provides them with unique property combinations. Sponge spicules combine mechanical strength with excellent optical properties. They exhibit advantageous properties compared to materials offered by engineering such as technical optical fibers,[27,28] based on their composite structure and their lamellar architecture, resulting in enhanced fracture toughness, as well as their low-temperature synthesis, and the presence of dopants (sodium), raising the refractive index of the fibers. The process of silica deposition in the some siliceous sponges is enzymatically mediated and matrix-guided.[20,29,30] As mentioned above, not only the enzyme silicatein, in its different isoforms, is present in the axial filament of these sponges but also many other proteins. Very often proteins must bind to other specific proteins *in vivo* in order to function. The proteins are required to bind to only one or a few other proteins of the few thousand proteins typically present *in vivo*.[31-33] In the exemplified sponge spicules, this case is not an exception, as recently a new protein was isolated from the spicule axial filament, silintaphin-1, which is believed to act through its sticky domains as a scaffold/backbone for silicatein binding and assembly.[18]

One intriguing question is whether the hierarchical mineral skeleton that is encountered in sponge spicules can be modelled synthetically through a layer-by-layer deposition of inorganic nanoparticles on a soft polymer or rigid inorganic backbone template. In this contribution, we address the question whether a concentric layer of silica nanoparticles can be deposited in biomimetic manner using surface immobilized silicatein as a hydrolytic catalyst. We have demonstrated previously that recombinant silicatein[34] retains its biocatalytic activity after immobilization onto metal oxide surfaces.[35,36] His-tagged silicatein was immobilized in self-assembled monolayeres (SAMs) on Au(111) with nitrilotriacetic acid (NTA) terminated thiols, which bind to the His-tag chelating anchor through Ni^{2+} complexation.[35] The recombinant protein, bound through a His-tag affinity sequence to the chelator NTA, was able to catalyze the formation of silica nanospheres with diameters of 70-300 nm. The principle of binding silicatein molecules to a self-assembled polymer layer was applied for the preparation of functional spicule-like core-shell materials with (alternating) metal oxide layers. Using this approach we could immobilize silicatein not only onto the surface of isolated spicules to synthesize new silica lamellae,[37] but also on the surface of magnetic oxide nanoparticles to

generate silica coatings by the immobilized enzyme.[38] Such particles are of extreme interest for targeting cell surface receptors[35] and for protein separation.[39,40]

In order to reduce the number non-biocompatible reaction steps silicatein was immobilized, in this work, onto titania nanowires with a glutamate-tag in the c-terminus of silicatein-α. The glutamate tag in silicatein-α was shown before to allow a specific binding of silicatein to hydroxyapatite.[41] An improvement of the morphological control over the polymerized silica layer could be achieved with the aid of silintaphin-1 which binds specifically and strongly to the immobilized silicatein-α *in vitro*. [18] This conjugated matrix still allows silicatein to be active towards the formation of silica and other metal oxides (e.g. zirconia). The difference in the oxide coatings with only silicatein and with silicatein/silintaphin-1 was also tested, showing that a denser organic matrix allows for an increased deposition of oxides, even though silintaphin-1 itself is not catalytically active. We anticipate that the model method described here can be generalized using other metal oxide nanostructures allowing the synthesis of a wide range of nanocomposite materials under physiological conditions.

2.2 Results and Discussion

TiO_2 nanowires were used as backbone for the immobilization and subsequent co-assembly of proteins and further to probe the influence of silintaphin-1 on the mineralization process. The TiO_2 nanowires were synthesized hydrothermally as described previously.[42] Further details on characterization of the nanowires can be found on the Supporting Information, Figure S2.

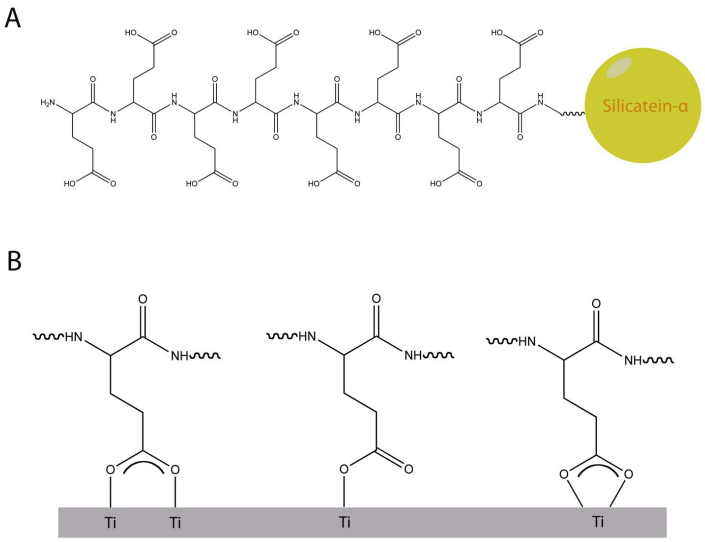

Figure 2.1. Modified silicatein-α with an 8x glutamate tag (A) and different possible binding modes of glutamate to a titania surface (B). Schemes are not to scale.

The functionalization of the TiO_2 nanowires was achieved by incubating the naked nanowires with the modified silicatein-α which possesses an eight time glutamate-tag (Glu-tag, Figure 2.1A) in TBS buffer (Tris buffer saline) at pH 7.4 for 2 hours. Carboxylic groups have been shown previously to bind efficiently to metal oxides (particularly to titanium dioxide) surfaces, either by an ester-like linkage, bridging or chelating with the metal centers on the surface, depending on the available surface coordination sites.[44,45] A scheme of the possible binding modes of glu-tag silicatein-α on TiO_2 surface is provided in Figure 2.1B.

The binding of Glu-tagged silicatein-α onto TiO_2 nanowires surface was monitored by confocal laser scanning microscopy (CLSM) using anti-silicatein primary antibodies and fluorophore (Cy3) conjugated secondary antibodies. The CLSM image in Figure 2.2A shows that virtually every nanowire imaged emitted red fluorescence when excited using a 580 nm filter due to the presence of Cy3 fluorophore, and a higher magnification clearly reveals several protein-antibody coupled globular structures. As a control experiment, TiO_2 nanowires were incubated with normal recombinant histidine-tag silicatein-α under a comparable set of conditions (TBS buffer, pH 7.4 for 2 h), where no fluorescence was observed (Supporting Information**,** Figure S3), thus proving that the binding of glu-tagged silicatein-α to metal oxide surfaces is specific to the rich glutamate tag and not due to physical adsorption or nonspecific interactions with other protein domains.

In order to study the bio-specific interaction of silintaphin-1 with silicatein *in vitro*, the TiO_2 nanowires functionalized with Glu-tag silicatein-α were incubated with silintaphin-1 (in TBS buffer, pH 7.4, 50μg/mL) for 1 h, accordingly with previous reported work.[18] Afterwards the presence of both silicatein-α and silintaphin-1 was monitored through immunostaining with specific primary antibodies for each protein and secondary antibodies labeled with different fluorophores (Cy3 for silicatein-α and AlexaFluor 488 for silintaphin-1). The Glu-tagged silicatein-α is present all over the nanowires (Figure 2.2A and D), as well as silintaphin-1 (Figure 2.2B and E) and a overlaid immunostained fluorescence image of the proteins on the TiO_2 nanowires show a significant co-localization of both silicatein-α and silintaphin-1 on the surfaces, proving that the interaction has indeed occurred (Figure 2.2C and F).

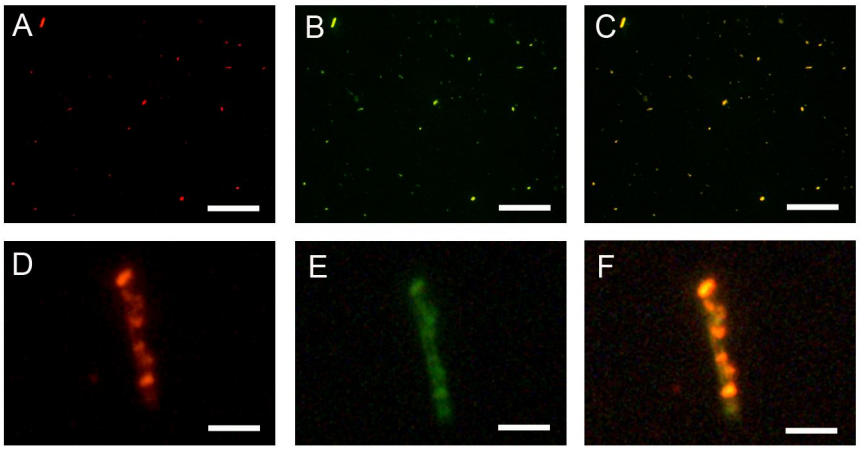

Figure 2.2. CLSM images of co-localization of silicatein-α and silintaphin-1. Immunocomplexes were visualized through treatment with secondary labelled antibodies with Cy3 (red) for silicatein-α or AlexaFluor 488 (green) for silintaphin-1. Overview and single nanowire functionalized with silicatein-α (A and D), and silintaphin-1 (B and E) respectively. Overlay image showing the co-localization of both proteins on the same nanowires (C and F). Scale bar in top row 60 µm and on bottom row 2 µm.

In addition to confirm the immobilization of silicatein and self-assembly of silintaphin-1 onto TiO_2 nanowires, atomic force microscopy (AFM) was performed on TiO_2 nanowires only with silicatein-α and with both silicatein-α and silintaphin-1. The AFM analysis of the as-synthesized TiO_2 nanowires (Figure 2.3A) showed a rather clean and smooth surface with an average roughness of 0.7 nm. The nanowires functionalized with Glu-tagged silicatein (Figure 2.3B) show a heterogeneous coating of protein with some possible protein aggregates, while the silicatein/silintaphin-1 functionalized nanowires show a more homogenous distribution of protein on the surfaces due to the increase of organic matrix (Figure 2.3C).

To confirm that the immobilized Glu-tagged silicatein-α retains its catalytic activity towards the formation of silica and zirconia (as a proof of concept for the synthesis of a metal oxide layer), the TiO_2 nanowires functionalized with only Glu-tagged silicatein-α were incubated with a 5 mM solution of tetraethyl orthosilicate (TEOS) and potassium hexafluorozirconate (K_2ZrF_6) for 5 h at room temperature. As a control, bare nanowires were incubated with the above mentioned precursor solutions under the otherwise identical conditions. In the latter case, no product was formed (*data not shown*). Subsequent TEM analysis revealed that the silicatein-α functionalized nanowires are effectively decorated with silica and zirconia nanoaggregates, resulting in an inhomogeneous coverage of the material (Figure 2.4A and 2.4D). Images at higher resolution show the amorphous character of the silica domains. It is apparent that the thickness of deposited material is non-uniform over the length of the

nanowires (Figure 2.4B and 2.4E). Higher resolution micrographs show that the deposited zirconium dioxide is composed of nanoagglomerates over the complete sample. On addition, the presence of silica and zirconia was confirmed by EDX profiling of a single nanowire where the elemental composition of the material shows the presence of Si or Zr, O and Ti. Additional Cu peaks were detected due to the copper grids employed for sample analysis (Figure 2.4C and 2.4F).

Varying the concentration of precursors, either for silica or zirconia formation, or time of incubation did not vary considerably the aspect or thickness of the silica or metal oxide layer deposited over the length of nanowires.

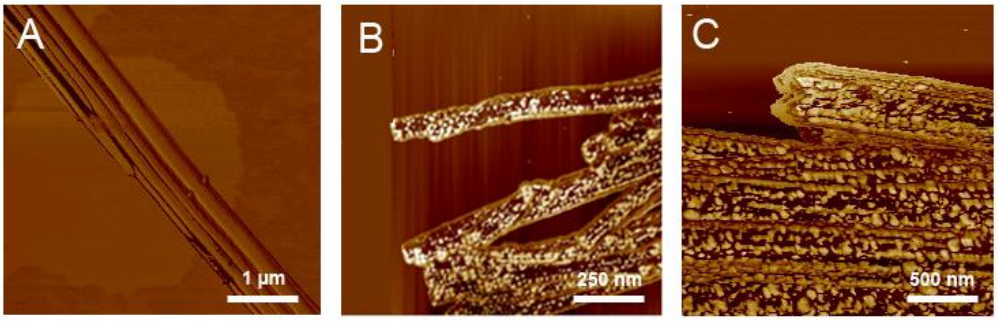

Figure 2.3. AFM phase contrast images of TiO_2 nanowires. A) as-synthesized, B) with immobilized silicatein-α and C) with immobilized silicatein-α and silintaphin-1.

Hence in order to achieve nanocomposites with characteristics closer to those found in nature, it is important to take in account the organic matrix present *in vivo*. The effect of interactors of silicatein-α on silica or metal oxides mineralization was studied using silintaphin-1 which was shown to bind to silicatein-α, even when the later is immobilized on surfaces.[34] The binding mode of silicatein-α and silintaphin-1 is still under study. It is believed not to involve the active site of silicatein, i.e. usually one silicatein protein seems to interact with more than one silintaphin molecule.

As the interaction between silicatein-α and silintaphin-1 is not expected to be related with the active site of silicatein-α, the catalyzing effect towards the formation of silica and zirconia was tested as performed previously with Glu-tagged silicatein-α. Incubation of the functionalized TiO_2 nanowires with 5 mM solution (in TBS, pH 7.4) of either TEOS or potassium hexafluorozirconate was performed for 5 h at room temperature. As a control experiment, and to exclude a catalytic effect of silintaphin-1, TiO_2 nanowires were funtionalized only with silintaphin-1 (Figure S4), with a polymeric ligand that binds histidine-

tag proteins to the surface of metal oxides, as described before (see Supporting Information for polymer synthesis and functionalization, Figure S1).[36] The silintaphin-1 functionalized nanowires were incubated under similar conditions with TEOS and potassium hexafluorozirconate.

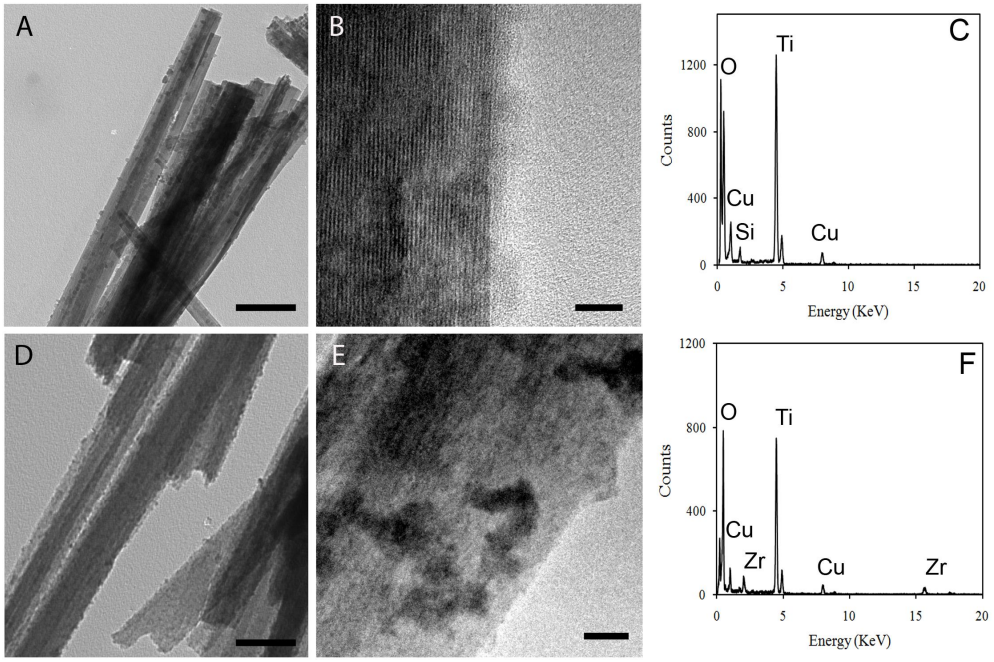

Figure 2.4. Formation of silica (A,B,C) or zirconia (D, E, F) by immobilized glu-tagged silicatein-α on TiO_2 nanowires. A) TEM overview image of TiO_2 nanowires covered with SiO_2 catalyzed by silicatein. B) Higher magnification of the surface of TiO_2 nanowires covered with SiO_2. C) EDX spectra of TiO_2 nanowires covered with SiO_2, thus indicating the presence of Ti, Si and O. D) TEM overview image of TiO_2 nanowires covered with ZrO_2 catalysed by silicatein. E) Higher magnification of TiO_2 nanowires covered with ZrO_2. D) EDX spectra of TiO_2 nanowires covered with ZrO_2, thus indicating the presence of Ti, Zr and O. Scale bars: A) 100 nm, B) 10 nm, D) 50 nm, E) 10 nm

The resulting composites were analyzed by transmission electron microscopy, as shown in Figure 2.5A and 2.5D. The silica coated nanowires in the presence of both proteins show a layer with an uniform average thickness of 14.6 ± 3.9 nm , when compared with the coating obtain in the presence of silicatein only (Figure 2.4A) which only showed domains with an average thickness about 6.4 ± 1.6 nm. High resolution images of the silica-titania interface show the amorphous aspect as well as the uniform coverage over the complete surface (Figure 2.5B). Further EDX analysis confirms only the presence of only Si, Ti and O as expected (Figure 2.5C).

For the ZrO_2 coated TiO_2 nanowires in the presence of both proteins, a thicker surface coverage was achieved (Figure 2.5D) in comparison with the coating using only silicatein (Figure 2.4D)**.** The average thickness of the ZrO_2 coating (in the presence of both proteins) was estimated to be around 22.2 ± 3.2 nm. In contrast in the presence of only silicatein-α the average thickness was of 10.3 ± 2.1 nm. At higher resolution the increased thickness of the zirconia layer (Figure 2.5E) is clearly visible. In addition, crystalline domains with a fringe spacing of 2.96 Å (the (111) lattice spacing of cubic zirconia) were observed.[46] (Supporting Information, Figure S1.6B). These domains appear sparsely over the whole sample but this is particularly interesting as the high temperature polymorph of zirconia can be synthesized under a physiological set of conditions (Figure S6C).[47] EDX analysis shows the presence of Zr, Ti and O pointing to the presence of a zirconium dioxide layer on top of the titania nanowires (Cu peaks are due to the grid used for sample analysis) (Figure 2.5F).

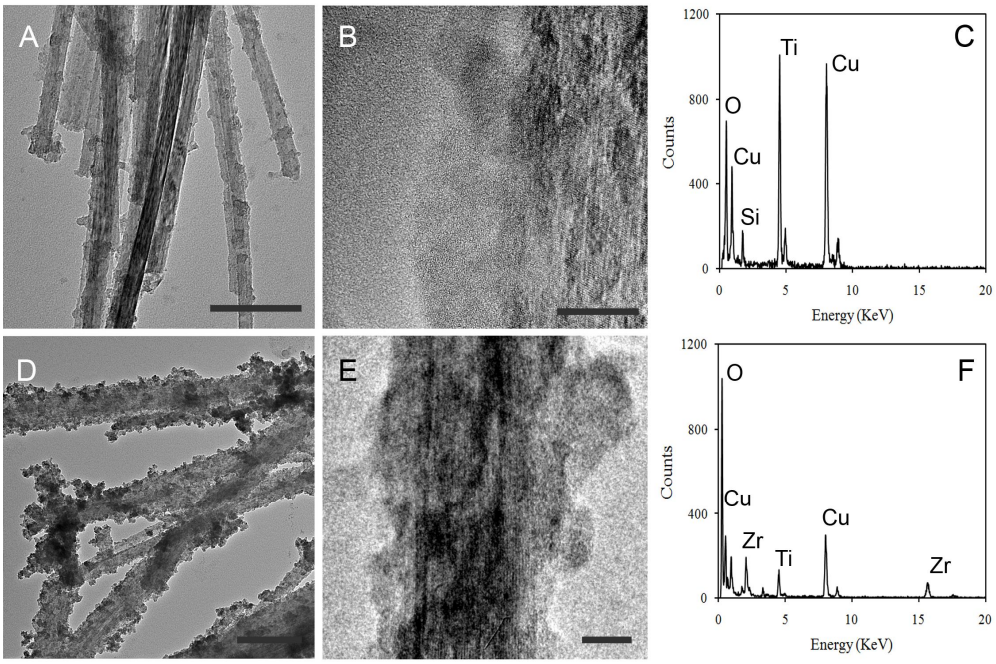

Figure 2.5. Formation of silica (A,B,C) or zirconia (D, E, F) by immobilized glu-tagged silicatein-α and silintaphin-1 on TiO_2 nanowires. A) TEM overview image of TiO_2 nanowires covered with SiO_2 catalysed by silicatein/silintaphin. B) Higher magnification of the surface of TiO_2 nanowires covered with SiO_2. C) EDX spectra of TiO_2 nanowires covered with SiO_2, thus indicating the presence of Ti, Si and O. D) TEM overview image of TiO_2 nanowires covered with ZrO_2 catalysed by silicatein/silintaphin. E) Higher magnification of TiO_2 nanowires covered with ZrO_2. D) EDX spectra of TiO_2 nanowires covered with ZrO_2, thus indicating the presence of Ti, Zr and O. Scale bars: A) 100 nm; B) 10 nm; D) 100 nm; E) 10 nm.

Further quantification of the deposited layers of oxides using the different protein combinations was done through the analysis of EDX data by comparing the intensity for the Ti, Zr and Si peaks in the EDX profiles. Values for comparison were made along several nanowires and averaged out. All measures were taken from the centers of the nanowires, in order to have comparable values, since the nanowires vary in diameter and length. Otherwise, as referred before, the mineralized coatings, especially for the silicatein/silintaphin samples are homogenously deposited along the different nanowires (meaning no difference was observed, for example, between the middle and the tips of the nanowires).

The ratios of Si/Ti or Zr/Ti for the different samples are summarized in Table 1, where it is possible to confirm that higher amounts of either silica or zirconia are achieved, when both proteins where immobilized onto TiO_2 nanowires.

Table 2.1. Ratios of Si/Ti and Zr/Ti for the samples where either one protein was used (silicatein) or two proteins were used (silicatein/silintaphin). The values were obtained by evaluating the ration of the peak intensity detected by EDX in the different samples.

Sample	Si/Ti	Zr/Ti
Silicatein	0.24 ± 0.10	0.31 ± 0.11
Silicatein/Silintaphin	0.74 ± 0.06	0.76 ± 0.10

Thus it is shown that even though silintaphin-1 was added “on top” of silicatein-α, the active sites of silicatein-α are still available for catalyzing the formation of the oxides. The control experiment using TiO_2 nanowires functionalized with silintaphin-1 showed no significant formation of either silica or zirconia (Figure S5), which indicates that silintaphin-1 by itself, has no catalytic effect on the formation of either silica or other metal oxides.

We can assume that when only one protein is present, a more heterogeneous organic layer is present as seen in Figure 2.3B, and consequently during mineralization also a heterogeneous coating is formed. On the other side, when both proteins are present a more homogeneous organic layer is present resulting thus in a more homogeneous coating after mineralization.

The addition of silintaphin-1 lead to the formation of a more uniform organic layer, which gives rise to more homogenous distribution of the oxide layer. Furthermore, silintaphin-1 is

expected to have a synergistic effect towards silicatein-α, though not being active itself (as shown here, Figure S5), by creating protein-protein aggregates, an interconnected network of proteins that is formed allowing a more homogenous mineralization.[18]

2.3 Conclusion

In summary, we have used the principles of surface functionalization, self-assembly and enzyme catalysis to achieve a dense coating of TiO_2 nanowires with the metal oxides SiO_2 and ZrO_2. For this purpose we have used glutamate-tagged silicatein-α to functionalize the surface of TiO_2 nanowires. Silicatein-α retains its catalytic activity when immobilized on the surface of the nanowires. The surface-immobilized protein was shown to remain active by catalyzing the formation of silica and zirconia (as model metal oxides). Hence it was shown that the direct immobilization of silicatein-α using incorporated surface specific tags, is a simple and efficient method for one-step functionalization under mild physiological conditions (buffer solution, neutral pH and at room temperature).

The tuning of the silica or metal oxide layer was further improved by the use of silintaphin-1, a silicatein-α interactor. It was shown that silintaphin-1 binds specifically to silicatein-α, even when the later is immobilized on a surface and that silicatein-α still remains active towards the formation of metal oxides or silica. Silintaphin-1 by itself showed no noticeable catalytic effect towards the formation of these oxides.

The formation of silica or zirconia in the presence of both proteins produced a thick uniform surface coverage. Average coatings of 14.6 nm for silica and 22.2 nm for zirconia were obtained, all over the whole samples when using both proteins. In contrast, attempts to fabricate homogeneous films with silicatein-α only produced a surface coverage with an average thickness of 6.4 nm for silica and 10.3 nm for zirconium dioxide under otherwise identical reaction conditions.

Hence, a fine tuning of the formation of silica or zirconia by silicatein-α was achieved, which is of special interest in materials where surface properties at the nanoscale are of vital importance for the overall properties of the composites. Also, the synergistic effect of the several spicule protein matrix constituents was demonstrated, which may shed light into future work in the topic of artificial mineral formation.

2.4 Experimental Section

Materials. Titanium isopropoxide (ACROS, 99 %), tetraethyl orthosilicate (TEOS, Sigma-Aldrich, 99.9%), potassium hexafluorozirconate (K_2ZrF_6, Sigma-aldrich, 99%), Tris buffered saline (TBS, Sigma-aldrich), milk powder (Carl Roth), Cy3-conjugated goat anti-rabbit antibody (Dianova) AlexaFluor488 conjugated anti-mouse antibody (Invitrogen) were purchased and used as received without further purification. Solvents, acids and bases, such as ethanol, dichloromethane, HCl, HNO_3 and NaOH, were purchased technical grade and used as received.

Synthesis of the TiO_2 nanowires. The TiO_2 nanowires were synthesized following a modified procedure given by Bruce and co-workers.[42] In brief, 1 g of titanium isopropoxide was taken in a Teflon vessel and 6 ml of analytical grade ethanol (99.8 %) were added into it. The Teflon vessel was kept in a desiccator. The precipitation of TiO_2 was initiated under moist atmosphere induced by placing a Petri dish filled with water at the bottom of the desiccator. The diffusion experiment was stopped after 12 h, followed by the addition of 25 ml of 10 M NaOH aqueous solution. Then the reaction vessel was sealed into a stainless steel hydrothermal bomb, which was placed in an oven maintained at 180 °C for 20 h. The obtained sample was filtered and repeatedly washed with 0.1 M HNO_3, 1 N HCl and de-ionized water. The product was dried under vacuum for 3 h. Further details concerning the characterization of the nanowires are given in the Supporting Information

Glu-tag silicatein-α and silintaphin-1 immobilization. Recombinant glutamate tagged silicatein-α and silintaphin-1 were prepared as described before.[18,41] For the functionalization of silicatein, 1 mg of TiO_2 nanowires were dispersed and sonicated in 5 mL of TBS buffer (pH 7.4) until they were totally dispersed. Subsequently, silicatein-α was added in order to obtain a final concentration of 30 nmol. The sample was incubated at room temperature for 2 h with agitation. The glu-tag silicatein-α immobilized TiO_2 nanowires were washed with TBS buffer (pH 7.4) to remove unbound protein. To further immobilize silintaphin-1 a solution of 30 nmol of protein in TBS buffer (pH 7.4) was added to the silicatein functionalized TiO_2 nanowires, incubating for 1 h with agitation.[18] Then the sample was washed with buffer to remove unbound protein. Prior to use all samples were re-suspended in TBS buffer (pH 7.4).

Immunostaining and confocal imaging. Specific anti-silicatein and anti-silintaphin antibodies were prepared as described before.[34,18] The immobilisation of silicatein and

silintaphin was monitored by incubating primary anti-silicatein (produced in rabbit) or anti-silintaphin (produced in mouse) polyclonal antibody (1:2000 dilution), in a 5% blocking solution (milk powder) for 2h at room temperature. The sample was washed several times using TBS, (Tris-buffered saline, pH 7.4) for 5 min. followed by the secondary antibody, anti-rabbit Cy3 labelled or anti-mouse AlexaFluor 488 labeled (1:2000 dilution), for silicatein-α and silintaphin-1 respectively, incubation in 5% blocking solution for 3h at room temperature, and then washed with TBS. As control TiO_2 nanowires without immobilized protein were used. The fluorescence analysis was performed with an Olympus AHBT3 light microscope, together with an AH3-RFC-reflected light fluorescence attachment at the emission wavelength of 580 nm and 499 nm.

Protein assisted synthesis of silica and zirconia. For the deposition of silica or zirconia, TiO_2 nanowires functionalized with just glu-tag silicatein-α or with both silicatein and silintaphin were used. In all experiments, for silica synthesis, the TiO_2 nanowires were incubated with a 5 mM solution of TEOS in TBS buffer (pH 7.4) for 5 h at room temperature with agitation. For zirconia synthesis, the TiO_2 nanowires were incubated with a 5mM solution of K_2ZnF_6 in TBS buffer (pH 7.4) for 5 h at room temperature with agitation. After incubation the nanowires were washed with MilliQ water and ethanol several times, and dried under a stream of N_2.

As a control, nanowires with silintaphin-1 directly immobilized were used. Further details regarding the functionalization can be found on the supporting information. The silintaphin-1 functionalized nanowires were incubated under the same conditions as above with TEOS or K_2ZrF_6, where no catalytic effect was observed.

Transmission electron microscopy. Characterization and morphology analysis of the samples was carried out using transmission electron microscopy (TEM) using a Philips 420 instrument with an acceleration voltage of 120 kV or for high resolution TEM, a Philips TECNAI F30 electron microscope (field-emission gun, 300 kV extraction voltage). The samples for TEM analysis were first washed with Milli-Q water and by centrifugation to remove the possible formation of buffer salts. Afterwards 5 μL of the products ressuspended in Milli-Q water were droped in a copper TEM grid covered with carbon and let to dry overnight at room temperature, before taking to analysis.

Thickness and ratio measurements of the SiO_2 or ZrO_2 layers. The thickness of the SiO_2 or ZrO_2 layers formed either by the catalytic action of silicatein or silicatein/silintaphin around the nanowires, was measured by analysis of TEM. A total of 10 nanowires were

analyzed. For the ratios of Si/Ti and Zr/Ti in the nanowires, EDX (energy-dispersive X-ray spectroscopy) peak intensities for the elements Ti, Zr, Si were evaluated for 5 nanowires in each sample (with one protein or with 2 proteins) and always in the middle of the nanowire in order for better comparison between samples. All measurements were made in triplicate, and the average of the measurements was taken. For statistical purposes a paired Student´s t-test was applied.[43]

Atomic Force Miscropy (AFM) analysis. Samples for AFM analysis were prepared by drop casting: One drop from a 20 µl syringe of sample solution was deposited on a freshly cleaved mica surface. Subsequently, the mica sheet was transferred into a high vacuum chamber and dried overnight. All SFM images were recorded at room temperature under ambient conditions using a commercial AFM (Multimode, Nanoscope IIIa controller, Veeco, California, USA) in tapping mode. This instrument was equipped with a piezoelectric scanner allowing a maximum x,y-scan size of 17 µm and a maximum z-extension of 3.9 mm. Silicon cantilevers (OMCL AC240 and OMCL AC160 (Olympus, Japan), nominal spring constants of 2 Nm^{-1} and 42 Nm^{-1} and nominal resonance frequencies of 70 kHz and 300 kHz, respectively) with an integrated tip and, a tip radius < 10 nm were plasma cleaned prior to use. Typically the tip was scanned at velocities from 0.5 to 1 μms^{-1}. For all samples the topography and phase contrast images were recorded. Raw data were modified by applying the first order ‘‘flatten’’ filter in order to achieve scan lines at the same average height and average tilt.

2.5 References

1. Daniel, M.-C.; Astruc, D. *Chem. Rev.* **2004,** *104,* 293-346.
2. Talapin**,** D. V.; Lee, J.-S.; Kovalenko, M. V.; Shevchenko, E. V. *Chem. Rev.* **2010**, *110*, 389-458.
3. Zhang, S. *Nature Biotechnol*. **2003**, *21*, 1171-1178.
4. Palmer, L. C.; Velichko, Y. S.; Olvera de la Cruz, M.; Stupp, S. I. *Phil. Trans. R. Soc. A* **2007**, *365*, 1417-1433.
5. Lehn, J. M.; Ball, P. In: The New Chemistry. Hall, N. Eds., Cambridge Univ. Press; Cambridge, U.K. 2000, pp. 300–351.
6. Desiraju, G. R. Crystal Engineering: The Design of Organic Solids. New York: Elsevier, 1989.

7. Alberts, B.; Bray D. ; Lewis, J.; Raff, M.; Roberts, K.; Watson, J. D. Molecular Biology of the Cell. New York: Garland, 1994.
8. Sahoo, J. K.; Tahir, M.N.; Yella, A.; Schladt, T. D.; Mugnaioli, E.; Kolb, U.; Tremel, W. *Angew. Chem.* **2010**, 120, 7741-7745; *Angew. Chem. Int. Ed.* **2010**, *49*, 7578–7582.
9. Hall, S. R. *Proc. R. Soc. A* **2009**, *465*, 335-366.
10. Bushan, B. *Phil. Trans. R. Soc. A* **2009**, 367, 1445-1486.
11. Lakes, R. *Nature* **1993**, *361*, 511-515.
12. Zhang, S.; Marini, D. M.; Hwang, W. Santoso, S. *Curr. Opin. Chem. Biol*. **2002**, *6*, 865-71.
13. Cattaneo-Vietti, R.; Bavstrello, G.; Cerrano, C.; Sara, M.; Benatti, U.; Giovine, M.; Gaino, E. *Nature* **1996**, *383*, 397-398.
14. Weiner, S.; Wagner, H. D. *Annu. Rev. Mater. Sci.* **1998**, *28*, 271-298.
15. Aizenberg, J.; Weaver, J. C.; Thanawala, M. S.; Sundar, V. C.; Morse, D. E.; Fratzl, P. *Science* **2005**, *309***,** 275-278
16. (a) Cha, J. N.; Shimizu, K.; Zhou, Y.; Christiansen, S. C.; Chmelka, B. F.; Stucky, G. D.; Morse, D. E. *Proc. Natl. Acad. Sci. U. S. A.* **1999**, *96*, 361–365. (b) Schröder, H. C.; Boreiko, A.; Korzhev, M.; Krasko, A.; Tahir, M. N.; Tremel, W.; Eckert, C.; Müller, I. M.; Müller., W. E. G. *J. Biol. Chem.* **2006**, *281*, 12001–12009.
17. Imhoff, J.M.; Garrone, R. *Connect. Tissue Res.* **1983**, *11*, 193-197.
18. Wiens, M.; Bausen, M.; Natalio, F.; Link, T.; Schloßmacher, U.; Müller, W.E.G. *Biomaterials* **2009**, *30*, 1648-1656.
19. Müller, W. E. G.; Belikov, S. I.; Tremel, W.; Gamulin, V.; Perry, C. C.; Boreiko, A.; Schröder, H. C. *Micron* **2006**, *37*, 107-120
20. Müller, W. E. G.; Rothenberger, M.; Boreiko, A.; Tremel, W.; Reiber, A.; Schröder, H. C. *Cell Tissue Res*. **2005**, *321*, 285-297
21. Uriz, M.J.; Turon, X.; Becerro, M.A. *Cell Tissue Res.* **2000**, 301, 299-309.
22. Sumerel, J. L.; Yang, W.; Kisailus, D.; Weaver, J.; Choi, J. H.; Morse, D. E. *Chem. Mater*. **2003**, *15*, 4804-4809.
23. Mueller, W.E.G.; Wang, X.H.; Kropf, K.; Ushijima, H.; Geurtsen, W.; Eckert, C.; Tahir, M.N.; Tremel, W; Boreiko, A.; Schlossmacher, U.; Li, J.; Schroeder, H.C. *J. Struct. Biol.***2008**, *161*, 188-203.

24. Tahir, M.N.; Théato, P.; Müller, W.E.G.; Schröder, H.C.; Boreijko, A.; Faiß, S.; Janshoff, A.; Huth, J.; Tremel, W. *Chem. Commun.* **2005**, *28*, 5533-5535.
25. Kisailus, D.; Choi, J.H.; Weaver, J.C.; Yang, W.; Morse, D.E. *Adv. Mater.* **2005**, *17*, 314-318.
26. Brutchey, R.L.; Morse, D.E. *Chem. Rev.* **2008**, **108**, 4915-4934.
27. Aizenberg, J.; Sundar, V. C.; Yablon, A. D.; Weaver, J. C.; Chen, G. *Proc. Natl. Acad. Sci. USA* **2004**, *101***,** 3358-3363.
28. Müller, W. E. G.; Wendt, K.; Geppert, C.; Wiens, M.; Reiber, A.; Schröder, H. C. *Biosensors and Bioelectronics* **2006**, *21*, 1149-1155.
29. Cha, J. N.; Shimizu, K.; Zhou, Y.; Christiansen, S. C.; Chmelka, B. F.; Stucky, G. D.; Morse, D. E. *Proc. Natl. Acad. Sci. USA* **1999**, *96*, 361-365.
30. Shimizu, K.; Cha, J.; Stucky, G. D.; Morse, D. E. *Proc. Natl. Acad. Sci. U.S.A.* **1998**, *95*, 6234-6238
31. Bartlett, J.D.; Ganss, B.; Goldberg, M.; Moradian-Oldak, J.; Paine, M.L.; Snead, M.L.; Wen, X.; White, S.N.; Zhou, Y.L. *Curr. Top. Dev. Biol.* **2006**, *74*, 57-115.
32. Dominguez, R.; Holmes, K.C. *Annu. Rev. Biophys.* **2011**, *40*, 169-186.
33. Rivas, J. De Las; Fonatanillo, C. *PLoS Comput. Biol.* **2010**, *6*, e1000807.
34. Krasko, A.; Batel, R.; Schröder, H. C.; Müller, I. M.; Müller, W. E. G. *Eur. J. Biochem.* **2000**, *267***,** 4878-4887
35. Tahir, M. N.; Théato, P.; Müller, W. E.G.; Schröder, H.C.; Janshoff, A.; Zhang, J.; Huth, J.; Tremel, W. *Chem. Commun.* **2004**, 2848-2849
36. Tahir, M. N.; Eberhardt, M.; Therese, H. A.; Kolb, U.; Theato, P.; Müller, W. E. G.; Schröder, H. C.; Tremel, W. *Angew. Chem.* **2006**, *118*, 4921-4927; *Angew. Chem. Int. Ed.* **2006**, *45*, 4803-4809.
37. Schröder, H. C.; Natalio, F.; Shukoor, I.; Tremel, W.; Schloßmacher, U.; Wang, X.; Müller, W. E. G. *J. Struct. Biol.* **2007**, *159***,** 325-334
38. Shukoor, M. I.; Natalio, F.; Tahir, M. N.; Metz, N.; Ksenofontov, V.; Theato, P.; Schröder, H. C.; Müller, W. E. G.; Tremel, W. *Chem. Mater.* **2008**, *20*, 3567–3573
39. Shukoor, M. I.; Natalio, F.; Krasko, A.; Schröder, H. C.; Müller, W. E. G.; Tremel, W. *Chem. Commun.* **2007,** 4677–4679.
40. Shukoor, M. I.; Natolio, F.; Glube, N.; Tahir, M. N.; Therese, H. A.; Ksenofontov, V.; Metz, N.; Theato, P.; Langguth, P.; Boissel, J.-P.; Schröder, H. C.; Müller, W. E. G.;

Tremel, W. *Angew. Chem.* **2008**, *120***,** 4826-4830; *Angew. Chem. Int. Ed.* **2008**, *47***,** 4748-4752.

41. Natalio, F.; Link, T.; Müller, W. E. G.; Schröder, H. C.; Cui, F.; Wang, X.; Wiens, M. *Acta Biomaterialia* **2010**, *6*, 3720-3728.
42. Armstrong, A. R.; Armstrong, G.; Canales, J.; Bruce, P. G. *Angew. Chem.* **2004**, *116*, 2336-2338; *Angew. Chem. Int. Ed.* **2004**, *43*, 2286-2288.
43. Sachs, L. *Angewandte Statistik*; Springer, Berlin, **1984**, 242-243
44. Umland, F.; Wünsch, G. Charakteristische Reaktionen Anorganischer Stoffe, 2nd Ed.; Aula Verlag, Wiesbaden, 1991.
45. Kaim, W.; Schwederski, B. Bioanorganische Chemie: Zur Funktion chemischer Elemente in Lebensprozessen, 4th Ed.; Vieweg+Teubner; Stuttgart, 2005.
46. Tahir, M. N.; Gorgishvili, L.; Li, J.; Gorelik, T.; Kolb, U.; Nasdala, L.; Tremel, W. *Solid State Sciences*, **2007**, *9*, 1105-1109
47. Navrotsky, A. *Geochem. Trans*. 2003, *4*, 34–37.

CHAPTER 3

Enzymatic Synthesis and Surface Deposition of Tin Dioxide using Silicatein-α

Associated publication: *Chem. Mater., 2011, 23 (24), 5358–5365*

3.1 Introduction

In biological systems such as diatoms and sponges, the formation of solid silica structures with precisely controlled morphologies is directed by proteins and polysaccharides and occurs in water media at neutral pH. Typical examples are marine sponge or diatoms where silicification is thought to occur at pH ≈ 5.4.[1,2] The control over mineralization achieved in biological systems has been an inspiration for the development of new synthetic routes to materials with technological interest.[3] Biological organisms are able to synthesize a myriad of inorganic materials (calcium carbonate, calcium phosphate, silica, iron oxide, etc.) using very simple precursors and under mild reaction conditions, usually at ambient temperature and almost neutral pH, resulting in highly complex structures with several levels of hierarchy from the nano to the macro level.[4]

Mostly, these mineralized materials are formed either by controlled condensation in specific compartments, e.g., by regulating the concentration of the inorganic precursors, or by enzymatic catalysis. In the case of demosponges like *Tethya aurentia* or *Suberites domuncula*, the inorganic skeleton composed of silica spicules is formed by the catalytic activity of mainly one class of proteins, the silicateins.[5,6] These proteins have proved very versatile: besides the formation of silica and polysilsesquioxanes,[7-9] they can also catalyze the formation of TiO_2,[10] ZrO_2,[11] $CaTiO_3$,[12] and $GaOH/Ga_2O_3$.[13] The slow hydrolysis and polycondensation in these syntheses were derived from a mechanism underlying biosilicification,[7,8] which was confirmed through cloning, site-directed mutagenesis and detailed biochemical investigations.[14]

The broad variety of "synthetic biomaterials" that can be obtained with silicatein indicates that this protein has a very flexible active site. Therefore a very general mechanism can be assumed to underlay its catalytic activity. Furthermore, the materials catalyzed by silicatein (native and recombinant) often exhibit crystalline polymorphs that are uncommon for low temperature syntheses (e.g. anatase TiO_2,[15,16] cubic ZrO_2[10] or γ-Ga_2O_3[13]) and that are usually only obtained at high temperatures or under extreme pH conditions.[17]

The mechanism underlying enzyme-mediated biosilicification was translated into a bioinspired approach (i) by using the intact axial protein filament from *T. aurantia* or their constitutional monomers obtained by disaggregation of the filaments,[18] (ii) or those produced from recombinant DNA templates cloned in bacteria.[7,19] (iii) The corresponding recombinant proteins could be surface bound to produce thin films of silica,[20] titania,[16] or zirconia.[10] (iv)

Finally, kinetically controlled catalytic hydrolysis and polycondensation could be achieved through development of synthetic analogs of the enzyme responsible for biosilicification.[9,21] The latter process uses vapor diffusion of a hydrolytic catalyst into the solution of a molecular precursor to establish temporal and spatial vectorial gradients of catalyst concentration for the kinetically slow hydrolysis of precursor monomers at room temperature and ambient pressure. Functionalized gold nanoparticles mimic catalytic activity of a polysiloxane-synthesizing enzyme. We recently found that core-shell TiO_2@SiO_2 and TiO_2@ZrO_2 nanofibers can be obtained via grafting of silicatein-α onto a TiO_2 nanowire backbone followed by a co-assembly of "sticky" protein, silintaphin-1, through its specifically interacting domains.[22] This mechanism can be harnessed for nanostructural control of patterned biosilica-based biomaterials. To test the possibility that the catalytic potential of silicatein can be used for building up complex functional inorganic/organic hybrid materials by successive hydrolysis and condensation reactions, we examined the formation of nanostructured crystalline tin dioxide using surface-bound silicatein in aqueous solution. Tin dioxide is a well-known wide band-gap semiconductor material that combines high conductivity with high optical transparency in the visible range,[23] making it an important component for optoelectronic applications. These properties have been already demonstrated in applications as transparent conducting oxides in electrodes for solar cells[24] or lithium-ion batteries.[25] Tin dioxide has also been used as a heterogeneous oxidation catalyst[26] or as a solid state gas sensor.[27]

The efficiency of these materials is closely related to their nanoscopic properties, the surface to volume ratio being of crucial importance. Furthermore semiconductor nanocrystals are attractive candidates for nanoscale devices due to their enhanced physicochemical properties compared with the bulk materials.[28] All these properties have raised a special interest in the synthesis of nanostructured tin dioxide in recent years. Several different morphologies have been achieved like nanodiscs,[29] nanobelts,[30] nanorods[31] between others, usually applying vapor deposition,[32] solvothermal[33] or microwave[34] routes. Hollow SnO_2 nanoparticles were prepared by a template-free hydrothermal route.[35] Also the formation of tin dioxide using amino acids via hydrothermal route or polypeptides at room temperature (reaction times up to 2 weeks) has been reported recently.[36] In all cases, the synthetic routes either demand for harsh conditions though with good structural control whereas milder conditions lead structures with less morphological and structural control.

A crucial point for the formation of metal oxides is the versatility of the synthetic route, as they have a broad field of application, either used as thin films or as free standing

nanoparticles. In this contribution we show that silicatein is able to produce not only nanostructured SnO_2 dispersed in solution but also when immobilized on surfaces (glass slide), thereby providing flexible and mild biomimetic pathways for the fabrication of SnO_2 based materials with potential applications in catalysis or optoelectronics.

3.2 Results and discussion

The synthesis of SnO_2 nanostructures was achieved by incubating 5 mM of Na_2SnF_6 precursor with recombinant silicatein-α (50 µg/mL) in TBS (Tris buffer saline) buffer pH 7.4 under agitation at room temperature. After approximately 4 h a visible white precipitate was formed. Controls using either only TBS buffer or the denaturated protein showed no precipitate formation or any other reaction product (supporting information, Figure S7). After extensive washing with water and ethanol, to remove unbound protein and buffer salts, the precipitate was dried and characterized by transmission electron microscopy (TEM). The overall sphere like morphology of the as-synthesized product can be seen in Figure 3.1A. The spherical agglomerates have an average size of 50 nm. Silicatein typically assembles in a fractal manner forming agglomerates. When incubated with silica precursors similar structures are obtained.[18] The morphology of the product in Figure 3.1 is assumed to arise from a templating effect of the protein agglomerates. Zooming into the sample shows that the sphere-like agglomerates are composed of smaller particles appearing as amorphous/nanocrystalline material (Figure 3.1B and C). TEM and HRTEM reveal that the product is made up of amorphous as well as small crystal domains (between 2 and 5 nm). EDX of the sample (Figure 3.1D) shows only the presence of carbon, tin and oxygen. The copper signal arises from the grids used for the sample preparation. In the crystal domains, a *d* spacing of 3.3 Å was obtained for the lattice fringes which is a good match to the (110) planes of SnO_2. Electron diffraction on the sample (inset in Figure 3.1C) supports the presence of some crystal domains.

X-ray diffractometry was used to determine the overall composition and structure of the products. It requires the availability of material in sufficient amount and purity. X-ray diffraction patterns of all samples (see Figure 3.1E) indicate the presence of SnO_2 (cassiterite, PDF 41-1445) independent of the choice of reaction parameters. The reflection broadening due to particle size effects prevents a quantitative determination of the pattern using Rietveld

methods. However, the presence of few very broad reflections in Figure 3.1E indicates the formation of a product composed of mainly amorphous and/or small crystallites. The position of the main reflections is compatible with the presence of tin dioxide.

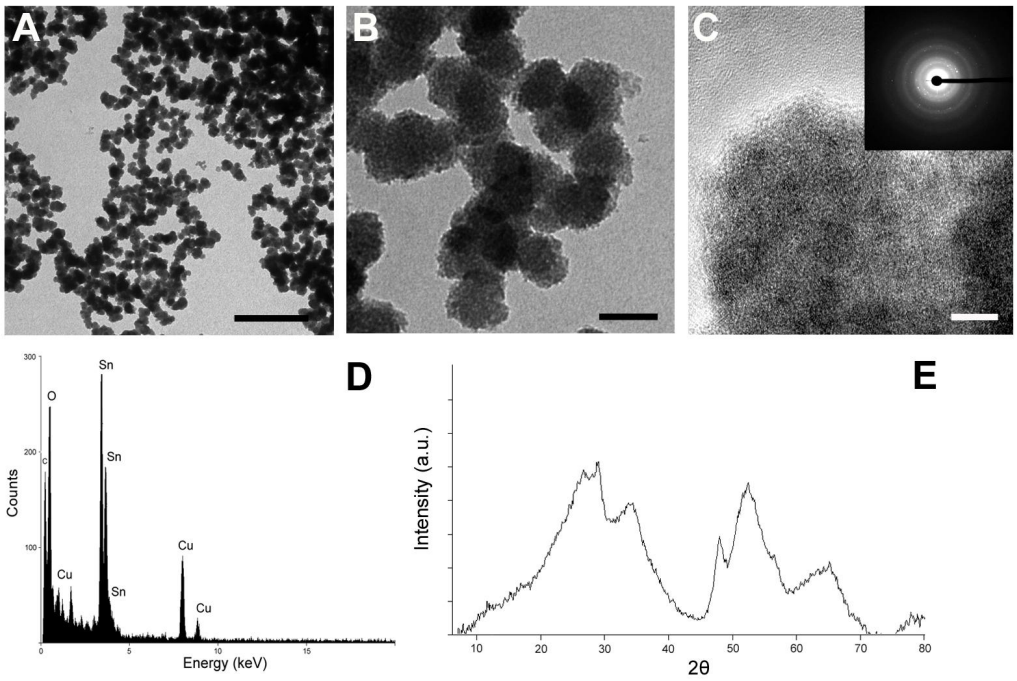

Figure 3.1. SnO_2 obtained by silicatein-mediated synthesis. (A) and (B) TEM micrographs of the as-synthesized product. (C) HRTEM micrograph of the as-synthesized product with electron diffraction pattern in the inset; (D) EDX and (E) XRD of the as-synthesized product. Scale bars: 200 nm, 50 nm and 5 nm respectively.

Heat treatment of the sample (200°C for 2 h) was used to further characterize the product and probe any possible phase transformation. TEM images in Figure 3.2A and B reveal a decrease in aggregate size to about 20 nm while maintaining the small crystallite size. HRTEM (Figure 3.2C) shows an increase in the crystal domain size with values ranging from 5 to 10 nm. Lattice fringe measurements still show an average value of 3.3 Å for the (110) plane of tin dioxide. For the larger particles shown in Figure 3.2C, the distances between two adjacent planes are 1.6; 2.4 and 3.3 Å, corresponding to the (220), (110) and (200) planes of cassiterite (Figure 3.2D). The powder X-ray diffraction pattern in Figure 3.2E shows sharpened reflections whose positions and relative intensities match well with expected pattern for cassiterite (PDF 41-1445, grey vertical lines in Figure 3.2E) as in the freshly synthesized product.

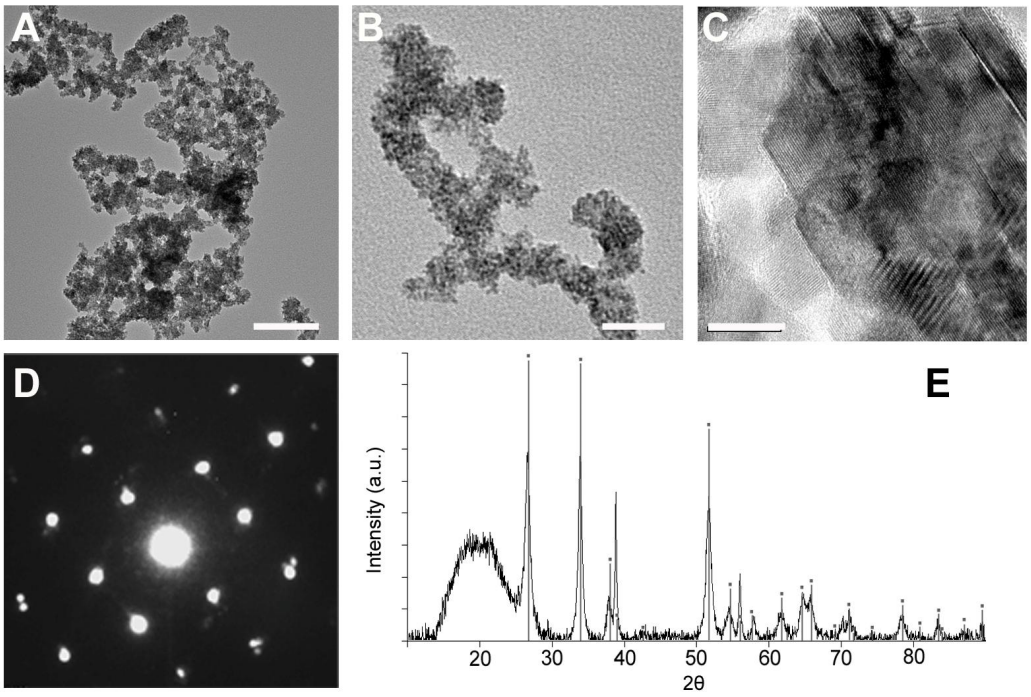

Figure 3.2. Characterization of SnO_2 synthesized using silicatein as hydrolytic catalyst, after annealing at 200°C. (A) and (B) TEM micrographs of the annealed product. (C) HRTEM of the annealed product. (D) Electron diffraction referring to the spot in (C). (E) XRD pattern of the annealed product and calculated powder pattern (grey vertical lines) for cassiterite (**PDF** 41-1445). Scale bars: 100nm, 20 nm and 10 nm respectively.

The typical plasmon band of SnO_2 was identified in both samples, as-synthesized and annealed, at around 280 nm as can be inferred from the UV-Vis spectra in Figure 3.3. The absorption band edge for SnO_2 was reported to be around 300 nm.[41] In the prepared samples the band edge is blue shifted to 280 nm which indicates - in agreement with the small particle size - the presence of a quantum size effect. For both, the as-synthesized and the annealed sample, the spectra are similar, showing that the annealing process does not change the intrinsic properties of the material.

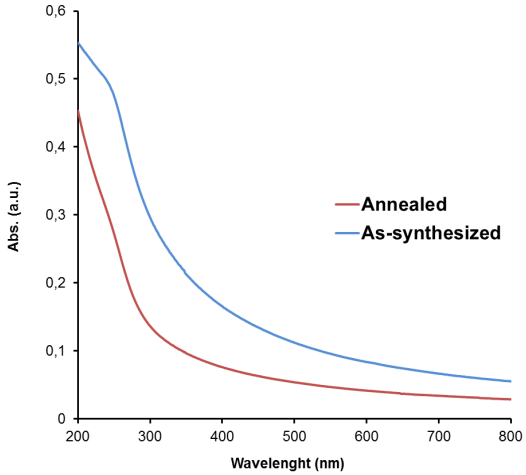

Figure 3.3. UV-Vis spectra of SnO_2 synthesized using silicatein as hydrolytic catalyst. Blue line: Spectrum of the as-synthesized product. Red line: spectrum of the annealed product (200°C).

Monoclonal antibodies directed against recombinant silicatein-α were used to demonstrate the binding of silicatein between the individual SnO_2 domains by CLSM through the positive cross-reaction between the SnO_2 particles and the polyclonal antibodies raised against silicatein-α (PoAb-aSILIC, Figure 3.4B).[42] To avoid protein damage, the product was washed with buffer several times to remove unbound protein, maintaining in that way the included protein responsible for the SnO_2 precipitation. The fluorescence microscope image in Figure 3.4B indicates that silicatein is distributed and included in the as-synthesized tin-oxide sample. No fluorescence was observed in the control experiments (Figure 3.4D). As a control (to rule out unspecific interaction of the antibodies with the material) the annealed SnO_2 samples were submitted to immunostaining, and no fluorescence could be detected (Figures 3.4C and D).

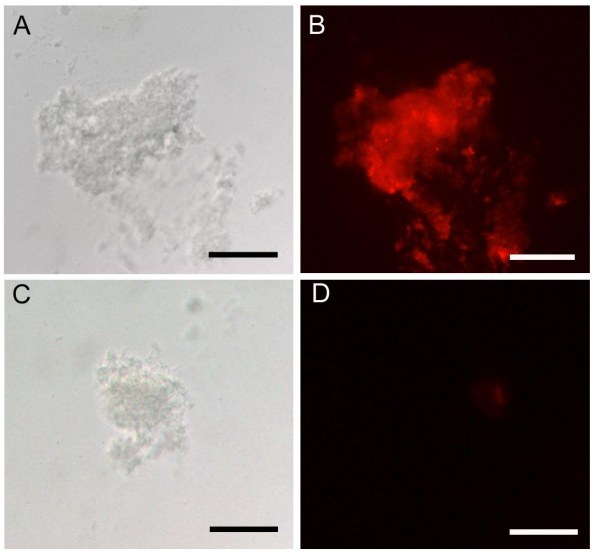

Figure 3.4. Light and fluorescence optical micrographs of the immunostaining against silicatein for SnO_2 formed in the presence of the protein. A) Light and B) fluorescence micrographs of immunostaining on as-synthesized product indicating the presence of silicatein. C) Light and fluorescence micrographs of immunostaining on annealed product where no specific binding was detected. Scale bar: 5 μm in all images.

When the reaction was performed under the same conditions but with denaturated silicatein-α, no precipitate was observed (supporting information, Figure S7*)*. This indicates that the catalytic activity of silicatein for the formation of SnO_2 is dependent on the three-dimensional integrity of the protein, and that silicatein is occluded in the formed structures.

Regarding the mechanism of formation of SnO_2 in the presence of silicatein, we can infer that the protein plays an active role in the hydrolysis of the precursor, which otherwise is quite stable in aqueous solution at room temperature (as shown in Figure S2.1). Attempts to determine the reactions intermediates by ^{119}Sn or ^{19}F NMR as well as FTIR were unsuccessful, most likely because the concentration of the protein and the precursors in solution were close to the detection limit of those methods.

Therefore, we propose that silicatein catalyzes the hydrolysis of the hexafluorstannate, which condensates in the subsequent step to form SnO_2 crystallites. Because of the lower Pearson hardness of Sn compared to Si and the resulting lower degree of hydration, small crystallites (rather than amorphous material) are formed. The nucleating SnO_2 nanocrystals are stabilized by surface binding of silicatein. Upon aggregation of these nanocrystals, domain crystals[43] with nanometer-sized domains are formed. These results indicate that silicatein has not only a catalytic but also a potential templating and constraining effect on the formation of SnO_2.

Tin dioxide is a well-studied and widely used semiconductor. Therefore facile and sustainable synthetic routes are necessary which can be expected to have a widespread application. As recombinant silicatein-α promotes the formation of SnO_2 at neutral pH, in aqueous media and at room temperature in an economic and simple fashion, we have studied the deposition of SnO_2 mediated by silicatein on glass surfaces.

Self-assembled monolayers (SAM) of alkanethiol derivatives on metal electrodes provide numerous possibilities for immobilizing proteins.[44] Glass surfaces were chosen as a common substrate for the deposition of tin dioxide and derived composite materials that form the basis for transparent semiconductor surfaces which have further applications in solar cell assembly or intelligent glass displays. Hence, recombinant silicatein was immobilized on glass surfaces by complexation with a histidine tag, Ni^{2+} and nitrilotriacetic acid (NTA) as decribed elsewhere.[45] In short, the glass slides were silanized with 3-(2,3-epoxypropoxy) propyltrimethoxysilane which was further functionalized with amine terminated nitrilotriacetic acid. This allowed, after incubation with Ni^{2+}, to immobilize histidine tagged silicatein on the surface, as illustrated in Figure 3.5.

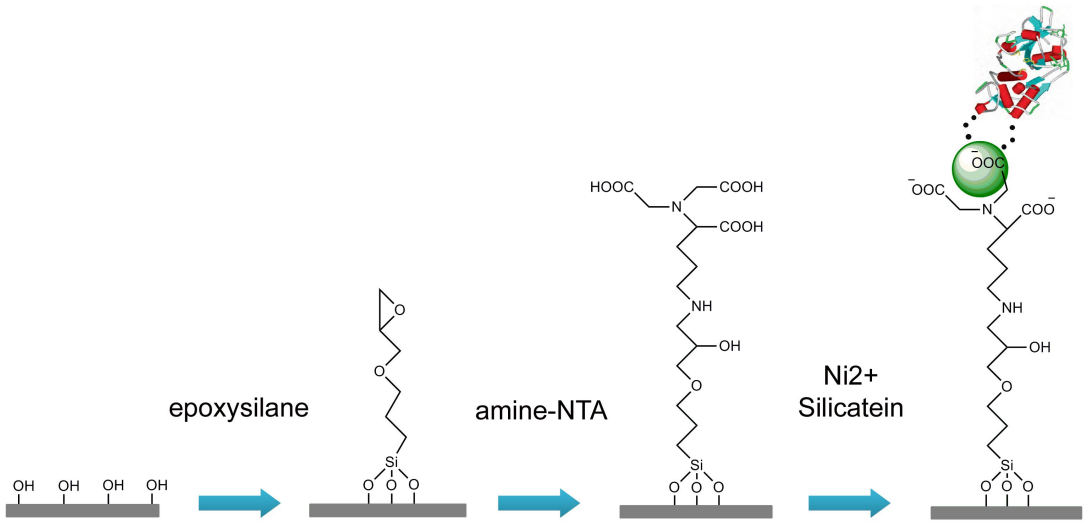

Figure 3.5. Scheme illustrating the steps for glass slide functionalization with histidine tagged silicatein (illustrations not to scale).

The presence of silicatein on glass surfaces was assessed by immunostaining with specific anti-silicatein antibodies, after blocking the surface with BSA, to avoid any unspecific interaction of the antibodies with the surface. As seen in Figure 3.6A a complete coverage of the surface was achieved. Bare glass surfaces (non-functionalized with NTA ligand) were also

incubated with protein, where no binding was observed (Figure 3.6B). Thus the functionalization method using a NTA linker on the glass surface proved to be efficient for further functionalization with the recombinant histidine tagged silicatein.

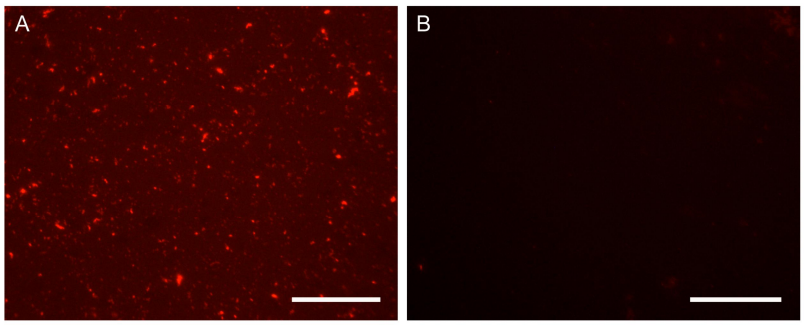

Figure 3.6. Fluorescence microscopy images showing the immunostaing against silicatein on (A) amine NTA/silicatein functionalized glass surfaces and (B) on non-functionalized glass surface (direct incubation with silicatein) as control. Scale bars: 5 µm.

To obtain a tin dioxide coating on the functionalized glass surface, incubation with Na_2SnF_6 (5 mM, TBS buffer pH 7.4) was performed for 4 h. Subsequently the surface was washed extensively with water and ethanol and dried at 60°C for 5 h. As a control, non-functionalized surfaces were incubated with the tin dioxide precursor under the same conditions.

The morphology of the surfaces with and without SnO_2 was investigated using SEM. Figure 3.7A shows the bare glass slide before functionalization. The control experiment (non-functionalized glass) does not show any significant deposition (Figure 3.7B**)**. The surfaces incubated with the tin dioxide precursor in the presence of silicatein (Figure 3.7C) show a substantial homogenous surface deposition, where the material as a similar aspect (inset Figure 3.7C) as the SnO_2 synthesized in solution by silicatein (Figure 3.1A). Elemental analysis with EDX clearly shows the presence of Sn, O and Si (from the glass) thus demonstrating that tin dioxide is present on the glass surface (Figure 3.7D).

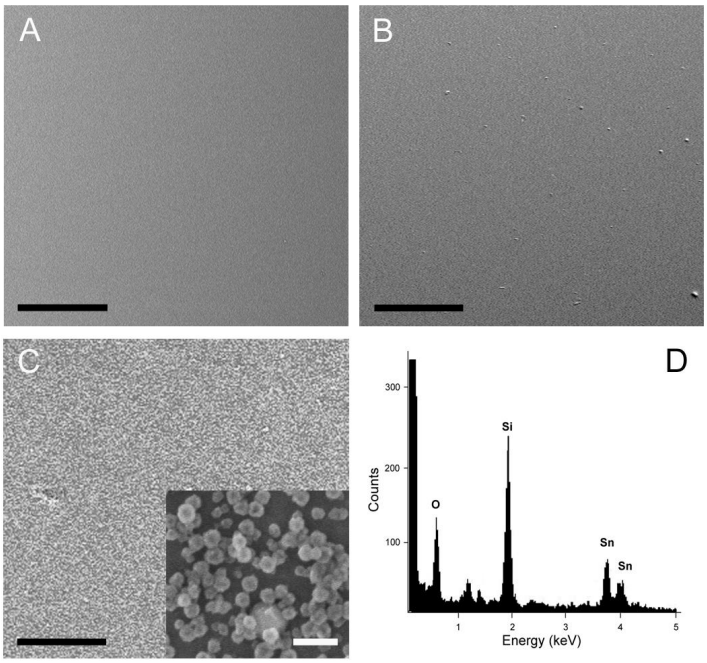

Figure 3.7. SEM images of (A) a bare glass slide. (B) Non-functionalized glass slide after incubation with the SnO_2 precursor. (C) NTA/silicatein functionalized glass slide after incubation with the SnO_2 precursor. Inset: High resolution of where the typical sphere like shapes are observed (scale bar: 100 nm). (D) SEM-EDX corresponding to the spot in (C). Scale bars: 5 µm.

The color of the glass slides did not change significantly after tin dioxide deposition, and the transparency in the visible light was maintained (Figure 3.8A), where - at the macroscopic level - both functionalized and non-functionalized surfaces look virtually identical. The transmittance of the surface in the UV range is similar for the bare and the SnO_2 covered glass slides (Figure 3.8B); only a slight decrease in transmittance is present between 200 and 250 nm for the SnO_2 coated glass.

The deposition profile of tin oxide on functionalized glass surfaces was monitored using a quartz crystal microbalance (QCM). With this method it is possible to obtain information on the mass deposited on the surface and on the elasticity of the deposited films. Silicon dioxide covered QCM sensors were used, which were functionalized with silicatein in the same manner as the previously shown glass slides. After addition of the precursor solution, the mass change (Δm) was monitored continuously with time. (Figure 3.9A) With the addition of the precursor solution the growth rate rapidly increases during the first 5 minutes and then it decreases during the remaining reaction time, possibly due to enzyme saturation. A control

experiment on a non-functionalized QCM sensor, using the same precursor concentration showed small or no deposition during the same reaction time (supporting information, Fig S8). Hence it can be concluded that the mass deposition is exclusively due to the presence of silicatein-α. Furthermore, the dissipation data (Figure 3.9B) indicates the formation of a rigid film (decrease in dissipation over time) which is as expected for a mineralized surface.

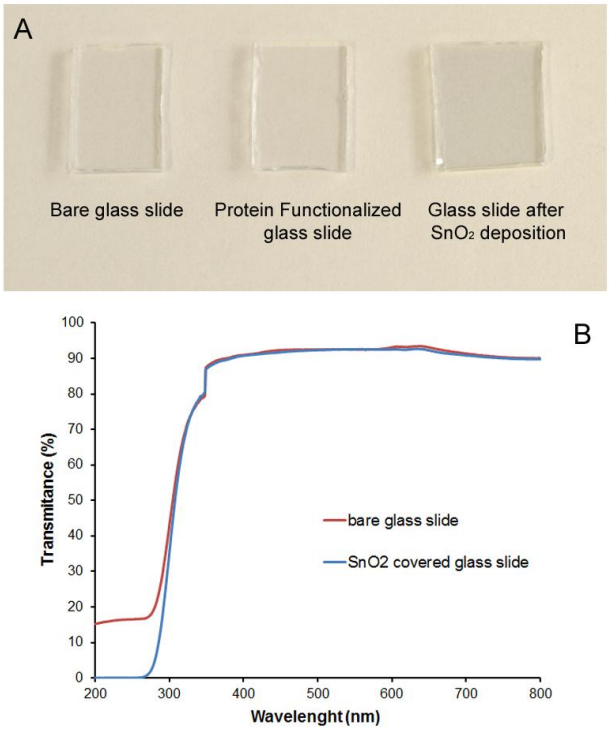

Figure 3.8. Optical images of glass slides covered SnO_2 mediated by silicatein. (A) Glass slides before and after SnO_2 deposition. Almost no color change was detected after functionalization with protein and deposition of SnO_2. (B) Transmittance in the UV-vis range of the bare glass slides (red) and the SnO_2 covered glass slides (blue).

SEM pictures were taken from the sensor after the reaction time (supporting information, Figure S9A) were the presence of similar structures as for the SnO2 deposition in the glass slides (Figure 3.7) is clearly visible. In the control experiment no significant deposition was observed (Figure S9B).

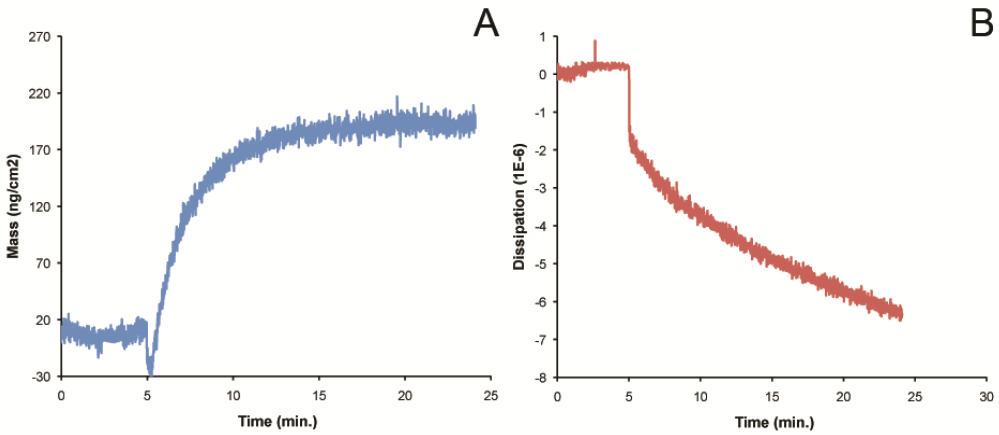

Figure 3.9. QCM measurement of tin oxide deposition on silicatein functionalized silicon dioxide sensors. Injection of tin oxide precursor was made after 5 minutes as indicated by the sudden change in the mass (frequency) and dissipation values. (A) Evolution of mass deposited over time and (B) Change in dissipation over reaction time.

3.3 Conclusions

In summary, we were able to demonstrate that recombinant silicatein-α can mediate the formation of nanostructured crystalline SnO_2 under mild conditions, i.e., at room temperature and neutral pH, in a buffered system. Silicatein can be assumed to have a catalytic effect on the synthesis of tin dioxide through the enhanced hydrolysis of the precursor compounds. The freshly synthesized product contains spherical agglomerates of smaller particles with crystalline domains of cassiterite. After annealing the product at 200°C the SnO_2 cassiterite phase was maintained. The typical surface plasmon absorption band for SnO_2 was identified by optical spectroscopy. Silicatein has a constraining effect on the particle size due do the agglomeration of the protein on the newly formed crystals. The SnO_2 product nanoparticles are stabilized by surface binding of silicatein through its functional (amino and/or carboxylate) groups, as shown by fluorescence microscopy using a fluorophore attached to silicatein by specific antigen-antibody interactions.

In addition, recombinant silicatein-α was immobilized on glass slides using epoxysilane/NTA ligands. After incubation with a tin oxide precursor, a layer of SnO_2 was successfully synthesized. The glass slides after the catalytic deposition of tin oxide, remain colorless and transparent in the UV range, thus indicating the potential application of this simple deposition

method in the development of new composite materials with technological interest for example, in production of transparent conductive oxides.

3.4 Experimental Section

Materials. Sodium hexafluorostannate (Na_2SnF_6, ABCR, 99%), Tris buffered saline (TBS, Sigma-aldrich), bovine serum albumin (BSA) blocking solution (Carl Roth), Cy3-conjugated goat anti-rabbit antibody (Dianova), 3-(2,3-epoxypropoxy)propyltrimethoxysilane (Sigma-Aldrich) and N,N-Bis(carboxymethyl)-L-lysine hydrate (Sigma-Aldrich) were purchased and used as received without further purification. Solvents, acids and bases, such as ethanol, dichloromethane, toluene, HCl, HNO_3 and NaOH, were purchased technical grade and used as received.

Silicatein-α production. Recombinant silicatein-α was prepared as described before.[6,37] Silicatein was obtained and used in TBS (Tris buffer saline, pH 7.4) as working buffer.

Protein assisted synthesis of tin oxide (SnO_2). For SnO_2 biosynthesis, 1 mL of 5 mM solution of sodium hexafluorostannate (Na_2SnF_6) in TBS buffer, pH 7.4 was added to 500μL of a solution of recombinant silicatein-α (50 mg/mL) in TBS buffer pH 7.4, and kept under agitation at room temperature for 4 hours. The white precipitate formed was washed several times with MilliQ water and ethanol and dried in an oven at 60°C overnight. The product was used as prepared or after annealing at 200°C under air, for 2 hours. As control experiments the same concentration of Na_2SnF_6 was incubated only in TBS buffer at pH 7.4, or with denaturated silicatein-α under the same conditions. For protein denaturation, a heat treatment at 95°C for 10 minutes was performed.

Immunostaing and light microscope imaging. Specific anti-silicatein antibodies were prepared as described before.[6] The presence of silicatein was monitored by incubating the as-synthesized tin-oxide with primary anti-silicatein (produced in mouse) polyclonal antibody (1:2000 dilution), in a 5% blocking solution (BSA) for 2 h at room temperature. The sample was washed several times using TBS buffer (pH 7.4) for 5 min. followed by the secondary antibody, anti-mouse Cy3 labeled (1:2000 dilution), incubation in 5% blocking solution (BSA) for 3h at room temperature, and then washed with TBS. The as-synthesized product was washed only with buffer (TBS, pH 7.4) before performing the immunostaing in order to maintain the included protein in the structures. As control, annealed SnO_2 samples were used,

where no protein was expected to be found due to the heat treatment. For immunostaining in functionalized glass surfaces the same procedure was used. The fluorescence analysis was performed with an Olympus AHBT3 light microscope, together with an AH3-RFC-reflected light fluorescence attachment at the emission wavelength of 580 nm and 499 nm.

Glass slide functionalization with recombinant silicatein-α. Glass slides with an average 1 cm x 1 cm in dimension were cleaned with piranha solution (H_2SO_4/H_2O_2, 1:3) for 30 min. at room temperature. The slides were rinsed several times with distilled water and dried under a stream of nitrogen. For the functionalization of the glass slides with the histidine-tagged silicatein a modified procedure by Chevalier et al.[38] was used. Briefly, the glass slides where added to a solution of 3-(2,3-epoxypropoxy)propyltrimethoxysilane (2% in toluene) and kept overnight at room temperature, under an argon atmosphere. After rinsing with dry toluene and 10 mM carbonate buffer pH 10, the glass supports were incubated with 20 mM N,N-Bis(carboxymethyl)-L-lysine hydrate (in carbonate buffer, 10 mM pH 10) overnight at room temperature. Once again the surfaces were rinsed with carbonate buffer and then submerged in a 100 mM $NiSO_4$ solution for 30 minutes. The surfaces were washed with a 150 mM solution of NaCl, and incubated with a 100 μg/mL solution of silicatein-α in TBS buffer, pH 7.4, for 2 h. To remove unbound protein the surfaces were washed with TBS buffer several times.

(High Resolution) Transmission electron microscopy (HR)TEM. Characterization and morphology analysis of the samples was carried out using transmission electron microscopy (TEM) using a Philips 420 instrument with an acceleration voltage of 120 kV or for high resolution TEM, a Philips TECNAI F30 electron microscope (field-emission gun, 300 kV extraction voltage).

Scanning electron microscopy and energy dispersive X-ray spectroscopy (SEM-EDX). The samples were mounted on aluminum stubs covered with adhesive carbon (Leit-Tabs No.: G 3347 [Plano, Wetzlar; Germany]) and analyzed by scanning electron microscopy using a Nova 600 NanoLab SEM equipped with an EDAX Division EDX analyzer.

X-ray powder diffraction. The sample was analyzed by X-ray powder diffraction (XRD) in θ/2θ reflection geometry using a Siemens D8 power diffractometer equipped with a position sensitive detector. The data were collected using Cu-Kα radiation at an operating potential of 40 kV and a current of 40 mA, and analyzed using the EVA software.[39]

UV-Vis spectroscopy. The SnO_2 powders were dispersed in Milli-Q water and slightly sonicated prior to transfer to quartz cuvettes. Glass slides were washed with Milli-Q water and dried at 60°C for 5 hours prior to measure. The samples were then measured at room temperature and in the range between 200 and 800 nm using a Varian Cary 5G UV/Vis spectrophotometer.

Quartz crystal microbalance (QCM). Measurements were performed on a Q-sense D300 instrument using the axial flow chamber and a quartz crystal sensor with the gold electrode coated with 50 nm of silicon dioxide (Q-sense QSX 303, AT-cut, 5 MHz). The silicon dioxide surface was functionalized *ex situ* with silicatein, using the procedure described above for the glass slides. For the measurement, the functionalized crystal was placed in the sensor chamber with TBS buffer (pH 7.4) until a stable frequency baseline established, and then the precursor solution (5 mM Na_2SnF_6) was introduced. The resonant frequency and dissipation were measured at intervals of 40 ms (25°C for 30 minutes), after which the sensor was washed with buffer to eliminate possible adsorbed precursor. The changes in mass were calculated using Sauerbrey equation: [40]

$$\Delta m = -17.7 \text{ng Hz}^{-1} \text{ cm}^{-2} \cdot \Delta f/n$$

Where m is de adsorbed mass, f is the frequency, and n is the overtone number.

3.5 References

1. Handbook of Biomineralization, 1st ed., Bäuerlein, E.; Behrens, P.; Epple, M. (eds.), Wiley-VCH, Weinheim, 2007.
2. Nassif, N.; Livage, J. Chem. Soc. Rev. 2011, 40, 849-859.
3. Mann, S.; Archibald, D. D.; Didymus, J. M.; Douglas, T.; Heywood, B. R.; Meldrum, F. C.; Reeves, N. J. *Science* **1993**, *261*, 1286-1292.
4. (a) Lakes, R. *Nature* **1993**, *361*, 511-515. (b) Ozin, G. A. *Acc. Chem. Res.* **1997**, *30*, 17-27. (c) Douglas, T. *Science* **2003**, *299*, 1192-1193.
5. Shimizu, K.; Cha, J.; Stucky, G. D.; Morse, D. E. *Proc. Natl. Acad. Sci*. **1998**, *95*, 6234-6238.(b) Brutchey, R. L.; Morse, D. E. *Chem. Rev.* **2008**, *108*, 4915–4934. (c) Schröder, H. C.; Wang, X.; Tremel, W.; Ushijima, H.; Müller, W. E. G. *Nat. Prod. Rep.* **2008,** *25*, 455-474. (d) Schröder, H.C; Wiens, M.; Schlossmacher, U.; Brandt, D.; Müller, W.E.G. *Silicon* **2010**, 1-9, DOI: 10.1007/s12633-010-9057-4.

6. (a) Krasko, A.; Batel, R.; Schröder, H. C.; Müller, I. M.; Müller, W. E. G. *Eur. J. Biochem.* **2000**, *267***,** 4878-4887.
7. Cha, J. N.; Shimizu, K.; Zhou, Y.; Christiansen, S. C.; Chmelka, B. F.; Stucky, G. D.; Morse, D. E. Proc. Natl. Acad. Sci. 1999, 96, 361-365.
8. Zhou, Y.; Shimizu, K.; Cha, J. N.; Stucky, G. D.; Morse, D. E. *Angew. Chem. Int. Ed.* **1999**, *38*, 779-782.
9. Wolf, S. E.; Schloßmacher, U.; Pietuch, A.; Mathiasch, B.; Schröder, H. C.; Müller, W. E. G.; Tremel, W. *Dalton Trans.* **2009**, *39*, 9245–9249.
10. Sumerel, J. L.; Yang, W.; Kisailus, D.; Weaver, J.; Choi, J. H.; Morse, D. E. *Chem. Mater*. **2003**, *15*, 4804-4809.
11. Tahir, M. N.; Théato, P.; Müller, W. E. G.; Schröder, H. C.; Boreijko, A.; Faiß, S.; Janshoff, A.; Huth, J.; Tremel, W. *Chem. Commun*. **2005**, *28*, 5533-5535.
12. Ould-Ely, T.; Luger, M.; Kaplan-Reinig, L.; Niesz, K.; Doherty, M.; Morse, D. E., *Nature Protocols* **2011**, *6*, 97–104.
13. Kisailus, D.; Choi, J. H.; Weaver, J. C.; Yang, W.; Morse, D. E. *Adv. Mater*. **2005**, *17*, 314-318.
14. Cha, J. N.; Stucky, G. A.; Morse, D. E.; Deming, T. E. *Nature* **2000**, *403*, 289–292.
15. Sumerel, J. L.; Yang, W.; Kisailus, D.; Weaver, J.; Choi, J. H.; Morse, D. E. *Chem. Mater*. **2003**, *15*, 4804–4809.
16. Mueller, W. E. G.; Wang, X.H.; Kropf, K.; Ushijima, H.; Geurtsen, W.; Eckert, C.; Tahir, M.N.; Tremel, W; Boreiko, A.; Schlossmacher, U.; Li, J.; Schroeder, H.C. *J. Struct. Biol.***2008**, *161*, 188–203.
17. (a) Jovilet, J. P. Metal Oxide Chemistry and Synthesis.: From Solution to Solid State; Wiley & Sons: New York, 2000. (b) Ovenstone, J.; Yanagisawa, K. *Chem. Mater*. **1999**, *11*, 2770-2774. (c) Roy, R.; Hill, V. G.; Osborn, E. F. *J. Am. Chem. Soc*. **1952**, *74*, 719-722.
18. Murr, M. M.; Morse, D. E. *Proc. Natl. Acad. Sci. USA* **2005**, *102*, 11657-11662.
19. Schröder, H. C.; Boreiko, A.; Korzhev, M.; Krasko, A.; Tahir, M. N.; Tremel, W.; Eckert, C.; Müller, I. M.; Müller., W. E.G. *J. Biol. Chem*. **2006**, *281*, 12001–12009.
20. Tahir, M. N.; Théato, P.; Müller, W. E. G.; Schröder, H. C.; Janshoff, A.; Zhang, J., Huth, J.; Tremel, W. *Chem. Commun*. **2004**, 2848–2849.
21. Kisailus, D.; Najarian, M.; Weaver, J. C.; Morse, D. E. *Adv. Mater.* **2005**, *17*, 1234-1239.

22. André, R.; Tahir, M. N.; Link, T.; Jochum, F. D.; Kolb, U.; Theato, P.; Berger, R.; Wiens, M.; Schröder, H. C.; Müller, W. E. G.; Tremel, W. *Langmuir* 2011, 27, 5664-5671.
23. Falabretti, B.; Robertson, J. *J. Appl. Phys.* **2007**, *102*, 123703/1–5.
24. (a) Yang, F.; Forrest, S. R. *Adv. Mat*. **2006**, *18*, 2018-2022. (b) Snaith, H. J.; Ducati, C. *Nano Lett*. **2010**, *10*, 1259-1265.
25. (a) Belliard, F.; Connor, P. A.; Irvine, J. T. S. *Solid State Ionics* **2000**, *134*, 163-167. (b) Meduri, P.; Pendyala, C.; Kumar, V. Sumanasekera, G.U.; Sunkara, M. K. *Nano Lett*. **2009**, *9*, 612-616.
26. Croft, G.; Fuller, M. J. *Nature* **1977**, *269*, 585-586.
27. (a) Leite, E. R.; Weber, I. T.; Longo, E. Varela, J. A. *Adv. Mater*. **2000**, *12*, 965-968. (b) Miller, T.A.; Bakrania, S.D.; Perez, C; Wooldridge, M.S. Functional Nanomaterials: Nanostructured Tin Oxide Materials for Gas Sensor Applications, American Scientific Publishers, 2006.
28. Vollath, D. Nanomaterials, Wiley-VCH, Weinheim 2008.
29. Dai, Z. R.; Pan, Z. W.; Wang, Z. L. *J. Am. Chem. Soc*.**2002**, *124*, 8673-8680.
30. Yang, R.; Wang, Z. L. *J. Am. Chem. Soc*. **2006**, *128*, 1466-1473.
31. (a) Chen, B.; Russell, J. M.; Shi, W.; Zhang, L.; Samuiski, E. T. *J. Am. Chem. Soc*. **2004**, *126*, 5972-5973. (b) Vayssieres, L.; Graetzel, M. *Angew. Chem. Int. Ed.* **2004**, *43*, 3666-3770.
32. Lin, Y.; Dong, J.; Liu, M. *Adv. Mater.* **2004**, *16*, 353-359.
33. Zhang, D.-F.; Sun, L.-D.; Yin, J.-L.; Yan, C.-H. *Adv. Mater*. **2003**, *15*, 1022-1025.
34. Birkel, A.; Reuter, F.; Koll, D.; Frank, S.; Branscheid, R.; Panthöfer, M.; Rentschler, E.; Tremel, W. *Cryst. Eng. Commun.* **2011**, *13*, 2487-2493.
35. Yang, H. G.; Zeng, H. C. *Angew. Chem., Int. Ed.* **2004**, *43*, 5930-5933.
36. Wu, S.; Cao, H.; Yin, S.; Liu, X.; Zhang, X. *J. Phys. Chem. C* **2009**, *113*, 17893-17898.
37. Wiens, M.; Bausen, M.; Natalio, F.; Link, T.; Schloßmacher, U.; Müller, W. E. G. *Biomaterials* **2009**, *30*, 1648-1656.
38. Chevalier, S.; Ayllon, C. C.; Grazu, V.; Luna, M.; Feracci, H; Fuente, J. M. *Langmuir* **2010**, *26*, 14707-14715.
39. EVA*Plus* Software Suite, Bruker AXS 2010.
40. G. Sauerbrey Z. Phys. 1959, 155, 206-222.

41. Roman, L. S.; Valaski, R.; Canestraro, C. D.; Magalhães, E. C. S.; Persson, C.; Ahuja, R.; da Silva, Jr., E. F.; Pepe, I.; Ferreira da Silva, A. *Appl. Surf. Sci*. **2006**, *252*, 5361-5364.
42. Müller, W. E. G.; Rothenberger, M.; Borejko, A.; Tremel, W.; Reiber A.; Schröder, H. C. *Cell Tissue Res*., 2005, **321,** 285-297.
43. Cölfen, H.; Antonietti, M. Mesocrystals and Nonclassical Crystallization: New Self-assembled Structures. Wiley-VCH, Weinheim 2008.
44. (a) Prime, K. L.; Whitesides, G. M. *Science* 1991, **252**, 1164-1167; (b) Willner, I.; E. Katz, E. *Angew. Chem. Int. Ed*. 2000, **38**, 1180-1218.
45. Chevalier, S.; Ayllon, C. C.; Grazu, V.; Luna, M.; Feracci, H; Fuente, J. M. *Langmuir* **2010**, *26*, 14707-14715.

CHAPTER 4

Self-Cleaning Antimicrobial Surfaces by Spermine-Catalyzed SnO_2 Coatings on Glass

Associated publication: *manuscript under preparation*

4.1 Introduction

Tin dioxide (SnO_2) is a non-toxic wide-gap n-type semiconductor-tor that combines high conductivity with high optical transparency in the visible range, making it an important component for optoelectronic applications.[1] Recently, SnO_2 has been shown to have great technological applications as transparent conducting oxides as electrodes for solar cells,[2] gas-sensors,[3] catalyst[4] or coatings for architectural glass.[5] SnO_2 is often doped with fluorine[6] or antimony[7] to improve its electrical conductivity. In addition, tin oxide is commonly used to dope indium oxide films to make indium tin oxide composites (ITO),[8,9] which is one of the most industrially important transparent conducting oxides. For many applications (e.g. for dye sensitized solar cells[10]) it is beneficial to apply SnO_2 as thin film, which has been accomplished by dc magnetron sputtering,[11] chemical vapor deposition,[12] spray pyrolysis[13] or atomic layer deposition ALD.[14]

Most of these methods require more or less high processing temperatures and instrumental efforts. Besides high production costs this may cause technical limitations that concern, for example, the complexity of structures and shapes, materials integration, shrinkage and restrictions in the type of substrate materials. This has triggered the search for new pathways that allow to decrease the processing temperature and to widen the range of structural complexity. In this context Nature provide ample evidence how functional materials can be obtained easily and under ambient conditions.

Mimicking the growth and assembly processes observed for natural materials enables new approaches for the design of synthetic materials with controlled nanoscale features.[15] Biomimetic syntheses generally occur under ambient reaction conditions, e.g. room temperature, aqueous environment, and neutral pH, and thus are advantageous when compared to traditional chemical synthetic routes.[16] In addition, the use of biomolecules as templates for the synthesis of inorganic nanoparticles has the potential to enable precise control over particle size, aggregation state, and spatial arrangement.[17]

The biochemical processes guiding the formation of complex biosilica skeletons have mainly been studied in marine sponges[18-20] and diatoms.[21-23] While the formation of biosilica from silicic acid esters in sponges is catalyzed by an enzyme (silicatein), biosilica formation and patterning in diatoms can be attributed to the presence of silaffins, a group of very specialized biological polymers that are built of a polypeptide backbone and polyamines as post-translational modifications (PTM's). Silaffins,[24] as well as long-chain polyamines (LCA's),[25]

have been shown to be constituents of biosilica and to promote the acceleration of silica precipitation in vitro.

While the materials produced by Nature can be functionally important, a complete set of technologically interesting inorganic compounds is not present within the biosphere (e.g. Ti, Zr, Ga derivatives). However, by emulating the chemistry of natural mineralization pathways, known biomineralization agents can be employed to fabricate new materials with non-natural compositions and unique properties.[26] For example, titania,[27-29] zirconia,[30] $CaTiO_3$,[31] $GaOH/Ga_2O_3$.[32] polysilsesquioxanes[33] or $CaMoO_4$[34] have been made using either the catalytic action of native and recombinant silicatein,[28,30-33] or silaffins and polyamines chemically related polymers.[29,34] In particular, natural occurring polyamines such as spermine, spermidine and putrescine were shown to efficiently accelerate the precipitation of silica and titania in vitro and under ambient conditions.[27,35] Also it has been shown that silicatein could catalyze the formation of SnO_2 at room temperature. (*see previous chapter*) However, none of these biologically inspired materials has been used so far for either (i) photocatalytic degradation of organic contaminants or (ii) for making use of the intrinsic antibiocidal properties of the surfaces – the so called self-cleaning surfaces.

In this work its demonstrated that spermine can accelerate the deposition of SnO_2 in solution and furthermore can be functionalized onto glass surfaces subsequently mediating the formation of a durable SnO_2 thin film under mild conditions (aqueous media, neutral pH and ambient conditions) leading ultimately to a homogenous, transparent surface coating. We anticipate that this method can be generalized to other surfaces and extended to large scale production because the starting materials are readily available. It is also demonstrated that the formed SnO_2 films are highly photoreactive and actively involved in the degradation of organic molecules upon exposition to sun light. Additionally, it is shown that these surfaces are able to photodegradate biological surface contaminants, thus being also an effective biocide. Finally, polyamine mediated SnO_2 films exhibits enhanced surface wettability under UV radiation and thus an amphiphilic behavior that, in combination with its photocatalytic and photobiocidal abilities, could pave the way for new and interesting biologically inspired technological applications such as self-cleaning surfaces.

4.2 Results and Discussion

The effect of spermine on the condensation of tin oxide was firstly tested by incubating 1 mM of spermine with 5 mM of Na_2SnF_6 in destilled water for 1 hour with agitation at room temperature. After this time the white precipitate formed was centrifuged and washed several times with water and ethanol to remove lateral salts formed (like NaF) and excess spermine. The hexafluorostannate salt was chosen since it has been shown already to be a stable precursor for the precipitation of SnO_2 with other biomolecules (*see Chapter 3*). Inspection of the structures with transmission electron microscopy (TEM) reveals an overall formation of nanosized irregular particles with average sizes of 20-50 nm (Figure 4.1A). High resolution TEM (HRTEM) on the same sample reveals a mostly amorphous character, though small crystal domains can be found (around 2 nm). (Figure 4.1B) Elemental analysis by EDX shows the presence of carbon, oxygen, tin and copper (due to the sample holder) as expected. (Figure 4.1C) To determine the phase of tin oxide was produced, X-ray crystallography was performed which indicated the presence of cassiterite SnO_2 (PDF-41-1445, supporting information, Figure S10). The reflection broadening is most likely due to particle size effects, indicating the presence of small particles and/or amorphous domains. Control experiments were made where only precursor was incubated under the described conditions and no precipitate was formed, indicating that the precursor is otherwise stable in solution, as seen before (*chapter 3*). The material aspect ratio and crystallinity is in agreement with results obtained before for the synthesis of TiO_2 with spermine.[29]

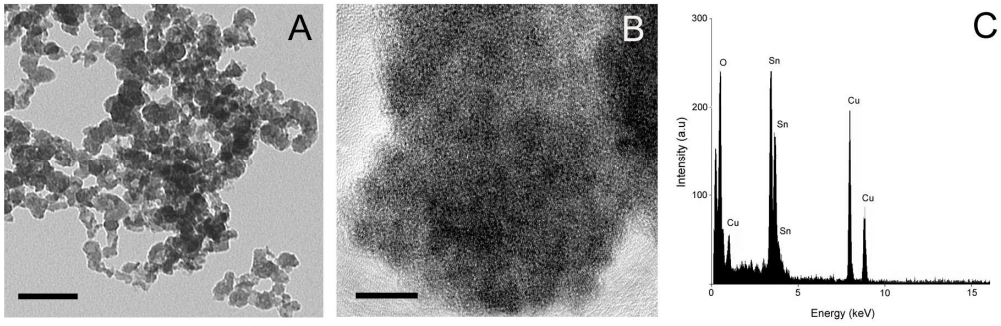

Figure 4.1 Spermine mediated synthesis of SnO_2. (A) TEM micrograph of the product precipitated in the presence of spermine (1mM) and (B) HRTEM showing the mostly amorphous character or the product. (C) EDX elemental analysis showing the presence of tin (Sn) and oxygen (O) as expected. The copper (Cu) presence is due to the support grids used in the sample preparation. Scale bars: 100 nm and 5 nm respectively.

We propose that the formation SnO_2 mediated by spermine is likely to proceed in a similar mechanistic manner as described for other metal oxides such as TiO_2 and SiO_2.[29] The spermine structure (positively charged) allows the complexation of two Sn atoms due to electrostatic interactions (schematically illustrated in Figure S11B, Supporting Information). Joining two of these complexation sites can be the starting point to induce initial stages of condensation and overcoming the required energetic barrier. Once a nuclei with a critical size is reached, the growing continues due to Ostwald ripening and certainly until the supply of SnF_6^{2-} in solution is exhausted. This proposed mechanism was further elucidated by auxiliary kinetic data (e.g, QCM measurements) (Figure S12, Supporting Information), where a rapid deposition of SnO_2 occurs during the first minutes immediately after the tin precursor gets into contact with the positively charged immobilized spermine chains, with Sn^{4+} species being rapidly complexated by a large number of free surface amine groups. When the amine groups become saturated, the deposition slows down as observed. This clearly indicates that the formation/growth of SnO_2 is promoted initially by a nucleation stage derived from polyamine-ion interaction and then proceeds to further tridimensional growth.

As spermine can mediate the formation of SnO_2 in aqueous media and at room temperature in an economical and simple fashion, we studied further the deposition of SnO_2 mediated by spermine on glass surfaces. The strategy used for polyamine (spermine) surface functionalization allows a flexible methodology that can be generalized to other glass morphologies and/or surfaces. Moreover, the biomolecule-mediated formation of SnO_2 transparent thin films permits on one hand the undetected functionalization of the surfaces (remains transparent) and on the other hand an highly photoreactive surface with intrinsic organic contaminants degrading and biocidal properties and an amphiphilic (light on/off) behavior.

The functionalization methodology is schematically displayed in Figure S11A (supporting information) and is based on previous reports for amine functionalization of glass surface.[36] Initially the glass surfaces were treated with a Piranha solution and silanized with an epoxide terminated silane (3-(2,3-epoxypropoxy) propyltrimetoxysilane). Then, we incubated the surface with a saturated solution of spermine (1h, RT) for allowing the end amines to covalently bind to the epoxy-containing surface. After washing and drying, the surface was analyzed by Fourier Transform Infrared spectroscopy with attenuated total reflection (FTIR-ATR). We confirmed the presence of the amine groups due to the existence of additional bands (when compared with unfunctionalized or epoxy functionalized glass surfaces) at 685,

1620, 3370 cm-1 corresponding to N-H wagging, scissoring and bending, respectively. (Figure S13, Supporting Information) To effectively confirm that available amine functionalities were present in the surface further fluorescence staining was performed using fluorescein isothiocyanate (FITC), which reacts directly with free primary amine groups. As control, half of the surface was kept unfunctionalized and also exposed to FITC where no fluorescence was detected. (supporting information, Figure S14) The spermine functionalized surface was also analyzed by atomic force microscopy (AFM) where a homogenous coating of organic material was visualized (Figure 4.2A) in contrast with the bare glass slide (supporting information Figure S15).

The spermine funtionalized glass surfaces were incubated with the tin precursor for 1h at room temperature after which some physical characterization was preformed. AFM and SEM images of the spermine/SnO_2 coated glass slides (for morphological comparison non-functionalized glass slides were used as controls, see supporting information Figure S15) showed that a dense SnO_2 layer had been formed (Figure 4.2B and C) with domains of small particles (diameter between 20 and 50 nm, Figure 4.2D) and an average surface roughness of approximately 4.0 nm with a maximum height of 37.1 nm. The successful polyamine-mediated SnO_2 deposition was confirmed by EDX analysis (the Si signal is due to the glass substrate, and Au due to the surface sputter process Figure 4.2E) where the presence of Sn, O and Si (glass slide) could be detected.

We used X-ray photoelectron spectroscopy (XPS) to determine the binding mode of Sn on the deposited surface, which showed the presence of Sn, Si, O, C and N due to the presence of SnO_2, spermine and the glass substrate (Figure S16). The observation of Si signal (derived from the glass surface) is indicative of a very thin film formation. Analysis of the Sn 3d and O 1s regions shows a binding energy of the Sn 3d5/2 peak at 489 eV which is compatible either with the presence of SnO or SnO_2, whose binding energies are similar. The O 1s peak at around 530 eV can be assigned to lattice oxygen atoms (Figure S16B, supporting information). The deposition is assumed to be mediated by condensation induced through the surface amine groups and is not expected to undergo any oxidation state change as it was shown above when using spermine in solution, and thus the surface composition can be safely affirmed to be SnO_2.

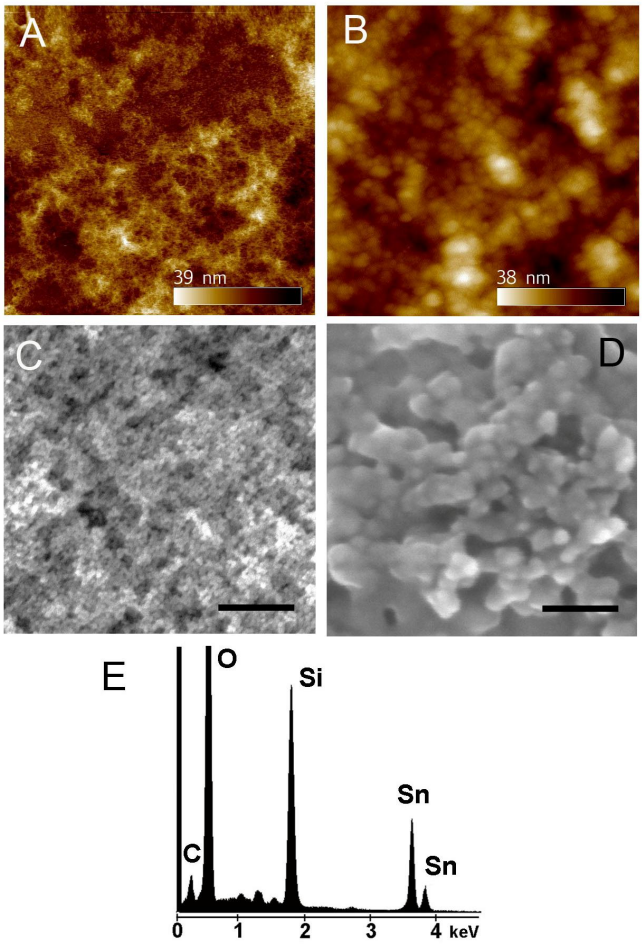

Figure 4.2 Physical characterization of spermine/SnO_2 coated glass slides. (A) AFM height analysis of glass surface functionalized with spermine showing a homogeneous functionalization (scan area 5 x 5 μm). (B) Spermine functionalized surface after incubation with tin precursor (1h, RT), showing the formation of particle aggregates (scan area 1 x 1 μm). (C) and (D) SEM images of spermine/SnO_2 coated surfaces at different resolutions (scale bars 2 μm and 200 nm respectively). (E) EDX analysis of area in (C) showing the presence of Sn, Si (glass surface) and O indicating the presence of a SnO_2 film mediated by spermine.

Semiconductors with photocatalytic activity like TiO_2 have attracted great interest due to their potential application in the degradation of organic pollutants where highly toxic and non-biodegradable dyes from the textile or printing industry are the most common examples.[37] The degradation of rhodamine B (usually used for testing degradation efficiency of photocatalysts) or other dyes by the photocatalytic activity of SnO_2 for free nanoparticles[38] or nanocomposites like SnO_2/TiO_2,[39] has been widely reported but neither for surface reactions nor bio-inspired biomimetic surface coatings. Typical methods to study dye photodegradation by SnO_2 involve the dispersion of the SnO_2 material in the target solution, which - after the reaction is complete – has to be separated by centrifugation/filtration making this procedure

difficult to apply from the technological point of view. In order to circumvent this problem, combinations of other photocatalysts like TiO_2 or TiO_2/Ag have been employed to fabricate reactive surfaces that integrate simultaneously self-cleaning and catalytic properties.

Initially we tested the capacity that these bioinspired SnO_2 surfaces would have in the formation of superoxide radicals ($O2^{-*}$) upon light exposition. For this purpose, we dipped the surfaces into a solution containing *p*-iodonitrotetrazolium (INT), that in the presence of superoxide radicals ($O2^{-*}$) oxidizes becoming red, and exposed it to direct sunlight for 30 min. Figure 4.3A shows UV-Vis spectra of a solution incubated with non-functionalized glass (Fig. 4.3A blue line) and with spermine mediated-SnO_2 coated glass (Fig. 4.3A green line) where a visible band between 550 and 600 nm is observed and this can be attributed to the typical oxidized form of INT. Digital images (Figure 4.3A inset) confirm the obtained spectral data, i.e., INT solution incubated with SnO_2 coated glass and exposed to the sun light exhibits a strong red color indicating its oxidation due to the presence of superoxide radicals ($O2^{-*}$). These data shows that these surfaces have the capacity to produce superoxide radicals ($O2^{-*}$) in the same fashion as other reported SnO_2 materials.[40] The photocatalytic properties of the polyamine-mediated SnO_2 surface layer was demonstrated by incubating a solution of rhodamine B (1 µg/mL aqueous solution) with the glass coated surface and kept under direct sunlight for 30 min. After about 30 minutes of exposure the pink rhodamine B solution became colorless (Figure 4.3B inset,) whereas in the control experiment (non-functionalized glass surface), the pink coloration remained upon exposition to identical conditions. We confirmed the degradation of the dye by analyzing UV-Vis spectra of the solutions before and after light exposure. The main absorption band of rhodamine B in Figure 4.3B disappears almost completely after irradiation with sunlight. We performed additional control experiments in which the functionalized surfaces and rhodamine B solution where kept in the dark, (Figure S17, supporting information). We observed no color change in both vials, indicating that the degradation of the dye is caused by the photocatalytic effect of the SnO_2 coating.

Another interesting feature of SnO_2 polyamine-mediated coatings is its intrinsic amphiphilic character upon exposition to a light source. For this purpose, we measured the contact angle of these surfaces in the presence of water. Figure 4.3C shows that under dark conditions, the surface is slightly hydrophobic, with a contact angle of 74° but upon illumination (30 min) the contact angle decreases to almost half, 35° showing an increased hydrophilicity. (Figure

4.3D). It could be seen that if the surfaces were dried and kept again in the dark for 1 hour, the behavior could be reverted, meaning the surface would again become hydrophobic.

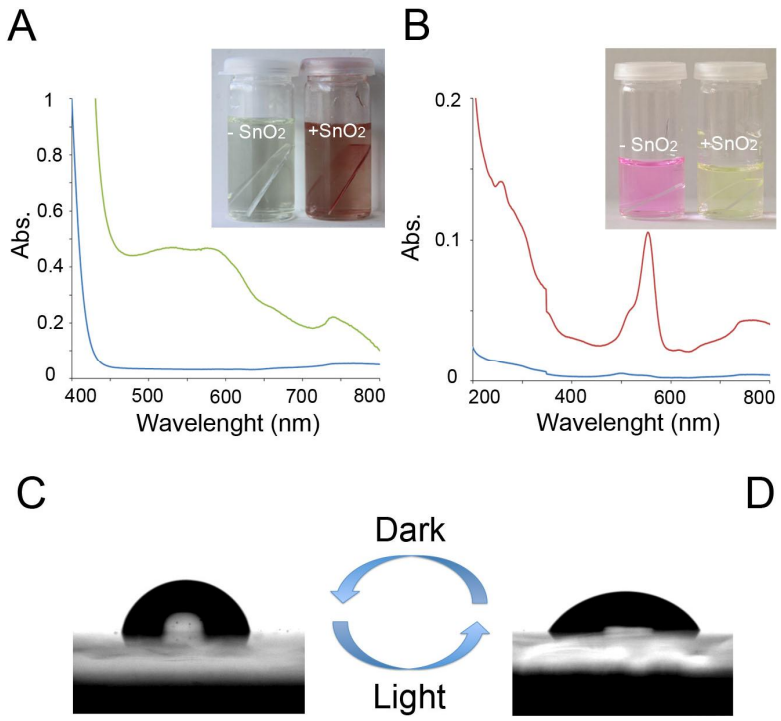

Figure 4.3 Photocatalytic activity of SnO_2 spermine-mediated coated surfaces. (A) UV-Vis spectra of the *p*-iodonitrotetrazolium (INT) solution after incubation with SnO_2 coated glass surfaces (*green line*) and non-functionalized glass surfaces (*blue line*), after exposition to sunlight for 30 min. *Inset:* The oxidation of INT occurs (*red color*) due to photocatalytic production of O_2^{-*} from SnO_2 (*right*). In the control, the solution remained colorless (*left*). (B) UV-Vis spectra showing the degradation of rhodamine B by SnO_2 coated glass (*blue line*) and uncoated glass (*red line*). *Inset:* digital photographs of dye solutions in uncoated (*left*) and SnO_2 coated (*right*) glass vials after sunlight exposure for 30 min. Amphiphilic properties of SnO_2 spermine-mediated coated surfaces. Contact angle measurements under (C) dark conditions and (D) after sunlight exposition. The formed angles are respectively 74° and 35° showing a hydrophobic/hydrophilic switch after light exposure (amphiphilic surface).

Besides the photodegradation of organic contaminants, it is of high technological interest to add antimicrobial properties to these self-cleaning surfaces. We propose that the photocatalytic properties of SnO_2 spermine-mediated coated surfaces can be exploited for antimicrobial applications through a similar mechanism as used for the degradation of organic dyes, i.e., by production of superoxide radicals ($O2^{-*}$) upon illumination. We demonstrated

the antimicrobial properties of these surfaces with cell cultures of *E. coli*, which is a common biological contaminant in environments such as wastewater and food. We incubated *E. coli* cultures on SnO_2 spermine-mediated coated surfaces for 2h at 37ºC under dark conditions. Afterwards, the surfaces containing adhered bacteria were exposed to direct sunlight for about 30 min. The control experiments were carried with non-functionalized glass surfaces under identical experimental conditions. After illumination, we examined both surfaces (also before sunlight exposition) by fluorescent microscopy to assess the physiological condition of the bacteria using a permeability assay with two nucleic acid stains, 4,6-diamidino-2-phenylindole dihydrochloride (DAPI) and propidium iodide (PI). DAPI is able to cross the cell membrane and thus stain both viable and non-viable (membrane compromised) bacterial cells, while PI is membrane impermeable and can stain nucleic acids only when the membrane has been partially damaged or compromised.[35] Before sunlight exposition we observed that the bacteria grow on SnO_2 spermine-mediated coated surfaces are mostly viable (Figure 4.4 A-C) whereas after exposition all bacteria showed a positive PI staining (red fluorescent signal) indicating that their membranes were compromised. This bacterial membrane damage is attributed to the formation of superoxide radicals ($O2^{-*}$) by the SnO_2 spermine-mediated coated surfaces, which compromise the bacterial cell membrane integrity. (Figure 4.4 D-F). In control experiments carried out with unfunctionalized glass surfaces we observed no effect on the viability of E. coli cells (Figure S18, supporting information). In order to confirm that the antimicrobial effect is related to the photobiocidal properties of SnO_2 and not due to possible surface toxicity, we performed further experiments in which SnO_2 spermine-mediated coated surfaces were kept under dark conditions. In the dark (under otherwise identical conditions) the bacteria remained viable for longer times without any indication of a toxic effect from the surface itself. (Figure S19, supporting information).

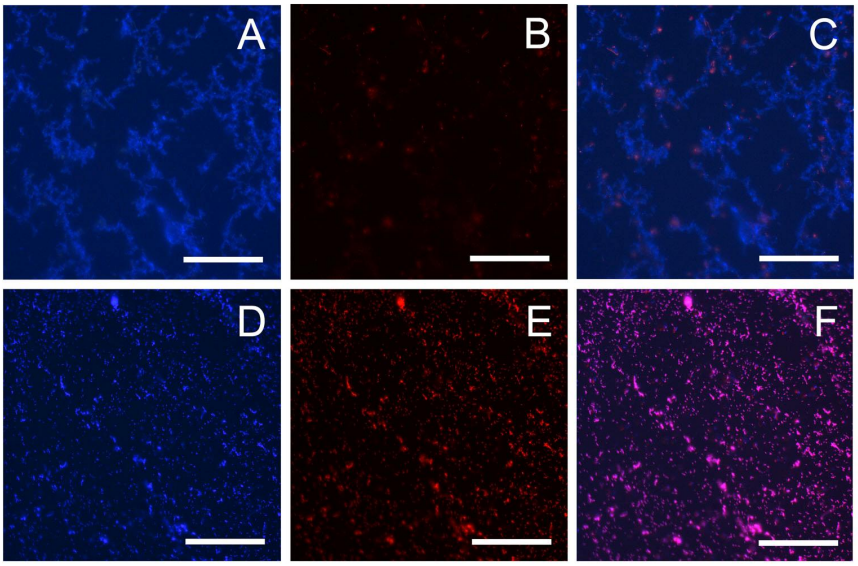

Figure 4.4 Photobiocidal activity of SnO_2 spermine-mediated coated surfaces against *E.coli*. The bacterial cells were initially grown under dark conditions for 2h at 37ºC (A-C) and afterwards exposed to direct sunlight for 30 min. (D-F). A and D represent cultures stained with DAPI (which targets viable and non-viable cells), **B** and **E** refer to cultures stained with PI (targeting only non-viable cells). **C** and **F** are overlaps of A/B and D/E images, respectively. Scale bar: 5 μm in all figures.

4.3 Conclusions

In conclusion, it was shown that spermine is able to accelerate the formation of SnO_2 under mild conditions (aqueous solution, neutral pH, room temperature) from simple water stable precursors through a similar mechanism as found for other metal oxides such as TiO_2 or SiO_2. The synthesized particles using spermine and tin precursor in solution present a nanosized irregular structure with particle sizes between 20-50 nm. Using a simple functionalization method, glass surfaces could be successfully functionalized with spermine, and further incubated with a tin precursor to yield a SnO_2 coated glass. The synthesized surfaces showed a homogenous coating with average nanoparticle size of 20-50 nm as excepted. We anticipate that this deposition method can be generalized to several different types of surfaces, just by adjusting the functionalization step. The biomolecule mediated coating is transparent and these surfaces are able to produce superoxide radicals ($O2^{-*}$) upon illumination in the same fashion as other SnO_2 materials chemically produced. Due to its intrinsic photocatalytic activity, the SnO_2 coated surfaces can degrade organic contaminants like rhodamine B, as well as act as an efficient photobiocidal towards bacterial pathogens like E.coli. To the best of

our knowledge this is the first time that SnO_2 is reported to have photobiocidal properties. Additionally, we showed that these surfaces present an amphiphilic behavior switching from slightly hydrophobic to hydrophilic upon sunlight exposition. We anticipate that the different properties of the SnO_2 spermine-mediated coated surfaces will allow the formation of inexpensive and highly efficient antibacterial, self-cleaning surfaces with a great potential application. For example, incorporation into house paints (external) that can, during the daytime, produce superoxide radicals ($O2^{-*}$) becoming simultaneously more hydrophilic (more surface reactive) and thus more bacteria would be exposed (more efficient) and in the night the increase of hydrophobicity will prevent bacteria adhesion and growth.

4.4 Experimental Section

Spermine mediated SnO_2 synthesis in solution. In a typical reaction, spermine (1 mM) was dissolved in 1 mL MilliQ water to which Na_2SnF_6 (sodium hexafluorostannate, Cat. No. AB105664, 99%, ABCR, Germany) was added to a concentration of 5 mM. The mixture was allow to incubate for 1 hour at room temperature with agitation, after which the formed precipitate was centrifuged (10 min, 5000 rpm) and washed with water and ethanol. The formed powder was allowed to dry at 60°C for 4 hours before analysis.

Spermine functionalization of glass surfaces. Glass slides with an average 1 cm x 1 cm in dimension were cleaned with piranha solution (H_2SO_4/H_2O_2, 1:3) for 30 min. at room temperature. The slides were rinsed several times with distilled water and dried under a stream of nitrogen. For the functionalization of the glass slides with spermine a modified procedure based on the one shown in Chapter 2, for silicatein, was used.[36] Briefly, the glass slides where added to a solution of 3-(2,3-epoxypropoxy)propyltrimethoxysilane (2% in toluene) and kept overnight at room temperature, under an argon atmosphere. After rinsing with dry toluene and 10 mM carbonate buffer pH 10, the glass supports were incubated with 20 mM spermine (Cat. No. S2876, Sigma-Aldrich, Germany) (excess concentration, in carbonate buffer, 10 mM pH 10) for 2 hours at room temperature. Then, unreacted epoxy reactive groups were quenched by treating the samples with 0.1 M ethanolamine (Cat. No. 110167, ReagentPlus®, ≥99% Sigma-Aldrich, Germany).

Fluorescein isothiocyanate (FITC) labeling of spermine functionalized surfaces. A stock solution of 1 mg/mL fluorescein isothiocyanate (FITC, Cat. No. F7250, ≥90% Sigma-

Aldrich, Germany) in dry DMSO was prepared. After functionalization with the epoxysilane, half of the glass surface was covered with tesa film and proceeded with the spermine functionalization step, after which the teas film was removed and the entire surface quenched with ethanolamine, as described in the previous section. The functionalized surface was placed in a 0.1M sodium carbonate buffer (pH 9) solution to which 10 µL of the FITC stock solution was added, and left to incubate in the dark, at 4°C for 4 hours. The reaction was quenched with the addition of 50 mM ammonium chloride. After washing with phosphate buffer saline (PBS) buffer the sample was analyzed with an Olympus AHBT3 light microscope, together with an AH3-RFC reflected light fluorescence attachment at the emission wavelength of 525 nm.

Tin dioxide (SnO_2) deposition on spermine-functionalized surfaces. Spermine functionalized surfaces were incubated with an aqueous solution of tin precursor, i.e., 5 mM of sodium hexafluorstannate (Na_2SnF_6) (Cat. No. AB105664, 99%, ABCR, Germany) for 1h at room temperature to allow the formation of a surface coating. Afterwards, the surfaces were washed with copious amounts of distilled water in order to remove unreacted precursor, air-dried under a nitrogen stream and used for further characterizations. As controls, untreated glass surfaces or vials were incubated with the same aqueous solution of tin precursor (5mM, Na_2SnF_6) and left to react for 1h at room temperature. The controls were further washed, dried and analyzed in parallel.

Fourier Transform Infrared spectroscopy with attenuated total reflection (FT-IR ATR). Infrared analysis of functionalized glass surfaces was performed using a Nicolet Nexus spectrometer fitted with a Golden Gate attenuated total reflection (ATR) accessory (Thermo Nicolet). Spectra were recorded at 4 cm^{-1} resolution, averaging 32 scans. As controls, unfuctionalized glass slides were analyzed in parallel.

Scanning Electron Microscopy (SEM). The samples were mounted on carbon stubs (carbon adhesive Leit-Tabs No.: G 3347 [Plano, Wetzlar; Germany]) and analyzed by scanning electron microscopy using a Nova 600 NanoLab SEM equipped with an EDAX Division EDX analyzer.

X-ray Photoelectron Spectroscopy (XPS). XPS analysis performed using a Thermo Scientific ESCALab250 instrument (Thermo Fisher Scientific, Waltham, USA) with a non-monochromatic Al Kα X-ray source (1486.6 eV) operated at 300 W and using a base pressure of 5x10-10 mbar. A pass energy of 20 eV was used with energy step size of 1 eV for the survey spectra. The spectra were recorded using a 45° take off angle relative to the surface

normal. The binding energies were referenced to the C1s line at 284.8 eV from alkyl or adventious carbon. The XPS scans were analyzed using the Avantage 4.15 software.

Atomic Force Microscopy (AFM). All AFM images were recorded under ambient conditions with a commercial AFM (Multimode, Nanoscope IIIa controller, Veeco, California, USA) in tapping mode. The instrument employed was equipped with a piezoelectric scanner, allowing a maximum x,y-scan size of 17 µm and a maximum z-extension of 3.9 µm. Olympus silicon cantilevers (OMCL-AC240TS; length 240 µm, width 30 µm, thickness 2.8 µm) with an integrated tip, a nominal spring constant of 2 N/m and 42 N/m, a tip radius <10 nm, and nominal resonance frequencies of 70 kHz/300 kHz were plasma-cleaned prior to application. Typically tips were scanned at velocities from 0.5-1 $\mu m.s^{-1}$. For all samples topography and phase contrast images were recorded. In order to obtain scan lines at the same average height and tilt the first order "flatten" filter was employed.

Contact Angle measurements. Contact angle goniometry was performed on a drop shape analysis system (DSA 10-Mk2, Krüss GmbH, Germany), equipped with a thermostat chamber (TC3010/3410, Krüss GmbH, Germany), which in turn is connected to a Thermo Haake K 10/ThermoHaake DC 10 circulation system for the temperature control inside the chamber. The reported water CAs are the average of at least three individual measurements.

Quartz crystal microbalance (QCM). Measurements were performed on a Q-sense D300 instrument using the axial flow chamber and a quartz crystal sensor with the gold electrode coated with 50 nm of silicon dioxide (Q-sense QSX 303, AT-cut, 5 MHz). The silica (SiO_2) surface was functionalized *ex-situ* with spermine, using the procedure described above for the glass slides. For the measurements, functionalized surface was placed in the sensor chamber and distilled water was added until a stable frequency baseline was reached. Than, the aqueous tin precursor solution (5 mM Na2SnF6) was introduced and the resonant frequency and dissipation were measured at intervals of 40 ms (25°C for 45 min). The changes in mass were calculated using Sauerbrey equation:

$$\Delta m = -17.7 ng\ Hz^{-1}.cm^{-2} \cdot \Delta f/n$$

Where m is de adsorbed mass, f is the frequency, and n is the overtone number. As control, the crystal sensor with a silica surface were initially stabilized with distilled water, incubated with aqueous tin precursor solution (5 mM, Na2SnF6) and measured at intervals of 40 ms (25°C for 45 min).

Detection of superoxide radicals (O_2^{*-}) formation in the presence of SnO_2 surfaces. The formation of superoxide radicals (O_2^{*-}) generated by SnO2 surfaces was determined using the superoxide assay based on the reduction of *p*-iodonitrotetrazolium chloride (INT) (Cat. No. I8377, Sigma-Aldrich, Germany) by O_2^{*-}.[41] For this purpose, SnO_2 coated glass surfaces were introduced into a glass vial in which a solution of *p*-iodonitrotetrazolium chloride (2.5 mM INT) was added until ¾ filled. The glass vials were than sealed and exposed to sunlight for 1h. Two sets of controls were carried out in parallel. On the first set, an uncoated glass surface was dipped into a solution of INT (2.5 mM) and exposed to direct sunlight for 1h and on the second set, two sealed vials containing INT solution (2.5 mM) and either glass surface or glass surface coated with SnO_2 were kept under dark conditions for 1h. Afterwards, aliquot (1mL) were taken and the UV-Vis spectra recorded using a Cary 5G UV-Vis-NIR spectrophotometer (Varian Inc., Palo Alto, CA, USA).

Photocatalytic degradation of rhodamine B. The ability of organic dye degradation was assessed by placing a SnO_2 coated surface in an aqueous solution of rhodamine B (1µg/mL) (Cat. No. R6626, 95%, Sigma-Aldrich, Germany) which was then sealed and exposed to direct sunlight for 1h. The following controls were performed: *(i)* the same aqueous solution of rhodamine B (1µg/mL) was incubated with an uncoated glass surface and *(ii)* both uncoated and SnO_2 coated glass surfaces were incubated with rhodamine B (1µg/mL) and kept in the dark for 1h. Afterwards, aliquots (1mL) were taken and the UV-Vis spectra recorded using a Cary 5G UV-Vis-NIR spectrophotometer (Varian Inc., Palo Alto, CA, USA).

Antimicrobial assays. All glass slides (with and without SnO_2) were sterilized with 70% ethanol before use. *E. coli* cells (Cat. No. C4040-10, OneShot© Chemically Competent *E. Coli*, Invitrogen, Germany) were incubated in LB medium (Cat. No. X968.2, Carl-Roth, Germany) overnight at 37°C under constant shaking. This culture was than diluted in LB medium (1:5), and an aliquot (2 mL) was placed on top of the uncoated and SnO_2 coated surfaces and left to incubate for 2 h under dark conditions to allow bacterial cell proliferation. Afterwards, the surfaces were exposed to direct sunlight for a maximum period of 30 min. Control experiments were made where uncoated and SnO_2 coated surfaces were left in the dark for the same period of time. After direct sunlight exposure, both surfaces were washed with phosphate buffered saline (PBS) buffer (pH 7.4), and stained with 4',6-Diamidino-2-phenylindole dihydrochloride (DAPI) (1µg/mL) (Cat. No. D8417, ≥98%, Sigma-Aldrich,

Germany,) and propidium iodide (PI) (1 µg/mL) (Cat. No. P4170, ≥94%, Sigma-Aldrich, Germany,) for 20 minutes in the dark. Fluorescence analysis was performed with an Olympus AHBT3 light microscope, together with an AH3-RFC reflected light fluorescence attachment at the emission wavelengths of 380 and 560 nm for DAPI and PI respectively.

4.5 References

1. B. Falabretti, J. Robertson, J. *J. Appl. Phys.* **2007**, *102*, 123703/1–5.
2. F. Yang, S. R. Forrest, *Adv. Mat*. **2006**, *18*, 2018.
3. E. R. Leite, I. T. Weber, E. Longo, J. A. Varela, *Adv. Mater.* **2000**, *12*, 965.
4. I. T. Weber, A. Valentini, L. F. D. Probst, E. Longo, E. R. Leite, *Materials Lett.* **2008**, *62*, 1677.
5. M. Vergohl, N. Malkomes, T. Matthee, G. Brauer, U. Richter, F. W. Nickol, J. Bruch, *Thin Solid Films* **2001**, *392*, 258.
6. M. Adnane, H. Cachet, G. Folcher, S. Hamzaoui, *Thin Solid Films* **2005**, *492*, 240.
7. H. Viirola, L. Niinisto, *Thin Solid Films* **1994**, *251*, 127.
8. H. Hosono, H. Ohta, M. Orita, K. Ueda, M. Hirano, *Vacuum* **2002**, *66*, 419.
9. V. Shrotriya, G. Li, Y. Yao, C. W. Chu, Y. Yang, *Appl. Phys. Lett.* **2006**, *88*, 073508/1-3.
10. (a) L. Vayssieres, M. Grätzel, *Angew. Chem. Int. Ed.* **2004**, *43*, 3666. (b) H. J. Snaith, C. Ducati, *Nano Letters* **2010**, *10*, 1259.
11. C. J. Jin, T. Yamazaki, K. Ito, T. Kikuta, N. Nakatani, *Vacuum* **2006**, *80*, 723.
12. Y. Liu, W. Zhu, O. K. Tan, X. Yao, Y. Shen, *J. Mater. Sci.: Mater. Electron*. **1996**, *7*, 279.
13. M. Adnane, H. Cachet, G. Folcher, S. Hamzaoui, *Thin Solid Films* **2005**, *492*, 240.
14. J. Sundqvist, J. Lu, M. Ottosson, A. Harsta, *Thin Solid Films* **2006**, *514*, 63.
15. (a) K. S. Guan, *Surf. Coat. Technol.* **2004**, 191, 155. (b) W. Y. Gan, S. W. Lam, K. Chaing, R. Amal, H. J. Zhao, M. P. Brungs, *J. Mater. Chem.* **2007**, *17*, 952. (b) J. M. Macak, M. Zlamal, J. Krysa, P. Schmuki, *Small* **2007**, *3*, 300.
16. L. Chunmei, D. Kaplan, Curr. Opin. Solid State Mater. Sci. 2003, 7, 265.
17. S. R. Hall, *Proc. R. Soc. A* **2009**, *465*, 335.
18 J. C. Weaver, D. E. Morse, *Microsc. Res. Tech.* **2003**, *62*, 356.
19. J. Aizenberg, J. C. Weaver, M. S. Thanawala, V. C. Sundar, D. E. Morse, P. Fratzl, *Science* **2005**, *309*, 275.

20. H. C. Schröder, X. Wang, W. Tremel, H. Ushijima, W. E. G. Müller, *Nat. Prod. Rep.*, **2008,** *25*, 455.
21. M. Hildebrand, B. E. Volcani, W. Gassmann, J. I. Schroeder, *Nature* **1997**, *385*, 688.
22. M. Sumper, E. Brunner, *Adv. Funct. Mater*. **2006**, *16*, 17.
23. N. Kröger, K. H. Sandhage, *MRS Bulletin* **2010**, *62*, 32.
24. N. Kröger, S. Lorenz, E. Brunner, M. Sumper, *Science* **2002**, *298*, 584.
25. (a) H. Menzel, S. Horstmann, P. Behrens, P. Bärnreuther, I. Krueger, M. Jahns, *Chem. Comm.* **2003**, 2994. (b) V. V. Annenkov, S. V. Patwardhan, D. Belton, E. N. Danilovtseva, C. C. Perry, *Chem. Commun.* **2006**, 1521. (c) K. Spinde, M. Kammer, K. Freyer, H. Ehrlich, J. N. Vournakis, E. Brunner, *Chem. Mater*. **2011**, *23*, 2973. (d) R. Wieneke, A. Bernecker, R. Riedel, M. Sumper, C. Steinem, A. Geyer, *Org. Biomol. Chem.*, **2011**, *9*, 5482.
26. M. B. Dickerson, K. H. Sandhage, R. R. Naik, *Chem. Rev*., **2008**, *108*, 4935.
27. X. B. Chen and S. S. Mao, *Chem. Rev.* **2007**, *107*, 2891.
28. (a) J. L. Sumerel, W. Yang, D. Kisailus, J. Weaver, J. H. Choi, D. E. Morse, *Chem. Mater*. **2003**, *15*, 4804. (b) M. N. Tahir, N. Zink, M. Eberhardt, H. A. Therese, U. Kolb, P. Theato, W. Tremel, *Small* **2007**, *3*, 829.
29. (a) K. E. Cole, A. M. Valentine, *Biomacromolecules* **2007**, *8*, 1641. (b) E. Kharlampieva, T. Tsukruk, J. M. Slocik, H. Ko, N. Poulsen, R. R. Naik, N. Kröger, V. V. Tsukruk, *Adv. Mater*. **2008**, *20*, 3274.
30. M. N. Tahir, P. Théato, W. E. G. Müller, H. C. Schröder, A. Boreijko, S. Faiß, A. Janshoff, J. Huth, W. Tremel, *Chem. Commun*. **2005**, *28*, 5533.
31. T. Ould-Ely, M. Luger, L. Kaplan-Reinig, K. Niesz, M. Doherty, D. E. Morse, *Nature Protocols* **2011**, *6*, 97.
32. D. Kisailus, J. H. Choi, J. C. Weaver, W. Yang, D. E. Morse, *Adv. Mater.* **2005**, *17*, 314.
33. (a) Y. Zhou, K. Shimizu, J. N. Cha, G. D. Stucky, D. E. Morse, *Angew. Chem. Int. Ed*. **1999**, *38*, 779. (b) S. E. Wolf, U. Schloßmacher, A. Pietuch, B. Mathiasch, H. C. Schröder, W. E. G. Müller, W. Tremel, *Dalton Trans.* **2009**, *39*, 9245.
34. G. E. Kharlampieva, T. Tsukruk, J. M. Slocik, H. Ko, N. Poulsen, R. R. Naik, N. Kröger, V. V. Tsukruk, *Adv. Mater*. **2008**, *20*, 3274.
35. (a) K. M. Delak, N. Sahai, *Chem. Mater*. **2005**, *17*, 3221. (b) D. J. Belton, S. V. Patwardhan, C. C. Perry, *J. Mater. Chem.* **2005**, *15*, 4629.

36. Chevalier, S.; Ayllon, C. C.; Grazu, V.; Luna, M.; Feracci, H; Fuente, J. M. Langmuir 2010, 26, 14707.

37. I. Oller, W. Gernjak, M. I. Maldonado, L. A. Pérez-Estrada, J. A. Sánchez-Pérez, S. Malato, *J. Haz. Mater*. **2006**, *138*, 507.

38. (a) Y. Han, X. Wu, Y. Ma, L. Gong, F. Qu, H. Fan, *Cryst. Eng. Comm.* **2011**, *13*, 3506. (b) B. Esen, T. Yumak, A. Sinag, T. Yildiz, *Photochemistry and Photobiology* **2011**, *87*, 267.

39. A. I. Martinez, D. R. Acosta, G. Cedillo, *Thin Solid Films* **2005**, *490*, 118.

40. S. Dai, Z. Yao, Applied Surface *Science* **2012**, *258*, 5703.

41. A.Z. Haghighi, R. Wei, *Analytical Lett.* **1998,** *31*, 981.

Part III

Inorganic Particles as Enzyme Mimics

CHAPTER 5

V_2O_5 nanowires with an intrinsic peroxidase-like activity

Associated publication: *Adv. Func. Mater., 2011, 21, 501-509*

5.1 Introduction

Vanadium oxide is a well-studied material with a broad range of applications such as in electrochromic/electrooptic devices,[1] electrodes for lithium batteries,[2] catalysis,[3] gas sensors,[4] electrochemistry,[5] and photocatalytic reactions.[6] From the many different compositions of vanadium oxide, V_2O_5 is the most widely studied, especially due to its unique layered structured which makes it also a very good intercalation material.[7] Compared to bulk vanadium (V) oxide, defined nano- and microstructures present significantly better performance in energy storage devices or sensing devices.[8] However, the catalytic activity of the nanostructured V_2O_5 has hardly been studied in contrast to corresponding bulk unstructured material. The presence of vanadium in biological systems is well known. The metal has been found in high concentrations in several marine and terrestrial organisms, like ascidians (tunicates), algae or fungi.[9] In some of these organisms its role is still unclear, but in most cases vanadium is associated with the active center or is part of a co-factor in enzymes like vanadium haloperoxidase (V-HPO) or vanadium nitrogenase.[10]

Vanadium haloperoxidases (V-HPOs) are enzymes that catalyze the oxidation of halides to the corresponding hypohalous acids using hydrogen peroxide (H_2O_2) as the oxidant. When suitable nucleophilic acceptors are present, halogenated compounds are formed. The presence of the haloperoxidases in organisms is thought to be related with the production of halogenated compounds with biocidal activity. V-HPOs have been used in a variety of biotransformations not only halogenations,[11] but also in sulfoxidation,[12] showing a remarkable stereoselectivity and regiospecifity.[13] Haloperoxidases also showed to possess activity towards classical peroxidase substrates,[14] in the same fashion as the well-known horseradish peroxidase (HRP) and extensively used in biochemistry, biological assays[15] as well as in wastewater treatment (i.e. to remove aromatic compounds).[16] Several mimetic compounds for V-HPOs have been discovered, consisting mostly of vanadium organometallic complexes or peroxocomplexes,[17] which exhibit good efficiency and selectivity in several oxidation reactions like halogenation,[18] sulfoxidation,[19] epoxidation, hydroxylation of alkenes,[20] and oxidation of primary and secondary alcohols.[21] The active species in these complexes has been identified as oxoperoxovanadium (V) complexes, and some structural characterization have been done.[22] However, the use of either the natural or recombinant enzymes, or biomimetic vanadium compounds brings up the issue regarding the costs of production and conditions of reaction. For example, the enzymes may have the disadvantage of a short half-life and may need very specific reaction conditions.[23] Although some V-HPOs withstand

organic solvents concentrations up to 60%, some biotransformations cannot be performed in the presence of water.[24] In addition, the production of recombinant enzymes is not always straightforward, as would be required in an industrial application and moreover the stability is always an issue. Some vanadium catalysts (vanadium complexes) used nowadays, such as bulk vanadium pentoxide, are required in high amounts[25] during the catalytic reaction and require for example, high amounts of acid.[26] These catalysts cannot be reused since they degrade during reaction, and their immobilization in polymer or zeolite supports is not so easy.[27]

For this work, we studied V_2O_5 nanowires that were obtained via hydrothermal synthesis in their ability to catalyze peroxidative reactions in aqueous media and other solvents. The reaction catalyzed by nanowires followed a Michaelis-Menten behavior showing an excellent catalytic activity superior in comparison to its natural counterparts, i.e., V-HPO and HRP. The kinetic parameters were also obtained and compared with peroxidase and haloperoxidase enzymes. The new nanostructured vanadium-based material is re-usable up to 10 times and retains its catalytic activity in different organic solvents (up to 90% v/v), making it a promising mimic of peroxidase catalysts.

5.2 Results and Discussion

Synthesis and characterization of V_2O_5 nanowires

V_2O_5 nanowires were prepared using a hydrothermal method as described elsewhere.[28] Briefly, for the synthesis of V_2O_5 nanowires water soluble vanadium (IV) oxosulfate ($VOSO_4$) was oxidized with potassium bromate ($KBrO_3$) by stirring for 30 minutes at room temperature. After lowering the pH using nitric acid, the reaction was kept at 180°C for 24h. After cooling to room temperature and extensive washing, the dark yellow precipitate was dried in an oven at 80°C overnight and analyzed by high-resolution transmission electron microscopy (HRTEM) and X-ray diffraction (XRD). The powder XRD pattern of the V_2O_5 nanowires in Figure 5.1A shows the presence of orthorhombic V_2O_5 (Shcherbianite, PDF - 003-0207). Transmission electron microscopy (TEM) images (Figure 5.1B) showed freshly synthesized V_2O_5 nanowires to have a variable size from 500 nm up to several µm in length and 100 nm width. Figure 5.1C shows a high-resolution transmission electron microscopy (HRTEM) image of such a crystalline nanowire with lattice fringes of 0.516 nm corresponding to orthorhombic V_2O_5. The Fast Fourier Transform (FFT) indicates single

crystalline behavior (Figure 5.1C, inset). Complementary analytical data on V_2O_5 nanowires using energy dispersive analysis of X-rays (EDX) confirmed that only vanadium and oxygen were present. (Figure 5.1D)

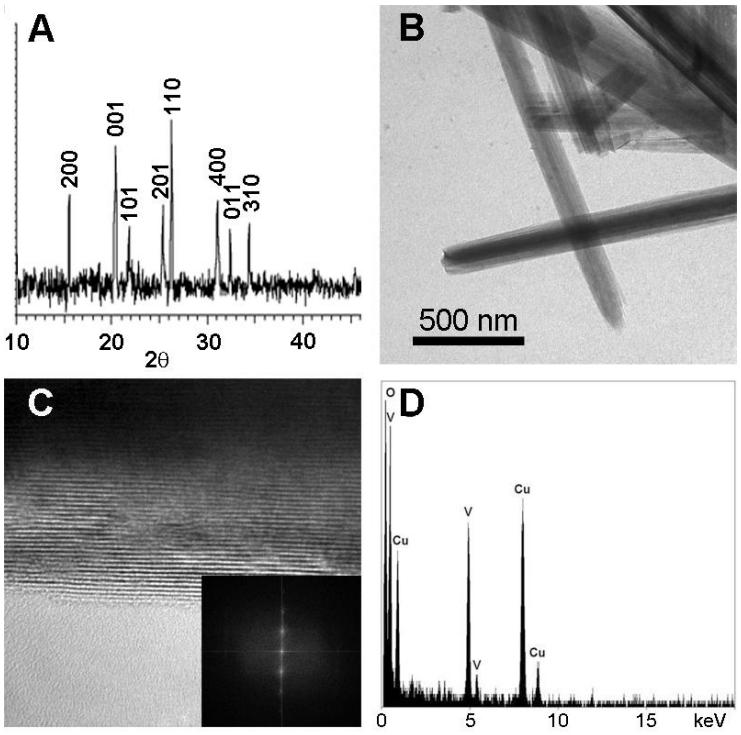

Figure 5.1. (**A**) XRD pattern of V_2O_5 nanowires. All reflections can be indexed to orthorhombic V_2O_5**.** Transmission electron microscopic (TEM) images of V_2O_5 nanowires (**B**) at low and (**C**) at high magnification showing the lattice fringes. The inset of (**C**) shows the Fast Fourier Transform (FFT). (**D**) Correspondent EDX spectra showing the presence of vanadium (V) and oxygen (O). Cupper (Cu) peaks originate from the TEM grid.

Peroxidase-like activity

The V_2O_5 nanowires are capable of catalyzing typical peroxidase reactions, as shown in Figure 5.2, using both chromogenic heme peroxidase substrates 2,2-azino-bis(3-ethylbenzothiazoline-6-sulfonic acid) (ABTS) (Figure 5.2A) and 3,3,5,5,-tetramethylbenzidine (TMB) (Figure 5.2B) in the presence of H_2O_2 to produce a green (maximum absorbance 405 nm) and blue color (maximum absorbance 652 nm) reaction respectively. Initially, these reactions were carried out by incubating 0.02 mg/mL of V_2O_5 nanowires with both substrates (0.68 mM) and H_2O_2 (1 mM) for 60 s at room temperature in a buffered solution (100 mM sodium acetate buffer, pH 4.0). This first approach indicates that these V_2O_5 nanowires have an intrinsic peroxidase–like activity towards these substrates. (Figure 5.2) The reactions were also carried out in the absence of nanowires and at this pH value no significant unspecific oxidation reaction was observed (*data not shown*). Additional

control experiments using V_2O_5 nanowires in the absence of either electron donor (ABTS/TMB) or H_2O_2 showed that no oxidative reaction occurs indicating that both components are required for the reaction to occur as is also the case in V-HPO.[29] For comparison purposes, the oxidation activity towards ABTS of commercially available bulk V_2O_5 was also tested. TEM analysis of bulk V_2O_5 shows an unstructured (Figure S20A) and/or agglomerated material (Figure S20B) composed of crystals with variable size. Although the XRD pattern obtained from bulk V_2O_5 matches the XRD pattern of V_2O_5 nanowires (Figure S20C) no ABTS oxidation activity of bulk V_2O_5 was observed under conditions used in the above experiments, thus highlighting the importance of the nanostructure for the catalytic properties. (Figure S20D)

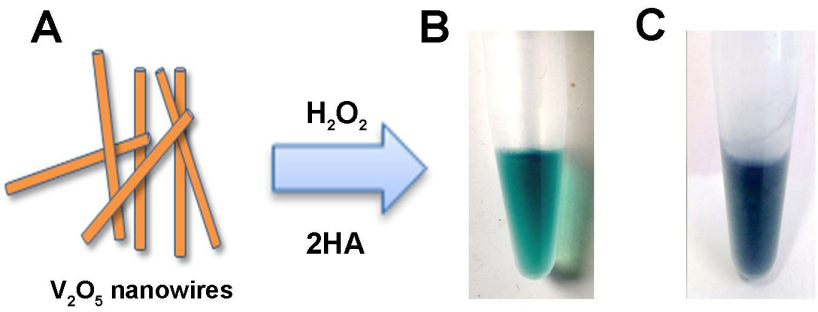

Figure 5.2. V_2O_5 nanowires (**A**) catalyze, in the presence of H_2O_2, the oxidation of various classical peroxidase substrates (HA): 2,2′-Azino-bis(3-ethylbenzothiazoline-6-sulfonic acid) (ABTS) (**B**) and 3,3,5,5,-tetramethylbenzdine (TMB) (**C**); displaying an intrinsic peroxidase- like activity.

The activity is related to the nano-V_2O_5 and not to free vanadate in solution from leaching processes

In order to demonstrate that the intrinsic peroxidase-like catalytic properties of V_2O_5 nanowires towards ABTS result from the surface properties of the nanostructure and not from free orthovanadate anions, VO_4^{3-} (10 µM) was incubated under the same experimental conditions (e.g. 100 mM acetate buffer pH 4.0, 0.68 mM of ABTS, 1 mM H_2O_2, 60 s, RT). Additionally, experiments were made where the supernatant of an aqueous solution of V_2O_5 nanowires (0.02 mg/mL) was tested towards an ABTS oxidation reaction. In both cases, no reaction occurred in the presence of VO_4^{3-} (Figure S4.2A) or the V_2O_5 aqueous supernatant

(Figure S21B), thus ruling out the possibility that the intrinsic peroxidase-like catalytic activity is due to an ion-leaching process from the nanowires.

Kinetic parameters and reaction mechanism

One of the most interesting features about the V_2O_5 nanowires is their ability to catalyze reactions under mild conditions attributed so far to enzymes only. Recently, it was reported that vanadium haloperoxidase (V-HPO) (e.g. recombinant vanadium chloroperoxidase - VCPO) from the fungus *C. inaequalis* catalyzes the oxidation of ABTS in the presence of H_2O_2. This striking similarity, prompted us to characterize the peroxidase-like activity of the V_2O_5 nanowires for ABTS in more detail (Figure 5.3). In a typical experiment, V_2O_5 oxidation activity was determined by monitoring of the absorbance at 405 nm (which increases because of $ABTS^{*+}$ formation) for 300 s at 25°C in acetate buffer (100 mM pH 4.0) for varying concentrations of the V_2O_5 nanowires (< 0.04 mg mL^{-1}) with respect to ABTS (0.68 mM) and H_2O_2 (1 mM). From Figure 5.3A it can be observed that ABTS oxidation rate catalyzed by V_2O_5 nanowires was dependent on the concentration of the nanowires. A control experiment with orthovanadate anions (VO_4^{3-}, 10 μM) in the presence of both H_2O_2 (1 mM) and ABTS (0.68 mM) showed no reaction demonstrating once more that the ABTS oxidation reaction is exclusively due to the V_2O_5 nanowires and not to a leaching process of vanadate ions into solution. The effect of pH on the peroxidase-like activity of the V_2O_5 nanowires (0.02 mg/mL) was measured by varying the pH from 3 to 10, whereas keeping ABTS and H_2O_2 concentrations constant. Interestingly, the catalytic activity of the V_2O_5 nanowires shows a sharp pH optimum at pH 4 (Figure 5.3B) indicating that the one electron oxidation of ABTS is only mediated under slightly acidic conditions, as has also been reported for V-CPO from *C. inaequalis*.[14] At this pH and in the absence of nanoparticles an unspecific reaction between ABTS (0.68 mM) and H_2O_2 (1 mM) was not observed (*data not shown*).

The mechanism of the peroxidase-like catalytic activity of the V_2O_5 nanowires was further investigated using steady-state kinetics. From previous control experiments, we showed that ABTS oxidation catalysis mediated by V_2O_5 nanowires is dependent on the substrate concentration (ABTS and H_2O_2) as one can observe in its natural counterpart, like HRP and V-HPO. [13,30] In order to get a deeper insight into this nanowire/substrate dependency, several experiments were performed by varying the concentrations of either ABTS or H_2O_2 while keeping the other concentration constant. The concentration of the V_2O_5 nanowires was kept

constant in all these experiments (Figure 5.4A and B). We observed that the oxidation reaction catalyzed by the V_2O_5 nanowires follows a Michaelis-Menten behavior towards both, ABTS and H_2O_2 (Figure 5.4A and B). The kinetic parameters for ABTS and H_2O_2 were determined at the pH optimum of 4.0. The V_{max} obtained was 0.2807 M s^{-1}, from which it was determined that the V_2O_5 nanowires mediate the oxidation of ABTS in the presence of H_2O_2 with a turnover frequency (k_{cat}) of $2.5x10^3$ s^{-1}. The k_{cat} is determined as

$k_{cat} = V_{max} / [V_2O_5]$

By using the Lineweaver-Burk linearization process (Figure 5.4C, D) a value for K_M ABTS of around 0.4 µM and K_M H_2O_2 of about 2.9 µM were found. When we compare the enzyme kinetics to this heterogeneously mediated catalysis step, the kinetic parameters show that H_2O_2 has a smaller K_M value (2.9 µM) than K_M value previously determined of the V-CPO (about 100 µM). [31] This suggests that H_2O_2 might have a higher affinity for the surface of the V_2O_5 nanowires compared to HRP and V-HPO at pH 4.0 [32,33] because of the presence of more "*active sites*" in the surface of the nanowires compared to the V-CPO, which only has one vanadate (VO_4^{3-}) ion at the active center.

By analogy with vanadium inorganic complexes, that have been shown to mediate the oxidation of a variety of organic compounds through an oxidation mechanism with the formation of a peroxo intermediate, we propose that ABTS oxidation mediated by V_2O_5 nanowires involves also the formation of an intermediate peroxo surface complex.

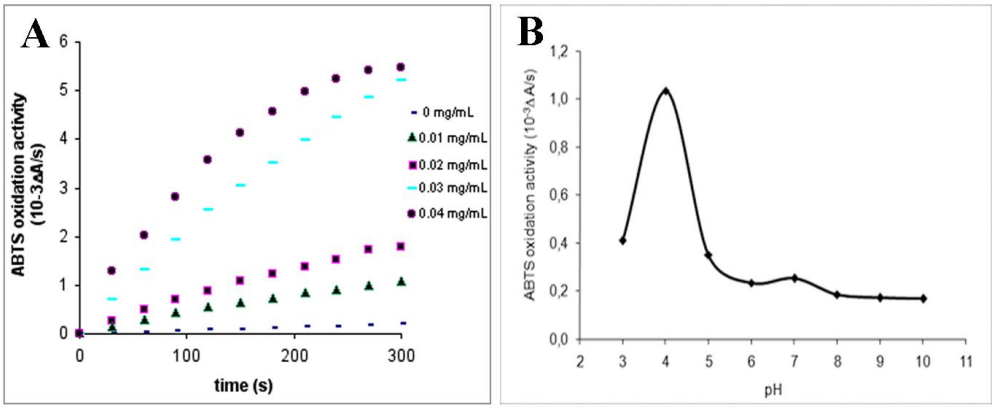

Figure 5.3. Dependency of ABTS oxidation activity on the V_2O_5 nanowire concentration. The rate of the reaction was determined by monitoring the increase of absorbance at 405 nm, due to the formation of $ABTS^{*+}$, for 300s at 25ºC. (**A**) V_2O_5 oxidation activity was determined in acetate buffer (100 mM pH 4.0) using a nanowire concentration ranging from 0 up to 0.04 mg/mL, ABTS (0. 68 mM) and H_2O_2 (1 mM) was added to initiate the reaction. (**B**) The pH dependency of the V_2O_5 on oxidation activity using different buffer composition for different pH values. Assay conditions: V_2O_5 nanowires (0.02 mg/mL), ABTS (0.68 mM) and H_2O_2 (1 mM).

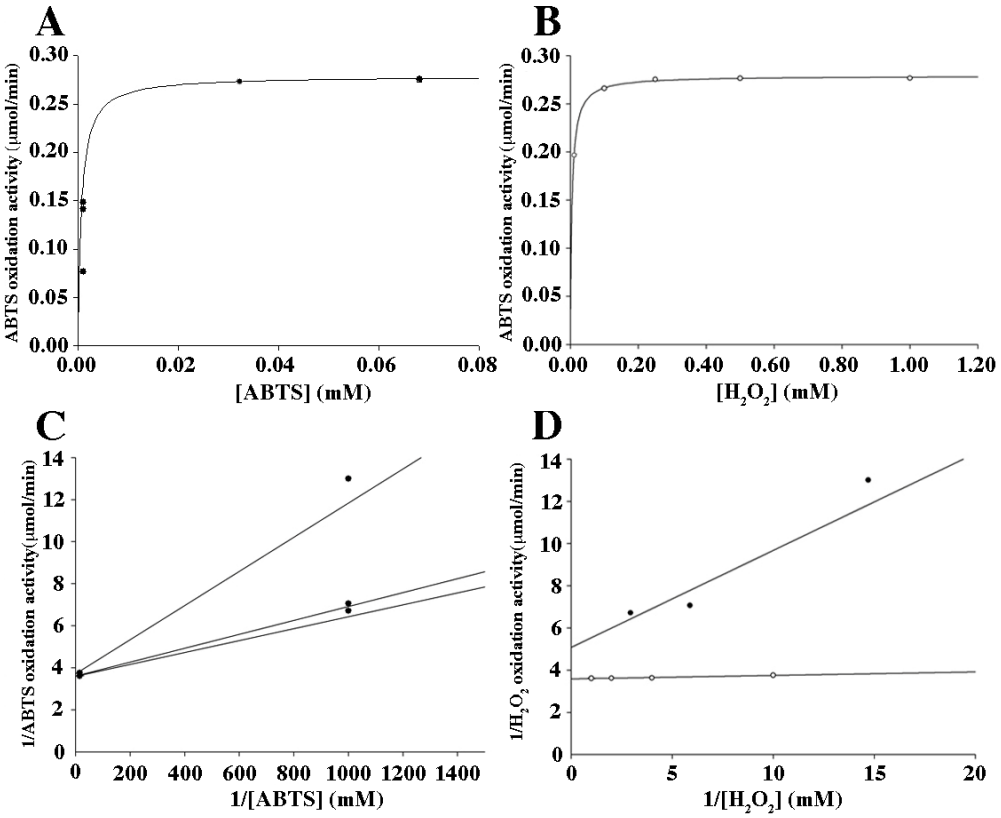

Figure 5.4. Steady-state kinetic study of V_2O_5 nanowires. Michaelis-Menten curve fit for **(A)** variation of ABTS concentration (0-0.68 mM) and keeping the H_2O_2 (1 mM) and V_2O_5 nanowire (0.02 mg/mL) concentration constant and **(B)** variation of H_2O_2 concentration (0-1 mM) and maintaining ABTS (0.68 mM) and V_2O_5 nanowire (0.02 mg/mL) concentration constant. The formation of $ABTS^{*+}$ at 405mn was monitored for 300 s at 25°C. Corresponding Lineweaver-Burk linearization for **(C)** ABTS and **(D)** H_2O_2 values.

A chemical model of the reaction

A possible catalytic mechanism mediated by the V_2O_5 nanowires is proposed after analyzing our experimental results based on the layered V_2O_5 orthorhombic structure. (Figure 5.5A)[34] These layers are made up of neutral coordinatively saturated vanadium cations and are stacked in the [001] direction. In contrast, the (110) surface is formed by the cleavage of covalent V-O bonds at the surface, thus resulting in coordinatively unsaturated V and O atoms at its side faces. The (001) surface is assumed to be responsible for the selective oxidation of hydrocarbons such as toluene, whereas the reactive (110) surface predominantly results in total oxidation. This surface is easily hydroxylated and as a result contains both Brönsted acid and base sites.

The exposed (010) lattice planes of the V_2O_5 nanowires display a vanadium coordination geometry similar to that of the active site of V-HPO,[35] and thus the peroxidase-like catalytic activity displayed by V_2O_5 nanowires may relate to the structure of these surface sites. In this

model, the V atoms in the (010) plane act as Lewis acid sites, while the electron lone pairs of bridging oxygen atoms behave as Lewis base sites where a nucleophilic addition of oxygen can occur. Consequently, the V_2O_5 nanowires are supposed to react in an initial step with H_2O_2 (Figure 5.5B) and forming an intermediate peroxo species. Structural data of peroxo species are available in detail for V-HPO[36] and organometallic vanadium (V) complexes.[37] In the latter case the formation of peroxo species is only favored at very acidic pH values. The formation of these peroxo species is considered an essential step in the oxidation activity.[38] However, the optimal pH value (ca. pH 4) for the oxidation activity of these V_2O_5 nanowires is similar to that found for V-HPO. In a subsequent step, the ABTS substrate binds to the vanadium peroxo species by a nucleophilic attack, thus allowing the oxidation reaction of ABTS to form the $ABTS^{*+}$ species. As hydrogen peroxide is a two electron oxidant another ABTS molecule is required to allow its regeneration, as is found in the natural enzyme (V-HPO).[14]

Two different types of oxygen can be distinguished on the (001) surface. The first type is terminal vanadyl oxygen sites and the second type is the bridging oxygen that connects either two or three vanadium centers. There is a higher electron density on the oxygen atoms with higher number of cation neighbors, that is, because of the π-back donation the charge on the bridging oxygen atoms is significantly larger than that on the terminal vanadyl oxygen atoms. On the other hand, heterolytic chemical sorption might occur through Brönsted acid-base interactions in the (100) and (001) planes.

Reactive oxygen species adsorbed on oxide surfaces are important intermediates in both, total and selective catalytic oxidation reactions.[38] In particular, the catalytic oxidation of several organic compounds, like alkanes for example, by H_2O_2 over TiO_2 or V_2O_5 has been investigated to understand the role of the active peroxo or peroxoacid species in the decomposition mechanism.[39] A key question in oxidative catalysis is whether a reactive surface-oxygen species is used to activate a covalent bond of the substrate or whether it is used for the addition of oxygen to reactive surface intermediates to form oxygenated products. The EPR spectrum in Figure 5.6 is characteristic of a superoxide (O_2^-) type-radical anion. The formal assignment of the signal to an O_2^- type species can be made based on the characteristic g tensor elements for the radical anion stabilized on metal oxides.[40] Furthermore, because the g_{zz} component is sensitive to the crystal field environment, the g values of 2.020, 2.020 and 2.005 observed in Figure 5.6 are consistent with those expected for O_2^- stabilized at a V^{5+} site.

As a control experiment, a dispersion of V_2O_5 nanowires was analyzed, and no EPR signal was observed as expected for vanadium (V) (*data not shown*).

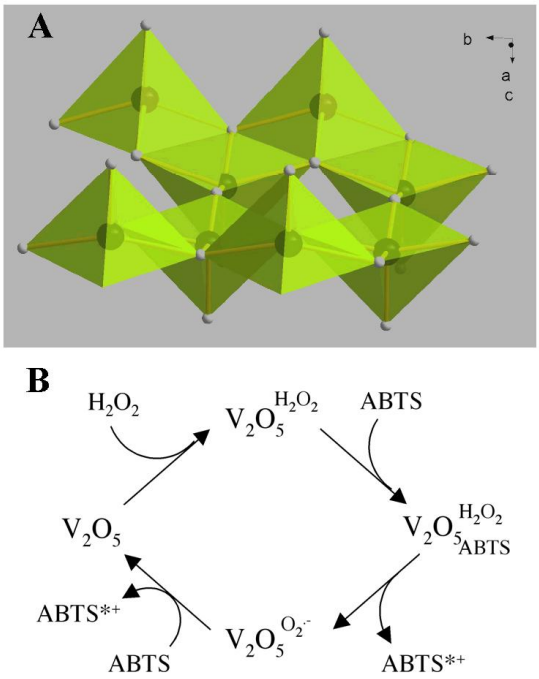

Figure 5.5. (**A**) Single layer from the V_2O_5 structure. In the V_2O_5 nanowires peroxidase-like catalytic activity these layers are stacked along [001], and wires extend along the [100] direction. A view of exposed (110) planes that shows a great similarity with the V-HPO active site. (**B**) Proposed mechanism for the formation of ABTS with the formation of a vanadium peroxo complex intermediate and oxidation attack of ABTS and release of the product ($ABTS^{*+}$). Since hydrogen peroxide is a 2-electron oxidant, another molecule of ABTS is required for V_2O_5 nanowires regeneration leading to formation of a new product ($ABTS^{*+}$).

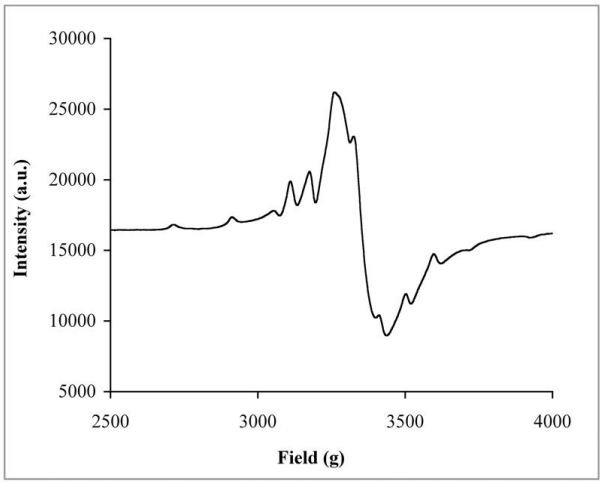

Figure 5.6. EPR spectrum of a superoxo-vanadium species formed on the surface of V_2O_5 nanowires (40 mg) in the presence H_2O_2 (7%) at room temperature. The spectrum was recorded at 80 K and 9.39 GHz. Parameters extracted from the spectrum: Superoxide (rhombic), g = 1.925, 2.005, 2.020. Linewidth = 12.5 mT. Vanadyl (axial), g = 1.980, 1.946 A (^{51}V)= 215, 549 MHz. Linewidth = 3.0 mT, approximately 82% superoxide and 18% vanadyl (□5%).[41]

Catalyst re-utilization and organic solvents catalysis

In order to test the re-utilization of the V_2O_5 nanowires a series of catalytic cycles were carried out. Basically, to a solution of 0.02 mg/mL of V_2O_5 nanowires prepared in acetate buffer (100 mM, pH 4.0), both substrates ABTS (0.68 mM) and H_2O_2 (1 mM) were added and the absorbance at 405 nm measured ($ABTS^{*+}$ formation). Subsequently, the nanowires were recovered, centrifuged and fresh substrates were added. Figure 5.7A shows that, after 10 cycles, the V_2O_5 nanowires partially retain their catalytic activity with some decrease after each cycle. Between each catalytic step an average decay of activity of 5.8 % is observed. Still, this highlights the excellent catalytic properties of V_2O_5 nanowires. Because of their versatility and easy recovery a wider applicability of this nanomaterial for larger scale application seems possible. After the 10 catalytic cycles, the V_2O_5 nanowires were transferred to a copper grid and analyzed by TEM. A representative image in Figure 5.7B shows that the nanowires remain intact, although an apparent layer of organic matter seems to cover their surface. This layer might be due to adsorption of reaction by-products that attach to the surface of nanowires decreasing the number of "*actives sites*" and resulting in the observed decrease in activity after each cycle.

However, in order to determine the influence this organic layer on the catalytic properties of the nanomaterial, the V_2O_5 nanowires were intensively washed with different organic solvents (hexane, acetone, ethanol in this order) after the 10^{th} catalytic cycle and the peroxidase activity assayed. TEM and kinetic analysis confirmed that the organic layer is responsible for the decay in activity. The TEM images of V_2O_5 nanowires after the 10^{th} cycle and organic solvent washing show partially clean surfaces (Figure S22B) when compared with the as prepared nanowires (Figure S22A). The kinetics studies also revealed an increased catalytic activity (Figure S22C) for the washed V_2O_5 nanowires in comparison with unwashed samples. Moreover, the catalytic activity of the washed samples showed a decay of 8% when compared to that of the as-prepared samples, indicating that surface adhesion of impurities may well be the responsible factor for the decrease in catalytic activity.

The most interesting applications of the V_2O_5 nanowires as well as V-HPO is in the industrial and pharmaceutical field. V-HPO was reported to be very stable in organic solvents, retaining up to 70% of its original activity.[42] Similarly, the ABTS oxidation catalyzed by these V_2O_5 nanowires was carried out in different organic solvents. However, because of the low solubility of ABTS in those organic solvents, all assays were performed in a mixture of 90%

organic solvent and 10% water. None of the organic solvents mixtures led to a non-specific reaction between ABTS and H_2O_2 (*data not shown*) confirming that the catalytic activity is strictly due to the V_2O_5 nanowires. Figure 5.8 shows that the oxidation reaction carried out either in ethanol (90%) or isopropanol (90%) has very similar profiles compared to the control reaction performed in a buffered solution. However, the oxidation rate increased 2-fold when the reaction was carried out in acetonitrile (90%). It has been shown that formation of transition metal peroxocomplexes occurs more easily in aprotic environments as the stability of the reduced form of the metal complex is promoted due to better solvation, which is not the case for proton-donor solvents.[43] In summary, our findings are in agreement with the proposed catalytic mechanism in which an essential peroxo complex is formed in the first step.

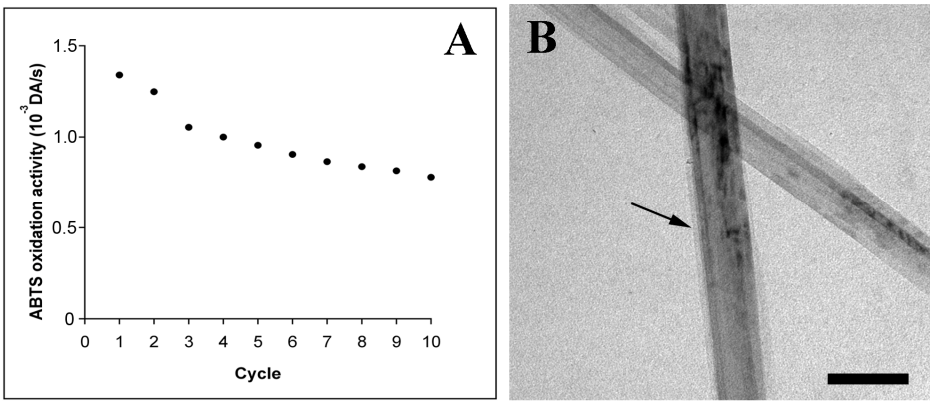

Figure 5.7. Re-utilization of V_2O_5 nanowires in the oxidation reaction of ABTS in the presence of hydrogen peroxide. (**A**) Catalytic activity of V_2O_5 nanowires over various cycles of re-utilization using identical reaction conditions and a constant oxidation rate. (**B**) TEM image of V_2O_5 nanowires after the 10^{th} reaction cycles (0.68 mM ABTS, 1 mM H_2O_2 in acetate buffer 100 mM, pH 4.0). No surface erosion is observed but the formation of an organic layer is clearly present. Scale bar: 100 nm. (The black arrow indicates a surface layer).

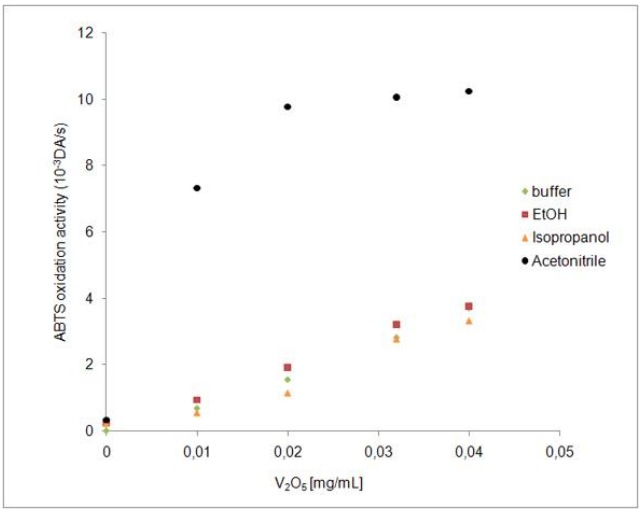

Figure 5.8. The effect of organic solvents (Ethanol-EtOH, Isopropanol and acetonitrile) at 90/10% (v/v) on the ABTS oxidation activity mediated by V_2O_5 nanowires. For comparison purposes, the reaction was carried out in acetate buffer (100mM, pH 4.0). The reactions were carried out using 0.68 mM ABTS, 1 mM H_2O_2 and different concentrations of V_2O_5 nanowires (0-0.04 mg/mL) (prepared in 90% organic solvents) and the formation of $ABTS^{*+}$ spectrophometrically monitored at 405nm.

5.3 Conclusions

V_2O_5 nanowires with a variable length between 500 nm and few µm and a width of 100 nm showed an intrinsic catalytic activity towards classical peroxidase substrates such as ABTS and TMB in the presence of H_2O_2. Similar to the vanadium haloperoxidases (V-HPO) these V_2O_5 nanowires show optimal activity at slightly acidic environments (pH 4.0) with a catalytic activity being dependent on the V_2O_5 concentration. The kinetics of the ABTS oxidation was determined and fitted according to the Michaelis-Menten model displaying a behavior very similar to its natural counterpart, V-HPO. The obtained K_m value for ABTS was approximately 0.4 µM and that for H_2O_2 was approximately 2.9 µM at a pH of 4.0. These values are significantly smaller than those reported for HRP and V-HPO indicating a stronger affinity of the substrates to the nanowires surface. Moreover, the turnover frequency (k_{cat}) was determined to be 2.5 x 10^3 s^{-1}. Based on these kinetic parameters and analogy with other inorganic complexes a mechanism was proposed where an intermediate metastable peroxo complex is formed during the first catalytic step leading to one electron oxidation reaction of ABTS. We conclude that the V_2O_5 nanowires mimic peroxidase enzymes. At the same time, they feature good stability in different organic solvents mixtures (up to 90% v/v) and they can be re-utilized without significant loss of catalytic activity.

5.4 Experimental Section

Synthesis of divanadium pentoxide (V_2O_5) nanowires. V_2O_5 nanowires were synthesized as described elsewhere,[28] with minor adjustments. In brief, 8 mmol of $VOSO_4.nH_2O$ (Alfa Aesar, purity >99.9%) and 5 mmol of $KBrO_3$ (Sigma Aldrich, purity > 98%) were dissolved in 30 mL of distilled water and stirred for 30 minutes at room temperature. Nitric acid (*Trace*SELECT® Ultra, for trace analysis, ≥65%, **Fluka** Chemie AG, Basel, Switzerland) was added dropwise under stirring until pH 2 was reached. The solution was transferred to a Teflon-lined stainless steel autoclave, which was maintained at 180°C for 24h. After cooling to room temperature the solution was filtered and washed several times with distilled water and ethanol. The dark yellow precipitate was dried in an oven at 80°C overnight and analyzed by high resolution transmission electron microscopy (HRTEM) and X-ray diffraction (XRD).

Physical characterization. The products were characterized using transmission electron microscopy (TEM) using a Philips 420 instrument with an acceleration voltage of 120 kV or a Philips TECNAI F30 electron microscope (field-emission gun, 300 kV extraction voltage). The sample was analyzed by X-ray powder diffraction (XRD) in θ/2θ reflection geometry using Siemens D8 power diffractometer equipped with a position sensitive detector. The data was collected using Cu-Kα radiation at an operating potential of 40 kV and a current of 40 mA, and analyzed using EVA software.

Peroxidase-like catalytic activity of V_2O_5 nanowires. The peroxidase-like activity of freshly synthesized V_2O_5 nanowires was determined spectrophotometrically by measuring the formation of ABTS*$^+$ from ABTS at 405 nm (ε=36.0 mM^{-1} cm^{-1}) using a multi-well plate reader (Titertek Multiscan PLUS, MKII, Rheinbach, Germany). Typically, ABTS oxidation activity was measured in 100 mM sodium acetate buffer (pH 4.0) with V_2O_5 nanowires (0-0.04 mg/mL) and ABTS (0.68 mM) (Cat. No. 102946, Boehringer Mannheim GmbH, Germany) during 300 sec at 25°C. Hydrogen peroxide (1 mM) (Cat. No. 8070.1, ROTIPURAN® p.a., ISO, stabilized, ***Carl Roth GmbH & Co.KG*** Karlsruhe, Germany) was added to start the reaction, unless otherwise specified. As a control, bulk V_2O_5 (0.02 mg/mL) (Cat. No. 221899, Sigma-Aldrich, Stenheim, Germany), a solution of sodium orthovanadate (Na_3VO_4, 10 µM) (Cat. No. 450243, Sigma-Aldrich, Stenheim, Germany) and a supernatant derived from an aqueous solution of V_2O_5 (0.02g/mL) were used under otherwise identical reaction conditions.

Determination of kinetic parameters. The steady state kinetics were performed by varying the concentration of V_2O_5 nanowires (0-0.04 mg/mL), H_2O_2 (0-1 mM) or ABTS (0-0.68 mM) each at a time. The reaction was carried out in 100 mM acetate buffer (pH 4.0) and monitored spectrophotometrically for 300s by measuring the formation of $ABTS^{*+}$ from ABTS at 405 nm (ε=36.0 mM^{-1} cm^{-1}) using a multi-well plate reader (Titertek Multiscan PLUS, MKII, Rheinbach, Germany). The kinetic curves were adjusted to the Michaelis-Menten model and Lineaweaver-Burk linearizations were performed using the software Sigma-Plot with the module enzyme kinetics (Systat Software Inc.).

pH measurements. The activity of the V_2O_5 nanowires in different pH was performed in the same conditions as above, except using 3 different buffer compositions for the different pH ranges. The reaction was carried out with 0.02 mg/mL of V_2O_5 to which ABTS (0.68 mM) and H_2O_2 (1mM) were added. Between pH 3 to 6, 100 mM sodium acetate buffer was used; pH 7, 10 mM Tris-Cl buffer was used and between pH 8 -10, 10 mM carbonate buffer was used. The pH of the different buffers was adjusted using pH meter (pH-Meter PCE-228, PCE Deutschland GmbH, Meschede, Germany).

Electron Paramagnetic Resonance (EPR) measurements. To 40 mg of the as-prepared V_2O_5 nanowires, distilled water (500 µL) was added until the sample was completely soaked. At room temperature, H_2O_2 (100 µL of 30% H_2O_2) was added to the sample in order to form the superoxo species. The sample was quenched immediately with liquid nitrogen and the spectrum recorded. The measurements were done in a Magnetec MS 300 spectrometer (X-band) with a frequency counter Hewlett Packard 5340A, at a microwave frequency of 9.39 GHz. As a control experiment, the V_2O_5 nanowires (40 mg) in presence of distilled water were analyzed under the same conditions.

"Re-utilization" assays. The re-utilization of the catalyst was tested using a scale-up of the reaction, in which 5 mg of V_2O_5 nanowires were used for the final concentration of 0.02 mg/mL. The reactions were carried out in 100 mM acetate buffer (pH 4.0), ABTS (0.68 mM) and H_2O_2 (1 mM) was added to start the reaction. The absorbance at 405 nm was measured using a Cary 5G UV-Vis-NIR spectrophotometer (Varian, Inc., Palo Alto, CA, USA) after which the catalyst was spun down by centrifugation (13000xrpm, 25 °C for 20 minutes). The V_2O_5 nanowires were washed with MilliQ water, and a new cycle of reaction (over a total of 10) was performed following the same procedure. In order to recover the V_2O_5 nanowires catalytic activity (after the 10^{th} cycle), the nanowires were intensively washed three times with hexane, then acetone and ethanol and the catalytic activity assayed as described above.

Peroxidase-like catalytic activity of V_2O_5 nanowires in organic solvents. The catalytic activity in the oxidation of ABTS by different concentrations of V_2O_5 nanowires (0-0.04 mg/mL) was assayed under the conditions described before, except that instead of acetate buffer (100 mM, pH 4.0), a mixture of 90% solvent (ethanol, isopropanol, acetonitrile) and 10% water was used to prepare all the solution. As control, the reaction was carried out either in the absence of ABTS or V_2O_5.

Statistical data. All the experiments concerning catalytic activity of V_2O_5 nanowires were performed in triplicate and the data analyzed using the ***paired Student's*** *t*-test.[44]

5.5 References

1. a) K.-C. Cheng, F.-R. Chen, J.-J. Kai, Solar Energy Mater. Solar Cells 2006, 90, 1156; b) S. Lamarque-Forget, O. Pelletier, I. Dozov, P. Davidson, P. Martinot-Lagarde, J. Livage, J. *Adv. Mater*. **2000**, *12*, 1267.
2. a) A. Singhal, G. Skandan, G. Amatucci, F. Badway, N. Ye, A. Manthiram, H. Ye, J. J. Xu, *J. Power Sources* **2004**, *129*, 38; b) M. Koltypin, V. Pol, A. Gedanken, D. Aurbach, *J. Electrochem. Soc*. **2007**, *154*, A605; c) T. J. Patey, S.H. Ng, R. Buechel, N. Tran, F. Krumeich, J. Wang, H.K. Liu, P. Novák, *Electrochem. Solid-State Lett.* **2008**, *11*, A47.
3. B. Schimmoeller, H. Schulz, S.E. Pratsinis, A. Bareiss, A. Reitzmann, B. Kraushaar-Czarnetzki, *J. Catal.* **2006**, *243*, 82.
4. a) J. Liu, X. Wang, Q. Peng, Y. Li, *Adv. Mater*. **2005**, *17*, 764; b) I. Raible, M. Burghard, U. Schlecht, A. Yasuda, T. Vossmeyer, *Sens. Actuators B* **2005**, *106*, 730; c) C.-J. Mao, H.-C. Pan, X.-C. Wu, J.-J. Zhu, H.-Y. Chen**,** *J. Phys. Chem. B* **2006,** *110*, 14709; d) L. Biette, F. Carn, M. Maugey, M.-F. Achard, J. Maquet, N. Steunou, J. Livage, H. Serier, R. Backov, *Adv. Mater.* **2005**, *17*, 2970.
5. a) F. Huguenin, R. M. Torresi, *J. Phys. Chem. C* **2008,** *112*, 2202; b) Y.S. Hu, X. Liu, J.-O. Müller, R. Schlögl, J. Maier, D. S. Su, *Angew. Chem*. **2009**, *121*, 216; *Angew. Chem. Int. Ed.* **2009**, *48*, 210.
6. a) F. Amano, T. Ito, S. Takenaka, T. Tanaka, *J. Phys. Chem. B* **2005,** *109*, 10973; b) F. Amano, T. Tanaka, T. Funabiki, *Langmuir* **2004,** *20*, 4236; c) B. Li, Y. Xu, G. Rong, M. Jing, Y. Xie, *Nanotechnology* **2006**, *17***,** 2560.

7. a) F. Donsanti, K. Kostourou, F. Decker, N. Ibris, A. M. Salvi, M. Liberatore, A. Thissen, W. Jaegerman, D. Lincot, *Surf. Interface Anal.* **2006**, *38,* 815; b) D. B. Le, S. Passerini, F. Coustier, J. Guo, T. Soderstrom, B. B. Owens, W. H. Smyrl, *Chem. Mater.* **1998,** *10,* 682; c) J. S. Braithwaite,C. R. A. Catlow, J. D. Gale, J. H. Harding, *Chem. Mater.* **1999,** *11,* 1990; d) C. K. Chan, H. Pen, R. D. T. Westen, K. Jarausch, X. F. Zhang, Y. Cui, *Nano Lett.* **2007**, *7,* 490; e) M. E. Spahr, P. Bitterli, R. Nesper, M. Müller, F. Krumeich, H. U. Nissen, *Angew. Chem.* **1998**, *110,* 1339; *Angew. Chem. Int. Ed.* **1998**, *37*, 1263; f) M. E. Spahr, P. Stoschitzki- Bitterli, R. Nesper, O. Haas, P. Novák, *J. Electrochem. Soc.* **1999**, *146,* 2780; g) A. Dobley, K. Ngalas, S. Yang, P. Y. Zavalij, M. S. Whittingham, *Chem. Mater.* **2001**, *13,* 4382; h) G. R. Patzke, F. Krumeich, R. Nesper, *Angew. Chem.* **2002**, *114,* 2554; *Angew. Chem. Int. Ed.* **2002**, *41*, 2446; i) F. Krumeich, H.-J. Muhr, M. Niederberger, F. Bieri, B. Schnyder, R Nesper, *J. Am. Chem. Soc.* **1999**, *121,* 8324.
8. a) Y. Wang, K. Takahashi, K. H. Lee, G. Z. Cao, *Adv. Funct. Mater.* **2006**, *16,* 1133; b) J. Livage, Nature Materials **2003**, ***2***, 297.
9. a) E. M. Oltz, R. C. Brüning, M. J. Smith, K. Kustin, K. J. Nakanishi, *Am. Chem. Soc.* **1988**, *110,* 6162; b) H. Vilter, *Phytochemistry* **1984**, *23,* 1387; b) J. W. P. M. Van Schijndel, E. G. M. Vollenbroek, R. Wever, *Biochim. Biophys. Acta* **1993**, *1161*, 249.
10. a) R. L. Robson, R. R. Eady, T. H. Richardson, R. W. Miller, M. Hawkins, J. R. Postgate, *Nature* **1986**, *322,* 388; b) E. de Boer, Y. van Kooyk, M. G. M. Tromp, H. Plat, R. Wever, *Biochim. Biophys. Acta* **1986**, *869,* 48.
11. a) J. S. Martinez, G. L. Carroll, R. A. Tschirret-Guth, G. Altenhoff, D. R. Little, A. Butler, *J. Am. Chem. Soc.* **2001**, *123,* 3289; b) P. Coughlin, S. Roberts, C. Rush, A. Willetts, B*iotechnol. Lett.*, **1993**, *15,* 907.
12. H. B. Ten Brink, A. Tuyman, H. L. Dekker, W. Hemrika, Y. Izumi, T. Oshiro, H. E. Schoemaker, R. Wever, *Inorg. Chem.* **1998**, *37,* 6780.
13. A. Butler, M. Sandy, *Nature* **2009,** *460,* 848.
14. H. B. Ten Brink, H. L. Dekker, H.E. Schoemaker, R. Wever, *J. Inorg. Biochem.* **2000**, *80,* 91.
15. a) M. Y. Rubtsova, G. V. Kovba, A. M. Egorov, *Biosens. Biolectron.* **1998**, *13,* 75; b) F. Wendzinski, B. Gründig, R. Renneberg, F. Spener, *Biosens. Bioelectron.* **1997**, *12*, 43.
16. J. Karam, J. A. Nicell, *J. Chem. Tech. Biotechnol.* **1997**, *69,* 141.
17. A. G. J. Ligtenbarg, R. Hage, B. L. Feringa, *Coord. Chem. Rev.* **2003**, *237,* 89.
18. M. J. Clague, N. L. Keder, A. Butler, *Inorg. Chem.* **1993**, *32*, 4754.

19. T. S. Smith, V. L. Pecoraro, *Inorg. Chem.* **2002**, *41*, 6754.
20. H. Mimoun, L. Saussine, E. Daire, M. Postel, J. Fischer, R. Weiss, *J. Am. Chem. Soc.* **1983**, *105*, 3101.
21. S. Velusamy, T. Punniyamurthy, *Org. Lett.* **2004**, *6*, 217.
22. A. Butler, M. J. Clague, G. E. Meister, *Chem. Rev.* **1994**, *94*, 625.
23. a) H. S. Soedjak, J. V. Walker, A. Butler, *Biochemistry* **1995**, *34*, 12689; b) M. F. Machado, J. Saraiva, *J.Mol. Catal. B: Enzymatic* **2002**, *19*, 451.
24. M. Almeida, S. Filipe, M. Humanes, M. F. Maia, R. Melo, N. Severino, J. A. K. da Silva, J. J. R. Fraústo da Silva, R. Wever, *Phytochemistry* **2001**, *57*, 633.
25. a) U. Bora, G. Bose, M. K. Chaudhuri, S. S. Dhar, R. Gopinath, A. T. Khan, B. K. Patel, *Org. Lett.* **2000**, *2*, 247; b) U. Bora, M. K. Chaudhuri, D. Dey, S. S. Dhar, *Pure Appl. Chem.* **2001**, *1*, 93.
26. G. Rothenberg, J. H. Clark, *Org. Proc. Res. Dev*. **2000**, *4*, 270.
27. (a) M. R. Maurya, U. Kumar, P. Manikandan, *Dalton Trans.* **2006**, 3561; b) M. R. Maurya, H. Saklani, S. Agarwal, *Catal. Commun*. **2004**, *10*, 563.
28. F. Zhou, X. Zhao, C. Yuan, L. Li, H. Xu, *Crystal Growth and Design* **2008**, *8*, 723.
29. a) R. Wever, W. Hemrika in *Handbook of Metalloproteins, Vol.2* (Eds.: A. Messerschmidt, R. Huber, T. Poulos, K. Wieghardt), John Wiley and Sons Ltd., Chichester, **2001**, pp. 1417–1428; b) A. Butler, *Coord. Chem. Rev.* **1999**, *187*, 17; c) D. C. Crans, J. J. Smee, E. Gaidamauskas, L. Yang, *Chem. Rev.* **2004**, *104*, 849.
30. H. B. Dunford, P. A. Jones, *Peroxidases and Catalases: Biochemistry, Biophysics, Biotechnology and Physiology*, John Wiley & Sons 2010.
31. N. Tanaka, Z. Hassan, R. Wever, *Inorg. Chim. Acta* **2003**, *356*, 288.
32. H. Gallati, H. Brodbeck, *J. Clin. Chem. Clin. Biochem*. **1982**, *20*, 221.
33. J.W.P.M. van Schijndel, E.G.M. Vollenbroek, R. Wever, *Biochim. Biophys. Acta* **1993**, *1161*, 249.
34. R. Enjalbert, J. Galy, *Acta Cryst.* **1986**, *C42*, 1467.
35. A. Butler, *Current Opinion in Chemical Biology*, **1998**, *2*, 279.
36. M. R. Maurya, *J. Chem. Sci*. **2006**, *113*, 503.
37. G. Zampella, P. Fantucci, V. L. Pecoraro, L. De Gioia, *J. Am. Chem. Soc.* **2005**, *127*, 953.
38. A. Bielanski, J. Haber, *Oxygen in Catalysis*, Dekker, New York, **1991**.
39. B. Notari, *Adv. Catal.*, **1996**, *41*, 253.

40. M. Chiesa, E. Giamello, M. C. Paganini, Z. Sojka, D. M. Murphy, *J. Chem. Phys.* **2002**, *116*, 4266.
41. S. Stoll, A. Schweiger, EasySpin, a comprehensive software package for spectral simulation and analysis in EPR. *J. Magn. Reson.* **2006**, *178*, 42.
42. H. G. Bernal, L. C. Caero, *Int. J. Chem. Reactor Eng.* **2005**, *3*, 1.
43. Z. V. Todres, *Organic Ion Radicals, Chemistry and Applications*, 2nd Ed. CRC Press 2009.
44. L. Sachs, *Angewandte Statistik*; Springer: Berlin, **1984**, 242.

CHAPTER 6

Application of V_2O_5 nanowires as haloperoxidase enzyme mimics

Associated publications: *J. Mater. Chem. 2011, 21, 11923-11929.*

Nature Nanotech. 2012, in press.

6.1 Introduction

In nature different types of halogenated compounds can be found in different species, with important regulatory and defensive functions. Many of these compounds are thought to be produced by enzymes involved in their metabolism like haloperoxidases. Many of these natural halogenated compounds have been proved to have interesting antifungal, antibacterial, antiviral or anti-inflammatory activities.[1-4] Thus mechanisms or more specifically enzymes and their mimics, which allow the effective production of these compounds, have particular interest for different types of industries. Haloperoxidases have been isolated from different species as well as recombinantly produced [5] and applied in antimicrobial coatings,[6] preservatives[7] and in different types of organic reactions.[8-10]

Haloperoxidases catalyze the oxidation of a halide (i.e., chloride, bromide, or iodide) by hydrogen peroxide to the corresponding hypohalous acid. The hypohalous acid produced can further react with different nucleophilic acceptors to form a diversity of halogenated compounds, according to:[11,12]

$$R - H + H_2O_2 + X^- + H^+ \rightarrow X - R + 2\,H_2O$$

Different classes of haloperoxidases have been identified. Two types of haloperoxidases carry a prosthetic group: a heme group in the case of the heme-containing haloperoxidases and a vanadate ion (VO_4^{3-}) in the case of the vanadium-containing haloperoxidases (V-HPO).[11,13](*Chapter 1, section 1.3*)

Most organisms react to oxygen stress by producing oxygen-scavenging enzymes or molecules like melanin, which can scavenge free radicals.[14] Melanin is a pigment found in many organisms and belongs to the class of polycyclic biopolymers. These polymers of phenolic compounds are synthesized by polymerization of indole-type rings, in both the quinone and hydroquinone oxidation state, randomly cross-linked with structural units linked through heterogenous nonhydrolyzable bonds. These units represent the product of complex oxidation cycles that start from different precursors and follow various pathways of synthesis, depending on their localization in the organism. The biosynthetic pathway occurs in vivo in melanocytes, and the process is catalyzed, in the first steps, by tyrosinase, a specific enzyme, which converts tyrosine to L-dopa and then to dopaquinone.[15,16] This highly reactive chemical

species is subject to oxidative polymerizations, and the polymers further aggregate in black-brown granules.[17] Natural melanin and synthetic melanin-like polymers have shown potential application in the field of conductive materials as well as metal scavenging and filtering products.[18,19] Vanadium haloperoxidases have been recently shown to be able to catalyze the formation of synthetic melanin by producing highly reactive HOI species, which can accelerate the oxidation of dopamine to dopaquinone and consequent polymerization to form the black synthetic melanin.[20] On the other side, due to the formation of the reactive HOX species, naturally occurring vanadium haloperoxidase (V-HPOs) enzymes have been shown to prevent bacteria from colonizing the surface of certain seaweeds (biofilm formation)[21,22] and they have been considered as inspirational source for additives in antifouling paints.[23,24]

Because hypohalous acids such as hypochlorous acid (HOCl) and hypobromous acid (HOBr) induce severe damages to many organisms, it is generally accepted that these highly reactive molecules help to prevent biofilm formation through either a biocidal action or the oxidation of the biofilm.[23]

Seawater has a pH of 8 to 8.2 and contains about 1mM Br^- and 500mM Cl^-, and as long as sufficient amounts of peroxides are present, an antifouling paint based on haloperoxidases will continuously generate hypohalous acids as a bactericidal agent. However, H_2O_2 may be a limiting factor because seawater contains only between 100 and 250 nM of H_2O_2. [25]

The natural V-HPO can withstand organic solvents and high concentrations of H_2O_2, but using them as industrial scale catalysts for halogenation or as additives in antifouling paints remains a challenged due to the expensive upscaling production and their stability/reactivity under the needed conditions (for example in seawater). [26]

In the previous chapter it was shown that vanadium pentoxide (V_2O_5) nanowires - a widely used catalyst material that is stable, inexpensive and readily available - possesses peroxidase-like activity. Here it's shown that V_2O_5 nanowires have intrinsic iodination and bromination activity as found for V-HPOs and can produce HOI or HOBr, and $^1O_2$ species, which can be taken advantage of for the synthesis of a synthetic melanin-like polymer with semiconductive properties or for exerting a strong biocidal activity against both Gram positive (*S. aureus*) and Gram negative (*E. coli*) bacteria. Moreover, V_2O_5 nanowires are shown not to be toxic to marine biota. *In situ* experiments revealed that paints containing V_2O_5 nanowires could prevent the biofouling of surfaces when exposed to seawater up to 60 days.

6.2 Results and Discussion

The synthesis of the V_2O_5 nanowires was carried out as described in the previous chapter using a hydrothermal method. This produces orthorhombic V_2O_5 nanowires with average sizes of 500 nm length and 20-100 nm width. (see Chapter 5 for material characterization)

Iodination activity of V_2O_5 nanowires and production of synthetic melanin

The halogenation activity (respectively iodination activity) of the V_2O_5 nanowires was determined using thymol blue (TB).[27] When the nanowires were allowed to react with TB in the presence of hydrogen peroxide and iodide at pH 8.0, a rapid conversion (aproximatly 1 min) of the yellow color to a deep blue color occurred. The absorption spectrum of TB at pH 8.0 in the presence of only H_2O_2/I^- shows two bands. However, when the reaction was carried out in the presence of V_2O_5 nanowires ($TB/H_2O_2/I^-$), the UV-Vis spectrum showed an increase of the 620 nm band (Figure 6.1, red line). These results are in agreement with previous studies where it was shown that the TB solution turns deep blue after undergoing the catalytic halogenation reaction (V-BPO iodination catalysis) leading ultimately to an absorption increase at 610 nm.[27] Furthermore, in our experiments triiodide (I^{3-}) accumulation (350 nm) was not observed suggesting the presence of a mechanism similar to V-HPO, with no competing side reactions.

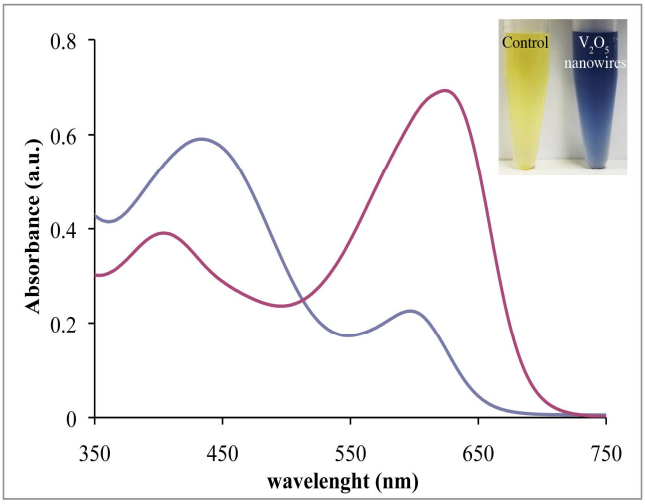

Figure 6.1 UV-Vis absorption spectrum of thymol blue (TB) (25 mM) (blue line) in PBS (pH 8.0) in the presence of H_2O_2/I^- and the reaction product of the V_2O_5 nanowire catalyzed reaction with TB in the presence of H_2O_2/I^- (red line). Inset: digital images of the $TB/H_2O_2/I^-$ (yellow) and V_2O_5 nanowires/$TB/H_2O_2/I^-$ catalyzed reaction (blue).

In control experiments, both sodium orthovanadate and bulk V_2O_5 were used in parallel as well as in the absence of V_2O_5 nanowires. In all cases, TB did not show any color change (e.g. it remained yellow) indicating the absence of a non-catalytic reaction between TB and H_2O_2/I^- at pH 8.0 during the assay time used for accessing the biomimetic activity of the V_2O_5 nanowires.[27] For identification purposes, the yellow solution resulting from the V_2O_5 catalyzed reaction of $TB/H_2O_2/I^-$ was dried under vacuum, re-suspended in chloroform and analyzed by mass spectrometry (FD-MS). Analysis of the deep blue solution with FD-MS revealed compounds with molecular ion peaks at *m/e* 592 and 718 corresponding to mono and di-iodinated forms of TB (as reported before, ref 27) confirming in this way the iodination catalytic activity of the V_2O_5 nanowires.

For the production of synthetic melanin, the reaction between the V_2O_5 nanowires (1 mg/mL), KI (40 mM) and H_2O_2 (1 mM) in the presence of dopamine (10 mM) was carried out in aqueous solution at slightly basic pH values (pH 8.0) and monitored spectrophotometrically for 140 min (RT). Figure 6.2 displays the resulting spectra indicating a multistep reaction. Initially, the solution is colorless (Figure 6.2, inset), but after 10 min a band at 480 nm appears and the color of the solution turns pink/orange (Figure 6.2, inset). The corresponding band can be attributed to dopachrome formation [28,29] or eventually to a di-iodinated form of dopamine. After 105 min a maximal absorbance change was reached. A decrease in the band intensity was observed indicating further reactions, and a black color developed slowly. Finally, a black precipitate was formed leaving a clear supernatant (Figure 6.2, inset). This precipitate was insoluble in water and organic solvents such as methanol, ethanol, isopropanol, DMSO and THF. Interestingly, when the reaction was carried out either in 100 mM acetate buffer (pH 4.0) the reaction was similar to the one performed in buffered solution (PBS, pH 8.0). However, the black precipitate formed more slowly and the reaction rate was 4-fold slower and incomplete, i.e., the solution remained slightly pink for a longer period (>5 h). A set of control experiments was carried out in parallel. When the reaction was performed in the absence of H_2O_2 (1 mM) or in the presence of sodium orthovanadate (1 mM) no oxidation reaction occurred indicating that H_2O_2 is essential for the development of the reaction and that monomeric vanadate anion (VO_4^{3-}) is not involved in the catalysis in line. When the reaction was carried out in the absence of V_2O_5 nanowires, catalysis occurred with similar spectral features, but after a longer time period (>24 h) showing that a specific reaction does occur, but with a very slow (10-fold) rate.[30] Additional control experiments

using bulk V_2O_5 (1 mg/mL) showed that the reaction occurs but at a slower rate (10-fold), remaining pink/orange after 140 min, indicating the importance of well-structured materials in catalysis. (For comparison purposes see supporting information Figure S23)

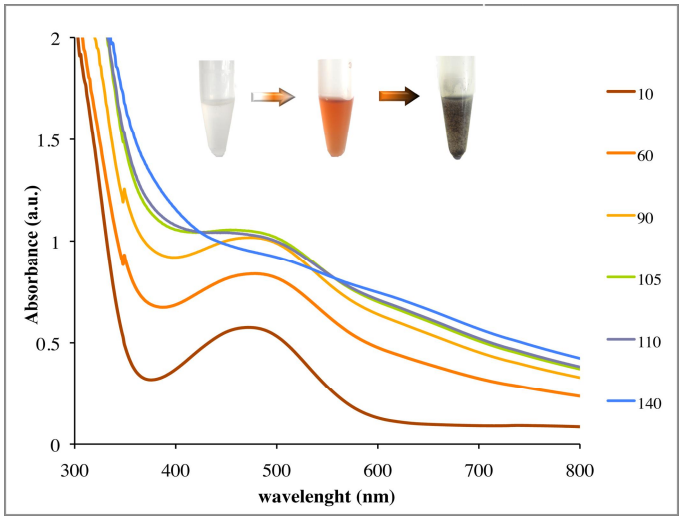

Figure 6.2 Time course catalysis of dopamine in the presence the V_2O_5 nanowires, iodide (40 mM), H_2O_2 peroxide (1 mM) in aqueous solution (pH 8) monitored spectrophotometrically for 140 min. The reaction proceeds by two-steps. Initially, the reaction is colorless and after 10 min a band at 480 nm starts to form originating a pink/orange solution that continues to increase until 105 min. In the second step, this pink/orange intermediate proceeds to a black precipitate leading to the decrease of 480 nm band and clear supernatant. Inset: colored images describing a twostep reaction.

Instead of using dopamine the reaction catalyzed by V_2O_5 nanowires was also studied with L-dopa (10 mM) under identical experimental conditions. The reaction profile is exactly the same, indicating that the presence of additional –COOH groups does not influence the reaction (*data not shown*). The final black material was washed thoroughly with distilled water, pelleted by centrifugation, air-dried and characterized by scanning electron microscopy (SEM), UV-Vis, FT-IR and electric conductivity. The SEM overview image in Figure 6.3A shows a fibrillar and porous structure. Higher magnification revealed small spherical features, associated with the polymeric fibrils (Figure 6.3B). In an image with higher resolution, polymer nanospheres of about 50 nm (average size) are integrated within the polymeric fibrils (Figure 6.3C). For comparison purposes, we analyzed in parallel natural occurring melanin (melanin from cuttlefish—*Sepia officinalis*). Figure 6.3D shows a representative

morphological analysis of natural melanin, which is composed of spheres with a variable size diameter (100–200 nm).[31] However, when L-dopa was used and V_2O_5 nanowires were added, a porous network was formed but neither polymeric fibrils nor nanospheres were observed (*data not shown*). Although the kinetics of the reaction are virtually identical to those using dopamine the presence of the –COOH group in the initial monomer apparently influences strongly the final morphology of the polymer. Therefore it is very likely that the mechanism of polymerization involves the aromatic ring instead of the amino and carboxylic groups.

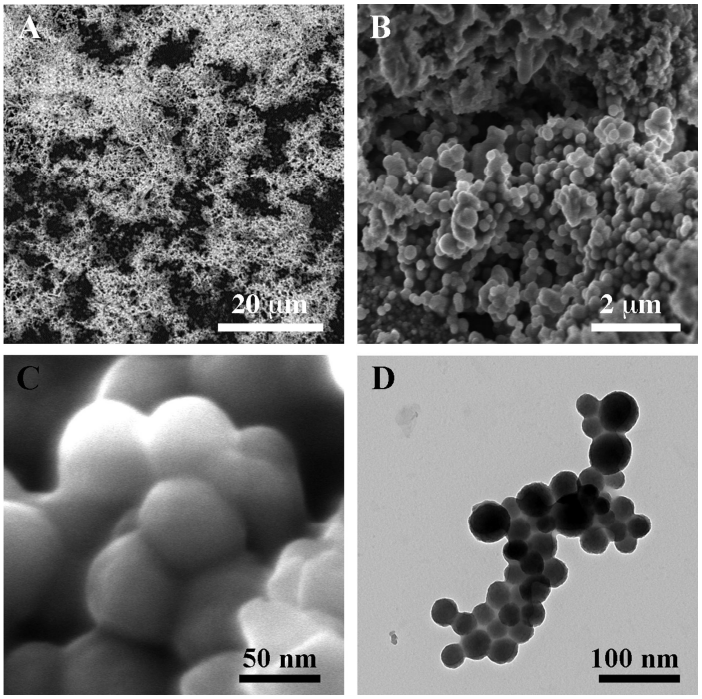

Figure 6.3 Microscopic analysis of the product obtained by the catalytic polymerizing of dopamine with V2O5 nanowires (1 mg/mL) in the presence of iodide (40 mM) and hydrogen peroxide (1 mM); (A) SEM image displays a fibrillar and porous structure. (B) At higher magnification spherical features closely associated with the fibrils are observed. (C) The polymeric nanospheres display an average size diameter of 50 nm. (D) Naturally occurring melanin extracted from a cuttlefish. This type of melanin has a spherical morphology with a diameter of 100– 200 nm.

Since from a morphological point of view, the black precipitate obtained by the catalysis of dopamine in the presence of V_2O_5 nanowires/I^-/H_2O_2 shows remarkable similarities with naturally occurring melanin and the black precipitate was further characterized by UV/Vis and FT-IR. As may be expected the absorption spectra of the black product measured in the visible spectral range showed no maxima or minima (Figure 6.4A, solid line), but show only a

monotonic decrease from 375 to 800 nm similar to other melanins (Figure 6.4A, dashed line).[32-35] This absorption spectrum is the result of unstructured melanin films and the small differences between the natural melanin and V_2O_5 nanowires produced black precipitate absorption can be attributed to different degrees of polymerization.[36] It is very atypical of organic compounds but resembles spectra of some disordered amorphous inorganic semiconductors.[37] The amorphous structure of the black precipitate as well as of natural derived melanin was confirmed by XRD (Figure S24A, supporting information).

A comparative analysis of the IR spectra of the black material and naturally occurring melanin may help to unveil the structure and main functional groups of this material. Figure 6.4B shows remarkable similarity between the black synthetic material (Figure 6.4B, dashed line) and natural melanin (Fig. 6.4B, solid line) in accordance with vibrational spectra in the literature.[38] Both spectra display a broad band at 3400 cm^{-1}, attributed to stretching vibrations of phenolic –OH and $–NH_2$ groups, a strong band at 1610 and 1640 cm^{-1} due to stretching vibration of aromatic double carbon bonds and –COOH. Two bands localized at 2923 cm^{-1} and 2853 cm^{-1} in both spectra can be assigned to aliphatic C–H. The absence of peaks at 1700–1750 cm^{-1} corresponding to –C=O stretching vibrations indicates that –COOH groups are not present, neither in our product nor in the natural melanin. In contrast COOH groups are observed in the spectra of the black product when the reaction was carried out using L-dopa (*data not shown*). An additional significant band is found at 1383 cm^{-1} which corresponds to phenolic bending bands and indolic and phenolic –NH stretching vibrations.[38]

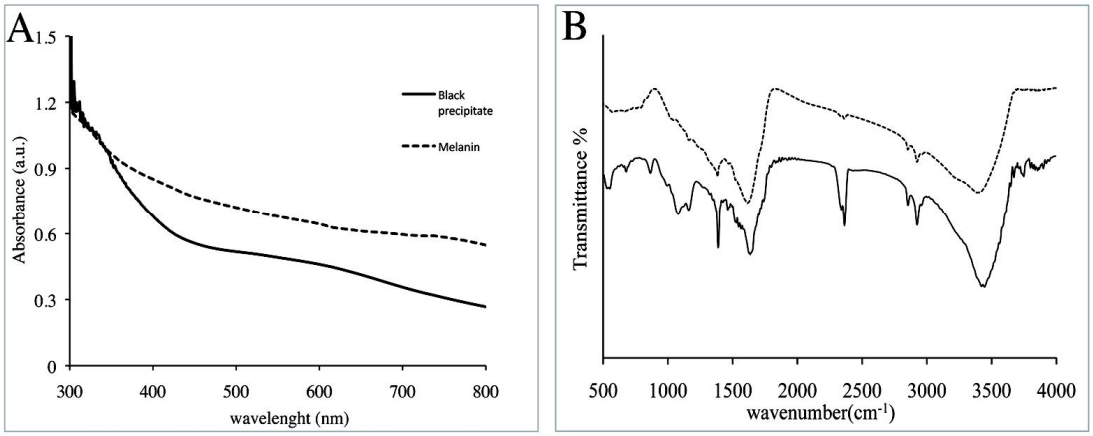

Figure 6.4 (A) UV-Vis spectra of the black precipitate (solid line) showing the same featureless absorption as in the spectrum of melanin (dashed). (B) FT-IR spectra (transmittance) of the black product produced by the nanowires (solid line) and of commercially available melanin (dashed line).

These results strongly suggest that the black synthetic material has a structure similar to that of natural melanin. As additional characterization, electric conductivity measurements for both materials, i.e., naturally occurring melanin and the black synthetic precipitate were carried out. For this purpose, and due to the insolubility associated to this type of polymers, pellets of both polymers with a diameter of 6 mm and a thickness of 2 mm were made and several *I–V* curves were recorded on each material at different positions using the four-point-probe setup. The measurements were performed at room temperature (25 ± 2 °C).

From the obtained *I–V* curves, the conductivity was determined and the error as the standard deviation of the mean value. For the naturally occurring melanin, a value of conductivity of $5.3 \times 10^{-8} \pm 1.1 \times 10^{-8}$ S cm^{-1} was found where for the black precipitate a conductivity value of $3.7 \times 10^{-8} \pm 0.6 \times 10^{-8}$ S cm^{-1} was obtained indicating that this newly formed biopolymer displays semiconductive properties as reported for other melanins (natural and synthetic).[39-42]

In the presence of H_2O_2, the V_2O_5 nanowires form a surface peroxo complex as demonstrated by EPR in Chapter 5. This peroxo complex undergoes nucleophilic attack by the halide (I^-) yielding the highly reactive oxidant species hypoiodous acid (HOI) that is released into solution (Scheme 6.1, blue dashed box).[43] Once hypoiodous acid is released into solution it will first (Scheme 6.1, red dashed box) oxidize the dopamine to dopaquinone. Normally, in biological systems this process is carried out by the enzyme tyrosinase where two copper atoms are present in the active site which react with the dioxygen to form a highly reactive intermediate that oxidizes the substrate.[44] The oxidized dopamine induces cyclization and formation of a colored intermediate named dopachrome (light pink). According to our experiments dopachrome is not formed when one of the components (V_2O_5 nanowires, KI and H_2O_2) in the catalytic system is absent. Subsequent formation of the black precipitate requires the iodination of the orange compound (dopachrome) at the activated ortho positions in the aromatic rings. The same chemical species and also a black precipitate were formed when L-dopa was used corroborating that the iodination reaction targets the aromatic ring and not the aliphatic chain. Presumably the double iodination of the aromatic ring induces instability of the electronic system in the ring. As iodide is a good leaving group, the halogen is released and radicals are formed. In the final step, a radical polymerization occurred leading to the formation of biopolymer (black precipitate) similar to melanin (Scheme 6.1, purple box). These small biopolymers probably assemble via π-stacking into nanoscale structures (nanoplatelets) of several layers and then cluster together via van der Waals interactions by a

longitudinal arrangement of the nanoplatelets and formation of fibril-like structures[36] as observed by SEM/TEM.

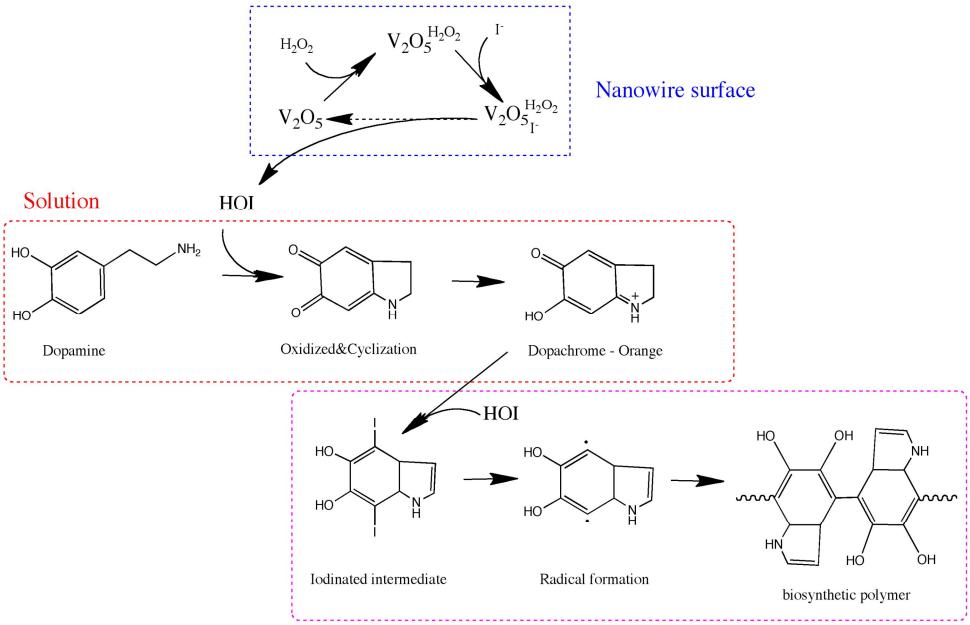

Scheme 6.1 Proposed mechanism for the formation of the melanin-like biopolymer by the catalytic action of V_2O_5 nanowires. A vanadium peroxo intermediate is formed that reacts with iodide forming an oxidative species (HOI) which oxidizes dopamine and which cyclizes. After iodination radical species are generated that initiate a polymerization reaction that leads to the formation of melanin.

Brominating activity of V_2O_5 nanowires and application in antifouling paint formulations

Investigation of the bromination activity was accessed by using 2-monochlorodimedone (MCD) assay as described for V-HPOs.[45] In the presence of different concentrations of V_2O_5 nanowires (0-0.03 mg/mL), Br^-(1 mM) and H_2O_2 (10 μM), a linear dependence of the rate of MCD bromination with the V_2O_5 nanowires concentration was observed (Figure 6.5, blue diamonds). Under identical experimental conditions, replacement of the nanowires by bulk V_2O_5, showed a significantly smaller bromination activity (Figure 6.5, green triangles) highlighting the advantage of nanostructured material and that this inorganic system can promote the bromination activity under aqueous, mild conditions in contrast with other functional inorganic V-HPO biomimetic models where harsh conditions (low pH) or organic solvents must be used.[46]

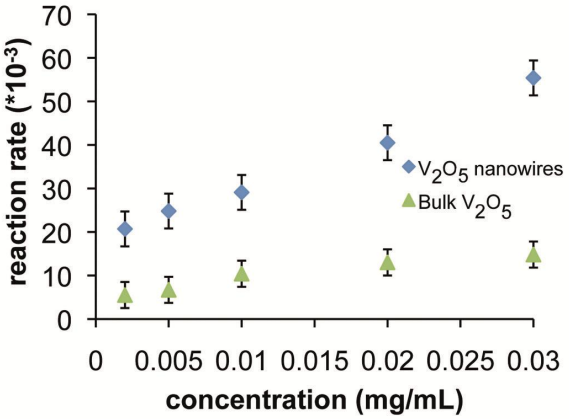

Figure 6.5 Concentration dependence of bromination activity of the V_2O_5 nanowires (blue diamonds) and bulk V_2O_5 (green triangles), determined by measuring the initial reaction rates of the MCD bromination from absorption at 290 nm for 180 s at 25 °C in the presence of constant concentrations of Br_2 (1 mM), H_2O_2 (10 mM), MCD (50 mM) and at constant pH (100mM Tris-SO_4 buffer, pH 8.3). A fourfold difference in activity of the nanoscale and bulk V_2O_5 indicates that the higher surface area of the nanostructured material is required to achieve higher catalytic efficiency.

We independently varied the concentrations of H_2O_2 (0 - 300 µM) and the concentrations of Br^- (0 - 5 mM) while keeping the concentrations of the remaining components constant. A typical Michaelis-Menten behavior towards both H_2O_2 and Br^- was observed (Figure 6.6A and B). At higher concentrations of Br^- (> 1mM), we observed a strongly inhibiting non-competitive effect of Br^-, equally observed for the V-HPOs from *A. nodosum*, *M. pyrifera*, *F. distichus*[47] and V-CPO from *C. inaequalis*.[48] As such inhibition is unexpected for an inorganic nanoparticle, we determined the steady state kinetics in a phosphate buffer (pH 8.0) where this effect did not occur (Figure S25, supporting information) suggesting that the buffer plays an important role in the catalysis. V_2O_5 nanowires can tolerate higher H_2O_2 concentrations without a reduction of their catalytic activity (Figure 6.6B) in contrast to the heme-containing chloroperoxidase from *Caldaromyces fumago*.[49]

Based on Lineweaver-Burk linearizations (Figure S26, supporting information), we determined the K_m values of ~10 µM for H_2O_2 and 0.2 mM for Br^- (it is not possible to obtain more accurate values for H2O2 because its minimum concentration is ~5 µM, leading to maximal changes of ~0.1 in absorbance in MCD at 290 nm). These kinetic parameters values fall within the same order of magnitude as those found for the biological samples *C.*

inaequalis V-CPO mutant (K_{mH2O2} 16 µM, K_{mBr-} 3.1mM) and *A. nodosum* V-BPO (K_{mH2O2} 22 µM, K_{mBr}- 18.1mM).[45] The V_2O_5 nanowires mediate the bromination of MCD in the presence of H_2O_2 and Br^- with a V_{max} of $7.3x10^{-10}$ M s^{-1} from which a turnover frequency (k_{cat}) of $7.3x10^{-6}$ s^{-1} could be determined. In comparison with the values determined for the *C. inaequalis* V-CPO mutant ($4.3x10^{-2}$ M s^{-1}, 100 s^{-1}, pH 8.0)[50] and *A. nodosum* V-BPO ($2.8x10^3$ $M^{-1}s^{-1}$, 50 s^{-1}, pH 7.9)[45] and inorganic functional V-HPOs biomimetic models such as $VO(O_2)$(Hbpg) (21 $M^{-1}s$, $10^{-3}s^{-1}$, pH<2)[51] and *cis*-dioxovanadium(V) (4.1 s, $2.3x10^{-2}$ s^{-1}, pH acidic)[52,53] these values are significantly lower. Worth to note that although the previously reported inorganic compounds show second order rate constant for oxidative bromination, they require strongly acidic conditions (pH<2) and/or non-aqueous solutions (acetonitrile) and do not show saturation kinetics. A pH optimum of pH 8.3 for V_2O_5 nanowires bromination activity was determined by varying the pH from 4 to 10 (Figure 6.6C). Using different buffer compositions with the same pH, we observed significant differences in the catalytic activity, suggesting that buffer composition strongly influences the stability of the peroxo complex formed at the nanowires' surface. (Chapter 5) We accessed the stability of V_2O_5 nanowires catalytic activity in a long-term exposition to H_2O_2/Br^- to ensure at least one catalytic turnover (reaction rate ~ 0.05 µM HOBr *per minute*). Figure 6.6D shows that the catalytic activity of the V_2O_5 nanowires remains stable throughout several catalytic cycles.

In the absence of an organic acceptor, singlet oxygen ($^1O_2$) is formed in the course of the reaction, decaying afterwards to a stable triplet state ($^3O_2$).[52,53] The decaying process was monitored by chemiluminescence at 1268 nm ($pH^{app}8.3$)[54,55] and by means of O_2-specific electrode. We observed an increase of the chemiluminescence after 30 s reaching a maximum after 75 s and dropping subsequently (Figure S27, supporting information) demonstrating that the H_2O_2 reacts with HOBr to form $^1O_2$. However, $^1O_2$ formation may compete with the reaction of HOBr for MCD, thereby lowering the MCD bromination rate and becoming a function of MCD concentration.[26,56] Additional experiments showed that the MCD bromination rate mediated by V_2O_5 nanowires is independent of the MCD concentration (pH 8.3), i.e., MCD still acts as a scavenger for HOBr (Figure S28, supporting information). We measured the rate of $^3O_2$ formation to be 0.05 µM min^{-1} in agreement with HOBr formation rate. Figure 6.6D left inset shows $^3O_2$ formation (bubbles) in the reaction vessel. A representative TEM image (Figure 6.6D right inset) shows that the nanowire morphology remained unchanged after long-term exposure. Figure 6.6E shows a mechanistic proposal for the bromination activity of V_2O_5 in the presence of Br^- and H_2O_2 based on the crystal structure

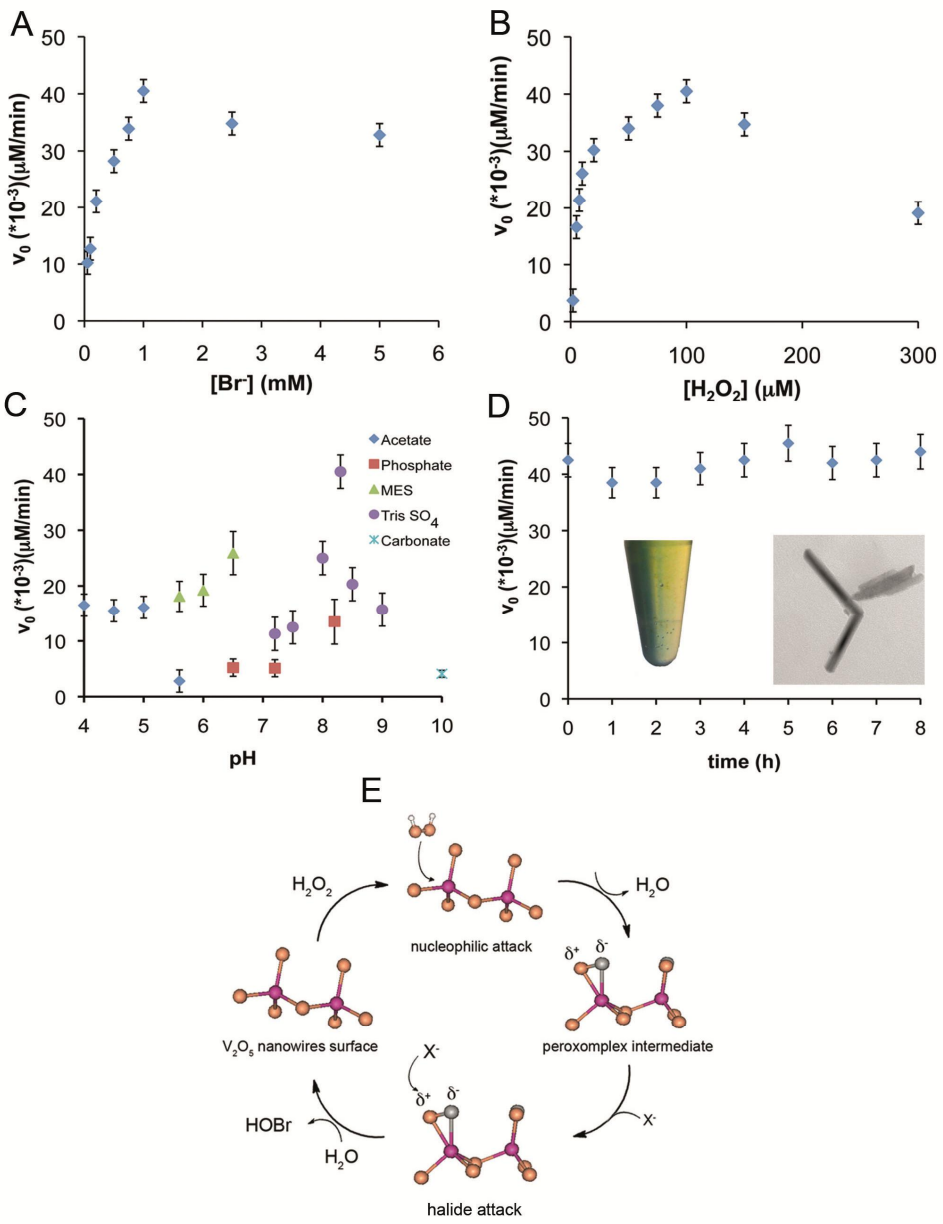

Figure 6.6 Steady-state kinetics of the V_2O_5 nanowires. (A) Variation of the H_2O_2 concentration (0-300 μM) while keeping the V_2O_5 nanowires (0.02 mg/mL), the Br^-(1mM) and the MCD (50 μM) concentrations constant. (B) Variation of the Br^- concentration (0-5 mM) while keeping the V_2O_5 nanowires (0.02 mg/mL), H_2O_2 (5 μM) and MCD (50 μM) concentrations constant. A Michaelis-Menten behavior was observed with a clear inhibition at values >100 μM for H2O2 and >1 mM for Br^-. (C) pH dependence (4-10) of the bromination reaction rate catalyzed by the V_2O_5 nanowires determined by using different buffer compositions and maintaining the reactant concentrations constant [V_2O_5 nanowires (0.02 mg/mL), Br^- (1mM), H_2O_2 (10 μM) and MCD (50 μM)]. (D) Stability of V_2O_5 nanowires in long-term. Left inset: digital image of reaction vial where bubbles can be observed as consequence of singlet oxygen ($^1O_2$) formation. Right inset: representative TEM image of V_2O_5 nanowires after 8h reaction. No change in surface morphology was observed. (E) Proposed catalytic bromination mechanism by the catalytic activity of the V_2O_5 nanowires.

of V_2O_5 (as seen in Chapter 5) and the kinetic parameters. The exposed lattice planes of the V_2O_5 nanowires have local vanadium coordination geometry similar to that of the active site of the V-HPOs (e.g. a terminal vanadyl oxygen atom and additional oxygen atoms bridging several vanadium centers). Thus the catalytic activity is related to those surface sites. The vanadium atoms act as reaction sites where the formation of the intermediate peroxo species occurs as indicated by the low K_m value of H_2O_2. The formation of these peroxo species has been considered an essential step of the oxidation activity, and its reactivity is crucial for the catalytic activity of both, V-HPOs[57] and the V_2O_5 nanowires (Figure 6.6C).At the active site of the enzyme, the reactivity of the peroxo complex has been attributed to an electron withdrawing effect of the vanadium and the interaction of one of oxygen atoms of the peroxide with an amine group of a lysine residue (Lys^{353} in *C. inaequalis*) that polarizes the bound peroxide and decreases the electron density on the other peroxide oxygen atom. In this way, the halide ions (X^-) can perform a nucleophilic attack on the more susceptible, less electron-rich oxygen atom of the bound peroxide group thereby promoting the formation of the corresponding hypohalous acid (Figure 6.6E). In the absence of an organic acceptor hypohalous acid (HOX) may react with another molecule of hydrogen peroxide to yield singlet oxygen ($^1O_2$). Based on the our results of kinetics in different buffer, we propose that the buffer system also plays an important role for the reactivity of the peroxo intermediate in the V_2O_5 surface-catalyzed bromination.

We evaluated the antibacterial activity of the V_2O_5 nanowires resulting catalytic activity at the optimal pH against Gram negative (*E. coli*) and Gram positive (*S. aureus*) bacteria. We observed a significant decrease of the bacterial growth - 78% for *E.coli* and 96% for *S. aureus* - in the presence of V_2O_5 nanowires (0.075 mg/mL), Br^- (1 mM) and H_2O_2 (10 μM) when compared with bacteria grown in the absence of additives. In the control experiments [Br (1mM)/H_2O_2(10 μM) or V_2O_5 nanowires (0.075 mg/mL)] minor suppression effect on bacterial growth was observed, i.e., ~28% and 13% (*E. coli*) or 5% and 8% (*S. aureus*) indicating that synergetic effect between the V_2O_5 nanowires, H_2O_2 and Br^- is required for strong antibacterial activity (Figure S29A and B). Figure 6.7 shows representative digital images after aliquot transfer and incubation for 8 h at 37ºC of bacterial cells with and without V_2O_5/Br^-/H_2O_2 to the respective culture plates (additional controls in Figure S29 C-F). A clear difference in the number of bacterial colonies is observed in agreement with the growth curves. (Figure S29A and B) Careful observation of the Mannitol Salt Phenol Red Agar plate after aliquot transfer and incubation shows a color change from red to slighty purple. This is

attributed to a reaction between HOBr and phenol red contained in bacterial growth medium as demonstrated (Figure S30), lending support to the activity displayed by V_2O_5 nanowires.

We tested the bromination activity of the V_2O_5 nanowires under realistic sea conditions. V_2O_5 nanowires are able to catalyze, in seawater, the formation of HOBr in a concentration dependent manner (Figure S31A) with V_{max} of $2.1x10^{-10}$M $s^{-1}$and k_{cat} of $2.1x10^{-6}$ s^{-1}. From Lineweaver-Burk linearizations, we calculated K_m values of ~10 µM for H_2O_2.A Km value for Br^- could not be obtained due to a strong inhibition by the bromide. Given that V_2O_5 nanowires display a bromination activity in realistic sea conditions, we assessed the acute toxicity (24h LD_{50}) exerted by different concentrations of V_2O_5 nanowires on a marine biota model (*A. franciscana* instar II-III larvae). We determined, in parallel, the acute toxicity of different concentrations of IMO (International Maritime Organization) approved compounds (Zn and Cu pyrithiones – Zn/CuPT). From the dose response curves (Figure S32), we found acute toxicity values of 0.0012, 0.085 and 1.2 mg/mL for CuPT, ZnPT and V_2O_5 nanowires, respectively. In terms of marine biota toxicity, V_2O_5 nanowires are 14 and 1000-fold less toxic than ZnPT and CuPT, respectively, representing an alternative to commercially available products.

We developed a formulation of V_2O_5 nanowires with a commercially available silicone alkyd based paint (yielding a grayish color) and applied it onto stainless steel half surfaces (Figure 6.8A, right half). For direct comparison, the remaining half was treated with paint containing no additives (Figure 6.8A, left half). The doubly painted stainless steel plates were immersed into either *E. coli* or *S. aureus* suspension for 4 d at 37ºC where the substrate (Br^- and H_2O_2) concentration was kept constant. After 4 d, the surfaces were analyzed for their bacterial surface density/adhesion using fluorescence microscopy. The fluorescence microscopy images show a total absence of bacterial adhesion (both strains) on the halves that were treated with paint formulation containing V_2O_5 nanowires (Figure 6.8B and C, right images). In contrast, in the absence of V_2O_5 nanowires (only paint) a dense bacterial population was observed for both control samples (Figure 6.8B and C, left images). As controls, we used the same experimental setup but without adding substrates. In this case, high bacterial adhesion/density was observed on both halves of the surface (Figure S33).

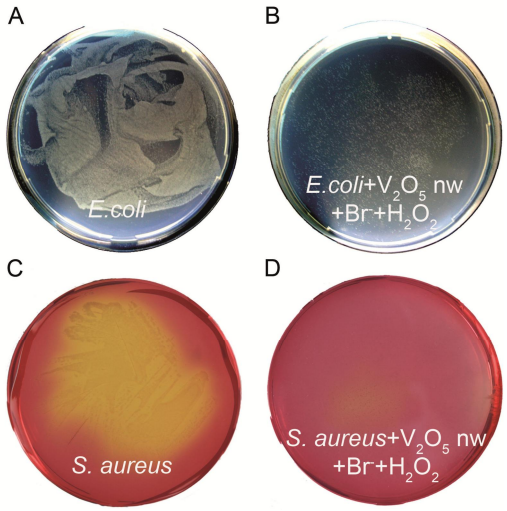

Figure 6.7 Representative digital images showing the influence of the catalytic activity of V_2O_5 nanowires on the growth of Gram positive (*S. aureus*) and Gram negative (*E. coli*) bacteria. After co-incubation for 180 min at 37ºC, the bacterial cells were platted in the respective medium (Agar-LB for *E. coli* and Mannitol Salt Phenol Red Agar for *S. aureus*) medium and left to incubate for 8h at 37ºC. Gram negative: (A) E. coli alone; (B) E. coli co-incubated with V_2O_5 nanowires (0.075 mg/mL), Br^- (1 mM) and H_2O_2 (10 µM). A significant decrease on the bacterial population is observed. Gram positive: (C) *S. aureus* only; (D) *S. aureus* co-incubated with V_2O_5 nanowires (0.075 mg/mL), Br^- (1 mM) and H_2O_2 (10 µM). The color change in (C) from red to yellow indicates the presence and growth of *S. aureus*. By comparison a significant decrease in the bacterial population (90%) can be observed.

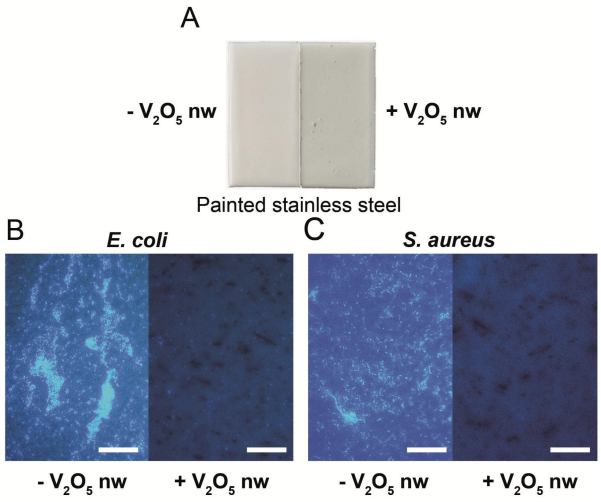

Figure 6.8 Application of V_2O_5 nanowires in marine paint with antibacterial/antifouling properties. (A) Digital image of a stainless steel plate (2x2cm) covered with a commercially available paint for boat hull without (-V_2O_5 nanowires, white left half) and with V_2O_5 nanowires (+ V_2O_5 nanowires, greenish right half). (B) and (C), Bacterial cell density/adhesion evaluated by fluorescence microscopy on the different halves of painted stainless steel plates after exposure to bacterial suspensions. The images were acquired after 4 days of incubation at 37ºC in the presence of Tris-SO_4 (100 mM, pH 8.3), Br^- (1 mM) and H_2O_2 (10 µM). The dark spots on the right sides show aggregates of V_2O_5 nanowires. A significant decrease of bacterial cell adhesion is clearly observed (e.g. absence of stained bacterial cells). Scale bar: 100 µm

We assessed the long-term stability of the catalytic activity of the V_2O_5 nanowires and V leaching under simulated marine environment conditions by immersing painted stainless steel plates in seawater for 9 weeks (set up in Figure S34A-B). The painted plates showed no signs of degradation or peeling after 9 weeks (Figure S34A). We tested the antibacterial efficiency against *E. coli* and verified that the plates painted with V_2O_5 nanowires showed complete absence of adhered bacterial cells (Figure S34D) whereas the painted stainless steel plates (without V_2O_5) exhibited a high surface coverage of bacterial cells (Figure S34C). In order to analyze V leaching, we periodically removed aliquots (week 1, 5, 7 and 9) and determined the V content by ICP-MS. The collected samples were treated for salt removal using a purification step. Based on a calibration curve [concentration(ppb) *vs.* $^{51}V/^{197}Au$ ratio] (Figure S35B), we determined the V content at week 1, 5, 7 and 9 of 5.95, 5.04 , 5.77 and 1.97 ppb respectively (see Figure S35C). These values fall within the same order of magnitude as the actual average V concentration in seawater (e.g. 35 nM)[58] representing no environmental threat. We exposed the painted stained steel plates to natural conditions to assess their efficiency *in situ* (lagoon with tidal waters directly connected to the Atlantic Ocean). Figure 6.9 A and B show the plates immediately after application (t = 0). The boat remained in seawater and was landed after 60 d. On the untreated plates an increased biofouling was observed indicating that during the 60 d period bacterial growth, that affects millions of boats worldwide, proceeded without delay; algae covered the stainless steel plates that did not contain additives (Figure 6.9C). On the other hand, the stainless steel plates treated with paint containing V_2O_5 nanowires showed no indication of biofouling (Figure 6.9D).

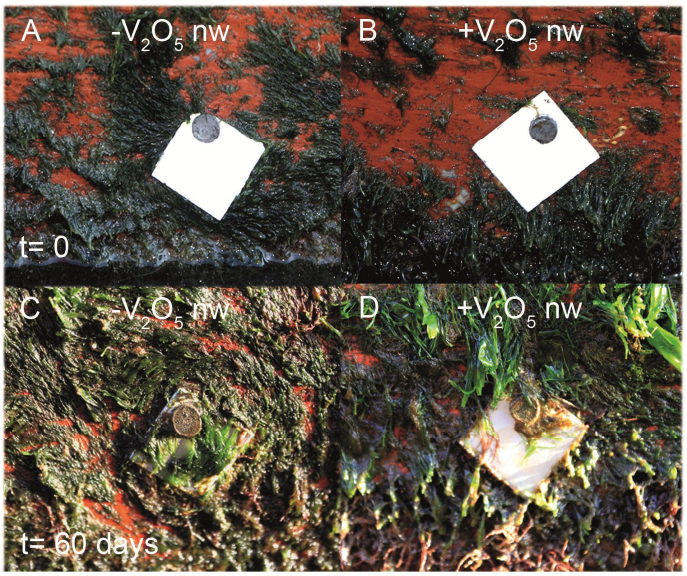

Figure 6.9 Summary of *in situ* experiments. Digital image of a stainless steel plate (2x2cm) covered with a commercially available paint for boat hull without ($-V_2O_5$ nw) and with V_2O_5 nanowires ($+V_2O_5$ nw). The plates were fixed to a boat hull. (A) and (B), Immediately after fixation both stainless steel plates (with and without V_2O_5 nanowires showed a clean surface. The boat was kept in seawater (lagoon with tidal water directly connected to the Atlantic Ocean). After 60 days, the boat was landed. (C) The painted stainless steel plates containing no V_2O_5 nanowires suffered from severe natural biofouling. (D) Plates with V_2O_5 nanowires showed a complete absence of biofouling.

6.3 Conclusions

In conclusion, we have shown that water dispersible V_2O_5 nanowires prepared by a hydrothermal method shown in Chapter 5, have iodinating activity which was demonstrated by a colorimetric assay using the classical substrate for V-HPO thymol blue as was well as by mass spectrometry. V_2O_5 nanowires also catalyze the formation of a biopolymer from dopamine. This product resembles melanin chemically and morphologically. The formation of biopolymers promotes the self-assembly into fibrils by π-stacking.

It was also shown that V_2O_5 nanowires work also as functional inorganic analogues of bromoperoxidase under laboratory (pH 8.3) as well as seawater conditions displaying a similar mechanism and forming HOBr and $^1O_2$ species, in the absence of organic acceptors. Consequently, this intrinsic activity exerts a strong antibacterial activity against both Gram negative (*E. coli*) and Gram positive (*S. aureus*) bacteria. We also showed that our system is less toxic that IMO approved antifouling products towards marine biota. The catalytic activity

of V_2O_5 nanowires upon incorporation into paint formulations is preserved and prevents, under realistic sea conditions, the formation of biofouling. Inspired in Nature – natural defense mechanism of seaweeds against biofouling - we developed stable, water insoluble, non-toxic, inexpensive mimetic approach that can replace enzymatic preservation systems (or conventional chemical biocides) by new antibacterial, antifouling and disinfection formulations towards a sustainable conservation concept. V_2O_5 nanowires can rival natural enzymes due to their easy preparation, a cost-effective synthetic platform for the production of biopolymers (melanin) or antifouling surfaces using sustainable products may become available in the future. Furthermore, the halogenation reaction can be further extended to other applications like, synthesis of industrially important halogenated compounds due to the reaction flexibility and stability of the inorganic product.

6.4 Experimental Section

Synthesis of V_2O_5 nanowires. V_2O_5 nanowires were synthesized as described elsewhere in Chapter 5. In brief, 8 mmol of $VOSO_4.nH_2O$ (Alfa Aesar, purity >99.9%) and 3.5 mmol of $KBrO_3$ (Alfa Aesar, purity > 98%) were dissolved in 30 mL of distilled water and stirred for 30 minutes at room temperature. Nitric acid (TraceSELECT® Ultra, for trace analysis, ≥65%, Fluka Chemie AG, Basel, Switzerland) was added dropwise under stirring until pH reached 2. The solution was transferred to a Teflon-lined stainless steel autoclave, which was maintained at 180°C for 32h. After cooling to room temperature the solution was filtered and washed several times with distilled water and ethanol.

"Iodoperoxidase" activity. Iodination activity of the V_2O_5 nanowires was determined colorometrically using thymol blue (TB) (Cat. No. 32728, Fluka, Steinheim, Germany) as described for vanadium haloperoxidases (V-HPO).[27] A stock solution of TB (25 mM) was prepared in distilled H_2O/dimethyl sulfoxide (DMSO) (4:1), and the assay carried out as follows. Typically, freshly prepared V_2O_5 nanowires (1 mg/mL prepared in distilled water) were added to a reaction mixture: Phosphate buffered saline solution (PBS, pH 8.0) and 40 mM potassium iodide (KI) (Cat. No. 60400, puriss. p.a., ACS reagent, ≥99.0% Sigma-Aldrich, Steinheim, Germany). For initiating the reaction, hydrogen peroxide (H_2O_2, 1 mM) was added to the sample. As a control, the reaction was carried out in the absence of V_2O_5 nanowires and H_2O_2 and in the presence of the bulk V_2O_5 (1mg/mL) (Cat.No. 14205, puriss.,

≥99%, Riedel-de Haën, Steinheim, Germany) and sodium orthovanadate (1 mM) (Cat. No. 450243, Sigma, Steinheim, Germany). The UV-Vis spectrum was recorded from 350 to 750 nm, at 25±0.5ºC, using a Cary 5G UV-Vis-NIR spectrophotometer (Varian, Inc., Palo Alto, CA, USA). The reactions were carried out at room temperature. The final compound, as well as the control experiment, were brought to dryness under vacuum, re-suspended in chloroform and analyzed by mass spectrometry.

Polymerization of dopamine. The reaction was carried out in aqueous solution (pH 8.0) near physiological conditions. Typically, the reaction mixture contained potassium iodide (40 mM), freshly prepared V_2O_5 nanowires (1 mg/mL dispersed in distilled water), and dopamine hydrochloride (10 mM) (Cat. No. DH8502, powder, Sigma, Steinheim, Germany) and for initiating the reaction, H_2O_2 (1 mM) was added. The reaction was followed by repeated scans (300-800 nm) every 5 min for a period of 140 min, at 25±0.5ºC, using a Cary 5G UV-Vis-NIR spectrophoto-meter. As a control, the reaction was carried out in the absence of V_2O_5 nanowires and H_2O_2 and in the presence of the bulk V_2O_5 (1 mg/mL) and sodium orthovanadate (1 mM). The samples were washed by centrifugation (5000 rpm, 5 min, RT) and distilled water, air-dried and analyzed by scanning electron microscopy (SEM), transmission electron microscopy (TEM) and FT-IR. Naturally occurring melanin (sepia melanin from cuttlefish *Sepia officinalis*) was purchased from Sigma (#M2649, Steinheim, Germany) and used as comparison for UV/Vis, FT-IR, TEM and electrical conductivity analysis.

Physical characterization. The products were characterized by TEM using a Philips 420 instrument with an acceleration voltage of 120 kV or a Philips TECNAI F30 electron microscope (field-emission gun, 300 kV extraction voltage). The final material was prepared by mixing dried precipitate with KBr in a mass ratio of ~ 1:1000 and characterized by FT-IR spectra (Mattson Instruments 2030 Galaxy-FT-IR spectrometer) operating in the wavelength range 4000-200 cm^{-1}. The samples were mounted on carbon stubs (carbon adhesive Leit-Tabs No.: G 3347 [Plano, Wetzlar; Germany]) and analyzed by scanning electron microscopy (Phenom, FEI, Eindhoven; Netherlands) operating at 0.5kV. Field desorption mass spectra (FD-MS) was obtained in MAT95 spectrometer (Finnigan, Thermo Scientific).

Conductivity measurements were carried out with a commercial four-point probe setup (Jandel Engineering Ltd., Linslade, UK) which was connected to a Keithley 6430 Source Meter (Keithley Instruments Inc.,Cleveland, Ohio, USA). The samples for the conductivity measurement were prepared by compressing 50 mg of the material to a circular pellet by a

hydraulic press with a force of 10 kN. The pellets had a diameter of 6 mm and a thickness of 2 mm. The measurements were made at room temperature (25±2ºC).

Bromination activity of the V_2O_5 nanowires. The bromination activity was measured for 180 s at 25±2°C either in 100 mM of Tris-SO_4 buffer at pH 8.3 or sterile filtered seawater by varying the concentration of the V_2O_5 nanowires (0-0.03 mg/mL) and keeping constant the MCD concentrations (50 μM, ε_{290nm}=19.9 $mM^{-1}cm^{-1}$), KBr (1mM) and H_2O_2 (10 μM).[45] H_2O_2 concentration was calculated spectrophotometrically (ε_{240nm}=43.6 $M^{-1}cm^{-1}$).[59] As controls, bulk V_2O_5 (0-0.03 mg/mL in 100 mM Tris-SO_4 buffer pH 8.3) was used and the MCD concentrations (5-75 μM) varied keeping the other reagents constant.

Determination of bromination kinetic parameters. Two independent sets of experiments either in Tris-SO_4 buffer (100 mM, pH 8.3) or seawater were performed: *(i)* H_2O_2 concentration was varied (0 to 300 μM) while keeping the concentration of Br^- (1 mM), V_2O_5 nanowires (0.02 mg/mL) and MCD (50 μM) constant; *(ii)* Br^- concentrations were varied from 0 to 5 mM while keeping H_2O_2 (10 μM), V_2O_5 nanowires (0.02 mg/mL) and MCD (50 μM) concentrations constant. The values were fit to the Michaelis-Menten model and kinetic parameters determined by Lineweaver-Burk linearizations.

Measurement of $^1O_2$ and $^3O_2$ production. Singlet oxygen ($^1O_2$) production was measured by chemiluminescence (emission at 1268 nm) as described.[55] All reagents were prepared in deuterium oxide (D_2O) and adjusted to pH^{app} 8.3. The rate of triplet oxygen ($^3O_2$) production was measured using an YSI Oxygen Electrode System at room temperature under continuous stirring. The electrode was 2-point calibrated using distilled water for 100% air-saturated solution (240 μM) and excess of sodium dithionite (anaerobic conditions). The formation of $^1O_2$ and $^3O_2$ was measured in Tris-SO_4 buffer (100 mM, pH 8.3) containing V_2O_5 nanowires (0.1 mg/mL) and Br^- (1mM) and H_2O_2 (1 mM).

pH measurements and stability assays. The following buffers were used for the different pH ranges: pH values 4-5.6, 100 mM sodium acetate buffer; pH values 5.6-7.2, 100 mM MES; pH values 6.5, 7.2 and 8.2 phosphate buffer; pH values 7.0 to 9.0, 100 mM Tris-SO_4 buffer; pH of 10, 10 mM carbonate buffer. The assays carried out as described above. The stability assays were carried out by incubating V_2O_5 nanowires (0.2 mg/mL), of Br^- (1 mM) in Tris-SO_4 buffer (100 mM, pH 8.3) and H_2O_2 (100 μM) and left for 480 min at room temperature. Aliquots (25 μL) were taken at selected time intervals and bromination activity accessed. Afterwards, the morphology of V_2O_5 nanowires was analyzed under TEM.

Vanadium leaching by ICP-MS. Samples collected at certain time points were treated with ionic exchange (SPR-IDA) according to the described protocol.[60] Concentrations of V (1, 2, 4, 6, 8 and 10 ppb) were freshly prepared and an Au solution (10 ppb) added to all solutions. The calibration curve was built by plotting concentration(ppb) *vs.* $^{51}V/^{197}Au$ ratio. Measurements were performed in the medium mass resolution mode (mass resolution R = 4000) of a Thermo Element2 ICP mass spectrometer. Operating parameters were RF power = 1260 W, cool gas flow rate = 16 l min^{-1}, carrier gas (Ar) flow rate = 0.91 L min^{-1}, samples per peak = 20, sample time = 0.01 s, time per scan = 2.2 s, number of scans = 30.

Suspension assay and bacterial inactivation. *E. coli* and *S. aureus* were incubated in LB medium and Brain Heart Infusion Broth, respectively, with V_2O_5 nanowires (0.075 µg/mL), Br^- (1 mM) and H_2O_2 (10 µM) for 180 min at 37ºC. The optical density at 592 nm was measured at different time points. As controls, either V_2O_5 nanowires (0.075 µg/mL) or H_2O_2/Br^- (1mM/10 µM) were added to the cultures. Subsequently, the 50 µL of *E. coli* and *S. aureus* were platted on Agar-LB medium and Mannitol Salt Phenol Red Agar plates, respectively and left to grow for 8 h at 37ºC.

Bioassays. Serial dilutions (2.5, 0.625, 0.156, 0.039 and 0.009 mg/mL) of the stock solutions of 1-hydroxypyridine-2-thione zinc and cupper salt (ZnPT/CuPT) (10 mg/mL)[61] and V_2O_5 nanowires (10 mg/mL) were prepared in 10% DMSO and seawater (ASTM Standard Guide E1440-91) and incubated with hatched instar II-III larvae of the brine shrimp *A. franciscana* for 24h, at 25ºC under dark conditions in accordance with the standard operational conditions prescribed for marine environments.[62] The toxicity was evaluated on basis of total imobility of the larvae during 10 s. Dose response curve was built and the acute toxicity values (LD_{50}) determined using the Probit linearization method.

Stability and *in situ* experiments. Commercially available silicone alkyd based paint (1mL) was mixed with V_2O_5 nanowires (5 mg), applied onto a stainless steel plates (2x2 cm) and exposed to bacterial suspension of either *E. coli* or *S. aureus* supplemented with Br^- (1 mM) and H_2O_2 (10µM) for 4 days at 37ºC. As controls, painted surfaces without and with V_2O_5 nanowires were used. In the former case, no substrates (e.g. Br^- and H_2O_2) were added. Bacterial cells were stained with DAPI (1µg/mL) and the fluorescence analysis was performed using Olympus AHBT3 light microscope, together with an AH3-RFC reflected light fluorescence attachment. For stability experiments, painted plates were immersed in seawater for 9 weeks at room temperature with gentle stirring. At week 1, 5, 7 and 9, 5mL aliquot was removed and kept at +4ºC. Br^- (1 mM) and H_2O_2 (10 µM) were weekly added.

Vanadium content was analyzed by ICP-MS and the surfaces assayed for antibacterial activity (*E. coli*). For *in situ* experiments, painted plates (with and without V_2O_5 nanowires) were fixed to a boat hull moored into a lagoon with tidal waters connected to the Atlantic Ocean (Foz do Arelho, Portugal) and left for 60 days (from May to end of June). The boat was removed from the seawater and the images captured using a normal digital camera.

6.5 References

1. R. Renirie, A. Dewilde, C. Pierlot, R. Wever, D. Hober, J.-M. Aubry, *J. Appl. Microbiol.*, **2008**, *105*, 264.
2. J. M. Raaijmakers, M. Vlami and J. T. de Souza, *Antonie van Leeuwenhoek*, **2002**, *81*, 537.
3. E. Montesinos, *FEMS Microbiol. Lett.*, **2007**, *270*, 1.
4. F. C. Odds, A. J. P. Brown and N. A. R. Gow, *Trends Microbiol.*,**2003**, *11*, 272.
5. W. Hemrika, R. Renirie, S. Macedo-Ribeiro, A. Messerschmidt, R. Wever, *J. Biol. Chem.* **1999**, *274*, 23820.
6. P. Barnett, D.H. Simons, L.H. Simons, P.F. Ter Steeg and R. Wever, "Enzymatic antimicrobial compositions." Patent PCT, W095/27046.
7. T. T. Hansen and P.H. Nielsen, "Production of paperboard of improved strenght-by treating pulp with a phenol oxidizing enzyme system after completion of grinding and refining of logs." Patent W093/23606.
8. J. S. Martinez, G.L. Carroll, R.A. Tschirret-Guth, G. Altenhoff, D.R. Little, A. Butler, . *J. Am. Chem. Soc.* **2001**, *123*, 3289.
9. P. Coughlin, S. Roberts, C. Rush, A. Willetts, *Biotechnol. Lett.* **1993**, *15*, 907.
10. H. B. Ten Brink, A. Tuyman, H. L. Dekker, W. Hemrika, Y. Izumi, T. Oshiro, H. E. Schoemaker, R. Wever , *Inorg. Chem.* **1998**, *37*, 6780.
11. M. C. R. Franssen, H. C. van der Plas, *Adv. Appl. Microbiol.*, **1992**, *37*, 41.
12. R. Wever, W. Hemrika, in *Handbook of Metalloproteins*, ed. A. Messerschmidt, R. Huber, K. Wieghardt and T. Poulos, Wiley & Sons (England) Ltd., Chichester, 2001, pp. 1417–1428.
13. A. Messerschmidt, L. Prade and R. Wever, *Biol. Chem.*, **1997**, *378*, 309.
14. B. Duffy, A. Schouten, J. M. Raaijmakers, *Annu. Rev. Phytopathol.*, **2003**, *41*, 501.
15. G. Prota, *Melanins and Melanogenesis*, Academic Press, 1992.

16. R. E. Boissy, *Dermatol. Clin.*, **1988**, *6*, 161.
17. L. Zeise, L. B. Murr, R. M. Chedekel, *Pigm. Cell Res.*, **1992**, *5*, 132.

18. J. P. Bothma, J. de Boor, U. Divakar, P.E. Schwenn, P. Meredith, *Adv. Mater*. **2008**, *20*, 3539.
19. L. Hong, Y. Liu, J. D. Simon *Photochemistry and Photobiology* **2004**, *80*, 477.
20. M. Nicolai, G. Gonçalves, F. Natalio, M. Humanes, *J Inorg Biochem.* **2011**, *105*, 887.
21. S.A. Borchardt, et al. *Appl. Environ. Microbiol.* **2001**, *67*, 3174.
22. R. Wever, M.G. Tromp, B.E. Krenn, A. Marjani, M. van Tol, *Environ. Sci. Technol*. **1991**, *25*, 446.
23. P. Barnett, D. Hondmann, L.H. Simons, P.F. Ter Steeg, R. Wever, "Vanadium Haloperoxidases and their Uses", Patent WO/1995/027046.
24. R. Wever, H.L. Dekker, J.W.P.M. Van Schijndel, E.G.M. Vollenbroek, "Antifouling Paint Containing Haloperoxidase and Method to Determine Halide." Patent WO/1995/027009.
25. R. Weller, O. Schrems, *Geophys. Res. Lett*. **1993**, *20*, 125.
26. H. S. Soedjak, J.V. Walker, A. Butler, *Biochemistry* **1995**, *34*, 12689.
27. E. Verhaeghe, D. Buisson, E. Zekri, C. Leblanc, P. Potin and Y. Ambroise, *Anal. Biochem.*, **2008**, *379*, 60.
28. L. A. Burzio, J. H. Waite, *Protein Sci*., **2001**, *10*, 735.
29. H. Mason, E. W. Peterson, *J. Biol. Chem*., **1955**, *212*, 485.
30. H. Lee, S. M. Dellatore, W. M. Miller and P. B. Messersmith, *Science*, **2007**, *318*, 426.
31. C. M. R. Clancy, J. B. Nofsinger, R. K. Hanks and J. D. Simon, *J. Phys. Chem. B*, **2000**, *104*, 7871.
32. D. H. Ellis, D. A. Griffiths, *Can. J. Microbiol*., **1974**, *20*, 1379.
33. P. Schaeffer, *Arch. Biochem. Biophys*., **1953**, *47*, 359.
34. S. Bartnicki-Garcia, E. Reyes, *Arch. Biochem. Biophys*., **1964**, *108*,125.
35. I. Chet, Y. Henis, R. Mitchell, *Can. J. Microbiol*., **1967**, *13*, 137.
36. J. D. Simon, *Acc. Chem. Res*., **2000**, *33*, 307.
37. N. F. Mott, E. A. Davis, *Electronic Processes in Non-Crystalline Materials*, Clarendon Press, Oxford, 1979.
38. D. N. Moses, J. H. Harreld, G. D. Stucky and J. H. Waite, *J. Biol. Chem.*, **2006**, *281*, 34826.

39. P. R. Crippa, V. Cristofoletti and N. Romeo, *Biochim. Biophys. Acta, Gen. Subj.*, **1978**, *538*, 164.

40. J. E. Mcginness, P. Corry and P. Proctor, *Science*, **1974**, *183*, 853.

41. M. M. Jastrzebska, H. Isotalo, J. Paloheimo, H. Stubb, B. Pilawa, *J. Biomater. Sci., Polym. Ed.*, **1996**, *7*, 781.

42. M. M. Jastrzebska, H. Isotalo, J. Paloheimo, H. Stubb, *J. Biomater. Sci., Polym. Ed.*, **1995**, *7*, 577.

43. M. G. Almeida, M. Humanes, R. Melo, J. A. Silva, J. J. R. Frausto da Silva and R. Wever, *Phytochemistry*, **2000**, *54*, 5.

44. J. Duchon, T. Fitzpatrick, M. Seiji, in *Yearbook of Dermatology*, ed. A. Kopf and R. Andradeeds, Yearbook Publishers, Chicago, 1968, pp. 6–33.

45. E. de Boer, R. Wever, *J. Biol. Chem.* **1998**, *263*, 12326.

46. D.C. Crans, J.J. Smee, E. Gaidamauskas, L. Yang, *Chem. Rev*. **2004**, *104*, 849.

47. A. Butler, *Vanadium haloperoxidases*. In *Bioinorganic Catalysis*. 2nd ed, Reedijk, J. & Bouwman, E. (Eds.), Marcel Dekker, 1991, New York, USA, chapter 5, pp. 55-79.

48. W. Hemrika, R. Renirie, H.L. Dekker, P. Barnett, R. Wever, *Proc. Natl. Acad. Sci. USA* **1997**, *94*, 2145.

49. A. N. Shevelkova, A.D. Ryabov, *IUBMB Life* **1996**, *39*, 665.

50. A. Butler, M.J. Clague, G.E. Meister, *Chem. Rev*. **1994**, *94*, 625.

51. G.J. Colpas, B.J. Hamstra, J.W. Kampf, V.L. Pecoraro, *J. Am. Chem. Soc*. **1996**, *118*, 3469.

52. R. I. de la Rosa, M.J. Clague, A. Butler, *J. Am. Chem. Soc.* **1992**, *114*, 760.

53. M.J. Clague, A. Butler *J. Am. Chem. Soc*. **1995**, *117*, 3475.

54. A.G.J. Ligtenbarg, R. Hage, B.L. Feringa, *Coord. Chem. Rev.* **2003**, *237*, 89.

55. R. Renirie, C. Pierlot, J.-M. Aubry, A.F. Hartog, H.E. Schoemaker, P.L. Alsters, R. Wever. *Adv. Synth. Catal.* **2003**, *345*, 849.

56. H.S. Soedjak, A. Butler, *Biochim. Biophys. Acta.* **1991**, *1079*, 1.

57. Z. Hasan, R. Renirie, R. Kerkman, H.J. Ruijssenaars, A.F. Hartog, R. Wever, *J. Biol. Chem.* **2006**, *281*, 9738.

58. A. Butler, *Science* **1998**, *281*, 207.

59. R.F. Beers, I.W. Sizer, *J. Biol. Chem.* **1952**, *195*, 133.

60. D. Wang, S.A. Sañudo-Wilhelmy, *Mar. Chem.* **2008**, *112*, 72.

61. M. Marcheselli, C. Rustichelli, M. Mauri, *Environ. Toxicol. Chem*. **2010**, *29*, 2583.
62. Creasel (1990). AR1OXKI1 M: Artemia Toxicity Screening Test for Estuarine and Marine Waters, Standard Operational Procedure, V071090

CHAPTER 7

Conclusions and Outlook

The present dissertation demonstrates new approaches to the development of bioinspired materials, using mainly two different approaches. On one side available biomolecules involved in the formation of inorganic materials in vivo (silicatein, silintaphin) or approximate mimics (spermine) were used as catalysts and templates to synthesize new composite (organic-inorganic) nano-materials. On the other side, synthetic inorganic nanoparticles (V_2O_5) were demonstrated to be mimics of natural enzymes (peroxidase, haloperoxidase). These design approaches brings organic functional molecules and inorganic nanoparticles in a common platform, to be used in the development of new materials with extreme potential in technical applications like in antifouling products or self-cleaning surfaces. In the first part of this thesis a introduction on concepts of bioinspired and biomimetic material synthesis and properties was given, with special emphasis on the most recent developments in literature. In the second part of this work the idea of bioinspired mineralization was demonstrated. Initially a new approach on surface functionalization of

metal oxides with proteins was demonstrated using a recombinant silicatein-α with a glutamate tag (Glu-tag). The protein was shown to bind directly to TiO_2 nanowires surfaces with no extra functionalization necessary. Furthermore it could be seen that the protein remains active in the formation of SiO_2 and ZrO_2 after surface immobilization, demonstrating that the functionalization process does not affect the tridimensional structure of the protein and its active site. In an attempt to try to mimic the mineralization matrix present in vivo, another protein was used – silintaphin-1. This protein interacts specifically with silicatein-α and so no extra functionalization was needed to attach silintaphin-1 to the silicatein-α functionalized TiO_2 nanowires. Using one protein or two proteins a fine-tunning of the coating of SiO_2 or ZrO_2 on the titania nanowires was achieved. It could be demonstrated that in the presence of both proteins an increase in silica or metal oxide deposition occurs. These ability to control the deposition of metal oxides by tunning the organic matrix is of special interest in materials where surface properties at the nanoscale are of extreme importance for the overall properties of the composites. This approach to create metal oxide coatings using biomolecules instead of harsh chemical synthesis can bring advantages also in several other bioapplications (implant materials, drug delivery, biosensors) by improving biocompatibility. Also, the synergistic effect of the several spicule protein matrix constituents was demonstrated, which may shed light into future work in the topic of artificial mineral formation.

The flexibility of silicatein-α in metal oxide synthesis was also demonstrated here by showing the synthesis of SnO_2 (cassiterite) under mild conditions (room temperature, neutral pH). It was demonstrated that the protein takes an essential role in the control of the formed product due to its constraining effect on the particle size and at the same time in the stabilization of the particles surface. The immobilization of silicatein-α on glass surfaces was achieved with a simple functionalization method based on a NTA chelating ligand that allowed the protein to remain active after functionalization. This was shown by the deposition of a SnO_2 coating on the silicatein-functionalized glass. The SnO_2 coated glass surfaces reveal a high transparency thus indicating the potential of this synthesis approach in the development of materials with technological interest for example, in the production of transparent conductive oxide surfaces. Once again since this is a biocompatible synthetic approach, these surfaces could be further used in applications that involve interaction with physiological samples, for example.

The production of SnO_2 coatings could be further amplified by using a simplified approach based on the polyamines present in diatoms. In this case spermine was shown to be able to

induce the deposition of SnO_2 and by immobilizing the molecule on glass surfaces, dense coatings of the metal oxide could be achieved, under mild conditions. Furthermore the SnO2 coated surfaces were shown to have interesting physical-chemical properties when exposed to light. A hydrophilic/hydrophobic switching was observed as well as the production of radicals in solution when exposed to light. This material was applied to develop a self-cleaning surface that when exposed to light can degrade organic pollutants as well as kill any microbiological contaminants. We anticipate that this coating method can be generalized to several different types of surfaces just by adjusting the functionalization methods.

Further work in this bioinspired mineralization approach comprises further studies of other possible metal oxides or other materials that can be synthesized recurring to these biomolecules. Also in the particular case of silicatein and silintaphin, current studies are undergoing to determine the binding forces between these proteins. Also undergoing is the study of other different tags for silicatein, in particular a cysteine tag that would allow to further extend the functionalization flexibility for this molecules. In the case of spermine coated surfaces, preliminary work showed in fact that the deposition of SnO_2 could be achieve in several different surfaces resulting in self-cleaning products which can have extreme technological potential.

In part 3 of this work a different approach was taken, by creating inorganic nanoparticles of V_2O_5 that can imitate the activity of natural enzymes, like vanadium haloperoxidases. The V_2O_5 nanowires were synthesized using a simple hydrothermal synthesis, resulting in a nanocrytalline product, which is quite water dispersible. Initially it was shown that these nanowires had a peroxidase-like activity towards typical peroxidase substrates (ABTS, TMB) and it could be also demonstrated that the material has a Michaelis-Menten like kinetic profile in the oxidation of ABTS. The nanowires showed an optimum working pH of 4 like in the natural vanadium haloperoxidase. Furthermore it could be shown that the nanoparticles could carry out the oxidation reaction of ABTS mediated by H_2O_2 in several different solvents (up to 90% v/v), demonstrating the increased stability of the material when compared with the natural enzymes. Also the nanoparticles could be re-utilized after several catalytic cycles without significant loss of catalytic activity. Also the iodination activity of the V_2O_5 nanowires could be demonstrated by using a colorimetric assay with thymol blue as a reporter substrate. This iodination activity could be used to synthesize a melanin-like polymer with semi-conductive properties (as reported for natural melanin). On the other side the bromination activity of V_2O_5 nanowires could be demonstrated using monochlorodimedone

(MCD). The nanowires could be further applied in the development of antimicrobial and antifouling surfaces. It could be initially shown that in the presence of H_2O_2 and Br^- the V_2O_5 nanowires would inhibit the growth of gram-positive and gram-negative bacteria in culture conditions, and further it was shown that by applying the material in painted surfaces exposed to seawater conditions, fouling on the surfaces could be almost totally inhibited. The incredible versatility of the V_2O_5 material (H_2O_2 mediated oxidation and halogenation) make them an interesting product for technological applications, since they show an increased stability and versatility when compared to natural enzymes. Furthermore production of the material is economically more viable than the application of enzymes. V_2O_5 nanowires can be used either in a series of catalytic reactions with particular interest in organic chemistry (halogenation, oxidation) as well as in the development of antimicrobial/antifouling surfaces as it was shown.

Further work in this subject includes the study of the chlorination activity of the V_2O_5 nanowires, which could also have an interesting application in catalysis. On the other side the study of the influence of the particle structure and size on the catalytic activity is undergoing at the moment. This is of particular interest in order to simplify the synthesis of the material to make it economically interesting for the final applications. Also important is the study of materials of other compositions, as mentioned in chapter 1. Studies of molybdenum oxides and iron oxides as haloperoxidase mimics are also undergoing. Of course as an ultimate goal, it will be extremely interesting to understand to what extend nanoparticles can mimic the several different existing metal-center (and other) enzymes, since this topic has only started to be studied.

CHAPTER 8

Appendix

8.1 Supporting information

Chapter 2

NTA-dopamine polymer synthesis.

The poly (active ester) poly(pentafluorophenylacrylate) **PFA** was prepared as reported earlier[1,2]. GPC analysis of the obtained polymer (THF, light scattering detection) gave the following values: M_n = 29.7 kg/mol; M_w = 58.5 kg/mol, where the number of repeating units (246) is based on the M_w value. For the synthesis of the multifunctional poly (acrylamides), poly (active ester) **PFA** (110 mg, 0.46 mmol) was dissolved in 3 ml dry DMF. A solution of 3-hydroxytyramine hydrochloride (10.5 mg, 0.055 mmol) in 1.5 ml DMF and 0.1ml triethylamine was added and the clear mixture stirred for 1 hour at 50°C. In the next step amino-functionalized **NTA** (120 mg, 0.46 mmol) in 0.9 ml MilliQ water and 2.1 ml triethylamine were added and the resulting mixture kept at 50°C for 6 hours. The slight excess of **NTA** was used to ensure complete conversion of the remaining active ester groups. After removal of the DMF the pH of the solution was adjusted to 3 and the crude viscous product was cleaned by dialysis in MilliQ water, isolated and finally dried in a vacuum oven at 40°C for 1 hour. 64 mg of a white polymeric powder were obtained.

Polymer functionalization of TiO_2 nanowires.

Then 5 mg of TiO_2 nanowires were dispersed in 10 ml of benzyl alcohol and sonicated for 15 minutes. In a separate vial were dissolved 10 mg of polymer ligand in 10 ml of benzyl alcohol. Both suspension and solution were mixed under inert conditions and stirred at 60°C for four hours. Then polymer functionalized nanowires were isolated and purified by repeated washing with CH_2Cl_2 using centrifugation, followed by drying under vacuum and dispersing under water.

References

1 Theato, P.; *J. Polym. Sci. Part A: Polym. Chem.* **2008**, *46*, 6677-6687.

2 Shukoor, M. I.; Natalio, F.; Tahir, M. N.; Wiens, M.; Tarantola, M.; Therese, H. A.; Barz, M.; Weber, S.; Terekhov, M.; Schröder, H. C.; Müller, W. E. G.; Janshoff, A.; Theato, P.; Zentel, R.; Schreiber, L. M.; Tremel, W.; *Adv. Funct. Mater.* **2009**, *19*, 285-291.

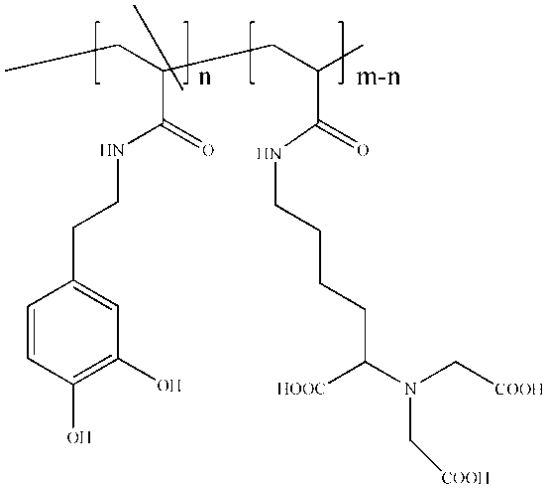

Figure S1. Structure of the multifunctional polymer used for binding His-tag silintaphin-1 to TiO_2 nanowires.

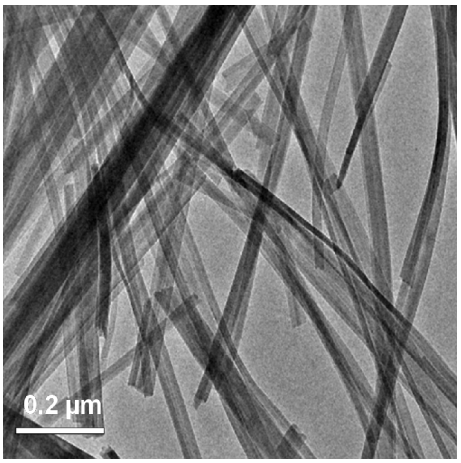

Figure S2. Overview TEM micrograph of as synthesized TiO_2 nanowires.

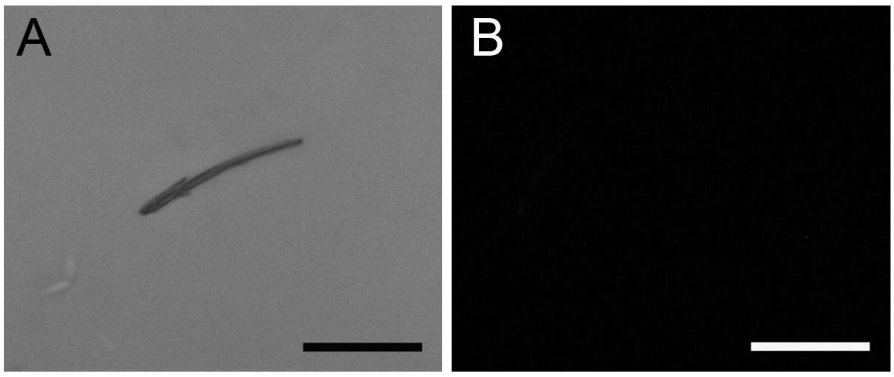

Figure S3. Optical and fluorescence microscopy images of the control experiments, where TiO_2 nanowires were submited to immunostaining with secondary labeled antibodies (Cy3) for silicatein. (A) Optical and (B) fluorescence imaging of nanowires incubated with histidine-tagged silicatein-α (with no ligands). No functionalization with the his-tag protein occurs.

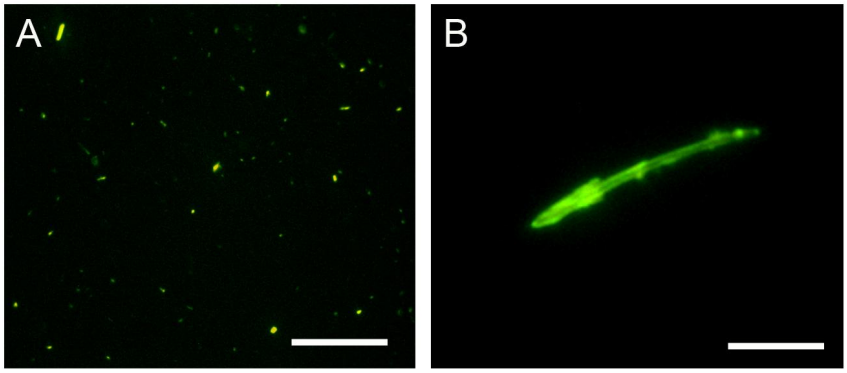

Figure S4. CLSM images of fluorophore (AlexaFluor 488) labelled silintaphin-1, immobilized on TiO_2 nanowires, using a NTA polymeric ligand. a) Overview image showing several functionalized nanowires. Scale bar 60 µm. b) Single TiO_2 nanowire were it is possible to see the globular presence silintaphin-1. Scale bar 2 µm.

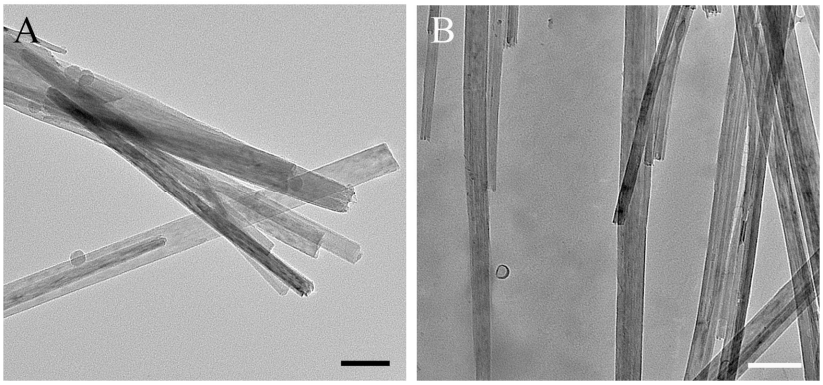

Figure S5. Control experiments with silintaphin only functionalized TiO_2 nanowires. A) Incubation with TEOS, 5 mM and B) incubation with K_2ZrF_6, 5 mM.

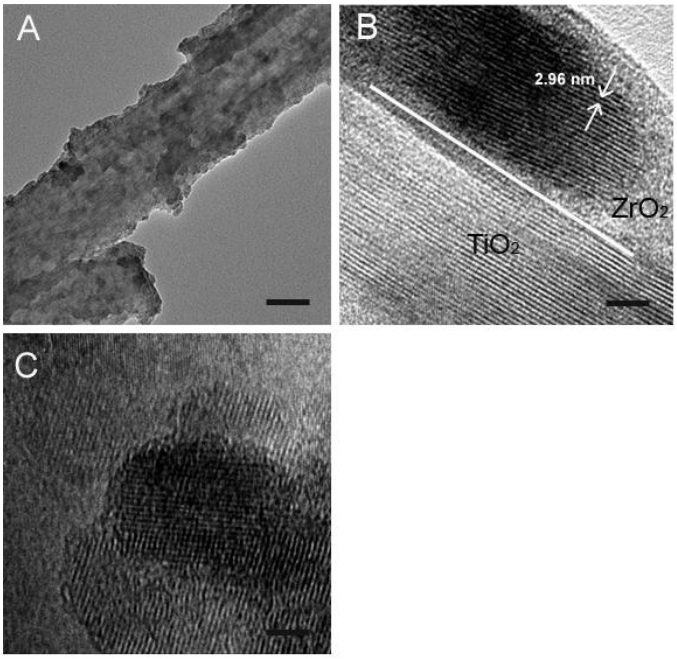

Figure S6. High resolution TEM images of zirconia covered TiO_2 nanowires, in the presence of silicatein-α and silintaphin-1. Overview of covered nanowire (A) and higher resolution images of interface of zirconia layer an

titania surface (B) and only the zirconia layer (C) where the fringe spacing is visible and a match to cubic zirconium dioxide. Scale bars: 70 nm in A, 20 nm in B and 15 nm in C.

Chapter 3

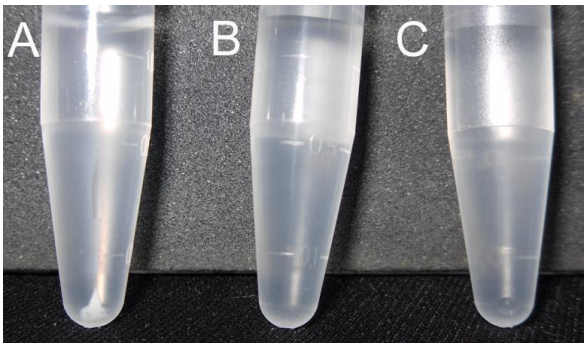

Figure S7. Optical image of reaction products A) in the presence of silicatein-α, B) using only buffer (TBS, pH 7.4) and C) using denaturated silicatein-α. Formation of a white precipitate (SnO_2) is only visible in the presence of functional silicatein (A).

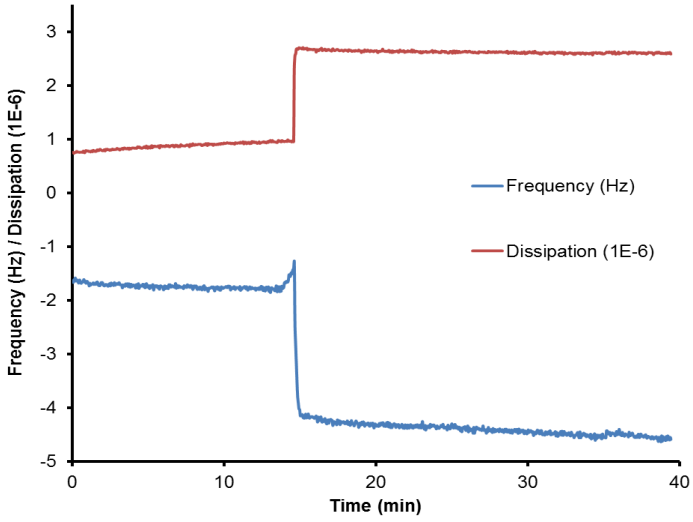

Figure S8. QCM analysis on non-functionalized sensors (absence of silicatein). Injection of precursor solution was performed at 15 minutes of analysis as visible in the sudden change in both frequency and dissipation values. After 25 minutes of incubation, no significant changes in the frequency or dissipation are observed, indicating that the precursor is stable when no protein is present.

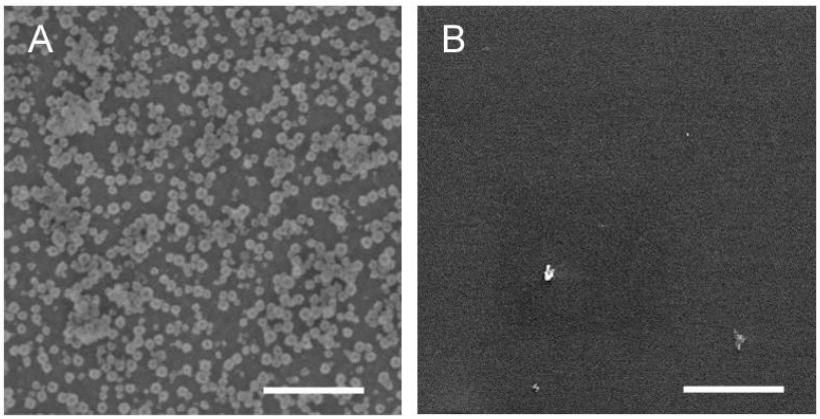

Figure S9. SEM images of QCM sensors after incubation with tin oxide precursor. A) In the presence of silicatein and B) control experiment in the absence of silicatein (referring to experiment in Figure S2).

Chapter 4

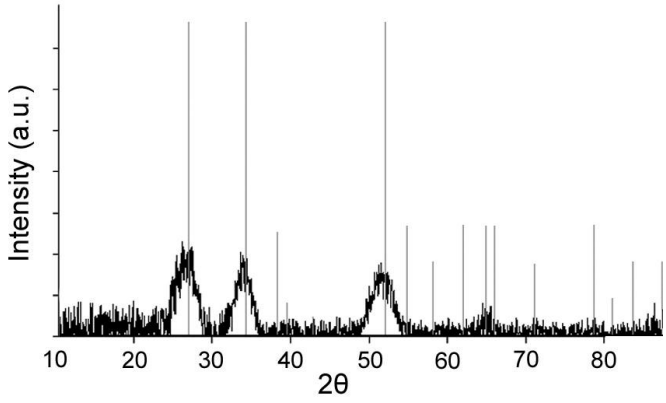

Figure S10 XRD pattern of as-synthesized product obtained with spermine and tin precursor (black line) and reported pattern for cassiterite SnO_2 (PDF-41-1445, gray line).

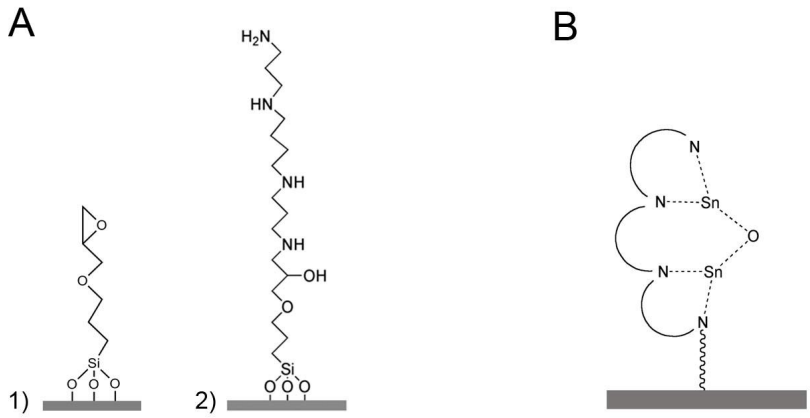

Figure S11 (A) Schematic representation of functionalization of glass surfaces with spermine. Steps of functionalization in A: 1) silanization of glass surface with epoxy terminated silane and 2) addition of spermine. (B) illustration of the proposed complexation process for SnO_2 on the amine functionalities.

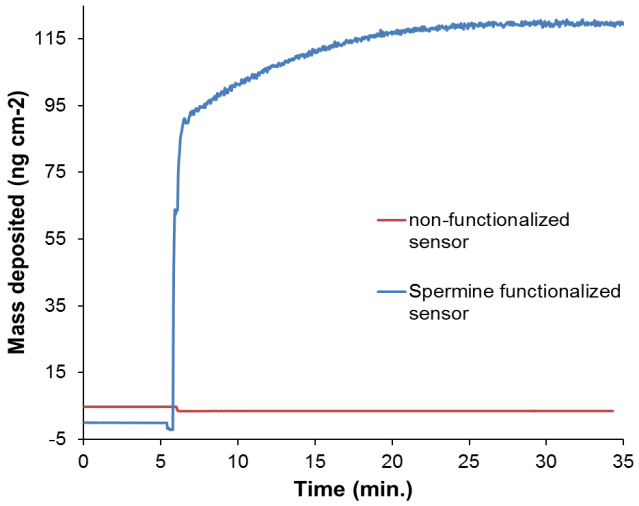

Figure S12 QCM measurement of SnO_2 deposition on spermine functionalized silica-based sensors (*blue line*) and on non-functionalized sensors (*red line*). Injection of water stable tin oxide precursor was made after 5 min as indicated by the sudden change in the mass (frequency) and dissipation values in the spermine functionalized glass-based sensors whereas no changes are observed on non-functionalized glass surfaces.

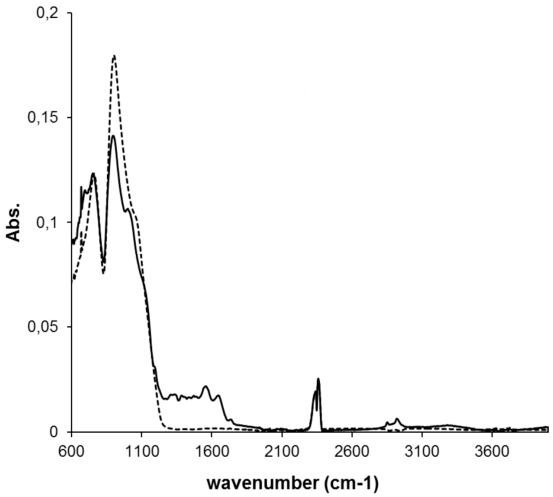

Figure S13 FTIR-ATR analysis of polyamine (spermine) functionalized glass surfaces (*solid line*) and non-functionalized glass surfaces (*dashed line*). The peaks after functionalization indicate the successful spermine immobilization.

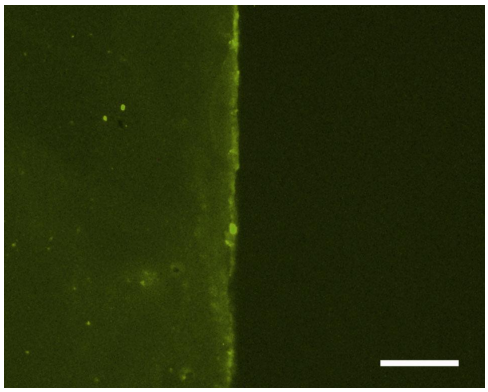

Figure S14 Detection of free amines on a spermine-functionalized surface, using FITC (fluorescein isothiocyanate). Half of the surface (right side) was covered with tape before funtionalization with spermine, while the left side was allow to incubate with spermine. On the left side the presence of a green fluorescence indicates the presence of free amine groups (from spermine). Sclae bar: 10 μm.

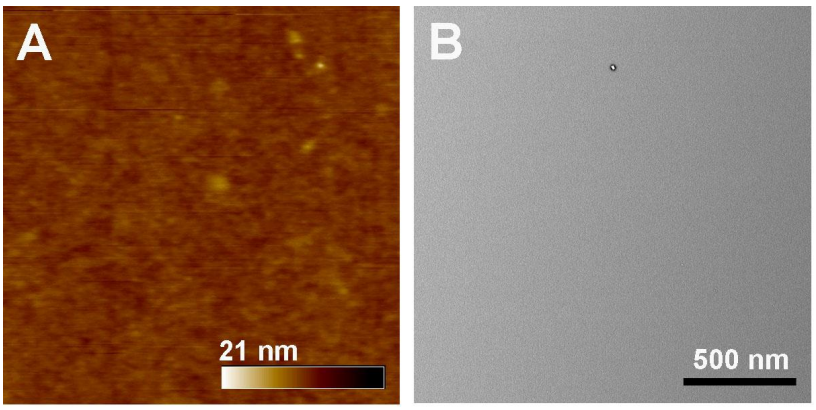

Figure S15 (A) AFM height analysis and (B) SEM micrograph of non-functionalized glass surfaces showing a relatively smooth surface.

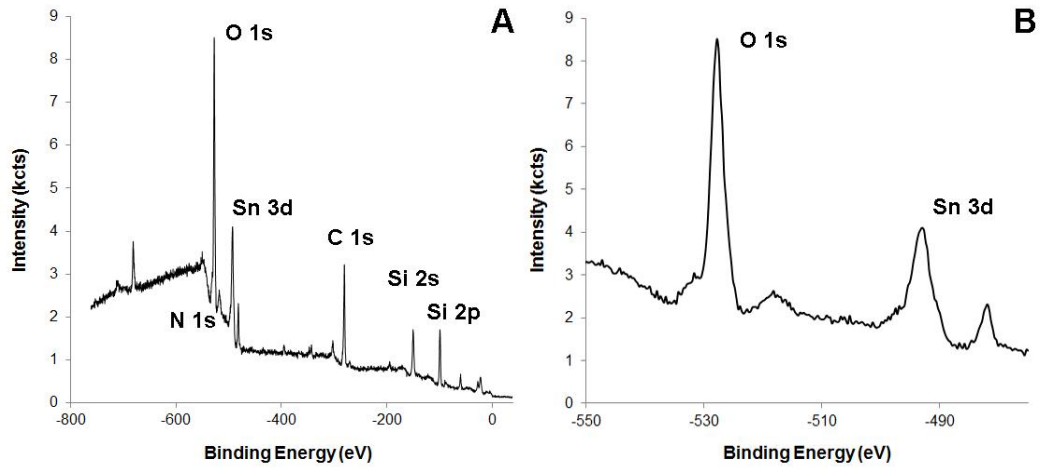

Figure S16 XPS analysis of tin oxide covered glass surface mediated by immobilized polyamines. (A) Full range spectra. (B) Zoom in of the area corresponding to Sn 3d and O 1s binding energies.

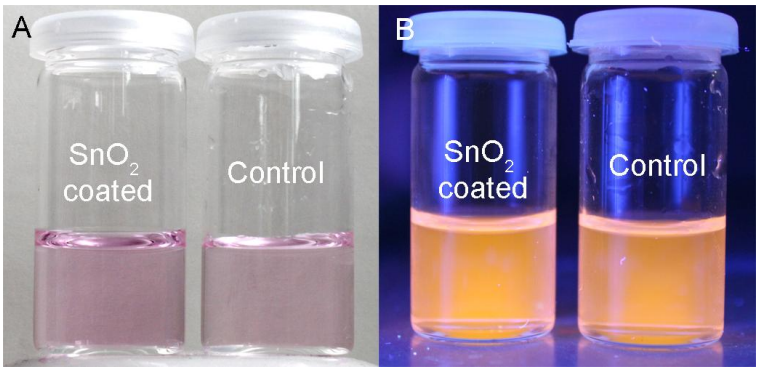

Figure S17 Control experiment for the photodegradation of rhodamine B by SnO_2 spermine-mediated coated glass vials. Both non-functionalized vial (left vial) and internal surface SnO_2 coated vial (right vial) were kept under dark conditions. From the digital images it can be observed that no photodegradation of the dye occurs in neither of the vials as confirmed by (A) normal light imaging and (B) under UV light (λ_{ex}=254nm)

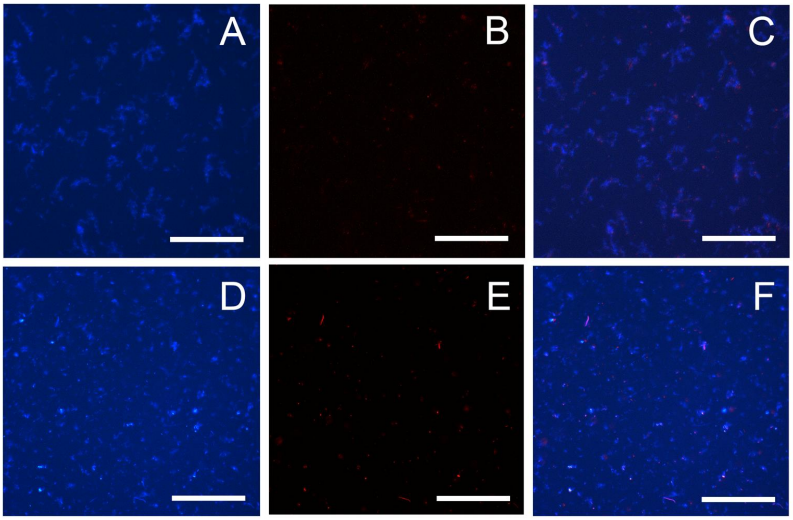

Figure S18 Incubation of non-functionalized glass surfaces with *E.coli*. (A) under dark conditions for 2 h at 37ºC and (D) after exposed to light for 30 min. A and D correspond to the staining with DAPI and B and E to the staining with PI. C and F are overlays of A/B and D/E respectively. No positive staining with PI was observed indicating that the bacterial cells remain viable on non-functionalized glass surfaces.

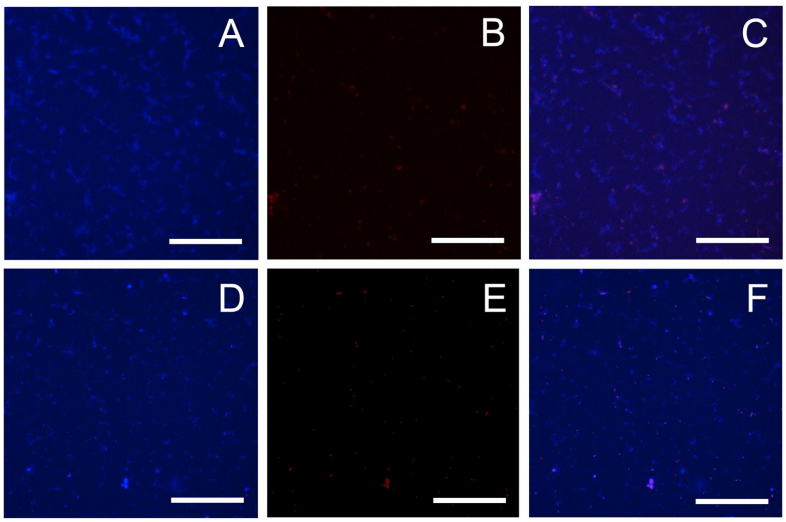

Figure S19 Incubation of SnO_2 spermine-mediated coating of glass surfaces with *E.coli* (**A**) under dark conditions for 2h (**A**) and for (**D**) 4h. **A** and **D** correspond to the staining with DAPI and **B** and **E** to the staining with PI. **C** and **F** are overlays of **A/B** and **D/E** respectively. No positive staining with PI was observed indicating that the bacterial cells remain viable and this surface is not toxic *per se*.

Chapter 5

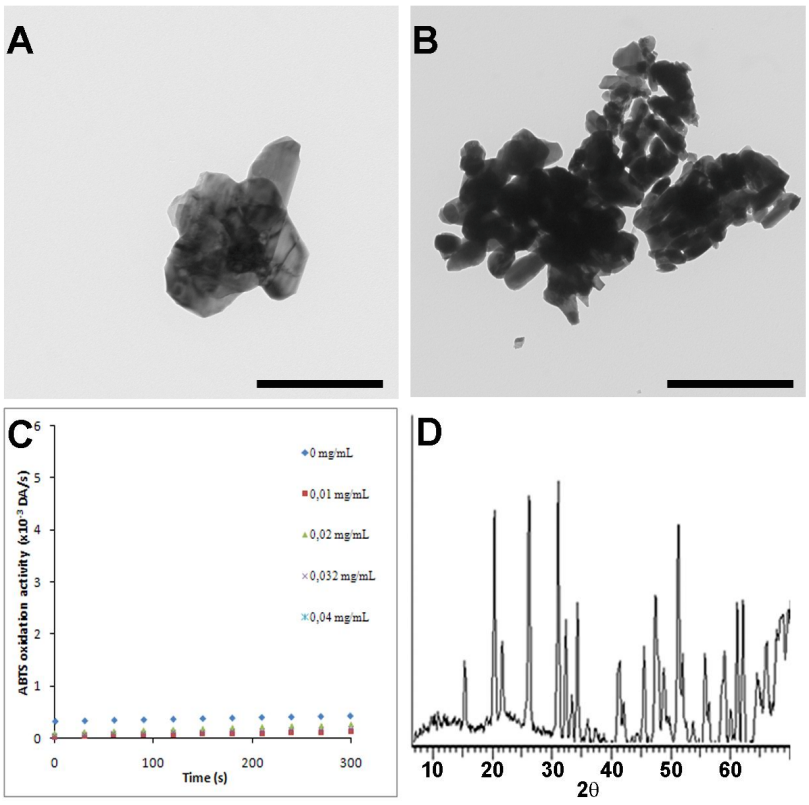

Figure S20 Structure and activity of commercially available bulk V_2O_5. **(A, B)** Transmission electron microscopic (TEM) images of bulk V_2O_5. Scale bar: 500nm. (**C**) ABTS oxidation activity dependency on bulk V_2O_5 concentration was determined by following the increase of absorbance at 405 nm, due to the formation of $ABTS^{*+}$, for 300s at 25ºC. The oxidation activity was carried out in acetate buffer (100 mM pH 4.0) using concentrations ranging of 0-0.04 mg/mL, ABTS (0.68 mM) and H_2O_2 (1 mM) was added to initiate the reaction. (**D**) XRD pattern of bulk V_2O_5

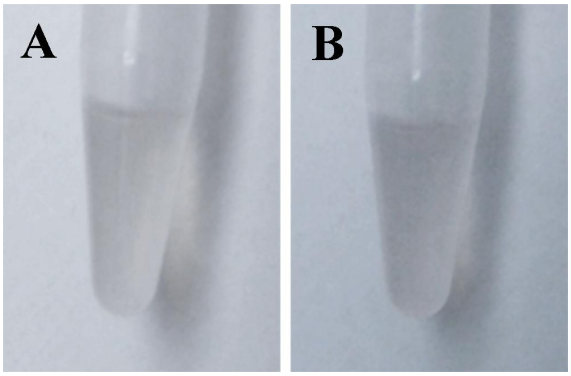

Figure S21 Digital images of ABTS oxidation reaction in the presence of (**A**) free orthovanadate anions VO_4^{3-} (10 µM prepared in distilled water) and (**B**) supernatant derived from an aqueous solution of V_2O_5 nanowires. In both cases, no reaction is observed (colorless solution).

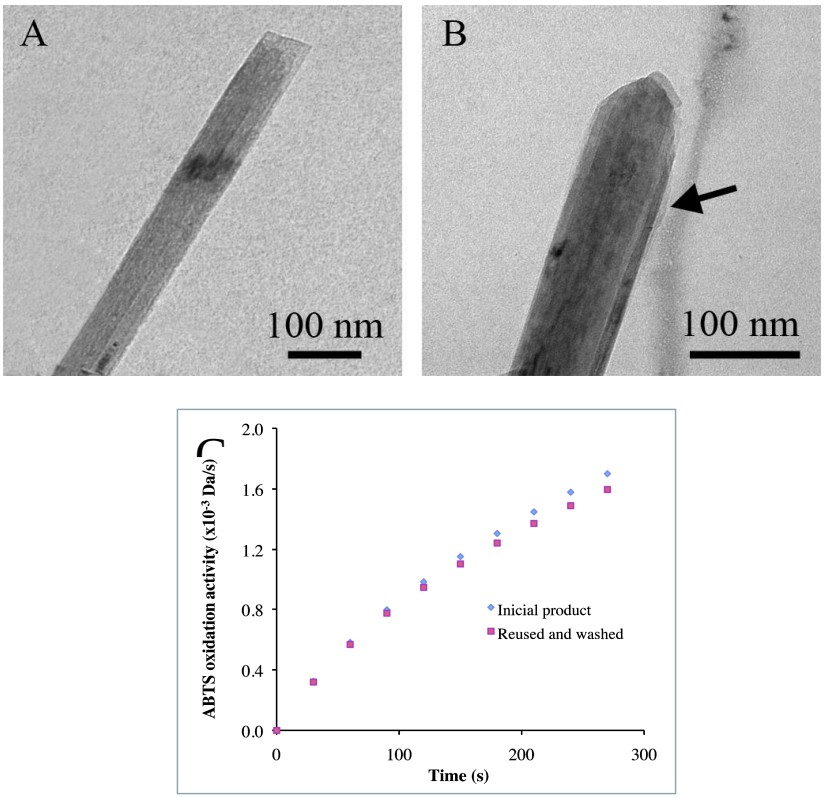

Figure S22 Trasmission electron microscope images of V_2O_5 nanowires taken after different re-utilization (catalytic) cycles. (**A**) as-prepared and (**B**) after 10^{th} catalytic cycles and intensively washed with a succession of organic solvents (hexane/acetone/ethanol). The black arrow indicates partial removal of surface layer on the V_2O_5 nanowires. (**C**) ABTS oxidation activity of V_2O_5 nanowires after 10 cycles and organic solvent washing was determined by following the increase of absorbance at 405 nm, due to the formation of $ABTS^{*+}$, for 300s at 25ºC. The oxidation activity was carried out in acetate buffer (100 mM pH 4.0) using 0.02 mg/mL of V_2O_5 nanowires, ABTS (0.68 mM) and H_2O_2 (1 mM) was added to initiate the reaction. For comparison purposes the as-prepared V_2O_5 nanowires were used. A reduction of only 8% on its catalytic activity can be observed.

Chapter 6

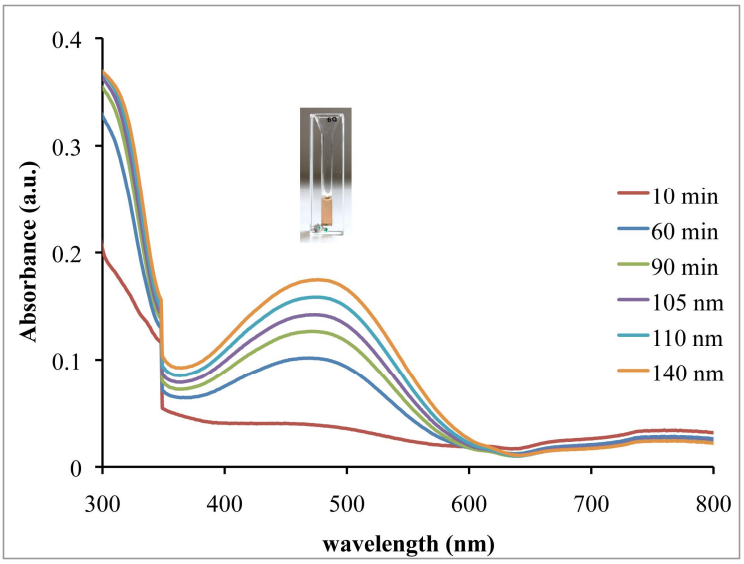

Figure S23 Time coursing of of bulk V_2O_5 (1 mg/mL) was mixed with KI (40 mM) and H_2O_2 (1 mM) in the presence of dopamine (10 mM) was carried out in aqueous solution at slightly basic pH values (pH 8.0) and monitored spectrophotometrically for 140 min (RT). Inset: digital images of reaction vial after 140 min reaction.

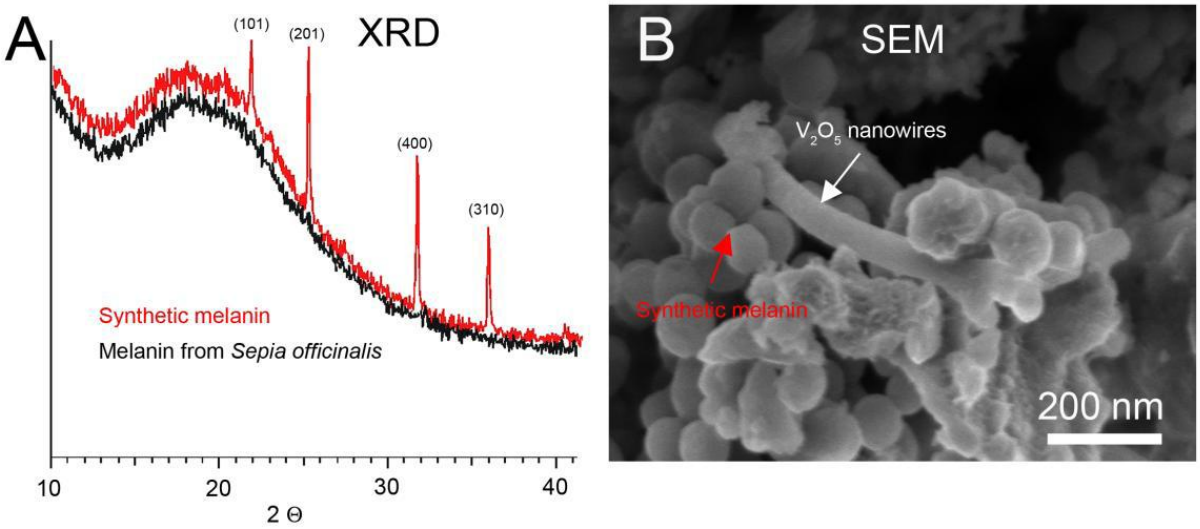

Figure S24 (A) XRD pattern of cuttlefish melanin (*Sepia officinalis*) (black line) and the black precipitate (red line) where reflections derived from the V_2O_5 nanowires can be observed. (B) SEM image of the black precipitate containing a V_2O_5 nanowire.

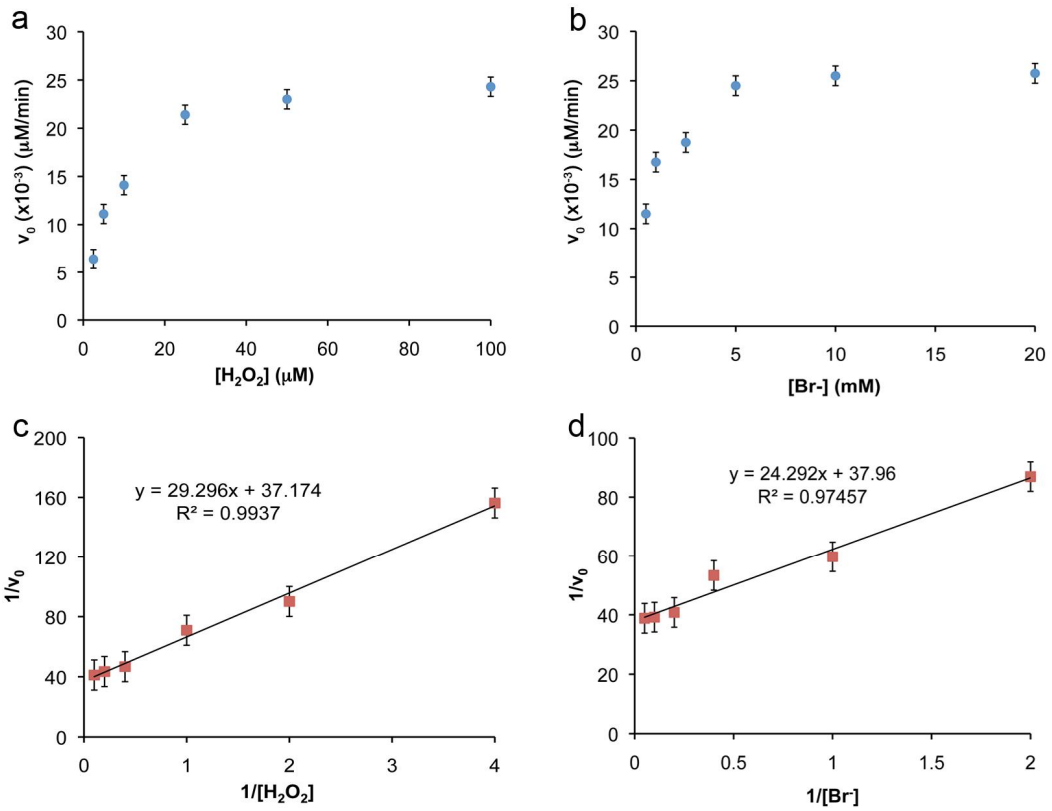

Figure S25 Steady-state kinetic experiments carried out by measuring the absorbance changes of the MCD at 290 nm ($\varepsilon_{290\ nm}$ =19.9 $mM^{-1}.cm^{-1}$) in *phosphate buffer* pH 8.2 for 180 s at 25±2ºC. Two independent sets of experiments were performed. a For the first set, the concentration of H_2O_2 was varied from 0 to 100 µM while keeping the concentration of Br^- (1 mM), V_2O_5 nanowires (0.02 mg/mL) and MCD (50 µM) constant. b For the second set of experiments, the Br^-concentrations were varied from 0 to 20 mM while keeping the other components constant, i.e., H_2O_2 (10 µM), V_2O_5 nanowires (0.02 mg/mL) and MCD (50 µM). Mean values of the initial bromination rates of three traces were used in the calculations. c and d The correspondent Lineweaver-Burk linearizations plots of initial rate values. The kinetic parameters calculated to be: V_{max}= 4.3x10^{-10} M.s^{-1}, k_{cat}= 4.3x10^{-6} s^{-1} and K_M values of 0.78 µM for H_2O_2 and 640 µM for Br^-. The k_{cat} was determined as follows: k_{cat} = V_{max} / [V_2O_5] and considering a concentration of 100 µM in the assay.

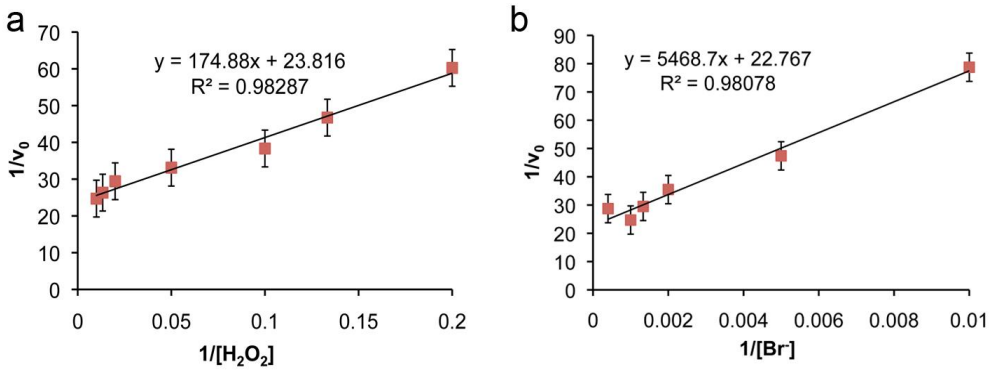

Figure S26 Lineweaver-Burk linearizations. (A) for different concentrations of H_2O_2 and (B) for different concentrations of Br^-.

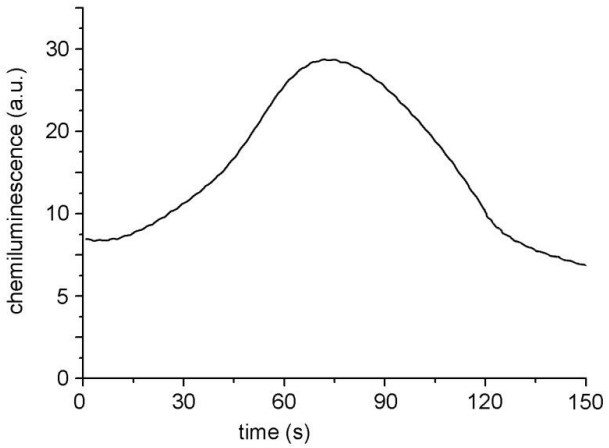

Figure S27 $^1O_2$ formation. The chemiluminescence derived from singlet oxygen ($^1O_2$,$^1\Delta_g$) transition to stable triplet ($^1O_2$, $^3\Sigma_g$) originated by V_2O_5 nanowires was measured at 1268 nm and in Tris-SO_4 buffer (100 mM, prepared in deuterium oxide, 99.994% purity) with an apparent pH (pH^{app}) of 8.3. The initial solutions of Br^-, H_2O_2 and V_2O_5 nanowires were also prepared in deuterium oxide (D_2O). The reaction was performed in the presence of V_2O_5 nanowires (0.2mg/mL), Br^- (1mM) and H_2O_2 (5mM) was added to start the reaction. A clear increase during the first 30 s is observed reaching its maximum at 75s and dropping afterwards due to H_2O_2 consumption.

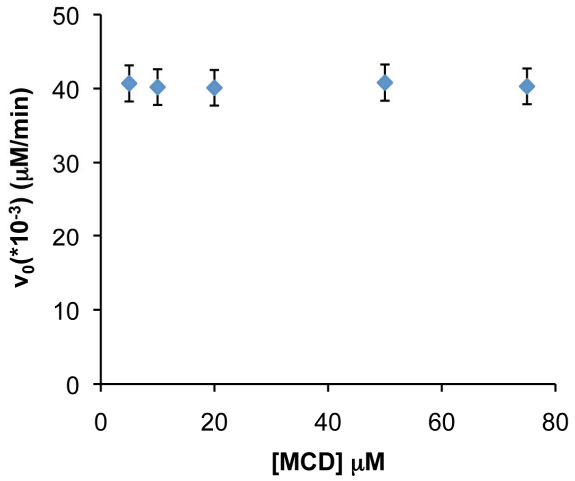

Figure S28 Dependence of the bromination activity of V_2O_5 nanowires on the MCD concentration. The measurement was carried out in 100 mM of Tris-SO_4 buffer at pH 8.3 by measuring absorbance changes of 2-chlorodimedone bromination at 290 nm (ε_{290nm} =19.9 mM^{-1} cm^{-1}) for 180 s. The concentrations of V_2O_5 nanowires (0.02 mg/mL), Br^- (1mM) and H_2O_2 (10μM) were kept constant but the concentrations of the concentrations of MCD were varied (5-75 μM). Mean values of the initial bromination rates of three traces were used in the calculations. The MCD concentration is independent of the intrinsic catalytic activity displayed by V_2O_5 nanowires.

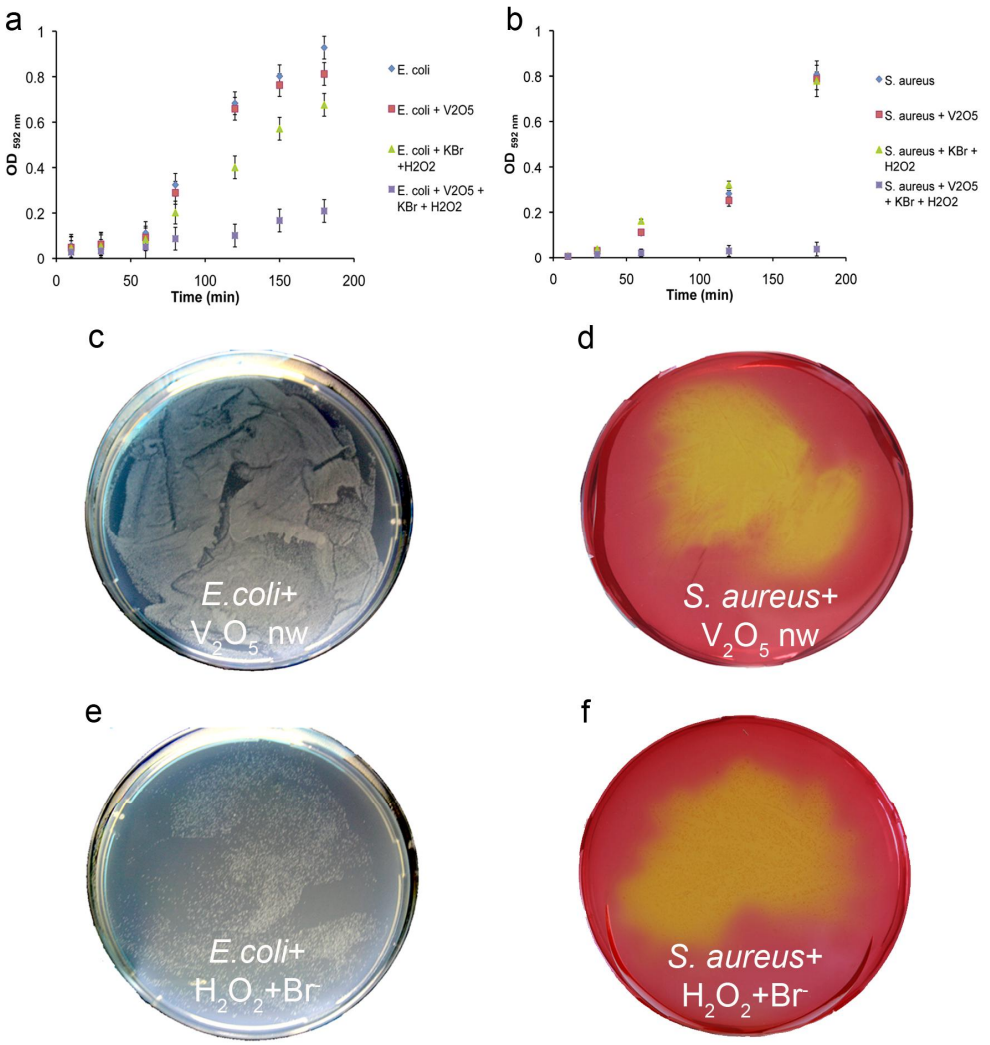

Figure S29 Bacterial growth curves. The OD was measured at 592 nm at different time points until 180 min. Experimental conditions: a *E. coli* (in LB medium), *E. coli* (in LB medium)+V_2O_5 nanowires (0.075 mg/mL), *E. coli* (in LB medium)+Br^- (1 mM)+H_2O_2 (10 µM) and *E. coli* (in LB medium)+V_2O_5 nanowires (0.075 mg/mL) +Br^-(1 mM)+H_2O_2 (10 µM). b *S. aureus* (in Brain Heart Infusion (BHI) medium), *S. aureus* (in Brain Heart Infusion (BHI) medium)+V_2O_5 nanowires (0.075 mg/mL), *S. aureus* (in Brain Heart Infusion (BHI) medium)+Br^-(1 mM)+H_2O_2 (10 µM) and *S. aureus* (in Brain Heart Infusion (BHI) medium)+V_2O_5 nanowires (0.075 mg/mL) +Br^- (1 mM)+H_2O_2 (10 µM). In both cases, a significant decrease in bacterial growth is observed in the latter sample as a consequence of HOBr formation. c and e Representative digital images of control experiments performed after incubation for 180 min at 37ºC and Agar-LB medium plating (incubation 8h at 37ºC). c *E. coli* co-incubated with V_2O_5 nanowires (0.075 mg/mL). No toxicity was observed. e *E. coli* co-incubated Br^-(1 mM) and H_2O_2 (10 µM). When Br^- and H_2O_2 were present a small decrease in bacterial growth was observed. d and f Representative digital images of control experiments performed after incubation for 180 min at 37ºC and Mannitol Salt Phenol Red Agar plating (incubated for 8h at 37ºC). d *S. aureus* co-incubated either with V_2O_5 nanowires (0.075 mg/mL). f Br^- (1 mM) and H_2O_2 (10 µM). Neither the bare V_2O_5 nanowires nor the bare substrates were toxic *per se*.

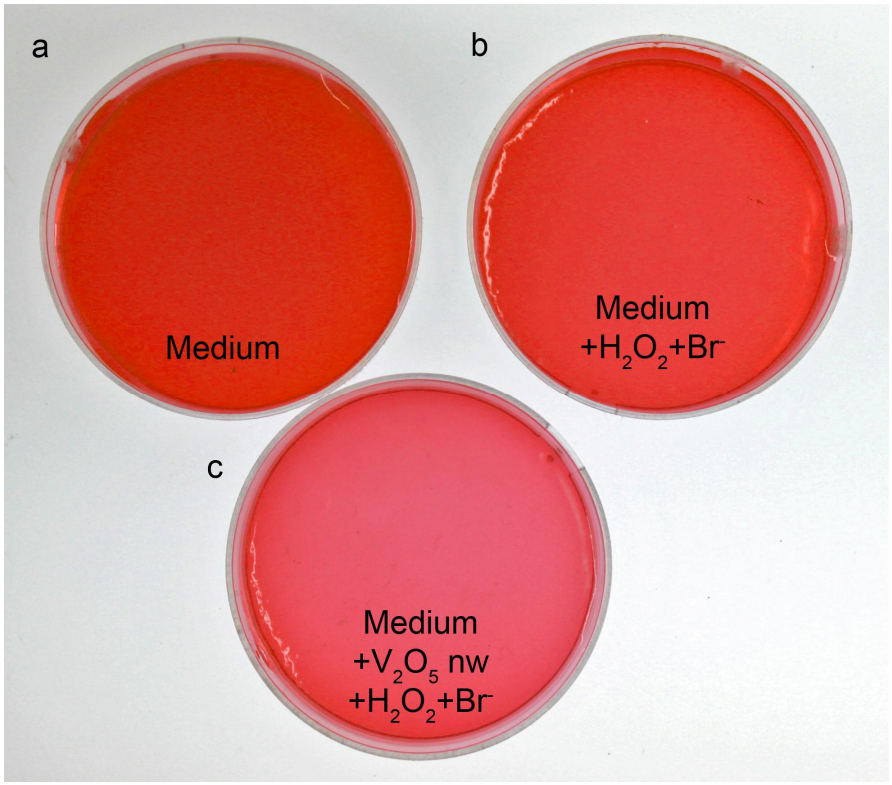

Figure S30 Bromination of phenol red contained in the Mannitol Salt Phenol Red Agar (*S. aureus* growth medium) by V_2O_5 nanowires after 8h incubation at 37°C. a Pure medium. b Medium to which H_2O_2 (10 μM) and Br^- (1mM) were added. No significant color changes occur. c Medium to which V_2O_5 nanowires (0.02m/mL), H_2O_2 (10 μM) and Br^- (1mM) were added. A significant color change is observed due to the V_2O_5 mediated formation of HOBr that diffuses and reacts strongly with phenol red converting it to bromophenol. This data confirms that the V_2O_5 nanowires, in the presence of H_2O_2 and Br^-, display an intrinsic brominating activity.

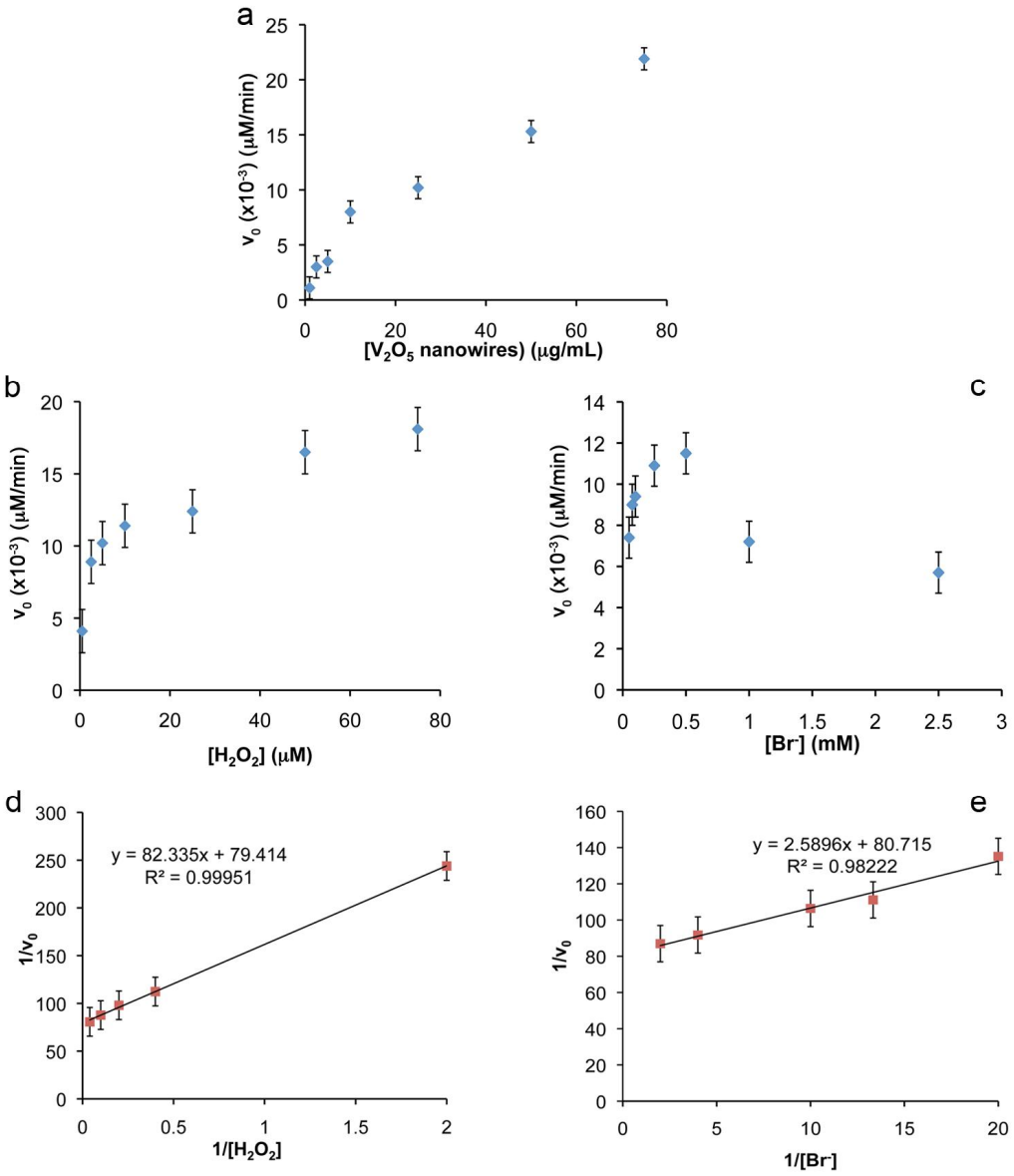

Figure S31 Steady-state kinetic experiments of the brominating activity of V_2O_5 nanowires in seawater. The rate of the reaction was determined by measuring the absorption changes of the MCD at 290 nm ($\varepsilon_{290\ nm}$ =19.9 $mM^{-1}.cm^{-1}$) in sterile filtered seawater for 180 s at 25±2ºC. a Variation of the V_2O_5 nanowires (0-0.08mg/mL) while keeping the Br^- and H_2O_2 concentrations constant. Two independent sets of experiments were performed. b For the first set, the concentration of H_2O_2 was varied from 0 to 80 µM while keeping the concentration of Br^- (1 mM), V_2O_5 nanowires (0.02 mg/mL) and MCD (50 µM) constant. c For the second set of experiments, the Br^- concentrations were varied from 0 to 5 mM while keeping the other components constant, i.e., H_2O_2 (10 µM), V_2O_5 nanowires (0.02 mg/mL) and MCD (50 µM). Mean values of the initial bromination rates of three traces were used in the calculations. d and e Corresponding Lineweaver-Burk linearization plots of the initial rate values. Extracted kinetic parameters: V_{max}= 2.1x10^{-10} M.s^{-1}, k_{cat}= 2.1x10^{-6} s^{-1} and K_M values of 1.04 µM for H_2O_2 and 32 µM for Br^-, respectively The k_{cat} was determined as follows: $k_{cat} = V_{max} / [V_2O_5]$ and considering a

concentration of 100 μM in the assay.

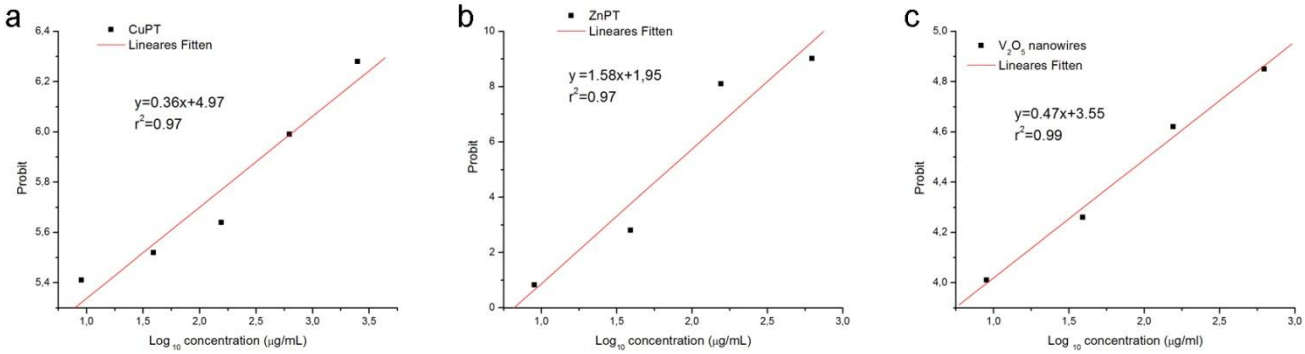

Figure S32 Bioassays/acute toxicity (24h LD_{50}). The dose response curve was build for: a CuPT, b ZnPT and c V_2O_5 nanowires. The acute toxicity (24h, LD_{50}) was determined by Probit linearization: 0.0012, 0.085 and 1.2 mg/mL for CuPT, ZnPT and V_2O_5 nanowires, respectively.

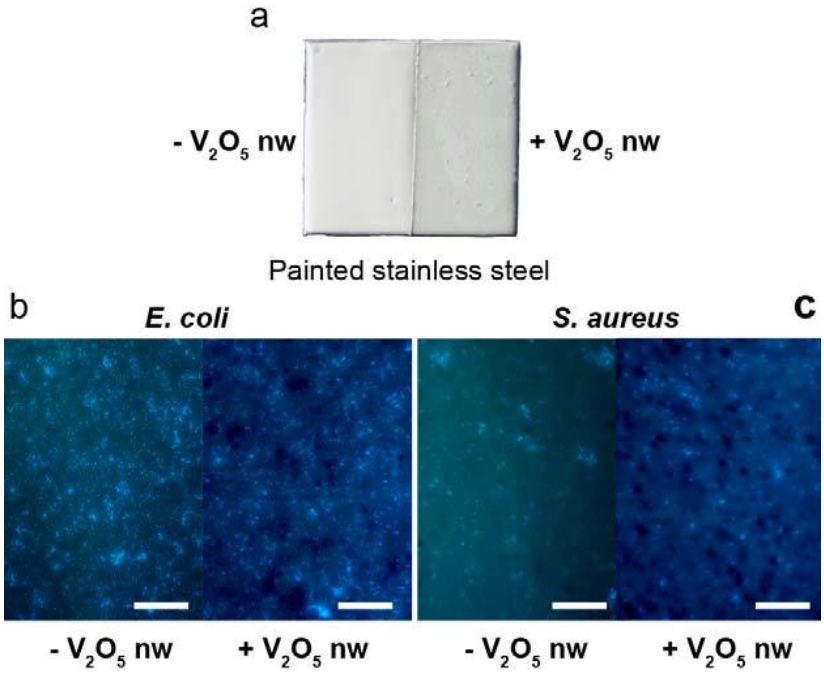

Figure S33 Potential biotechnological application of V_2O_5 nanowires as additive for marine paints with antibacterial/antifouling properties. a Digital images of stainless steel plate (2x2cm) after painting with commercially available paint for boat hull (white left half, -V_2O_5 nanowires) and the same supplemented with V_2O_5 nanowires (greenish right half, + V_2O_5 nanowires). b and c Bacterial cell density/adhesion evaluated by fluorescence microscopy on the different halves of painted stainless steel plates. The images were acquired after 4 days of incubation of bacterial suspensions at 37ºC in the presence of Tris-SO_4 (100 mM, pH 8.3) but in the absence of Br^- (1 mM) and H_2O_2 (10 μM). In the images on the left the observed dark spots are V_2O_5 nanowires clusters. No significant decrease of bacterial cells adhesion is observed indicating that the V_2O_5 nanowires are not toxic per se and is active only the presence of the correspondent substrates (Br^- and H_2O_2). Scale bar: 100 μm.

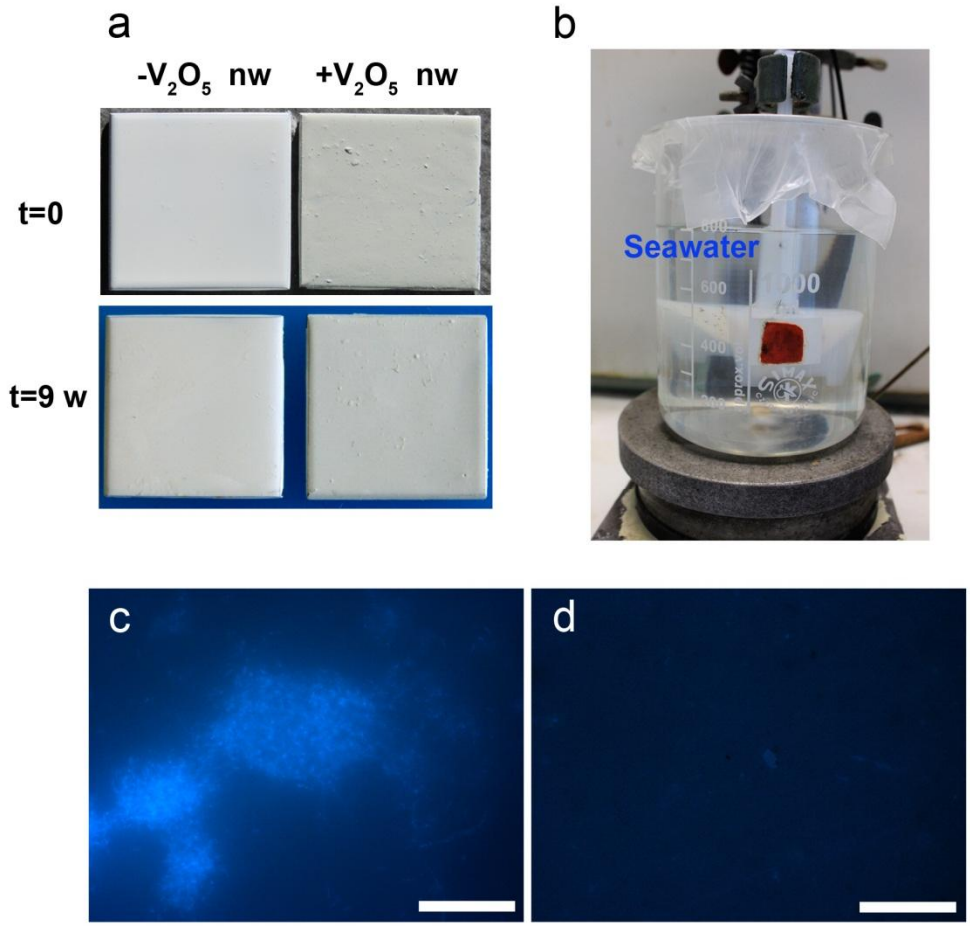

Figure S34 a Stainless steel plates painted with commercial available boat paint (white, -V_2O_5 nw, left) without and with V_2O_5 nanowires (greenish, +V_2O_5 nw, right) before incubation with sterile filtered seawater (t=0). After 9 weeks of incubation under simulated marine environment (t=9 weeks) the stainless steel plates painted with commercially available paint (white, -V_2O_5 nw, left) and commercially available paint supplemented with V_2O_5 nanowires (greenish, +V_2O_5 nw, right) were retrieved and signs of degradation were not observed. b Digital imaging showing the set up for mimicking seawater conditions. The plates were immersed vertically in seawater and left at room temperature for 9 weeks with slow stirring. Additional fresh H_2O_2 (10 μM) and Br^- (1 mM) was given at certain time periods. c and d Fluorescent microscopy images of bacterial cell (*E. coli*) density/adhesion on stainless steel plates painted with commercial available boat paint without (c) and with (d) V_2O_5 nanowires after immersion for 9 weeks in sterile filtered seawater supplemented with additional Br^- (1 mM) and H_2O_2 (10 μM). The V_2O_5 supplemented painted surface (d) shows a large decrease of bacterial cell (*E.coli*) coverage compared with commercially available paint (c) highlighting the efficiency and durability of the V_2O_5 nanowires. Scale bar: 50 μm.

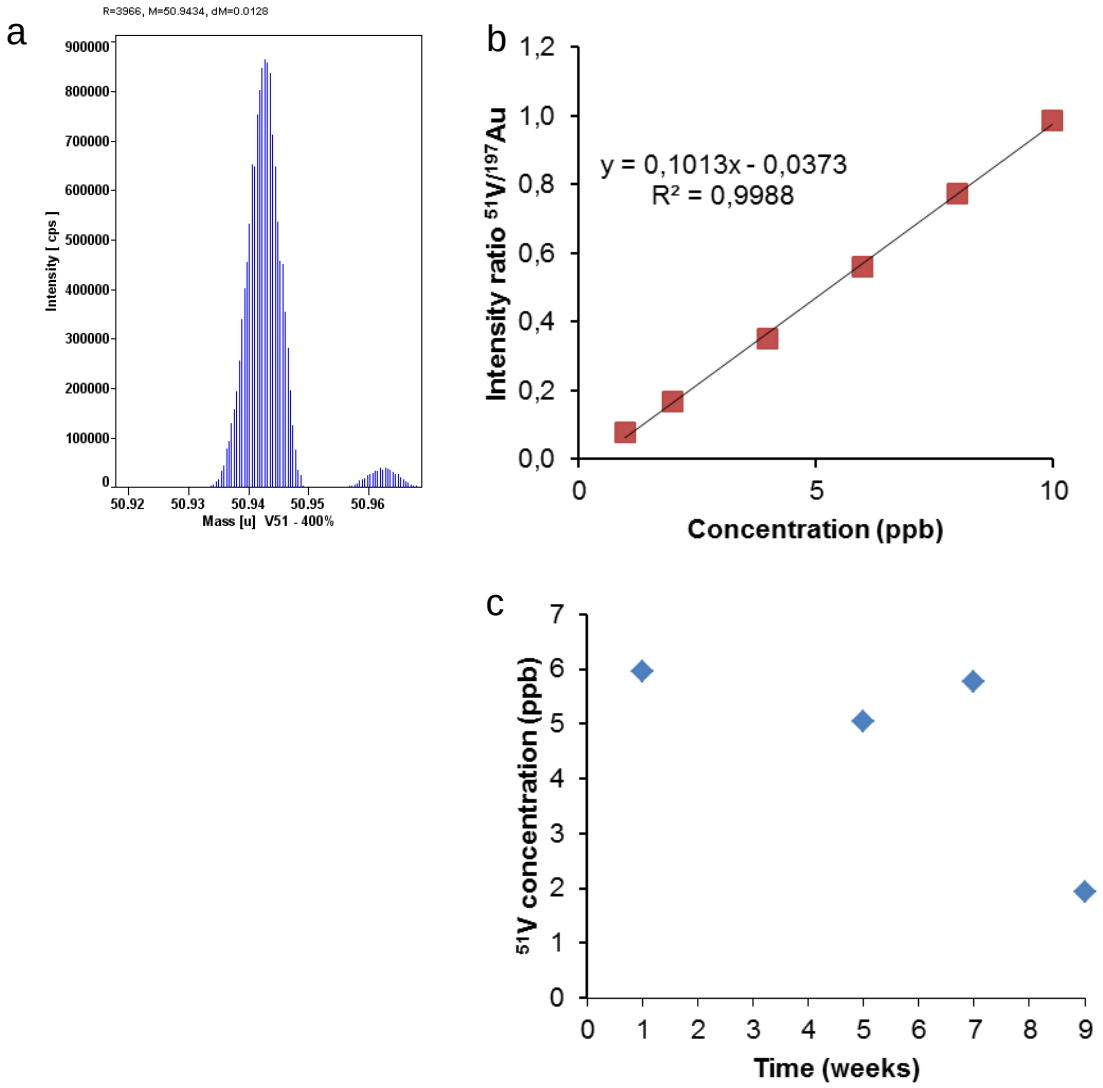

Figure S35 Vanadium leaching studies using ICP-MS. a Mass spectrum at mass number 51 obtained from the 6 ppb V standard solution (in 2% HNO_3) using a mass resolution of about 4000 of the ICP-MS. The high mass resolution separates the ^{51}V peak (left) from the disturbing $^{16}O^{35}Cl$ molecular peak (right less intense). b Calibration curve of V concentration (ppb).*vs.* $^{51}V/^{197}Au$ ratio intensity. A solution of Au (10 ppb) was used for internal standardization. Calibration curve concentration of intensity of the $^{51}V/^{197}Au$ ratio versus concentration (ppb). A solution of Au (10 ppb) was used as internal standard. All values were corrected for residual values of V and Au present in the blank solution (distilled water with HNO_3). c Stainless steel plates painted with a paint formulation containing V_2O_5 nanowires were exposed to simulated marine environment conditions (sterile filtered artificial seawater) for 9 weeks with periodic addition of H_2O_2 (10 µM) and Br^- (1mM). Aliquots (5 mL) were removed periodically at week 1, 5, 7 and 9. The samples were further treated to remove salts, acidified using 2% HNO_3, trace metals such as vanadium were specifically extracted by ion exchange (SPR-IDA) chromotography and the vanadium content determined. After the 9th week a significant decay in V leaching is observed.